DISSERTATION

PRECIPITATION OBSERVATIONS FROM HIGH FREQUENCY SPACEBORNE POLARIMETRIC SYNTHETIC APERTURE RADAR AND GROUND-BASED RADAR: THEORY AND MODEL VALIDATION

Submitted by

Jason P. Fritz

Department of Electrical and Computer Engineering

In partial fulfillment of the requirements

for the Degree of Doctor of Philosophy

Colorado State University

Fort Collins, Colorado

Fall, 2010

Doctoral Committee:

Department Head: Anthony A. Maciejewski

Advisor: V. Chandrasekar
Anura P. Jayasumana
Branislav M. Notaros
Paul W. Mielke

ABSTRACT OF DISSERTATION

PRECIPITATION OBSERVATIONS FROM HIGH FREQUENCY SPACEBORNE POLARIMETRIC SYNTHETIC APERTURE RADAR AND GROUND-BASED RADAR: THEORY AND MODEL VALIDATION

Global weather monitoring is a very useful tool to better understand the Earth's hydrological cycle and provide critical information for emergency and warning systems in severe cases. Developed countries have installed numerous ground-based radars for this purpose, but they obviously are not global in extent. To address this issue, the Tropical Rainfall Measurement Mission (TRMM) was launched in 1997 and has been quite successful. The follow-on Global Precipitation Measurement (GPM) mission will replace TRMM once it is launched. However, a single precipitation radar satellite is still limited, so it would be beneficial if additional existing satellite platforms can be used for meteorological purposes. Within the past few years, several X-band Synthetic Aperture Radar (SAR) satellites have been launched and more are planned. While the primary SAR application is surface monitoring, and they are heralded as "all weather" systems, strong precipitation induces propagation and backscatter effects in the data. Thus, there exists a potential for weather monitoring using this technology. The process of extracting meteorological parameters from radar measurements is essentially an inversion problem that has been extensively studied for radars designed to estimate these parameters. Before attempting to solve the inverse problem for SAR data, however, the forward problem must be addressed to gain knowledge on exactly how precipitation impacts SAR imagery. This is accomplished by simulating storms in SAR data starting from real measurements of a storm by ground-based polarimetric radar. In addition, real storm observations by current SAR platforms are also quantitatively analyzed

by comparison to theoretical results using simultaneous acquisitions by ground radars even in single polarization. For storm simulation, a novel approach is presented here using neural networks to accommodate the oscillations present when the particle scattering requires the Mie solution, i.e., particle diameter is close to the radar wavelength. The process of transforming the real ground measurements to spaceborne SAR is also described, and results are presented in detail. These results are then compared to real observations of storms acquired by the German TerraSAR-X satellite and by one of the Italian COSMO-SkyMed satellites both operating in co-polar mode (i.e., HH and VV). In the TerraSAR-X case, two horizontal polarization ground radars provided simultaneous observations, from which theoretical attenuation is derived assuming all rain hydrometeors. A C-band fully polarimetric ground radar simultaneously observed the storm captured by the COSMO-SkyMed SAR, providing a case to begin validating the simulation model. While previous research has identified the backscatter and attenuation effects of precipitation on X-band SAR imagery, and some have noted an impact on polarimetric observations, the research presented here is the first to quantify it in a holistic sense and demonstrate it using a detailed model of actual storms observed by ground radars. In addition to volumetric effects from precipitation, the land backscatter is altered when water is on or near the surface. This is explored using TRMM, Canada's RADARSAT-1 C-band SAR and Level 3 NEXRAD ground radar data. A weak correlation is determined, and further investigation is warranted. Options for future research are then proposed.

ACKNOWLEDGEMENTS

This work was funded by NASA Earth and Space Science Fellowship Program - Grant NNX07AO55H. TerraSAR-X data were purchased from DLR under their science program, and additional thanks goes to the DLR scientists who answered questions and granted the proposal award in order to conduct this research. COSMO-SkyMed data were obtained through a proposal to ASI whose principal investigator is Luca Baldini at the Institute of Atmospheric Sciences and Climate (ISAC) of the Italian National Research Council (CNR). Dr. Baldini was also critical for scheduling the CSK acquisitions and obtaining answers to technical questions regarding the data, plus he provided valuable insight into the effect of precipitation on C-band polarimetric radars and theoretical conversion to X-band. Bric della Croce radar data were provided by Renzo Bechini at Arpa Piemonte in Turino, Italy who provided valuable assistance in dealing with the data and some of the nuances of their radar system. WSR-88D data were provided by the NOAA National Climatic Data Center. Vexcel, a Microsoft Company, provided software for polarimetric visualization and analysis plus focusing and geocoding of RADARSAT-1 data. Vexcel also provided an environment within which I was able to learn the foundations of SAR from Marty Marra, Alan FitzGerrell, Marzban Palsetia and John Beaver. TSX processing in Doris advice was provided by the University of Miami's Space Geodesy Lab, namely from Batu Osmanoglu. RADARSAT-1 data was provided by the Alaska Satellite Facility through their science program. Thanks also goes to Leon Tolstoy for translating one of the classic Pichugin articles from Russian. Some material presented here and in my oral presentations was graciously provided by Ramon Hanssen at Delft University of Technology and by Richard Bamler at DLR. In addition, I would like to thank Andreas Danklmayer from DLR who encouraged me to submit my work to the 2009 EUCAP and for several discussions related

to observing precipitation with SAR. Most importantly, however, I would like to thank my advisor, Prof. Chandra, for his philosophy of educating PhD students, and his guidance and wisdom over the years I have been at CSU. To learn more about this research, I can be reached at jpfritz@ieee.org.

DEDICATION

To my wife, Sandy, whose love and support made this possible.

To my daughters Amelia, Nikelle and Kalyn born during this pursuit who added further inspiration to complete it.

To my mother, Susan, who always encouraged me to strive for excellence.

In memory of my father, Anthony (1944-2009), who was unable to witness the fulfillment of my goal, but whose spirit will always be with me. May he rest in peace.

TABLE OF CONTENTS

LIST OF FIGURES

LIST OF TABLES

CHAPTER 1

INTRODUCTION

Any intelligent fool can make things bigger and more complex...
It takes a touch of genius - and a lot of courage to move in the opposite direction.

- Albert Einstein

1.1 Motivation and Background

Synthetic Aperture Radars (SAR) were designed for surface monitoring. A slant angle viewing geometry and Doppler processing provide exceptionally high resolution in the cross-track and along-track directions respectively. Processed SAR data appears similar to optical images, hence, they are often referred to as imaging radars. However, one distinct advantage of a SAR over optical sensors is the ability to generate quality data at night and in the presence of clouds and storms. Through the use of interferometric capabilities and multiple polarizations, detailed structures of a dynamic planetary surface can be analyzed. Applications include digital elevation model (DEM) generation (including extraterrestrial bodies such as Mars and the moons of Earth and Jupiter), surface deformation monitoring (volcanology, plate tectonics, subsidence, glacier movement, etc.), vegetation and soil study, snow and ice characteristics, oil slick detection, ocean current monitoring, change detection, and target detection [Oliver and Quegan (2004); Curlander and McDonough (1991); Cumming and Wong (2005)]. As recently as February 2010, a NASA SAR aboard India's Chandrayaan-1 spacecraft detected water near the north pole of the moon [NASA (2010)]. At microwave wavelengths greater than 4 cm, precipitation has a very minor impact on the SAR images, although phase delays through severe storms can appear as subsidence signatures in C-band interferometry. However, at X-band and shorter wavelengths, hydrometeors

can alter data characteristics by introducing attenuation and additional backscatter. For traditional applications, this is considered clutter, much the way precipitation echoes were classified in very early radar systems. Upon studying the problem, though, an entire branch of radar application (radar meteorology) was formed and has become invaluable for studying and forecasting weather. With newer high resolution SAR systems, it is conceivable that investigation of precipitation from SAR could lead to important insights into storm structure and contribute to radar meteorology.

Observations of meteorology from spaceborne radar actually began with early SAR missions. Atlas (1994) analyzed storms over the ocean as observed by the SEASAT satellite [Born et al. (1979)]. Atlas and Moore (1987) also developed theoretical expressions to measure precipitation using SAR while Pichugin and Spiridonov (1985) presented a geometric model from a real aperture side looking radar. In 1994, NASA Space Shuttle Radar Laboratory (SRL) missions provided the first multi-polarization, multi-frequency radar observations of precipitation from space [Moore et al. (1997); Jameson et al. (1997); Melsheimer et al. (1998)]. Observations of storms were made both at traditional SAR look angles and at nadir in preparation for the highly successful Tropical Rainfall Measurement Mission (TRMM), a joint project launched in 1997 between the National Aeronautics and Space Administration (NASA) and the Japanese Aerospace Exploration Agency (JAXA) [Kummerow et al. (1998); Liu et al. (2008)]. Building on the success of TRMM, the follow-on Global Precipitation Measurement (GPM) [Bundas (2006)] mission scheduled to be launched in 2013. In addition to microwave radiometers, a dual-frequency (Ku/Ka band) nadir scanning radar will provide the core satellite of GPM with a more detailed precipitation measurement instrument. However, the X-band SAR that was part of the SIR-C/X-SAR missions had only one polarization: vertical. These studies showed the potential of SAR for precipitation measurement, especially at and above the X band where the signal is attenuated the most. C-band SAR observations of storms over the ocean have also been compared with ground-based weather radar [Lin et al. (2001); Melsheimer et al. (2001)], where the homogeneous background simplifies the estimation of the attenuation caused by the precipitation.

Since the turn of the century, several X-band SAR (X-SAR) missions have been successfully launched or are planned for the near future, providing new opportunities to investigate global precipitation with high resolution spaceborne radar. In 2007, the Deutches Zentrum für Luft und Raumfahrt (DLR or German Aerospace Center) launched the multi-polarization X-SAR, TerraSAR-X (TSX) and are planning the follow-on mission TanDEM-X. The year 2007 also saw the launch of the first two of four satellites in the COSMO-SkyMed multi-polarization X-SAR constellation by the Agenzia Spaziale Italiana (ASI or Italian Space Agency). As of August 2009, three COSMO-SkyMed systems are orbiting the planet. Within the next several years more X-SARs will be launched by Korea (KOMPSat-5), Russia (Severjanin on METEOR-M) and others. In addition, Ku-band SAR can also be used, such as the planned European Space Agency (ESA) CoReH2O mission with X-band and Ku-band dual polarized SARs [Hélière et al. (2010)] and the Cassini spacecraft sent to observe the Titan moon of Saturn. As a result of these new sensors, and the fact that precipitation has more of an impact on shorter wavelengths, renewed interest in SAR precipitation measurement has surfaced. Danklmayer et al. (2008) reported the first images of storms observed by TSX during the commissioning phase, and the first polarimetric storm observations at X band were described in Fritz and Chandrasekar (2009c). Meanwhile, Marzano, Weinman et al. [Marzano et al. (2006); Marzano and Weinman (2008); Weinman and Marzano (2008)] have made progress on model-based inversion algorithms. Currently, however, the algorithms assume that the surface backscatter is constant, or at least from a single distribution.

1.2 Problem statement

Characterizing precipitation from space-based radar is a growing field. Currently, there is only one orbiting precipitation radar (TRMM-PR) and one planned for future launch (GPM). However, considering the number of X-band SAR satellites orbiting the planet, or in the planning stage, it would be beneficial if they could be used to investigate storms as well. Creation of models to study precipitation from X-SAR is only in its infancy and multi-polarization models do not exist. Once a thorough understanding of how storms affect SAR data is established, then researchers can proceed to investigate the inverse problem of

estimating parameters such as rain rate from SAR observations. The fundamental challenge lies in the use of a 2D surface imaging radar to observe 3D volumetric targets. Based on theory developed for ground validation of the TRMM rainfall estimation algorithms and known radar wave propagation through precipitation, however, it is possible to extend this to the slant viewing geometry of SAR to predict how a storm will ultimately affect the SAR products. In addition to providing another sensor to observe storms, an accurate model can be used to help mitigate the impact of storms for more traditional uses of SAR where attenuation and backscatter caused by hydrometeors are considered clutter. One of the more difficult problems to deal with when estimating precipitation induced attenuation using surface backscatter, though, is estimating what the observations would be by removing only the volumetric component. This involves understanding how the water in or near the surface modifies the backscatter, and this is very dependent upon the contents of the ground cover and soil.

1.3 Research objectives

There are a number of objectives for this research with the primary goal to establish how precipitation effects multi-polarization SAR imagery at frequencies in X-band and higher in a quantitative fashion. One objective is to develop a microphysics-based model to simulate storm observations from a short wavelength spaceborne radar using real ground-based polarimetric radar data. Another objective is to analyze and compare model results to real polarimetric X-SAR observations of storms with simultaneous data from ground-based weather radars. Lastly, the final objective is to characterize surface backscatter changes caused by recent or active precipitation as seen from spaceborne radar. The following list summarizes the details.

Precipitation affect on land backscatter

- Characterize land surface change due to precipitation using repeat orbit SAR data
- Study σ^0 and potential impact to the TRMM SRT algorithm

Model precipitation to simulate spaceborne radar observations

- Generate Particle Size Distributions (PSDs) for various hydrometeor types
- Develop models to transform 0° elevation dual-polarized S-band observations to higher frequency, high elevation angle observations
- Evaluate the performance of a new nonlinear regression model to perform the frequency transformation of Mie scatterers such as large raindrops and hail

Storm observations from X-SAR

- Characterize storm observations from a slant angle, dual-polarized radar using real ground-based data
- Quantitative analysis of storm attenuation in SAR data using ground radar observations
- Simulate X-SAR storm backscatter and attenuation using real polarimetric ground radar measurements
- Qualitative analysis of dual-polarization X-SAR propagation effects

1.4 Thesis Overview

Chapter 2 Introduces the theoretical background used throughout this dissertation. This includes radar polarimetry and distributed particle scattering, polarimetric synthetic aperture radar theory, neural networks and nonlinear regression techniques, as well as essential information regarding the various radars used in this research.

Chapter 3 presents surface backscatter change and analysis using X-band and C-band SAR as well as ground-based weather radars and TRMM-PR. The results provide implications for the TRMM rainfall estimation algorithm and how SAR can improve it where the surface backscatter has high variability due to soil moisture and seasons.

Chapter 4 provides the microphysical model to simulate high frequency spaceborne polarimetric precipitation observations from real ground-based polarimetric S-band data. A novel method is presented using a simulation trained regression model to handle the variability introduced by Mie scattering, especially in the presence of hail. Results are shown by converting horizontal S and C band to slant angle X and Ku band.

Chapter 5 demonstrates the results of applying the microphysical model to simulate the effect of precipitation on a spaceborne SAR. The process of resampling a volume of ground-based weather radar observations for slant angle SAR is described and results using data from CSU-CHILL are shown over TerraSAR-X data.

Chapter 6 presents observations and analysis of several case studies using the TerraSAR-X system and two NEXRAD WSR-88D weather radars over Florida in 2008 plus the COSMO-SkyMed constellation with simultaneous observations from a polarimetric C-band ground radar. The latter provides initial validation of the model presented in earlier chapters.

Chapter 7 summarizes the findings of this thesis and discusses conclusions drawn from it. In addition, future work is suggested.

CHAPTER 2

THEORETICAL BACKGROUND AND INSTRUMENTATION

If I have seen further than others, it is by standing upon the shoulders of giants.

- Sir Isaac Newton

2.1 Radar Polarimetry and Scattering from Distributed Particles

2.1.1 The Radar Equation

One of the most fundamental concepts for all types of radar is known as the Radar Equation, and even though it is based on the physics of electromagnetic propagation from and to an antenna, there are as many ways to write the equation as there are researchers who do. Different representations depend on the assumptions made, how variables are combined and the primary parameter of interest, which could be range, power, signal-to-noise ratio (SNR), etc. Variations in radars such as antenna pattern, volume vs. surface scanning or signal processing (e.g., pulse compression or synthetic aperture processing) also alter the equation. Starting from the basics, the received power from a scattering body at range R can be written as

$$P_R = (P_T G_T)\left(\frac{1}{4\pi R^2}\right)\sigma\left(\frac{1}{4\pi R^2}\right)A_e\left(\frac{1}{L_{sys}L_{atmos}}\right) = \frac{P_T G_T \sigma A_e}{(4\pi)^2 R^4 L_{sys} L_{atmos}} \tag{2.1}$$

where

$$
\begin{aligned}
P_R &= \text{received power (W)} \\
P_T &= \text{peak transmitted power (W)} \\
G_T &= \text{transmitter antenna gain} \\
R &= \text{range to target from antenna (m)} \\
\sigma &= \text{target Radar Cross Section (RCS) (m}^2\text{)} \\
A_e &= \text{effective receiver antenna area (m}^2\text{)} \\
L_{sys} &= \text{losses within transmitter and receiver systems} \\
L_{atmos} &= \text{atmospheric propagation loss factor.}
\end{aligned}
$$

The terms in parentheses in the middle of (2.1) can be described as follows: transmitted power density, isotropic (solid angle) radiation loss, target scattering characteristic, isotropic re-radiation loss, receiving antenna characteristic and losses due to system hardware and atmospheric phenomena such as water vapor or hydrometeors. Frequently, the effective receive antenna area is written in terms of gain and wavelength using the relationship $G_R = 4\pi A_e/\lambda^2$. Noise is also a major factor, so (2.1) is often written as SNR by dividing through by the noise power to give [Doerry (2006)]

$$
SNR_P = \frac{P_R}{N_R} = \frac{\lambda^2 P_T G_T G_R \sigma}{(4\pi)^3 R^4 L_{sys} L_{atmos} (kTF_N) B} \tag{2.2}
$$

for a single radar pulse where

$$
\begin{aligned}
k &= \text{Boltzmann's constant } = 1.38 \times 10^{-23}\text{J/K} \\
T &= \text{nominal noise temperature} \approx 290\text{K} \\
F_N &= \text{receiver system noise factor} \\
B &= \text{bandwidth at the antenna port.}
\end{aligned}
$$

For monostatic radars, $G_R = G_T$ so $G_T G_R$ becomes simply G^2. In weather radars, the Radar Cross Section (RCS) is over a unit volume (m^2m^{-3}) and called reflectivity and is a function of range and antenna beamwidth. The received power is expressed as an integral over the volume weighted by the antenna gain function and transmitted waveform [Bringi

and Chandrasekar (2001)]. Performing this integration and considering $dV = R^2 d\Omega dR$ ($d\Omega$ is the elemental solid angle) as well as $\Delta R = cT_0/2$, (2.1) results in the well known weather radar equation after range normalizing the RCS for mean receive power:

$$\bar{P_R} = \left(\frac{cT_0}{2}\right)\left[\frac{\lambda^2 P_T G_0^2}{(4\pi)^3}\right]\left(\frac{\pi\theta_1\phi_1}{8\ln 2}\right)\frac{\eta(R)}{R^2} \tag{2.3}$$

where c is the speed of light, T_0 is the pulse width, G_0 is the peak power gain and θ_1 and ϕ_1 are the 3 dB beamwidths for a pencil-beam antenna pattern [Probert-Jones (1962)]. Losses in the receiver system are not included here, nor are atmospheric losses which are occasionally the parameter of interest.

In a SAR system, the use of pulse compression and the formation of the synthetic aperture by coherently combining pulses modifies (2.2) to improve the SNR. For pulse compression τ_0 is defined as the compressed pulse width and τ_u as the uncompressed version the system bandwidth $B = 1/\tau_0$. An azimuth (along track) resolution of δ_{az} at a distance R and wavelength λ is achieved by requiring the synthetic aperture length to be

$$L_{SA} = \frac{R\lambda}{2\delta_{az}}. \tag{2.4}$$

Incorporating pulse compression into (2.2) and considering an additional loss L_r due to non-ideal range filtering yields

$$SNR_{cp} = \frac{\lambda^2 P_T \tau_u G_T G_R \sigma}{(4\pi)^3 R^4 (kTF_N) L_{sys} L_{atmos} L_r (B\tau_0)}. \tag{2.5}$$

In the absence of more detailed system information, the range filtering loss can be estimated as $L_r \approx a_{wr} \approx 1.2$, where a_{wr} is the broadening factor of the range impulse response due to weighting or windowing the data [Doerry (2006)]. With a pulse repetition frequency (PRF) of F, platform velocity v_p and (2.4), the number of pulses to coherently integrate is

$$N = \frac{FL_{SA}}{v_p} = \frac{FR\lambda}{2v_p\delta_{az}}. \tag{2.6}$$

The fully focused system with synthetic aperture formation from (2.5) and (2.6) with a loss term to account for non-ideal azimuth filtering ($L_a \approx 1.2$) is then

$$\begin{aligned} SNR_f &= \frac{\lambda^2 (P_T \tau_u F) R\lambda G_T G_R \sigma}{(4\pi)^3 R^4 (kTF_N) L_{sys} L_{atmos} L_r L_a 2v_p\delta_{az}} \\ &= \frac{\lambda^3 P_{avg} G_T G_R \sigma}{128\pi^3 R^3 (kTF_N) L_{sys} L_{atmos} L_r L_a v_p \delta_{az}} \end{aligned} \tag{2.7}$$

given that the average transmit power is $P_{avg} = P_T \tau_u F$. An important result here is that the SNR is inversely proportional to R^3 as opposed to R^4 for a point target or R^2 in weather radars. For a monostatic radar, (2.7) is often written in terms of the effective antenna aperture as

$$SNR_{fa} = \frac{P_{avg} A_e^2 \sigma}{2\,(4\pi)\,R^3 \lambda\,(kTF_N)\,L_{sys} L_{atmos} L_r L_a v_p \delta_{az}}. \tag{2.8}$$

Although the form is very different, Atlas and Moore (1987) showed that the SAR radar equation, when using it as a precipitation radar, is essentially the same as (2.3).

2.1.2 Scattering Matrix and Radar Cross Section

Electromagnetic wave propagation and scattering upon intersecting with dielectric particles provides the fundamental physics involved with radar remote sensing of precipitation. Using a plane wave approximation, the incident electric field to a plane of constant phase at range $\vec{r}$ and orthogonal to the direction of wave travel $\hat{i}$ is

$$\vec{E}^i = \widehat{e_i} E_0 \mathrm{e}^{-jk_0 \hat{i}\cdot\vec{r}} = E_h^i \widehat{h_i} + E_v^i \widehat{v_i} \tag{2.9}$$

where the wave number $k_0 = 2\pi/\lambda$, E_0 is the wave amplitude and $\widehat{e_i}$ defines the polarization state [Bringi and Chandrasekar (2001)]. Fig. 2.1.2 displays the incident and scattering geometry and variable definitions. The horizontal and vertical unit vectors $\widehat{h_i}$ and $\widehat{v_i}$ respectively relate to the spherical unit vectors via $\widehat{k_i} = \widehat{\theta_i} \times \widehat{\phi_i} = \widehat{h_i} \times \widehat{v_i}$. Similarly, $\widehat{k_s} = \widehat{\theta_s} \times \widehat{\phi_s} = \widehat{h_s} \times \widehat{v_s}$. This results in a far field scattered plane wave as

$$\vec{E}^s = \frac{\vec{f}\left(\hat{s}, \hat{i}\right)}{r} \mathrm{e}^{-jk_0 r} = E_h^s \widehat{h_s} + E_v^s \widehat{v_s} \tag{2.10}$$

where r is the magnitude of $\vec{r}$. The far field vector scattering amplitude $\vec{f}$ is defined as

$$\vec{f} = \frac{k_0^2\,(\epsilon_r - 1)}{4\pi} \int_\tau \left[\vec{E}_T^{in}(\vec{r\prime}) - \hat{r}(\hat{r}\cdot\vec{E}_T^{in})\right] \mathrm{e}^{-jk_0 \vec{r\prime}\cdot\hat{r}} d\tau\prime \tag{2.11}$$

where ϵ_r is the relative permittivity of the dielectric material, $\vec{E}_T^{in}$ is the electric field vector inside the particle and τ is the volume. The incident and scattered waves are related via the scattering matrix $\mathbf{S}$, also known as the Sinclair matrix, written as

$$\begin{bmatrix} E_h^s \\ E_v^s \end{bmatrix} = \frac{1}{r} \mathrm{e}^{-jk_0 r} \mathbf{S}_{\mathrm{FSA}} \begin{bmatrix} E_h^i \\ E_v^i \end{bmatrix} = \frac{1}{r} \mathrm{e}^{-jk_0 r} \begin{bmatrix} S_{hh} & S_{hv} \\ S_{vh} & S_{vv} \end{bmatrix}_{\mathrm{FSA}} \begin{bmatrix} E_h^i \\ E_v^i \end{bmatrix} \tag{2.12}$$

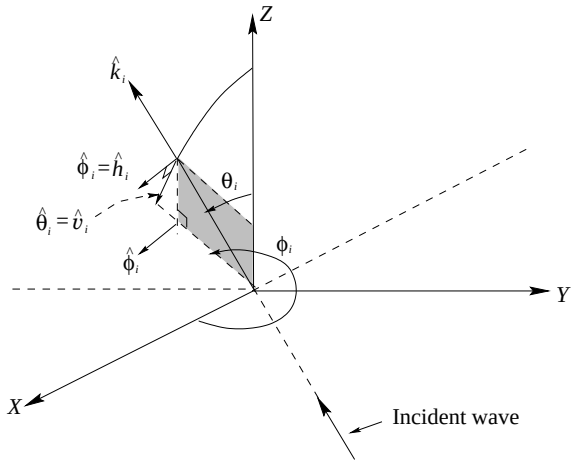

(a)

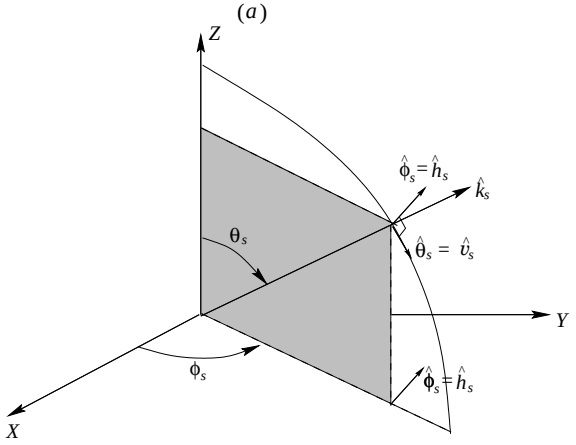

(b)

Figure 2.1: (a) Incident wave direction, specified by $\widehat{k_i} = \widehat{\theta_i} \times \widehat{\phi_i}$ and (b) the scattered wave direction in FSA convention specified by $\widehat{k_s} = \widehat{\theta_s} \times \widehat{\phi_s}$ [adopted from Bringi and Chandrasekar (2001) with permission].

where FSA indicates the Forward Scattering Alignment convention. The Backward Scattering Alignment (BSA) convention uses "reflected" versus "scattered" and is related to FSA fields via

$$\begin{bmatrix} E_h^r \\ E_v^r \end{bmatrix} = \begin{bmatrix} -1 & 0 \\ 0 & 1 \end{bmatrix} \begin{bmatrix} E_h^s \\ E_v^s \end{bmatrix} \tag{2.13}$$

i.e., $\widehat{k_r} = -\widehat{k_s}$, $\widehat{h_r} = -\widehat{h_s}$ and $\widehat{v_r} = \widehat{v_s}$.

2.1.3 Radar Cross Section

In Section 2.1.1 the received power is a function of the RCS σ, or the volumetric RCS η for weather radars. The RCS depends on the characteristics of the target, but also depends on the wavelength of the radar. In general, the RCS is defined by

$$\sigma = 4\pi R^2 \lim_{R\to\infty} \left(\frac{P_r}{P_i}\right) \tag{2.14}$$

which is the limit of the ratio of received power to incident power as the range approaches infinity. There are three regions of scattering: Rayleigh, Mie or resonant, and optical. Consider a sphere with radius a. In the Rayleigh scattering limit $a << \lambda$, while in the optical region $a >> \lambda$. Between the two regions, the Mie solution to Maxwell's equations is applied. For a dielectric sphere, the Sinclair matrix in (2.12) can be written as

$$\mathbf{S}_{\text{FSA}} = \begin{bmatrix} \frac{j\cos\phi_s}{k_0} S_1(\theta_s) & \frac{-j\sin\phi_s}{k_0} S_1(\theta_s) \\ \frac{j\sin\phi_s}{k_0} S_2(\theta_s) & \frac{j\cos\phi_s}{k_0} S_2(\theta_s) \end{bmatrix}_{FSA} \tag{2.15}$$

where ϕ_s and θ_s are defined in Fig. 2.1.2 and $\theta_i = \phi_i = 0°$. The scattering operators are described by

$$S_1(\theta_s) = \sum_{n=1}^{\infty} \frac{2n+1}{n(n+1)} \left[\alpha_{o1n} \frac{P_n' \cos\theta_s}{d\theta_s} + \beta_{e1n} \frac{P_n' \cos\theta_s}{\sin\theta_s}\right] \tag{2.16a}$$

$$S_2(\theta_s) = \sum_{n=1}^{\infty} \frac{2n+1}{n(n+1)} \left[\alpha_{o1n} \frac{P_n' \cos\theta_s}{\sin\theta_s} + \beta_{e1n} \frac{P_n' \cos\theta_s}{d\theta_s}\right] \tag{2.16b}$$

where α_{o1n} and β_{e1n} are the scattered field expansion coefficients. These coefficients are given as [Bringi and Chandrasekar (2001)]

$$\alpha_{o1n} = \frac{\rho j_n(\rho)[\rho_0 j_n(\rho_0)]' - \sqrt{\epsilon_r}\rho_0 j_n(\rho_0)[\rho j_n(\rho)]'}{\sqrt{\epsilon_r}\rho_0 h_n^{(2)}(\rho_0)[\rho j_n(\rho)]' - \rho j_n(\rho)[\rho_0 h_n^{(2)}(\rho_0)]'} \tag{2.17a}$$

$$\beta_{e1n} = \frac{\rho_0 j_n(\rho_0)[\rho j_n(\rho)]' - \sqrt{\epsilon_r}\rho j_n(\rho)[\rho_0 j_n(\rho_0)]'}{\sqrt{\epsilon_r}\rho j_n(\rho)[\rho_0 h_n^{(2)}(\rho_0)]' - \rho_0 h_n^{(2)}(\rho_0)[\rho j_n(\rho)]'} \tag{2.17b}$$

where $\rho_0 = k_0 a$, $\rho = \rho_0\sqrt{\epsilon_r}$ and $[\rho z_n(\rho)]' = d[\rho z_n(\rho)]/d\rho$. In addition, $j_n(x)$ is a spherical Bessel function of the first kind and $h_n^{(2)}(x)$ is a Hankel function of the second kind.

In general, the radar cross section is considered the backscatter cross section and is expressed as

$$\sigma_b(\hat{s},\hat{i}) = 4\pi|\vec{f}(\hat{s},\hat{i})|^2 \tag{2.18}$$

where $\hat{s} = -\hat{i}$ for the monostatic case. The Mie solution in this case is given by

$$\sigma_b(-\hat{i},\hat{i}) = \frac{\pi}{k_0^2}\left|\sum_{n=1}^{\infty}(-1)^n(2n+1)(\alpha_{o1n}-\beta_{e1n})\right|^2 \tag{2.19}$$

In the Rayleigh limit up to order ρ^3, (2.19) simplifies to [Bringi and Chandrasekar (2001)]

$$\begin{aligned}\sigma_b(-\hat{i},\hat{i}) &= \frac{4\pi}{k_0^2}\left|\frac{\epsilon_r-1}{\epsilon_r+2}\right|^2 (k_0 a)^6 \\ &= \frac{\pi^5}{\lambda^4}\left|\frac{\epsilon_r-1}{\epsilon_r+2}\right|^2 D^6 \end{aligned} \tag{2.20}$$

where $D = 2a$ is the diameter.

Dielectric bodies also possess a characteristic known as the extinction cross section that consists of scattering and absorption components. Using the optical theorem [Bringi and Chandrasekar (2001)] and the Mie solution, the extinction cross section is given by

$$\sigma_{ext}(\hat{i},\hat{i}) = \frac{-4\pi}{k_0}\Im\left[\vec{f}(\hat{i},\hat{i})\cdot\hat{e}_i\right] \tag{2.21a}$$

$$= -\frac{2\pi}{k_0^2}\sum_{n=1}^{\infty}(2n+1)\Re\left(\alpha_{o1n}+\beta_{e1n}\right) \tag{2.21b}$$

Simplifying (2.21a) for the Rayleigh limit (correct up to ρ^3) yields

$$\begin{aligned}\sigma_{ext} &= \frac{4\pi}{k_0^2}\rho^3\Re\left(j\frac{\epsilon_r-1}{\epsilon_r+2}\right) \\ &= 9k_0V\frac{\epsilon_r''}{|\epsilon_r+2|^2}\end{aligned} \tag{2.22}$$

where V is the volume and ϵ_r'' indicates the imaginary part of ϵ_r. Plots of the backscatter and extinction cross sections for water spheres are shown in Fig. 2.2a-2.2c in addition to the RCS of a conducting sphere in Fig. 2.2d for comparison. The relative permittivity for the water spheres is calculated at a wavelength of 3.1 cm using the method described in Ray (1972) at -10 ℃ for pure ice (Fig. 2.2a) and 20 ℃ for liquid water (Fig. 2.2b). For the 3-phase mixture of water, ice and air shown in Fig. 2.2c, linear combinations of the Maxwell Garnett (MG) mixing formula [Maxwell Garnett (1904)] were used at 5 ℃ as described in Meneghini and Liao (1996). Using the combinations of phases solves the problem of $\mathrm{MG}_{1,2} \neq \mathrm{MG}_{2,1}$ for the same fractional water level where $\mathrm{MG}_{1,2}$ indicates material 1 is the matrix and material 2 is the inclusion (e.g., $\mathrm{MG}_{I,W}$ is ice with water inclusions). An alternative method of combining phases that avoids any discontinuities is presented in Section 4.3.2.

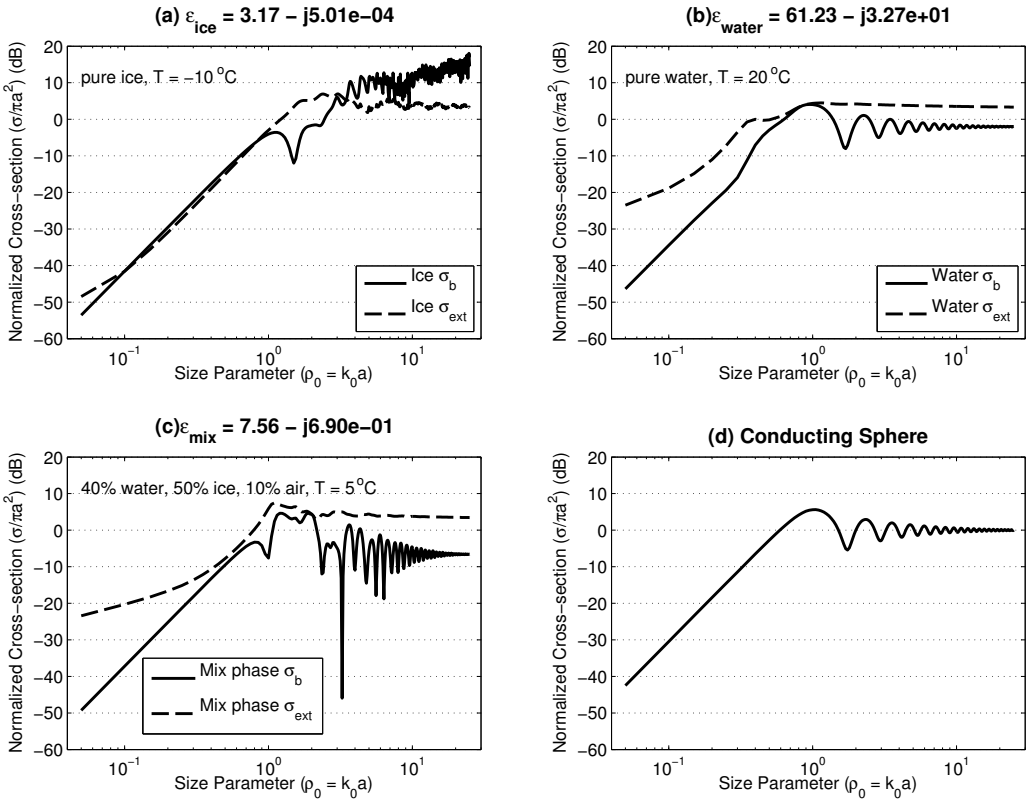

Figure 2.2: The normalized radar cross-sections (backscatter and extinction if applicable) versus size parameter using the Mie solution at $\lambda = 3.1$cm for (a) pure ice sphere at -10 ℃ with $\epsilon_r = 3.17 - j5\text{e-}4$ (b) pure water sphere at 20 ℃ with $\epsilon_r = 61 - j33$ (c) mixed phase sphere 5 ℃ consisting of 40% water, 50% ice and 10% air with $\epsilon_r = 7.6 - j0.7$ and (d) a conducting sphere for comparison.

2.1.4 Polarimetric Radar Observations

Typically, a multi-polarization radar observes all four components of the scattering matrix in (2.12), expressed in vector form as $\Omega = [S_{hh} \;\; S_{hv} \;\; S_{vh} \;\; S_{vv}]^T$ where the subscript pairs represent receive and transmit polarization respectively. The resulting 4×4 covariance matrix from $\mathbf{C} = \Omega\Omega^{*\mathrm{T}}$ contains the relationships among the observations. However, in most cases it is safe to assume reciprocity between the two cross-polar channels [Ulaby and Elachi (1990)]. Indeed, these two channels can be used to calibrate the system such that $S_{hv} = S_{vh}$ [Freeman et al. (1992)]. Under this assumption of reciprocity, the scattering vector can be written as $\Omega_{\mathrm{r}} = \left[S_{hh} \;\; \sqrt{2}S_{hv} \;\; S_{vv}\right]^T$ resulting in a 3×3 covariance matrix

$$\mathbf{C} = \Omega_{\mathrm{r}}\Omega_{\mathrm{r}}^{*\mathrm{T}} = \left\langle \begin{bmatrix} |S_{hh}|^2 & S_{hh}S_{hv}^* & S_{hh}S_{vv}^* \\ S_{hh}^*S_{hv} & 2|S_{hv}|^2 & S_{hv}S_{vv}^* \\ S_{hh}^*S_{vv} & S_{hv}^*S_{vv} & |S_{vv}|^2 \end{bmatrix} \right\rangle \tag{2.23}$$

where $\langle . \rangle$ denotes the ensemble average. Similarly under the reciprocity assumption, the Pauli scattering vector

$$\mathbf{k} = \frac{1}{\sqrt{2}} \begin{bmatrix} S_{hh} + S_{vv} & S_{hh} - S_{vv} & 2S_{hv} \end{bmatrix}^T \tag{2.24}$$

is used to generate the coherency matrix via Cloude and Pottier (1996)

$$\begin{aligned} \mathbf{T} &= \mathbf{k}\mathbf{k}^{*T} \\ &= \left\langle \frac{1}{2} \begin{bmatrix} |S_{hh} + S_{vv}|^2 & (S_{hh} + S_{vv})(S_{hh} - S_{vv})^* & 2(S_{hh} + S_{vv})S_{hv}^* \\ (S_{hh} + S_{vv})^*(S_{hh} - S_{vv}) & |S_{hh} - S_{vv}|^2 & 2(S_{hh} - S_{vv})S_{hv}^* \\ (S_{hh} + S_{vv})^* S_{hv} & 2(S_{hh} - S_{vv})^* S_{hv} & 4|S_{hv}|^2 \end{bmatrix} \right\rangle . \end{aligned} \tag{2.25}$$

The transform to the coherency matrix is used because the diagonal elements have a physical interpretation. T_{11} indicates single bounce or rough surface scattering and is maximum when the co-polar phase difference ϕ_{co} is 0°. T_{22} is interpreted as double bounce or dihedral scattering and is maximum when ϕ_{co} is 180°, while T_{33} indicates volume scattering. The subscripts of T indicate the row and column in (2.25). At the time of the data acquisitions, TerraSAR-X only provided any two of the elements of Ω and the two co-polar terms were selected for discussion here, thus allowing analysis of co-polar relationships.

A number of fundamental relationships for weather radar applications are applied in this work [Bringi and Chandrasekar (2001)]. The two basic phenomena of electromagnetic wave interaction with precipitation are backscatter and attenuation, described by the radar backscatter cross section per unit volume η ($\mathrm{m}^2\mathrm{m}^{-3}$), and the extinction cross section σ_{ext} (m^2) (see Section 2.1.1 and 2.1.3). The radar reflectivity factor, z, is related to the precipitation backscatter cross section as

$$\begin{aligned} z &= \frac{\lambda^4}{\pi^5 |K_p|^2} \eta \\ &= \frac{\lambda^4}{\pi^5 |K_p|^2} \int \sigma_p(D) N(D) dD, \qquad \mathrm{mm}^6\mathrm{m}^{-3} \end{aligned} \tag{2.26}$$

where λ is the wavelength, $|K_p|^2$ is the dielectric factor of hydrometeors, $\sigma_p(D)$ is the radar cross section for precipitation and N(D) is particle size distribution (PSD), i.e., the number of particles per unit volume with sizes in the interval $(D, D + \Delta D)$. (To avoid confusion, a lowercase z indicates reflectivity in linear units while uppercase Z is in dBZ.) At the time of observation, the ice content of particles, if any, is unknown, so the equivalent

reflectivity factor Z_e is calculated instead where $|K_p|^2 = |K_w|^2$ is the value appropriate for water (approximately 0.93). If the particle size is small enough to be within the Rayleigh scattering limit $\sigma_p(D) = D^6$ in (2.26) the two reflectivity factors are related by [Smith (1984); Bringi and Chandrasekar (2001)]

$$z_e = \frac{|K_p|^2}{|K_w|^2} z \tag{2.27}$$

Similarly, the specific coefficient of attenuation in horizontal polarization, A_h, as a function of σ_{ext} and $N(D)$ is expressed by

$$A_h = 4.343 \times 10^3 \int \sigma_{ext} N(D) dD, \qquad \mathrm{dB\,km^{-1}}. \tag{2.28}$$

Over a given range, r_1 to r_2, the signal attenuation is calculated using

$$l(r) = \exp\left(-0.2 \ln 10 \int_{r_1}^{r_2} A_h(\xi) d\xi\right), \tag{2.29}$$

and is also known as path integrated attenuation (PIA). The observed reflectivity is then $Z_{obs}(r) = Z(r) + L(r)$ where $L = 10 \log_{10} l$ and $L \leq 0$. A power law relationship describes the association between the specific attenuation and reflectivity factor, written as

$$a_h = \alpha z^{\beta}. \tag{2.30}$$

Due to the non-spherical nature of precipitation particles, a polarimetric radar can have differential observations between horizontal and vertical channels. This effect is often more pronounced at near horizontal elevation angles, but is still present at SAR look angles. The specific differential phase observed between the two channels is [Bringi and Chandrasekar (2001)]

$$K_{dp} = \frac{180\lambda}{\pi} \int \Re\left[f_h(D) - f_v(D)\right] N(D) dD, \qquad \mathrm{deg\,km^{-1}} \tag{2.31}$$

where f_h and f_v are the forward scattering amplitudes for the horizontal and vertical polarization states and $\Re$ refers to the real part of a complex number. The observed co-polar phase in a monostatic radar, however, is expressed as

$$\Psi_{dp} = 2 \int_{r_1}^{r_2} K_{dp}(r) dr + \phi_{co} \tag{2.32a}$$

$$= \Phi_{dp} + \phi_{co} \tag{2.32b}$$

where ϕ_{co} is the backscatter differential phase $\arg(S^*_{hh}S_{vv})$. Non-zero values of ϕ_{co} are indicative of Mie scattering [Bringi and Chandrasekar (2001)] and includes backscatter from the surface when applied to SAR. The specific differential attenuation is defined by

$$A_{dp} = \left(8.686 \times 10^3\right) \int \Im\left[f_h(D) - f_v(D)\right] N(D) dD, \qquad \mathrm{dB\,km^{-1}} \tag{2.33}$$

where $\Im$ refers to the imaginary part of a complex number.

Among these parameters, the co-polar correlation coefficient is calculated as

$$\rho_{co} = \frac{\langle S_{hh} S^*_{vv} \rangle}{\sqrt{\langle |S_{hh}|^2 \rangle \langle |S_{vv}|^2 \rangle}} = |\rho_{co}| e^{j\phi_{co}}. \tag{2.34}$$

The magnitude and phase of ρ_{co}, sometimes referred to as ρ_{hv}, provide information not only about surface scattering mechanisms, but also propagation effects when the radar wave passes through a volume of distributed particles. Another parameter that is available with just these two terms is the co-polar ratio, or differential reflectivity, Z_{dr} determined from

$$Z_{dr} = 10 \log_{10} \left(\frac{\langle |S_{hh}|^2 \rangle}{\langle |S_{vv}|^2 \rangle} \right), \ \mathrm{dB}. \tag{2.35}$$

The term Z_{dr} will be used to refer to this co-polar ratio even though SAR observations are not technically reflectivity measurements, but the calculation is the same because the hydrometeor specific terms cancel. For dual linear polarization radars, the measured (equivalent) reflectivity is typically from the horizontal polarization. Thus, Z_h is used for observations and Z_v can be calculated as $Z_v = Z_h - Z_{dr}$. Unless otherwise noted, Z_h means the *equivalent* reflectivity described in (2.27).

2.2 Polarimetric Synthetic Aperture Radar (polSAR)

Early "imaging" radar systems, such as the Side-Looking (Airborne) Radar (SLR or SLAR), consisted of an incoherent high frequency radar mounted on a moving platform with the beam pointed at the ground at low grazing angles. This geometry allowed for relatively high range resolution; however, along-track resolution was poor and degraded with aircraft height. A technique first known as "Doppler beam sharpening" accredited to Carl Wiley in 1951 [Curlander and McDonough (1991)] used the phase information and Doppler

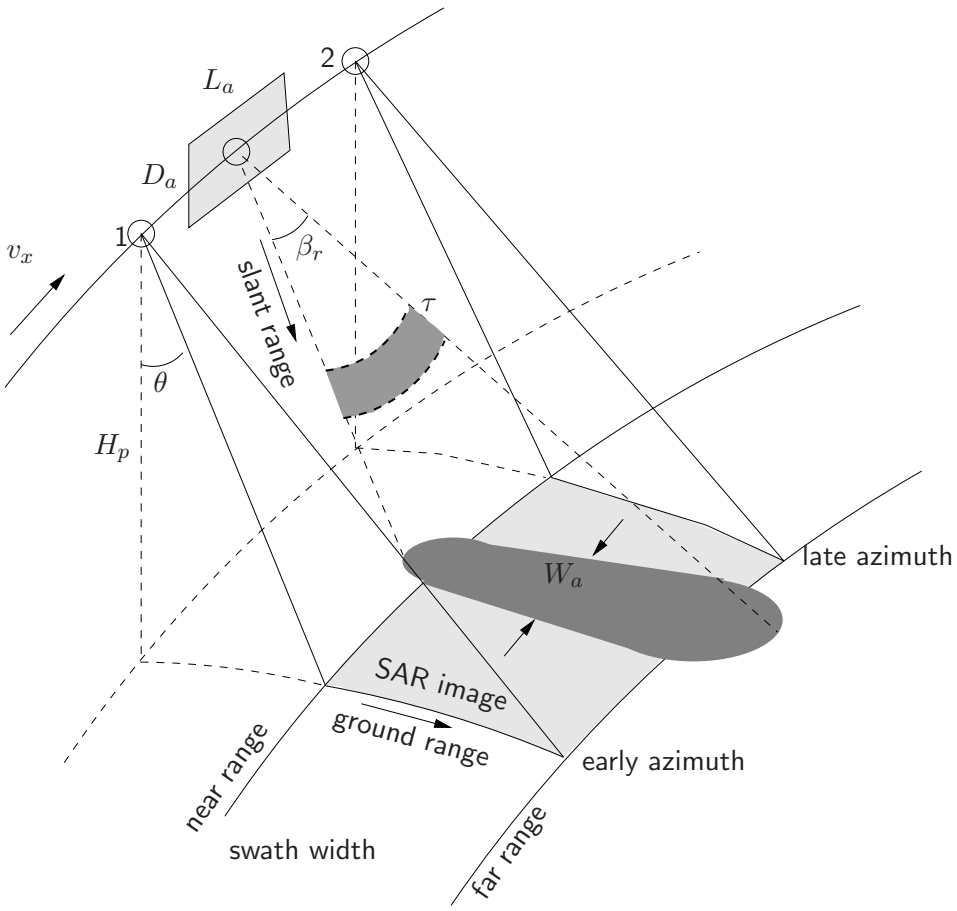

Figure 2.3: Imaging geometry of a SAR acquisition. Due to the platform velocity v_x the pulses illuminate a swath parallel to the platform track. The footprint of a single pulse is indicated by the dark shaded area. The total SAR image starts in azimuth at the "early azimuth" time, and lasts until the "late azimuth" time. In range direction, it covers an interval from "near range" to "far range," which corresponds to the light shaded area in ground range [adopted from Hanssen (2001) with permission].

processing to discriminate between targets within the beam as the radar moved. Thus, an artificial aperture was created by coherently summing pulse returns that dramatically increased the resolution along the path and the concept of the Synthetic Aperture Radar (SAR) became reality. Applications for SAR are many, although a significant majority involve surveillance or monitoring of the Earth's surface. The process of forming an image from the raw data involves multiple steps, and the geometry shown in Fig. 2.3 will aid in the discussion.

The process of reconstructing the response of surface scattering mechanisms from a series of pulse signals is known as image formation or synthetic aperture processing. Raw data is

also called raw phase history because the phase is critical in image formation. This allows resolution improvement in the along-track direction (also called the azimuth or "slow time" direction to relate it to conventional radar) from say a 4.5 km beam footprint to about 5-20 m. With a real antenna aperture of L_a by D_a as seen in Fig. 2.3, the platform flies along a specified trajectory at a velocity v_x and height H_p above the surface. The beam with 3 dB beam widths $\beta_r = 0.886\lambda/D_a$ and $\beta_a = 0.886\lambda/L_a$ is pointed toward the surface at a *look* angle of θ degrees from nadir illuminating a swath from "near range" to "far range". The beam footprint is then

$$W_a = \frac{\lambda}{L_a} R \tag{2.36}$$

where R is the range from the platform to the surface. Location "1" along the trajectory marks the beginning of the SAR image that ends at location "2" creating what is commonly referred to as a stripmap image. Other imaging modes involve manipulating the beam to either focus on a smaller patch at higher resolution (spotlight mode) or increase the swath width by effectively scanning the beam (scanSAR mode). The length of the synthetic aperture depends upon the pulse repetition frequency described by (2.4) results in an azimuth resolution of [Curlander and McDonough (1991)]

$$\delta_{az} \simeq \frac{L_a}{2}. \tag{2.37}$$

The corresponding bandwidth is on the order of $2v_x/L_a$ which is independent of both range and wavelength due to the proportionality of the synthetic aperture length with range and wavelength (2.4). Decreasing the L_a, however, also decreases the gain, which is proportional to the antenna area, and in turn, decreases SNR as seen in (2.7). Atlas and Moore (1987) also demonstrated the effect of hydrometeor spectral width σ_v on the resolution as

$$\delta_{azP} = \frac{2\sigma_v R}{v_x} \tag{2.38}$$

A closer look at the SAR geometry and relevant features is depicted in Fig. 2.4. SAR is inherently two-dimensional, and a monostatic system technically lacks the ability to resolve three-dimensional features. Given a slant range resolution of δ_r, Fig. 2.4 shows the effects of foreshortening (A), layover (B) and shadowing (C). These same effects also impact

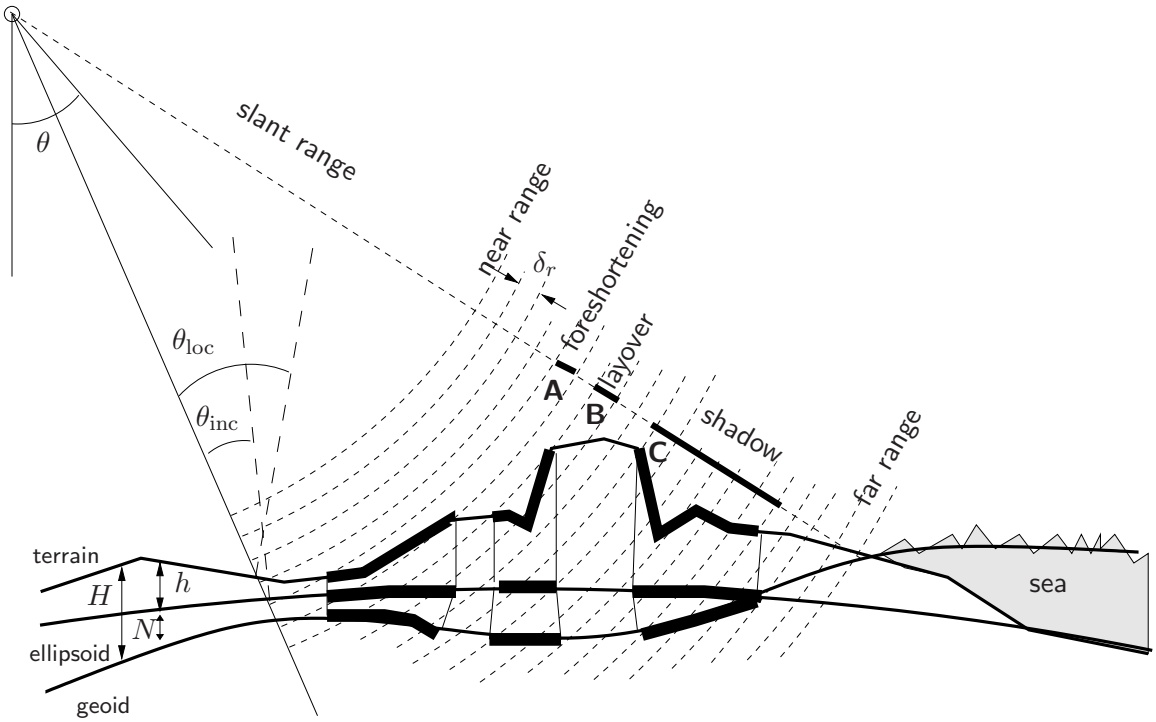

Figure 2.4: Imaging geometry and reference systems. Radar echoes are recorded between the concentric circle segments indicating near range and far range. A range resolution cell with size Δ_r is indicated by the spacing between the concentric lines. Area **A** indicates foreshortening, **B** indicates layover and **C** shadow. Ground-range coordinates can be referenced to the ellipsoid. Interferometric heights are referenced to the ellipsoid as well. In order to obtain orthometric heights H, the geoid height N needs to be taken into account. The look angle θ is defined w.r.t. the (geocentric) state vector, whereas the incidence angle θ_{inc} and the local incidence angle θ_{loc} are defined w.r.t. the local vertical to the ellipsoid and the local terrain, respectively [adopted from Hanssen (2001) with permission].

observations of atmospheric phenomena which are transformed to a ground-range/azimuth coordinate system projected on to the Earth ellipsoid model. Additionally, Fig. 2.4 shows three angles: look angle θ, incidence angle θ_{inc} and local incidence angle θ_{loc}. The local incidence angle is dependent on the terrain as opposed to the standard incidence angle which is relative to the ellipsoid model. It is the *local* incidence angle that will correctly determine the surface RCS σ^0. For this reason, slant range SAR data is almost always provided as "radar brightness" (Raney et al. (1994)) or β^0 related to σ^0 by

$$\sigma^0 = \beta^0 \sin\theta_{inc}. \tag{2.39}$$

2.2.1 Waveform and Signal Processing

Waveform generation and signal processing is key to creating the SAR images at such a high resolution. As alluded to in Section 2.1.1, SARs utilize pulse compression to improve range ("fast time") resolution with a chirp waveform. Typically, a linear frequency modulation (FM) waveform is used where the frequency $f(t)$ of the pulse changes linearly with slope κ (Hz/s), leading to a transmit signal of

$$s(t) = \text{rect}(t/\tau_u)\text{e}^{j\pi\kappa t^2/2} \tag{2.40}$$

where τ_u is the uncompressed pulse width. The bandwidth within the range $f(-\tau_0/2)$ to $f(\tau_0/2)$ then becomes $B = \kappa\tau_u = 1/\tau_0$ with time-bandwidth product $|\kappa|\tau_u^2$. Consequently, a matched filter can then be applied on the received signal to retrieve the scattering modified pulse, improving the range resolution to $\delta_r = c/(2|\kappa|\tau_u)$ where c is the speed of light [Cumming and Wong (2005)].

The Doppler effect allows for the improved resolution in SAR imagery and its role is illustrated in Fig. 2.5. A point target on the surface is illuminated between points A and C along the SAR platform path over the length of the synthetic aperture, L_s. Point B indicates the zero Doppler point, or "point of closest approach", at time $t = t_0$ and range R_0. The received signal strength and Doppler frequency are shown below this schematic. Fig. 2.5 indicates either a squint angle of 0° or the result of an early processing step that estimates the zero Doppler direction. The range to the target at the edges of the synthetic aperture are expressed as

$$R = \sqrt{R_0^2 + v_x^2(t-t_0)^2} \approx R_0 + \frac{v_x^2}{2R_0}(t-t_0)^2 \tag{2.41}$$

using a quadratic approximation. The change in range between a fixed point and the radar is called Range Cell Migration (RCM) because the range cell of a fixed point moves over time. Mitigating this effect is a major goal of the various image formation processes. The Doppler centroid frequency at $t = t_0$ is proportional to the rate of change of R(t) given by

$$f_{t_0} = -\frac{2}{\lambda}\frac{dR(t)}{dt}|_{t=t_0} = -\frac{2}{\lambda}\frac{v_x^2 t_0}{R(t_0)} = \frac{2v_x \sin\phi_s}{\lambda} \tag{2.42}$$

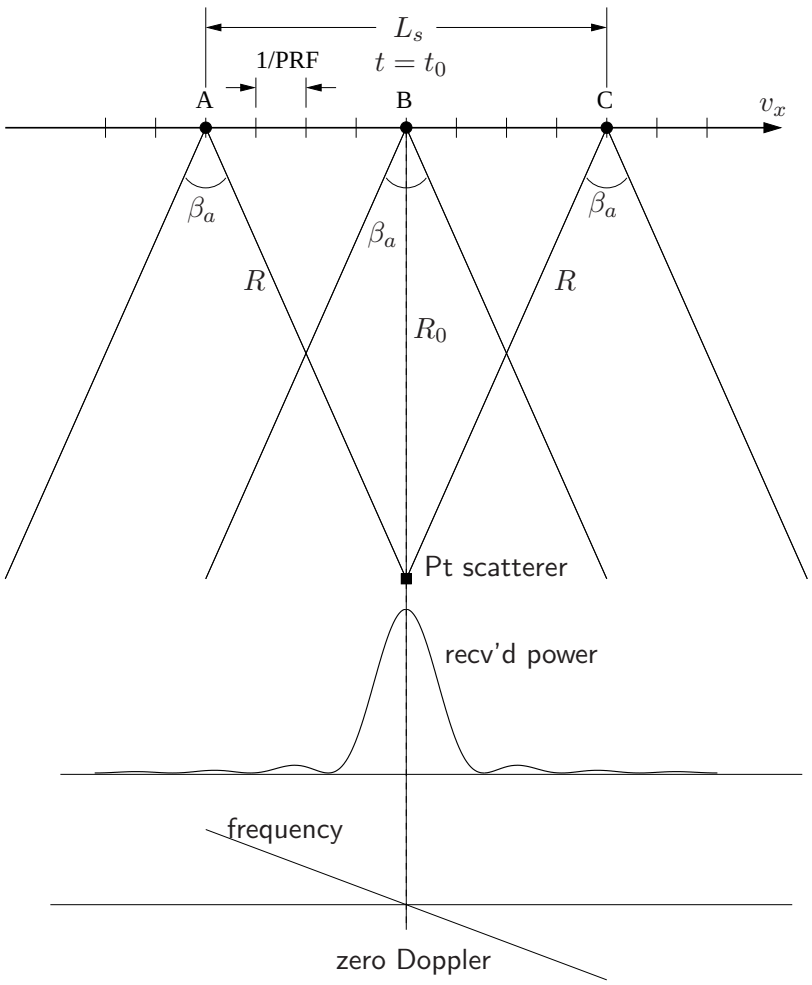

Figure 2.5: Schematic of SAR Doppler. A point scatter initially becomes illuminated by the SAR beam with azimuth beam width β_a at point A along the platform path with a distance R. At location B, the target is at range R_0: the "point of closest approach", also known as the zero Doppler point. This is also where the received signal power from the target is maximal. The point scatterer leaves the SAR beam at the end of the synthetic aperture (of length L_s) at point C, again at range R. The bottom plot shows the observed Doppler frequency vs. time.

where ϕ_s is the squint angle. From (2.42), the *azimuth* or Doppler bandwidth can be written as [Cumming and Wong (2005)]

$$B_{Dop} = \frac{2\cos\phi_s \beta_a v_x}{\lambda}. \tag{2.43}$$

Consequently, the azimuth resolution of the *focused* SAR image is v_x/B_{Dop}.

Similar to weather radars, using a multi-polarization SAR provides more information about the scattering mechanisms [van Zyl et al. (1987)]. At each range-azimuth resolution cell (pixel), the covariance matrix in (2.23) can be estimated. Applications such as

classification [Alberga (2004); Cloude and Pottier (1996); Lee et al. (1999); Freeman and Durden (1998)] and change detection [Conradsen et al. (2003); Fritz and Chandrasekar (2008)] have become prevalent. Combining radar polarimetry with interferometry, forming a 6×6 covariance matrix between 2 images provides additional methods to determine surface motion, etc. [Cloude and Papathanassiou (1998); Tabb et al. (2004)]. Therefore, it is reasonable to expect that polarimetric SAR can also be used to garner more information from hydrometeor scattering.

2.3 Radar Platforms

A number of different radar platforms were used in the course of the research presented here. These include two types of ground-based S-band and one C-band weather radars plus three spaceborne platforms: X-band dual-polarization SARs, a C-band single polarization SAR and a Ku-band nadir scanning precipitation radar. Specifications and basic details about each system are give in the subsequent subsections.

2.3.1 CSU-CHILL Radar

The Colorado State University - University of Chicago/Illinois State Water Survey (CSU-CHILL) radar is an advanced, trueansportable dual-polarized S-band weather radar system operated by Colorado State University under the sponsorship of the National Science Foundation and Colorado State University. The radar serves as an advanced research instrument for radar meteorology, radar engineering and remote sensing. Features include a high power dual-Klystron power amplifier, sophisticated transmitter controller, low side lobe antenna and digital receiver system. Radar operations are performed through an interactive radar control system which communicates with the radar system through a TCP/IP connection. Local and remote users can observe radar data in real-time, while the archival system can store both the processed radar measurements such as reflectivity and Doppler velocity as well as the digitized baseband signal data. Fig. 2.6 shows the antenna and pedestal as it looked until July 2007 when the dome and antenna were removed for upgrade to a new offset feed antenna. Table 2.1 lists basic system specifications for the older system, which was the configuration used for the data analyzed in Chapters 4 and 5.

Figure 2.6: The CSU-CHILL antenna and pedestal as it looked until July 2007 and the version used to collect data analyzed in this thesis.

2.3.2 WSR-88D Radar

During the late 1980s and early 1990s, the National Weather Service (NWS) deployed a vast number of S-band weather radars to cover the United States (see Fig. 2.7) known as NEXt generation weather RADar (NEXRAD). Specifically, these were Weather Surveillance Radar-1988 Doppler (WSR-88D) radars and the system processing was enhanced in 2008 to produce "super-resolution" data under 1.5° elevation [USDC/NOAA (2006); Torres and Curtis (2006)]. The single polarization WSR-88D radars are still in use, and data from two of them located in Florida were used to compare ground radar measurements with TerraSAR-X observations in August 2008 as detailed in Chapter 6. Specifications for the two systems during this data acquisition are shown in Table 2.2.

Table 2.1: CSU-CHILL radar specifications prior to July 2007.

Antenna	
Shape	Parabolic
Size	8.5 m
Feed type	scalar horn
Gain	43 dBi (includes waveguide loss)
3 dB Beamwidth	1.1 deg
Maximum sidelobe	-27 dB (along any ϕ-plane)
Inter-channel isolation	-45 dB
ICPR(two-way)	-38 dB
Transmitters	
Wavelength	11.01 cm (2.725 GHz)
Peak Power	1 MW (per channel)
Final PA Type	VA-87B/C (Klystron)
Pulse Width	0.2 - 1.6 μs
PRT	800 - 12000 μs
Available Polarizations	horizontal, vertical, alternating, slant $45^o/135^o$, right/left circular
Receivers/Digital Signal Processing	
Noise figure	3.4 dB
Noise Power	-113.0 dBm @ 1 MHz bandwidth
Dynamic range	80 dB
Bandwidth	Programmable. Simultaneous 1 MHz and 5 MHz channels available
Output Range Resolution	Programmable. 30 m minimum, typical: 150m
Maximum range gates	6000

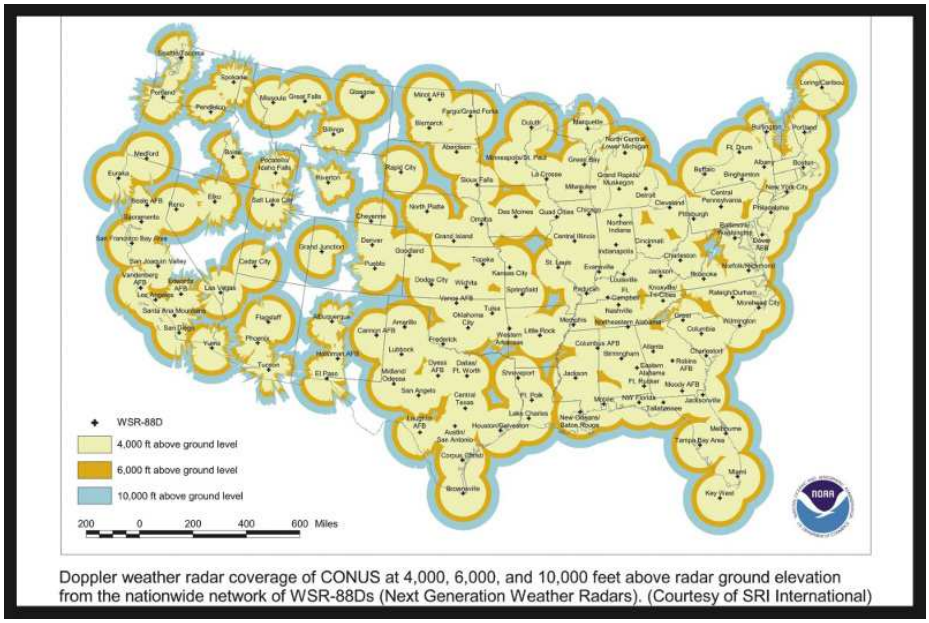

Figure 2.7: The coverage map of NEXRAD over the continental United States (CONUS).

Table 2.2: WSR-88D Radar specifications and operating parameters used in this research.

Parameter	**Radar**	
	KMLB	**KTBW**
Location	28.109° latitude -80.650° longitude	27.701° latitude -82.398° longitude
Altitude	10 m	13 m
Volume Coverage Pattern (VCP)	11, 12, 212	11, 212, 221
Data format	Level 2 full resolution	
Frequency	2700-3000 MHz	
Power	750 kW peak, 300-1300 W average	
Gain	45.5 dB @ 2850 MHz (including radome loss)	
Beamwidth	0.925° @ 2850 MHz	
Dynamic range	93 dB minimum	
PRF	318-1304 Hz short pulse 318-452 Hz long pulse	
Polarization	HH	
Elevation angles (deg)	0.5, 0.9, 1.3, 1.8, 2.4, 3.1, 4.0, 5.1, 6.4, 8.0, 10.0, 12.5, 15.6, 19.5	0.5, 1.5, 2.4, 3.4, 4.3, 6.0, 9.9, 14.6, 19.5
Azimuth spacing (w/ oversample)	0.5° $\leq$ 1.5° elevation[a], otherwise 1.0°	
Range resolution	250 m $\leq$ 1.5° elevation[a], otherwise 1000 m	
Ground range extent	300 km (radial)	

[a]WSR-88D uses a "super resolution" mode at elevation angles below 1.5°

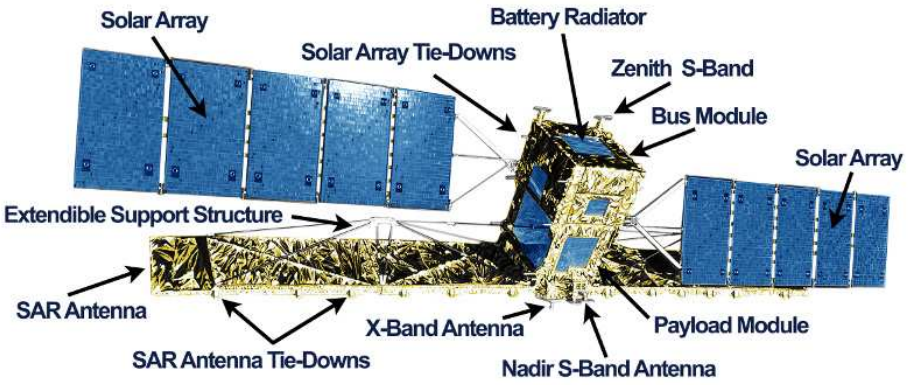

Figure 2.8: RADARSAT-1 system components (image ©CSA).

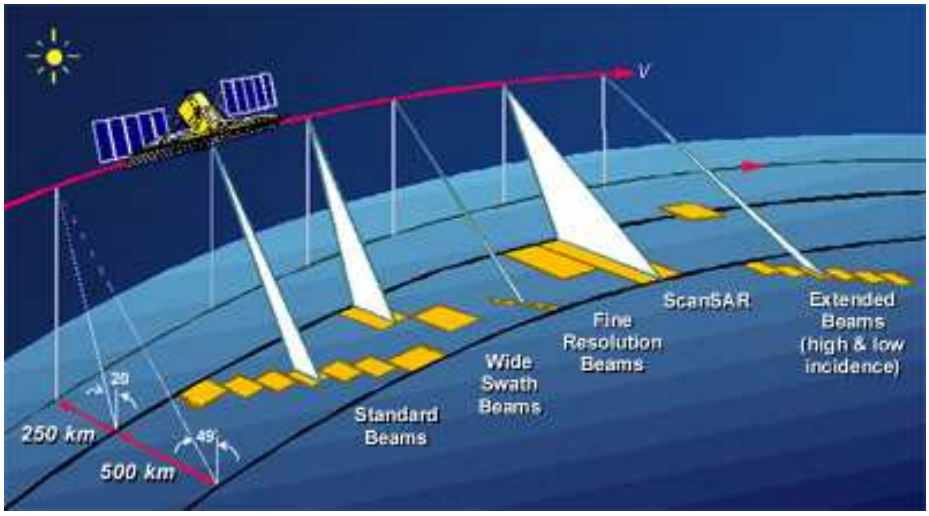

Figure 2.9: RADARSAT-1 imaging modes (image ©CSA).

2.3.3 RADARSAT-1 SAR

The Canadian Space Agency (CSA) launched the RADARSAT-1 C-band SAR into a sun-synchronous orbit in 1995. Designed to operate for 5 years, the system was finally decommissioned in 2008 when the subsequent RADARSAT-2 was commissioned. Components of the system are depicted in Fig. 2.8 and the various imaging modes are shown in Fig. 2.9. Table 2.3 gives basic specifications of this system for the data processed in this research which only used data from the Standard Beam Mode.

2.3.4 TerraSAR-X SAR

In 2007, the Deutches Zentrum für Luft und Raumfahrt (DLR) launched the multi-polarization X-band SAR, TerraSAR-X (TSX) [Buckreuss et al. (2003); Herrmann and

Table 2.3: RADARSAT-1 Specifications [CSA (1995)].

Parameter	**Value**
Frequency	5.3 GHz
Bandwidth	11.6, 17.3 or 30.0 MHz
Peak/average power	5000/300 W
Antenna aperture	15×1.5 m
Polarization	HH
Altitude (orbit)	793−821 km
Incidence angle	27.5 (Standard Mode 2), 37 (Standard Mode 4)
Standard Mode Nominal Resolution	30 m
Ground (surface) resolution	∼50 m^2
Swath width	100 km
Repeat orbit time	24 days

Bottero (2007)]. This was the first commercial SAR to provide 1 meter resolution (and even smaller in spotlight mode) and multiple polarizations. TerraSAR-X operates with a phased array antenna that can be split for short baseline along-track interferometry and repeat orbit interferometry with an 11 day cycle. Although the system can operate as a fully polarimetric radar, only double polarization products (any two of HH, VH, HV and VV) are available for general scientific use. Ironically, the first image provided (only four days after launch) exhibited distinct signs of significant rainfall as seen in Fig. 2.10. The flight path was right to left illuminating the storm from the bottom. Backscatter is visible on the near-range side as whitish clouds followed by attenuation.

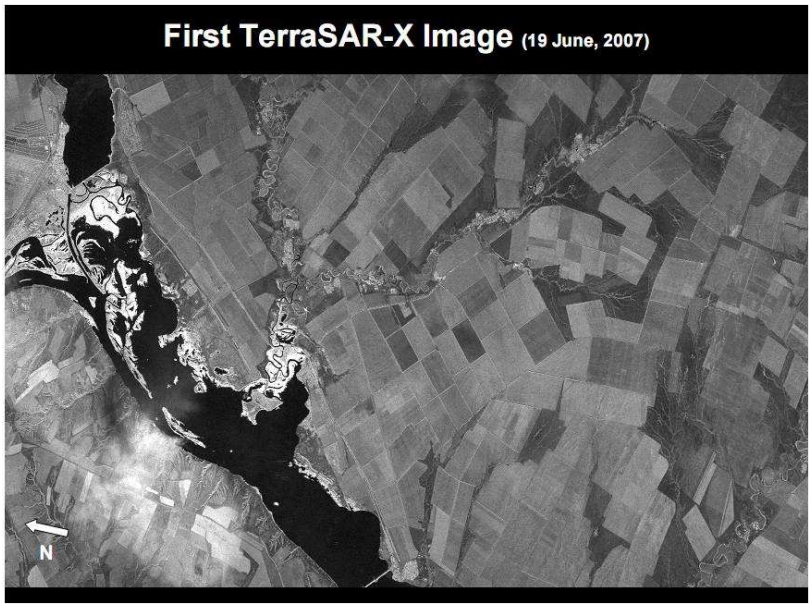

Figure 2.10: First TerraSAR-X image. The storm signature is visible near the bottom left, with the white backscatter on the near-range side followed by attenuation through the precipitation volume (image courtesy of R. Bamler, ©DLR).

Table 2.4: TerraSAR-X radar specifications and operating parameters used in this research.

Parameter	**Value for processed data**	**General Stripmap**
Data format	single look complex (SLC)	SLC, geocoded amplitude
Frequency	9.65 GHz (3.11 cm)	
PRF	2920 Hz	2.0 kHz-6.5 kHz
Range bandwidth	150 MHz	150 MHz, 300 MHz (advanced mode)
Polarization	HH, VV	any 2 of: HH, VH, HV, VV
Antenna	0.7 m×4.8 m	
Orbit	514 km	
Incidence angle	33° - 34.4°	20° - 45° (full performance)
Azimuth spacing (w/ oversample)	2.4 m	1 m - 16 m (mode and inc angle dependent)
Slant range resolution	1.2 m	0.65 m (advanced mode) - 1.5 m
Slant swath width	15 km	15 km (double polarization), 30 km (single polarization)
Repeat orbit time	11 days	

2.3.5 COSMO-SkyMed SAR

In an effort to significantly advance Earth observation capability, the Italian Space Agency (ASI) and the Italian Ministry of Defense (MoD) launched a series of X-band SAR satellites dubbed the COnstellation of small Satellites for Mediterranean basin Observation or COSMO-SkyMed. The full constellation consists of four satellites operating within the same orbital plan, but as of the writing of this document only three are launched and operational. Each satellite contains both horizontal and vertical transmitters and receivers; however, they cannot operate in a fully polarimetric mode where HH and VV are coherent and cross-polarization signals are available. The acquisition schemes only allow for bursts of pulses in a single polarization that will change to the other polarization if data is requested in the ping-pong mode. Thus, both HH and VV data acquisitions are available when requested, but co-polar correlation and phase difference are meaningless because the correlation is essentially zero and the phase is simply a uniform distribution between $-\pi$ and pi. With this constellation, it is possible to obtain data less than 24 hours apart between satellite number 2 and number 3 in an interferometric configuration. Unfortunately, data requests for acquisitions from all 3 are frequently not completely fulfilled. Table 2.5 provides some specifications about the configuration used for this research.

2.3.6 TRMM-Precipitation Radar

The first spaceborne system ever launched for the specific purpose of measuring global precipitation was the Tropical Rainfall Measurement Mission (TRMM) launched in 1997. TRMM is a joint project between the United States and Japanese space agencies, NASA and JAXA respectively, and has been proven extremely successful, still collecting data well beyond the 5 year design life. Figure 2.11 displays the overall TRMM viewing geometry parameters prior to the altitude boost from 350 km to 402 km in August 2001. Specifications for the TRMM Precipitation Radar (TRMM-PR) are listed in Table 2.6.

Table 2.5: COSMO-SkyMed radar specifications and operating parameters used in this research.

Parameter	**Value for processed data**	**General PingPong Stripmap**
Data format	single look complex (SLC)	SLC, geocoded amplitude
Frequency	9.6 GHz (3.12 cm)	
PRF	3151 Hz	2905.9 Hz - 3632.4 Hz
Range bandwidth	34.5 MHz	14.77 - 38.37 MHz (ping-pong mode)
Polarization	HH, VV	any 2 of: HH, VH, HV, VV
Antenna	5.6 m in azimuth direction	
Orbit	620 km	
Incidence angle	24.4°- 27.3°	20°- 60°
Azimuth spacing (w/ oversample)	2.19 m	$\leq$15 m (mode and inc angle dependent)
Slant range resolution	3.48 m	$\leq$15 m
Slant swath width	30 km	30 km (double polarization), 40 km (single polarization)
Repeat orbit time	16 days per satellite	

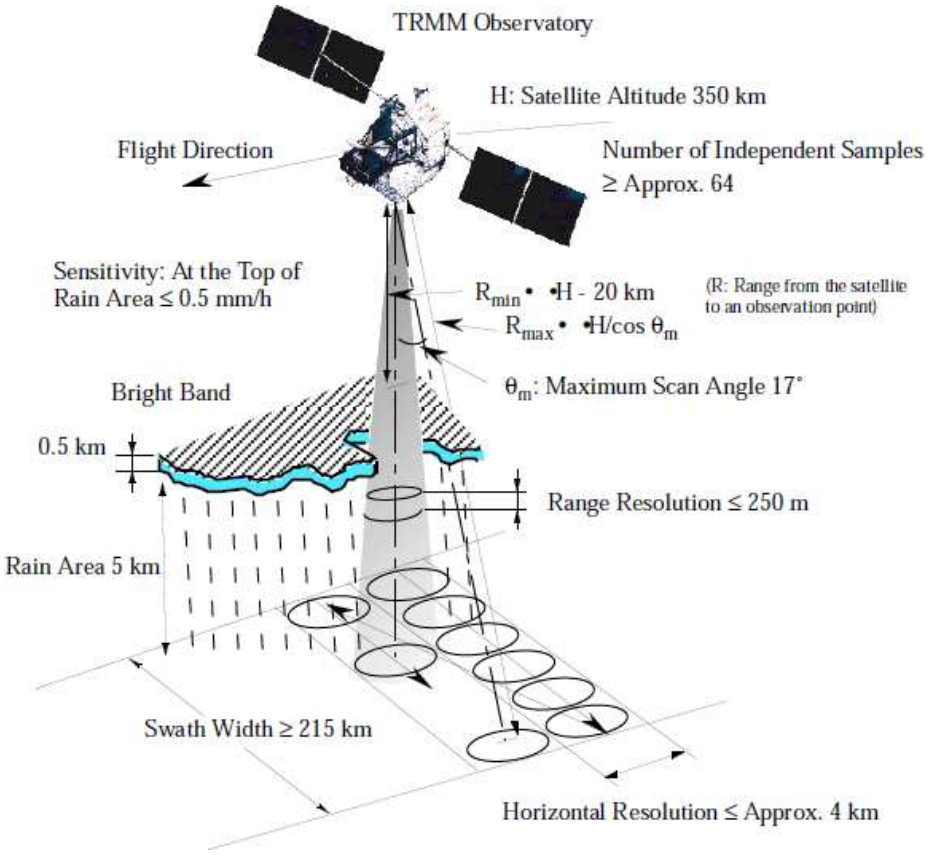

Figure 2.11: The TRMM observatory geometry before the altitude boost (adopted from NASDA (2001)).

Table 2.6: TRMM Precipitation Radar Specifications

Parameter	**Value**
Antenna aperture	2×2 m 128 element active phase array
Antenna gain	$\sim$ 47.4 dB
Frequency	13.796 - 13.802 (GHz)
Pulse width	1.6 μs $\times$ 2 channels
PRF	2776 Hz
Peak power	over 700 W
3 dB Beamwidth	0.71° by 0.71°
Dynamic range	$\sim$ 81.5 dB
Polarization	HH
Altitude (orbit)	350 km
Incidence angle	0° - 18°
Range resolution	250 m
Surface (horizontal) resolution	4.3 (nadir) to 5 km^2
Swath width	220 km
Revisit time	$\sim$1.5 days

2.4 Neural Networks

Neural networks have been successfully applied to many applications, notably pattern recognition and non-linear function estimation, and they can be created in a variety of configurations [Haykin (1999)]. Radial basis function networks (RBFNs) are particularly attractive due to their simplicity and the underlying functions are ideal for modeling non-uniformly sampled irregular data. Figure 2.12 depicts a schematic of an RBFN with N inputs and M outputs. The single hidden layer contains nodes or neurons that consist of individual transfer functions, which are often multivariate Gaussian. The training of the network consists of determining the center μ, width σ and the weight w of each RBF in order to minimize some error criteria between the input and output estimate. Given L hidden layer neurons with a Gaussian transfer function, the jth output is calculated as

$$\hat{y}_j = w_{j0} + \sum_{k=1}^{L} w_{jk}\phi_k\left(\mathbf{x}\right) \tag{2.44}$$

where $\phi_k\left(\mathbf{x}\right)$ denotes the kth transfer function and w_{jk} is the weight applied to the kth neuron connection to the output, with w_{j0} being an overall bias value for that output. The transfer function is written as

$$\phi_k\left(\mathbf{x}\right) = \exp\left(-\frac{\parallel \mathbf{x} - \underline{\mu_k} \parallel^2}{2\sigma_k^2}\right) \tag{2.45}$$

where $\parallel \bullet \parallel$ indicates the Euclidean norm, a distance measure.

The standard RBFN creates a neuron and updates all parameters for each training vector. Therefore, it becomes extremely computationally inefficient for high dimensional problems with a large training set. A number of algorithms have been developed to make the RBFN more efficient, and the implementation chosen for this research is adapted from Campa et al. (2002). Only neurons that are close to an input vector will have a noticeable effect on the output, so only those neurons within a given distance from an input training vector are updated in the learning process. This is known as the Extended-RBF, but it does not reduce the number of neurons.Li et al. (2000) analyzed the performance of the Minimal Resource Allocation Network (MRAN-RBF) algorithm, based on the RAN developed by J. C. Platt [Platt (1991)], that limits the hidden layer size to a user selected number.

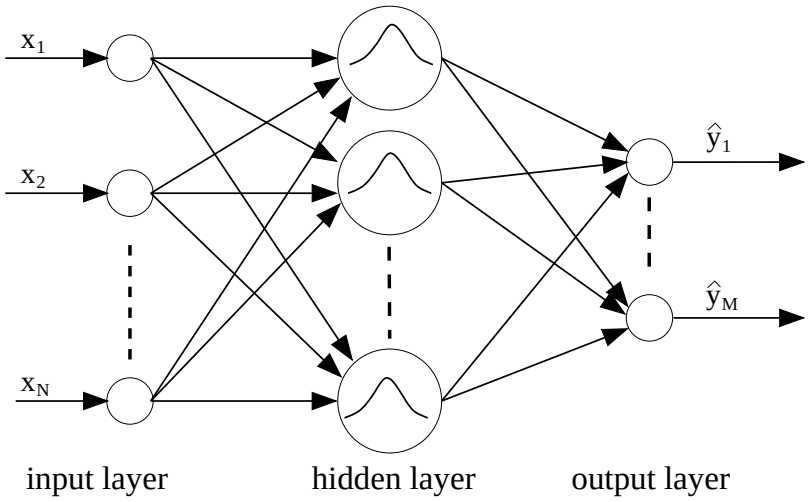

Figure 2.12: Radial basis function network model.

The learning algorithm begins with zero neurons and grows at each new input until the maximum number is reached, at which point neurons are culled to allow for a new neuron or just parameters are updated. The MRAN-RBF algorithm as implemented is detailed as follows.

Step 1: Calculate three errors

The first step involves calculating three error criteria to determine whether or not to add a new neuron for the current (ith) input:

a. Estimation error criterion

$$\| e_i \| = \| y_i - \hat{y}_i \| > E_1 \tag{2.46}$$

b. Novelty criterion (minimum distance to closest neuron)

$$d_{imin} = \min \| \mathbf{x}_i - \mu_i \| > E_2 \tag{2.47}$$

c. Windowed mean error criterion

$$e_{rmsi} = \sqrt{\frac{1}{M} \sum_{j=i-(M-1)}^{i} \| e_j \|^2} > E_3 \tag{2.48}$$

where M is the selected number of past outputs to consider in the filter. E_1, E_2 and E_3 are thresholds to be appropriately selected. A node is added only when all three criteria are met, assuring that the new node is sufficiently far from all existing nodes.

Step 2: New node location

Once it is determined to add a new node, the parameters of this node are:

$$w_{L+1} = e_i \qquad \underline{\mu}_{M+1} = \mathbf{x}_i \qquad \sigma_{M+1} = \kappa d_{imin} \tag{2.49}$$

where κ is the defined overlap factor. If the number of nodes is already at the maximum value, go to Step 5 to perform the pruning operation.

Step 3: Calculate the gradient

When all three of the criteria in Step 1 are *not* met, the current network is adapted to reduce the error. It is possible to reduce computation time by limiting the gradient calculation and parameter update to only those nodes within a given distance from the input vector, although this can be effectively disabled by setting the threshold sufficiently large. Consider the network parameters as a vector $\mathbf{q} = [\mathbf{w}_0^T, \mathbf{w}_1^T, \underline{\mu}_1^T, \sigma_1^T, \ldots \mathbf{w}_{L_D}^T, \underline{\mu}_{L_D}^T, \sigma_{L_D}^T]^T$, where L_D is the number of nodes within the threshold distance. The gradient matrix is then

$$\begin{aligned}\mathbf{B}_j = \nabla_q f(\mathbf{x}_j) &= \frac{\partial \hat{y}_j}{\partial \mathbf{q}_j}|_{(L_D)} \\ &= \Big[\mathbf{I},\ \phi_1(\mathbf{x}_j)\mathbf{I},\ \phi_1(\mathbf{x}_j)(2\mathbf{w}_1/\sigma_1^2),\ (\mathbf{x}_j - \underline{\mu}_1)^T,\ \phi_1(\mathbf{x}_j)(2\mathbf{w}_1/\sigma_1^3) \parallel \mathbf{x}_j - \underline{\mu}_1 \parallel^2, \ldots \\ &\quad \phi_{L_D}(\mathbf{x}_j)(2\mathbf{w}_{L_D}/\sigma_{L_D}^2),\ (\mathbf{x}_j - \underline{\mu}_{L_D})^T,\ \phi_{L_D}(\mathbf{x}_j)(2\mathbf{w}_{L_D}/\sigma_1^3) \parallel \mathbf{x}_j - \underline{\mu}_{L_D} \parallel^2\Big]^T\end{aligned} \tag{2.50}$$

At this point, the network can be updated by updating the vector $\mathbf{q}$.

Step 4: Update the network parameters

In general, the network parameters $\mathbf{q}$ are updated as

$$\mathbf{q}_j = \mathbf{q}_{j-1} + \mathbf{K}_j \mathbf{e}_j \tag{2.51}$$

where $\mathbf{K}_j$ can be the Kalman gain matrix as used in the EKF method [Li et al. (2000)] or simply by using $\mathbf{K}_j = -\eta \mathbf{B}_j$ where η is the learning rate.

Step 5: Pruning strategy

When the number of nodes reaches the maximum and the criteria of *Step 1* are met, the least significant node is pruned from the network to provide room for a new node to be added. This node is determined by evaluating the output of each node computed as the components of the sum in (2.44) for the minimum value.

The implementation used in this work was developed in Campa et al. (2002) in the Matlab Simulink environment, and the block diagram is depicted in Fig. 2.13. In addition to the core MRAN-RBF block, the input and output vectors are scaled so that they fall within $[-1, 1]$. This can be helpful when some input elements are much larger than others even though they both have relatively similar correlation with the desired output (e.g., reflectivity and differential reflectivity). We can also take advantage of this scaling by setting the minimum and maximum to reduce the impact of potentially noisy input elements, e.g., scaling $K_{dp} \in [-0.5, 0.5]$. A unique formula is used in this implementation to determine the distance threshold for the novelty criterion, and is expressed as

$$E_3 = \min\left(d_{max}^{gt}, d_{min}\right) \tag{2.52}$$

where t is time and g is typically close to 1 (e.g., 0.9999) to allow slow decay from the maximum to the minimum. In cases where time is arbitrary, t increments by one for each input vector.

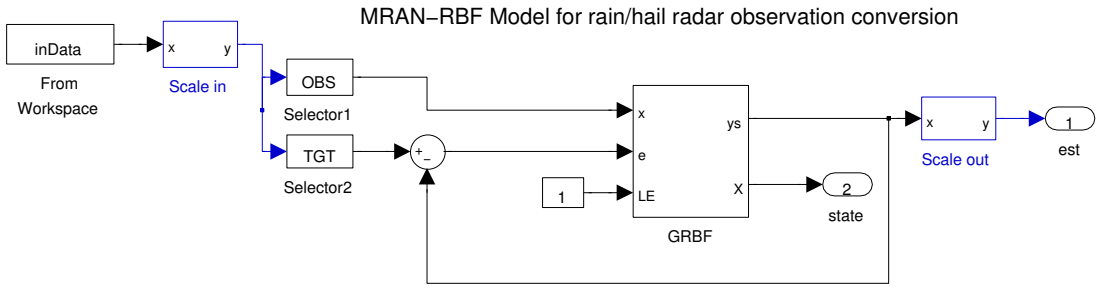

Figure 2.13: MRAN-RBFN Simulink block diagram.

CHAPTER 3

PRECIPITATION INDUCED LAND SURFACE CHANGE - IMPLICATIONS FOR TRMM

Anyone who attempts to generate random numbers by deterministic means is, of course, living in a state of sin.

- John von Neumann

3.1 Introduction

The Tropical Rainfall Measurement Mission Precipitation Radar (TRMM-PR) produces an estimate of the rain rate using the Surface Reference Technique (SRT) [Meneghini et al. (2000)]. Essentially, this technique subtracts the measured surface backscatter through precipitation from an estimate of the reflection without precipitation to obtain the attenuation along the path. A power law relationship with attenuation is then used to obtain a rain rate. Over land, there are four schemes currently being used to determine the reference (non-precipitation) backscatter, or Normalized Radar Cross-Section (NRCS). The predominant methods use a spatial reference calculated from the NRCS of nearby non-rain cells (fields of view) [Meneghini et al. (2000)]. One uses cells at the same incidence angle just prior to the rain cells and is referred to as the along-track spatial reference, while the other examines cross-track cells in an algorithm to handle different incidence angles and various conditions. While the SRT works reasonably well given the complex nature of NRCS over land, it has been shown that biases exist especially due to the impact of surface water due to recent precipitation [Seto and Iguchi (2007)].

One of the contributing factors to the complexity of land NRCS is the spatial variability. At the current altitude of the TRMM satellite, the TRMM-PR resolution cells on the

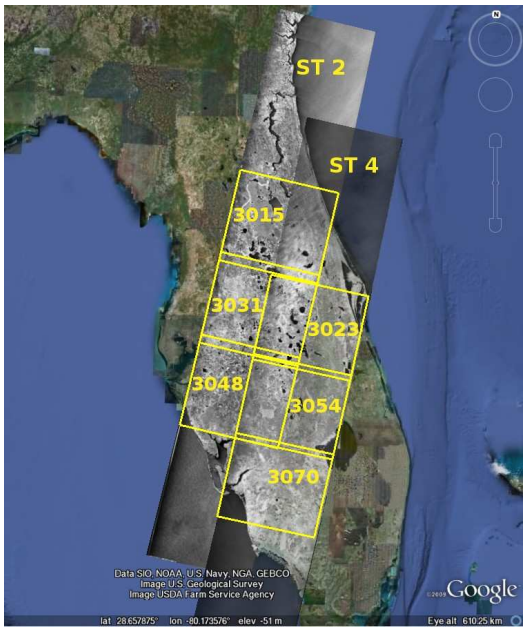

Figure 3.1: RADARSAT-1 mode ST2 and ST4 over a Google Earth image.

surface are approximately 4.3 km^2 at nadir expanding to about 5 km^2 at the extents of the TRMM-PR look angle (±17°). In contrast, Synthetic Aperture Radar (SAR) has a very high resolution, typically on the order of tens of meters or less. Although SARs operate in lower frequency ranges (P to X-band vs. Ku-band) and incidence angles above 18°, they can be a powerful tool for analyzing surface backscatter characteristics. The research described here presents the results of this analysis using the Canadian Space Agency RADARSAT-1 C-band SAR data over central Florida, USA. In particular, the effect of surface moisture is studied using precipitation products from nearby NEXRAD WSR-88D radars.

3.2 Radar Data Processing

RADARSAT-1 acquired data over two swaths repeatedly from January 2006 through April 2008 in Standard Beam Mode 2 (ST2) and Standard Beam Mode 4 (ST4). Each swath is broken up into multiple frames as seen in Fig. 3.1. The 6 frames shown were processed from raw phase data into ortho-rectified NRCS (σ^0) images using the Vexcel Focus and OrthoSAR products. The grid resolution is (1/2048)° in latitude and longitude or about 50 m^2. RADARSAT-1 repeats orbits every 24 days; however, only images that could form interferometric pairs were used to increase spectral and spatial overlap. Using the stack of

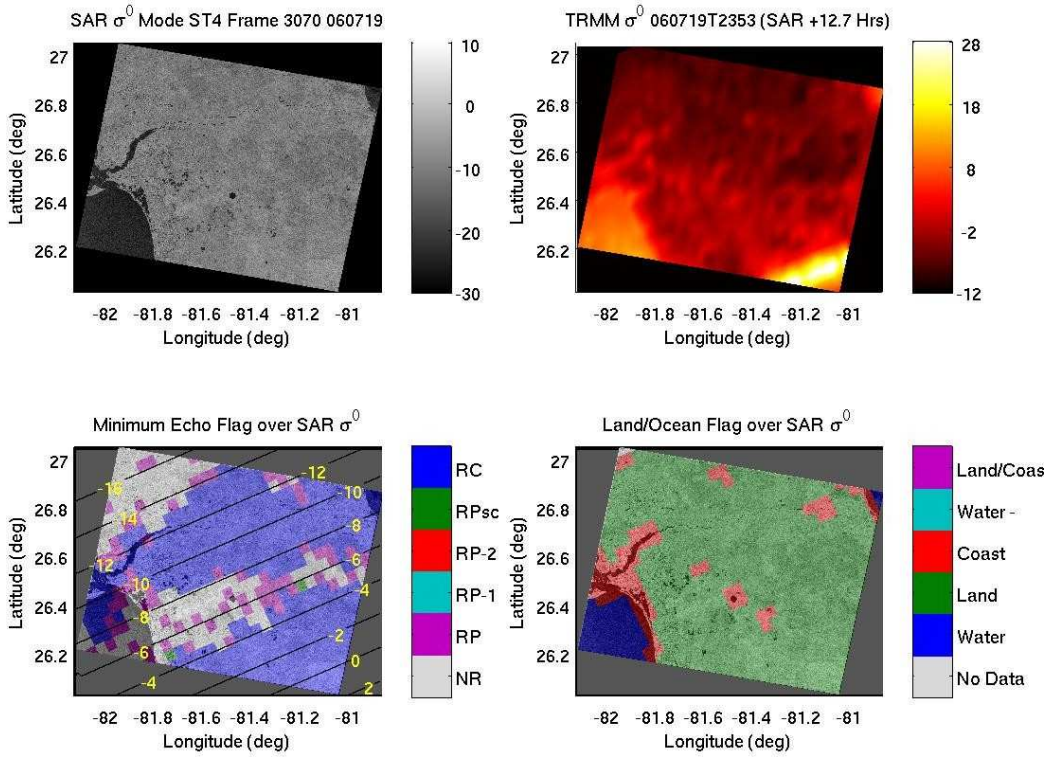

Figure 3.2: By resampling TRMM-PR data on the same geo-referenced grid as SAR data, direct comparisons can be made. The top 2 plots show σ^0 (the surface backscatter) from SAR and TRMM respectively. The bottom left shows the TRMM minimum echo flag (RC = rain certain, RPx = rain probable with certain conditions, RP = rain probable, NR = no rain). The lines with numbers show the TRMM-PR look angle (i.e., 0 = nadir). The bottom left plot displays the TRMM flags for land, ocean and coast. For both bottom plots, the blocks indicate TRMM-PR resolution (4.3 km^2) while the SAR is about 50 m^2.

images, a mask is generated to remove non-overlapping grid cells. The resulting "scene" refers to the common grid, and is used as the geo-spatial reference for other data types.

Data from the TRMM-PR are obtained via the 2A21 product containing σ^0, incidence angle and flags for distinguishing land, ocean and coast as well as a flag indicating that rain is present. TRMM-PR data are selected by determining which locations lie within the boundaries of each scene. Fig. 3.2 shows an example of TRMM data within the ST4 3070 frame indicated in Fig. 3.1. The SAR σ^0 is shown at the top left, with the TRMM σ^0 in the upper right panel and nadir returns clearly visible near a longitude of -81.2° and 26.1° latitude. In the bottom left panel is the TRMM minimum echo flag as a transparent overlay on the SAR σ^0. The blue regions indicate definite rain while the purple shows where rain is probable. A similar overlay is shown in the bottom right panel for land, ocean and

coastal flags. Over Florida, many regions are marked as coastal due to the numerous lakes present, some of which are visible in this scene. Coastal flags also change due to the specific incidence and viewing angle as well as surface conditions such as oversaturated soil. Using the processing to create Fig. 3.2, TRMM-PR data with rain and/or within a certain time of a SAR acquisition can be determined as well as isolating the land, coast and ocean returns.

The precipitation products in NEXRAD Level 3 data provide contiguous auxiliary information across the domain from radars in Melbourne (KMLB) and Tampa Bay (KTBW). Using the NOAA Weather and Climate Toolkit, the radial data are resampled and orthographically projected onto a grid of approximately 0.00425° latitude and longitude. Each point can then be tested to determine which scene, if any, it is within.

3.3 TRMM-PR Land Backscatter

Radar backscatter from land, and the effect of soil moisture, incidence angle and radar frequency, has been well studied and modeled [Moore et al. (1980); Ulaby et al. (1986); Ulaby and Dobson (1989)]. The surface response of TRMM-PR has also been investigated [Meneghini et al. (2000); Oki et al. (2000); Seto and Iguchi (2007)], however, the models have not been directly applied. Moore et al. (1980) suggested a model of the form $\sigma^0_{dB}(\theta, f) = A + B\theta + Cf + Df\theta$ where f is the radar transmit frequency and θ is the incidence angle. A different model was proposed by Ulaby and Dobson (1989) in the form $\sigma^0_{dB}(\theta) = P_1 + P_2 \exp(-P_3\theta) + P_4 \cos(P_5\theta + P_6)$ where a different set of coefficients accounts for both frequency and ground cover. With the goal of verifying an existing model or creating a new one, data were extracted from 2A21 files from 2004 through 2008 in order to provide a large sample set over such a small area (the scenes), and only pixels flagged as land with no rain were used. Fig. 3.3 depicts a 2D histogram of TRMM-PR σ^0 vs. θ within two scene regions similar to NRCS plots in [Meneghini et al. (2000); Oki et al. (2000); Seto and Iguchi (2007)]. Unfortunately, iterative least squares curve fitting techniques perform poorly at fitting the aforementioned models to this data. A modification to the Ulaby model is proposed in order to capture the trend of TRMM-PR land NRCS, given by

$$\sigma^0_{dB}(\theta) = k_1\theta^{k_2} + k_3 \exp(-k_4\theta). \tag{3.1}$$

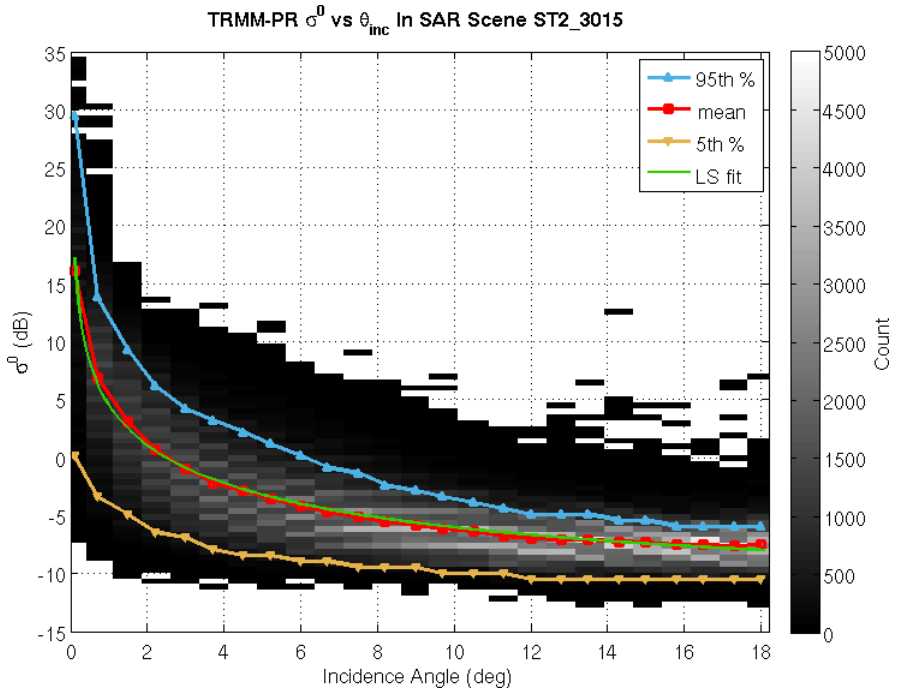

(a)

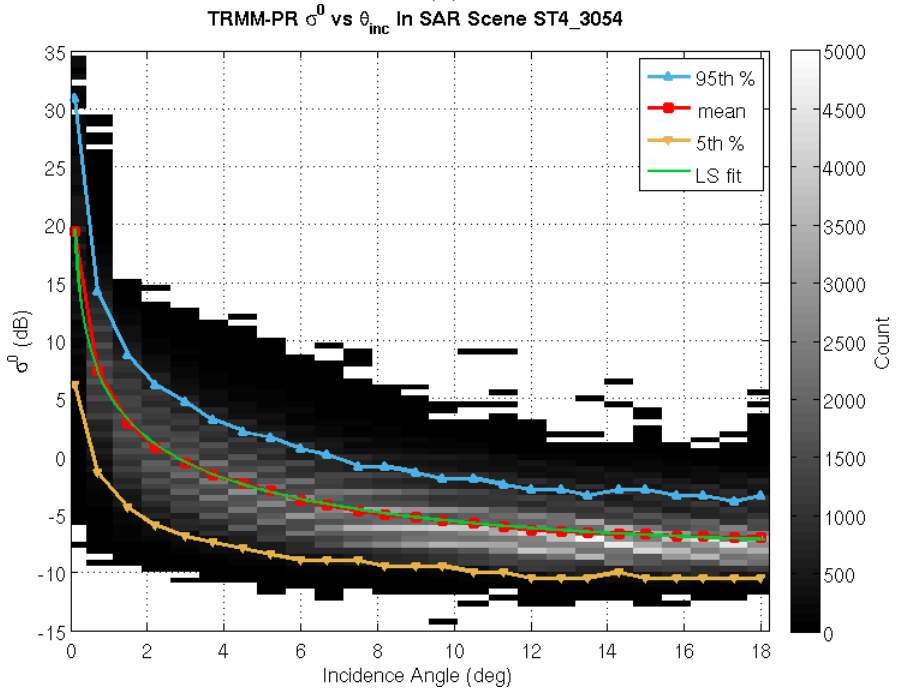

(b)

Figure 3.3: 2D histogram of TRMM-PR σ^0 vs. incidence angle (θ) within a RADARSAT-1 scene from 2004 through 2008. The lines with symbols are the calculated mean and 5% and 95% occurrence levels. In addition, the green line is the model fit from 3.1. (a) Data within scene ST2 3015 (b) Data within scene ST4 3054

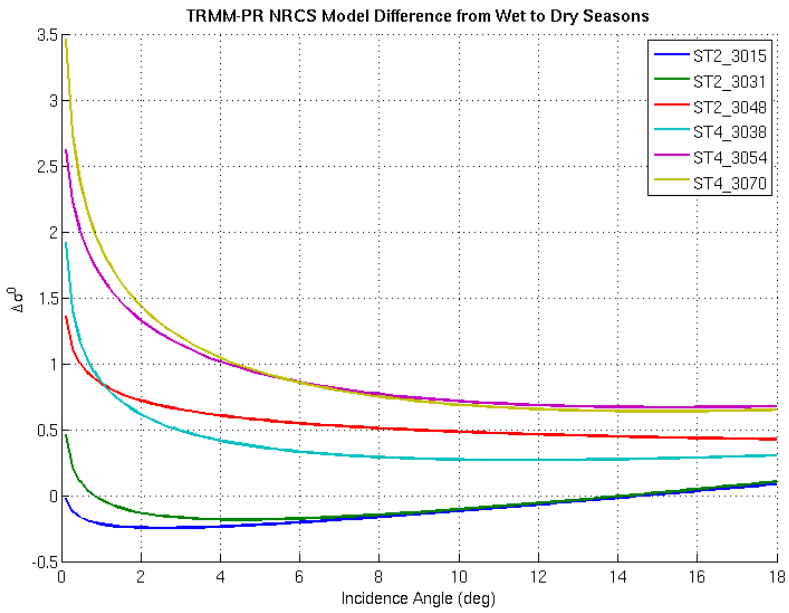

Figure 3.4: The model difference from (3.1) in NRCS (dB) between wet and dry seasons for all 6 scenes as a function of incidence angle. At lower incidence angles, this difference can be above 2 dB, and the trend increases roughly from east to west.

The curves produced from the non-linear least squares fit of (3.1) shown in Fig. 3.3, as the green line, to all the TRMM-PR data within each scene has an average RMS error of about 0.4 dB relative to the mean and 2.9 dB relative to all data due to a substantial variance. NRCS consistency with SAR is verified by extrapolating the model to 27.5°, resulting in an average of -9 dB while the SAR average at this angle is about -10.5 dB with a larger standard deviation. This is close to the 2-3 dB drop from Ku-band to C-band that most general models indicate [Moore et al. (1980); Ulaby et al. (1986); Ulaby and Dobson (1989)]. Unfortunately, (3.1) continues the flattening trend of TRMM-PR with incidence angle, so extrapolation to 37° is about the same.

Using the dates provided by Lascody (2002) to indicate the start of the wet and dry seasons, a noticeable difference in NRCS is revealed. After subtracting the dry season model fit from that of the wet season, in dB scale, the curves shown in Fig. 3.4 result. This plot indicates that lower incidence angles are more sensitive to the season where soil moisture, and to a lesser extent vegetation change, may play a role. There is also a greater difference in western scenes than eastern ones. The hundreds of small lakes in central Florida, notably

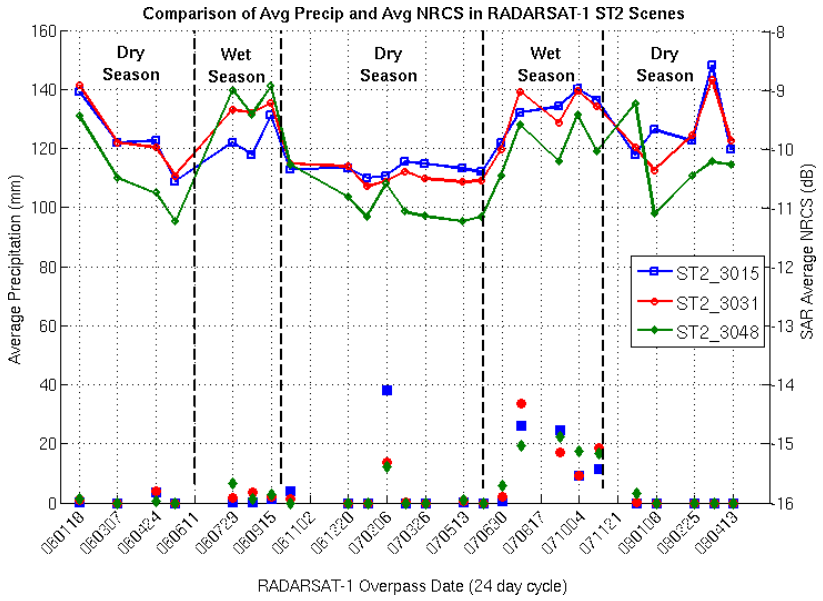

(a)

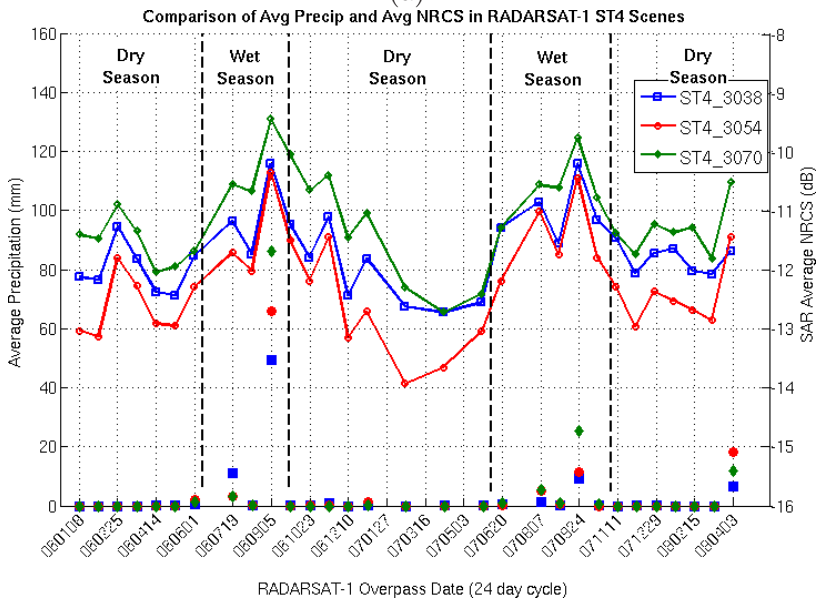

(b)

Figure 3.5: SAR $\bar{\sigma}^0$ and peak average precipitation within 12 hours prior to the SAR acquisition for (a) mode ST2 scenes and (b) mode ST4 scenes.

towards the east coast, may also impact the trend as well as wetlands such as the Everglades found in the southwestern part of the state. SAR data can now be used to examine the surface response further.

3.4 Correlation with Precipitation

The NEXRAD Level 3 Total Storm Precipitation product (NTP) is used for the initial evaluation of precipitation effect. This product accumulates precipitation until the 1-hour precipitation product indicates the storm has passed which resets the NTP output to zero. Since resetting the NTP does not change the surface water content, the maximum NTP is found within a 12-hour period preceding the SAR acquisition, and the maximum between KMLB and KTBW is selected. Once the peak time is identified, the average precipitation accumulation within each scene is calculated. The result is shown in Fig. 3.5 as the non-connected symbols at the scale of the left-hand axis. The abscissa is in increments of RADARSAT-1 repeat orbits, i.e., 24 days, to portray consistent time information.

In order to provide a comparable estimate of land NRCS from SAR, the extensive number of lakes along with the ocean should be excluded because wind and rain roughened water surfaces can drastically increase radar backscatter at larger incidence angles. In particular, the ocean observations can sometimes exceed that of land. The "high resolution" mask for oceans provided by the Generic Mapping Tools [Wessel and Smith (1995)] was used to remove ocean pixels, but the resolution for lakes is not high enough. On average, the radar reflections on the water bodies are very low and can be distinguished upon examining the power distribution. Extreme accuracy in identifying water is not required, so the process begins by applying a 3×3 moving average filter to the ortho-SAR images to further reduce speckle. Subsequently, all acquisitions for each scene are averaged and a threshold is selected to mask out the water. One threshold was selected for each mode/incidence angle based on the histogram and empirical observation on the result in conjunction with optical imagery. For ST 2 scenes, that threshold is -13.5 dB while it is -17.5 dB for ST 4. This removes a majority of the water, although some larger lakes were not completely masked.

With the water removed, the average of the remaining pixels in each SAR image is calculated, shown as the solid lines in Fig. 3.5. These plots also indicate the start of the dry and wet seasons. As expected, there is, generally an increase in $\bar{\sigma}^0$ during the wet season and a decrease when it tends to be drier. More importantly, there is some correspondence between significant precipitation within 12 hours of SAR acquisition and an increase in

$\bar{\sigma}^0$, although it is not always the case. Further analysis of precipitation trends is certainly warranted since Fig. 3.5 does not indicate within how much time the NTP accumulation occurred. The plots also show that the ST4 scenes tend to have higher variability versus ST2 data.

From the information displayed in Fig. 3.5, specific RADARSAT-1 scenes are selected to examine the jump in $\bar{\sigma}^0$. The change in σ^0 is evaluated by calculating the linear ratio of current values to the corresponding pixels in the previous acquisition. Noise is reduced by calculating this ratio from the 3×3 MA filtered images described above. Fig. 3.6 shows the result for the difference between 2006/08/12 (060812) and 2006/09/05 (060905) for ST4 3038. The values are clipped at ±7dB to enhance the visibility of more subtle changes and the variability of $\Delta\sigma^0$ shortly after a storm. A close inspection also reveals a decrease in σ^0 around small lakes where the water level has risen beyond the average level that created the mask. The set of all $\Delta\sigma^0$ images also indicates specific regions that tend to have a higher variance than others. For example, the area to the east of the large lakes contains a mixture of agriculture and swamps which could account for this dynamic. Noise is reduced by calculating this ratio from the 3×3 MA filtered images. Thus, for a given pixel between image B and the previous image A,

$$\Delta\sigma^0(dB) = 10\log_{10}\left(\frac{\sum_{u=-1}^{1}\sum_{v=-1}^{1}\sigma^0_{Buv}}{\sum_{u=-1}^{1}\sum_{v=-1}^{1}\sigma^0_{Auv}}\right) \tag{3.2}$$

where u and v indicate the relative position of pixels and σ^0_{Buv} is the next acquisition afterσ^0_{Auv} at location (u, v). Fig. 3.6a shows the result for ST 2 3031 between 2007/06/30 and 2007/07/24. Likewise, the difference between 2006/08/12 and 2006/09/05 for ST4 3054 is displayed in Fig. 3.6b. The values are clipped at ±7dB to make the mostly subtle changes visible.

A specific relationship between the trends in SAR NRCS and TRMM-PR NRCS is explored by looking at a time where a noticeable jump in SAR NRCS is followed by a drop. From Fig. 3.5, 2006/09/05 was selected, and scene ST4 3038 (Fig.3.6b) had the most TRMM-PR incidence angle coverage within 30 hours of the SAR acquisition. Decreasing the

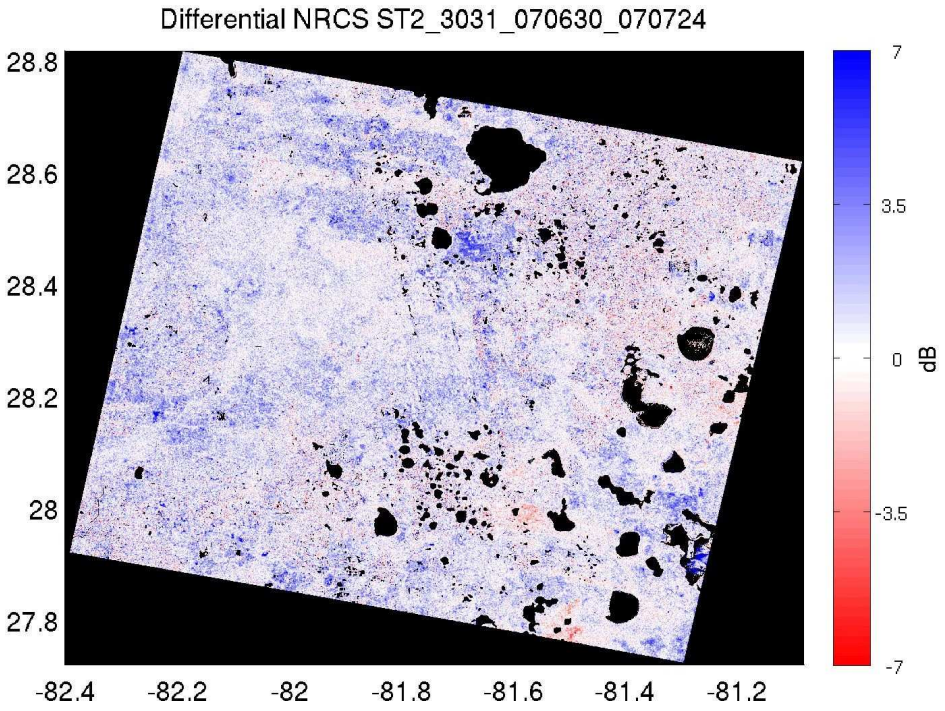

(a)

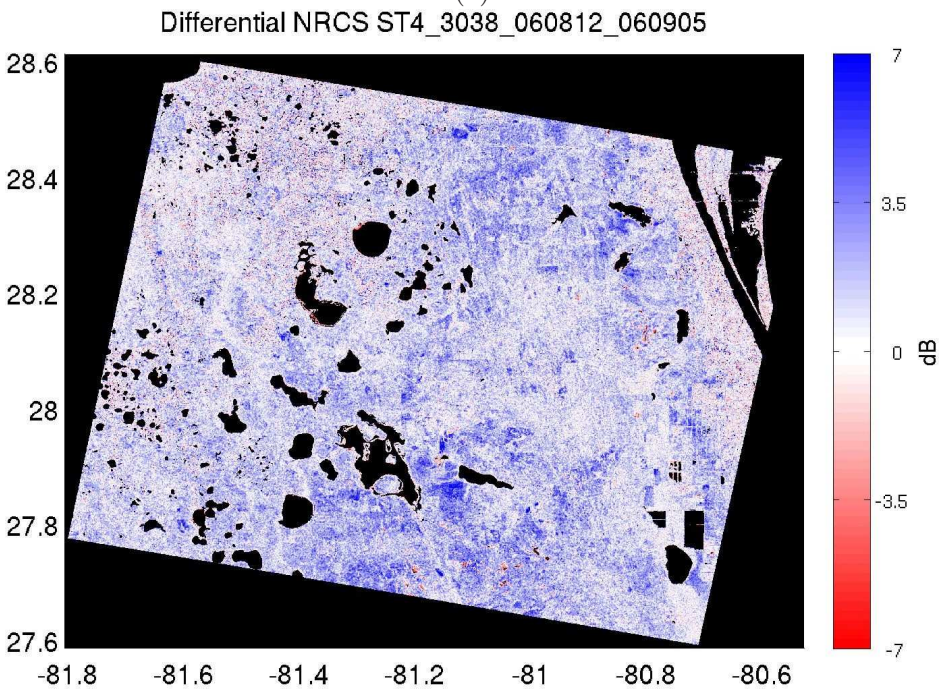

(b)

Figure 3.6: SAR $\Delta\sigma^0$(dB) for (a) scene ST2 3031 from 070630 to 070724 and (b) scene ST4 3038 from 060812 to 060905. Water bodies have been masked using the automated process described in the text. Blue indicates an increase in RCS while red indicates a decrease. In general, an increase is present after rain, but that is not the sole cause.

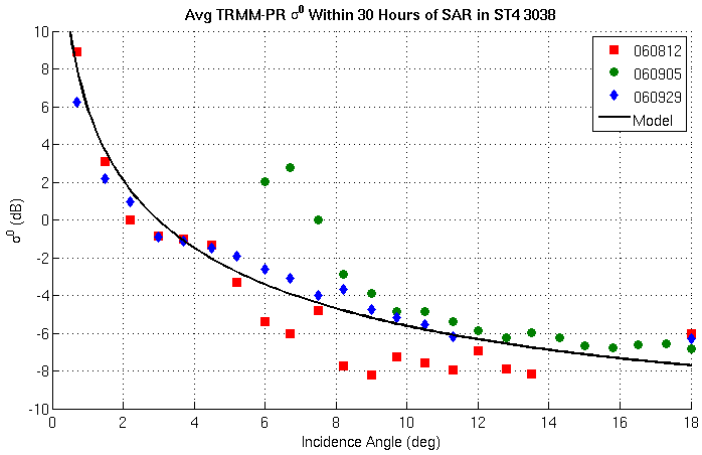

Figure 3.7: Average TRMM NRCS within 30 hours of a given SAR acquisition. The SAR acquisitions selected correspond to 2006.09.05 plus the adjacent dates that show a jump in $\bar{\sigma}^0$. For the most part, the average TRMM-PR $\bar{\sigma}^0$ exhibits a similar trend.

temporal window severely limits this coverage at the expense of changing surface conditions during that time. Much of the region around the larger lakes is flagged as "coast" by TRMM and is excluded from the comparison.

Fig. 3.7 depicts the TRMM-PR σ^0 where the colored symbols indicate the date of the associated SAR acquisition. For most samples, a similar trend is visible where data close to the target date are higher than the two adjacent dates. Given the 30 hour window, this provides the qualitative evidence of the relationship between SAR and TRMM-PR and the starting point for a more detailed analysis at specific locations. Also indicated in the figure is the model fit from (3.1) providing a reference to the average response. Clearly, 060812 observations are several decibels below 060905 observations, although they do not necessarily cover the same location.

3.5 Summary

Through the analysis presented here, an in-depth look at the impact of recent precipitation upon the observed backscatter of spaceborne radar is provided. Using a high resolution imaging radar like SAR, the surface changes within the TRMM-PR footprint can be explored at the temporal sampling rate of SAR. By focusing on specific regions over time, a correlation between recent precipitation and surface NRCS was shown. TRMM-PR data within 30 hours of a SAR acquisition exhibits the same trend, increasing near a significant

precipitation event, and decreasing afterwards. Within the TRMM-PR footprint, however, the surface varies significantly in terms of backscatter change. In addition, a model was presented that adequately reproduces the trend of land NRCS versus incidence angle for TRMM-PR, which is also useful for examining the differences between the dry and wet surface across the Florida peninsula. These results provide strong evidence that the σ^0 shortly after significant rainfall will increase and that the amount of increase can be estimated from high resolution SAR data. However, this will vary dramatically between geographic regions and requires regular, short interval acquisitions to accurately characterize. For regions such as Florida, though, that have significant inland bodies of water or easily saturated soil, SAR can provide valuable information to improve the accuracy of the TRMM SRT result when it is known to vary significantly. Further study with a larger amount of data, ideally at X-band with lower incidence angle, is warranted.

CHAPTER 4

MICROPHYSICAL MODEL TO SIMULATE SPACEBORNE PRECIPITATION OBSERVATIONS AT OFF-NADIR ANGLES

Every great and deep difficulty bears in itself its own solution.
It forces us to change our thinking in order to find it.

- Neils Bohr

4.1 Introduction

A microphysical model of precipitation allows for realistic simulation of observations by a high frequency spaceborne radar using real data from a ground-based system. An accurate model can then be used to invert the process to estimate meteorological parameters from the spaceborne systems, or possibly mitigate precipitation effects if they are considered clutter. Such a model is created by defining parameters of the Particle Size Distribution (PSD) for precipitation in addition to physical properties such as density in $\mathrm{g\,cm^{-3}}$, particle shape and canting angle distribution for the various hydrometeor types. Once these are defined, computational models for electromagnetic scattering by these particles (e.g., T-matrix [Mishchenko et al. (1996)]) are applied given a wavelength and pointing angle (azimuth and elevation) as well as an environmental temperature and set of particle parameters. The model outputs are the following polarimetric radar observable quantities for each specified radar system: horizontal polarization reflectivity Z_h (dBZ), differential reflectivity Z_{dr} (dB), specific differential phase K_{dp} ($\mathrm{deg\,km^{-1}}$), linear depolarization ratio LDR (dB), specific horizontal attenuation A_h ($\mathrm{dB\,km^{-1}}$), specific differential attenuation A_{dp} ($\mathrm{dB\,km^{-1}}$) and co-polar correlation coefficient ρ_{hv}. However, accurate representation of ρ_{hv} requires very advanced models of particle oscillation and vibration that are not included in available tools. The result is a ρ_{hv} that is very close to unity, when in reality

high quality measurements of precipitation can be as low as 0.9. In addition, simulated LDR is often much lower than what is typically measured (e.g., -30 dB vs. -10 dB) due to limitations of the simulation algorithm and measurement noise that increases observations of this sensitive parameter. Following the generation of all the aforementioned parameters, a regression algorithm is then used to determine coefficients of a mathematical model for converting observations of a hydrometeor class between radar systems.

The research documented here describes the parameters used for frozen, melting and liquid hydrometeors, the simulation output at several wavelengths and elevation angles, and the results applied to data collected by real polarimetric radars. For ground radars, horizontally pointing S and C band frequencies are simulated, while spaceborne radars include both X and Ku bands with incidence angles of 25° and 35° (corresponding to 65° and 55° elevation angle respectively). With this variety of frequencies and wavelengths, it is possible to consider both SAR systems at X and Ku bands as well as precipitation radars such as TRMM and GPM close to the edge of their scanning angles. PSD parameters for small frozen and melting particles are dependent on the height relative to the melting layer and were derived from an airborne dual frequency, polarized radar system. A least squares regression method is used to compute the coefficients of basic non-linear functions for the frequency transform. An LS technique is also common for rainfall [Chandrasekar et al. (2006)] using a broader range of PSD parameters; however, errors increase when Mie scattering is observed at higher frequencies such as X-band and above. When hail is considered, and Mie scattering occurs even at S-band, curve fitting techniques cannot adequately represent the oscillatory behavior and variability of radar observations. A novel approach to model rain and hail observations when one or more radars are operating at a short wavelength based on neural networks is presented here and applied to a variety of input scenarios to showcase its robustness. Comparisons are made to curve fitting in rainfall, and the result of applying it to real data are shown. In addition, the advantages and disadvantages of this approach are discussed.

4.2 Particle size distribution

The most common statistical representation for the PSD of precipitation is a three parameter gamma distribution written as [Ulbrich (1983); Bringi and Chandrasekar (2001)]

$$N(D) = N_0 D^{\mu} \mathrm{e}^{-\Lambda D}, (0 \leq D \leq D_{max}) \tag{4.1}$$

where $N(D)$ is the density of particles with diameters in mm per unit volume per unit size interval, and N_0, Λ and μ are the intercept, slope and shape parameters of the distribution respectively. The drop or particle diameter is represented by D. A normalized version of the PSD is described by Willis (1984) and Bringi et al. (2004) is

$$N(D) = N_w f(\mu) \left(\frac{D}{D_0}\right)^{\mu} \exp\left[-(3.67+\mu)\frac{D}{D_0}\right], \tag{4.2}$$

where

$$f(\mu) = \frac{6}{3.67^4}\frac{(3.67+\mu)^{\mu+4}}{\Gamma(\mu+4)}. \tag{4.3}$$

In (4.2) and (4.3), D_0 is the volume-weighted median drop diameter equivalent (mm), N_w is the slope intercept parameter ($\mathrm{mm}^{-1}\,\mathrm{m}^{-3}$), μ is a shape parameter and Γ represents the gamma probability density function (pdf). The PSD in (4.2) provides the framework for simulating the relationship between polarimetric X-band and S-band observations.

4.3 Simulating Small Frozen and Mixed Phase Hydrometeors

Representing the PSD of small frozen and mixed phase hydrometeors can be challenging due to fact that there is a broad range of parameter values that vary with altitude. One method to address this problem is to base the parameters on in situ observations of airborne radar. Using a procedure similar to the one described in Khajonrat (2008) and Chandrasekar and Khajonrat (2009) and the same Ku/Ka band data from the NASA African Monsoon Multidisciplinary Analysis (NAMMA) experiment in 2006, PSD values were determined for this research. The following sections provides the details of the results.

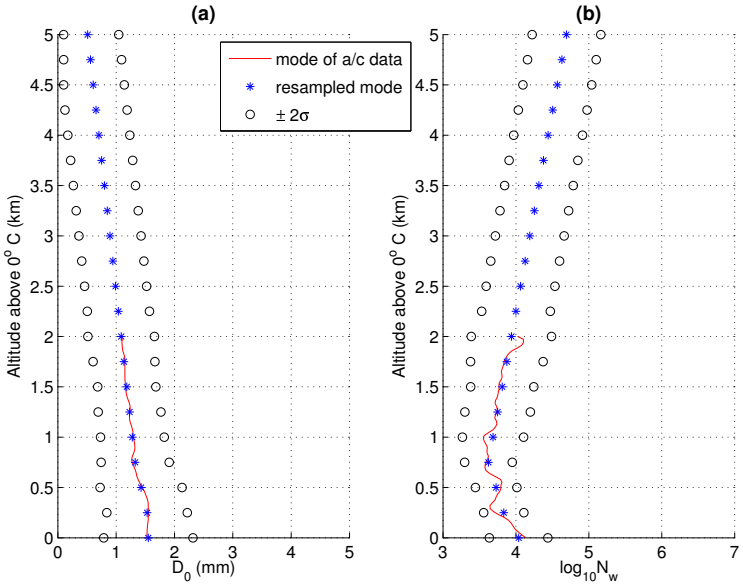

Figure 4.1: Dry graupel PSD parameters as a function of altitude relative to the melting layer. The solid line depicts the mode derived from the airborne data and the '*' is the resampled and extrapolated version. The 'o' represent the mode $\pm 2\sigma$ within specified limits for (a) D_0 and (b) $\log N_w$.

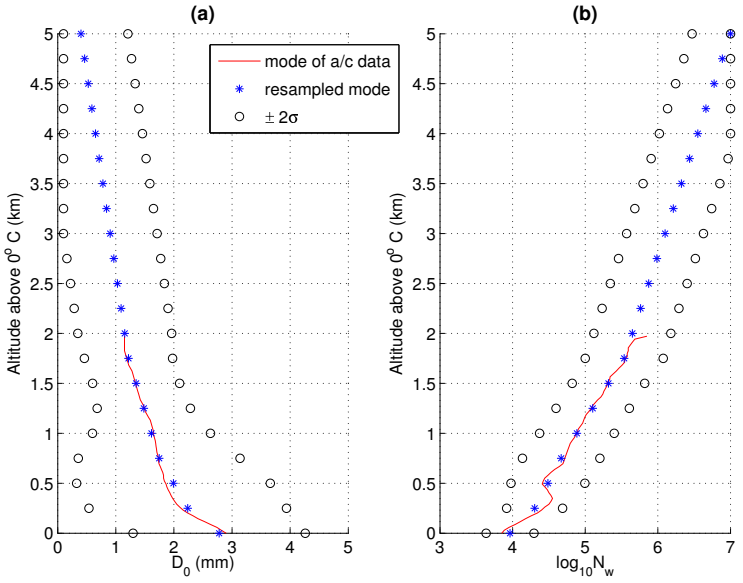

Figure 4.2: Dry snow (a) D_0 and (b) $\log N_w$ as a function of altitude relative to the melting layer. The symbols are defined in 4.1.

4.3.1 PSD Parameter Selection

Figs. 4.1-4.4 depict the characteristics of D_0 and N_w from (4.2) at various altitudes relative to the freezing level for dry graupel, dry snow, wet graupel and wet snow respectively.

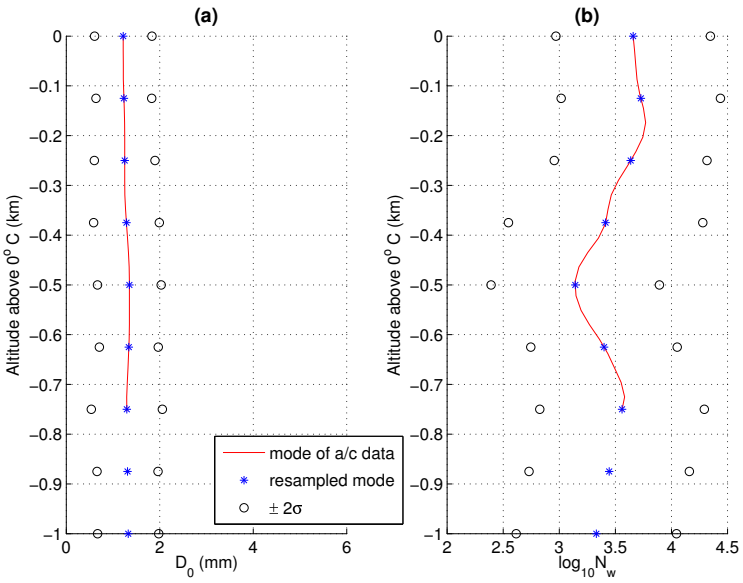

Figure 4.3: Wet graupel (a) D_0 and (b) $\log N_w$ as a function of altitude relative to the melting layer (i.e., below the 0 ° level. The symbols are defined in 4.1.

The third parameter, μ, is set to 0 for these particles thus implying an exponential distribution from (4.2). The mode of each parameter derived from the airborne data, shown as the solid line in the figures, is resampled at 500 m increments for dry particles and 125 m for melting ice. Linear extrapolation is then used to estimate the values at further distances from the melting layer. Chandrasekar and Khajonrat (2009) showed that the distributions for both parameters are approximately Gaussian which was replicated here. In order to avoid unrealistic outliers, limits of ±2 standard deviations from the mode are applied within hard limits of 0 to 5 for D_0 and 3 to 7 for $\log_{10} N_w$, shown in the figures as circles.

The EM scattering simulation results using the PSD parameters shown in Figures 4.1-4.4 were then used to generate observations at various wavelengths. In addition to PSD parameters, air temperature, particle density and water fraction values were selected. A rate of temperature change of 5° per km was used with a reference value of 0° at the freezing altitude. The total particle density ρ and phase fractions f are related by

$$\rho_{total} = \rho_{water} f_{water} + \rho_{ice} f_{ice} + \rho_{air} f_{air} \qquad g\,cm^{-3}. \tag{4.4}$$

4.4 is simplified by the fact that $\rho_{water} = 1$ and $\rho_{air} \ll 1$ with $\rho_{ice} = 0.917$.

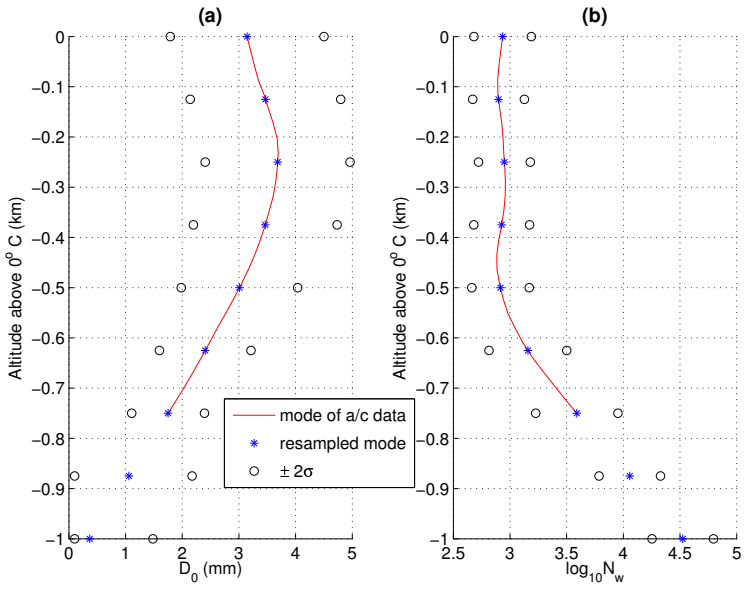

Figure 4.4: Wet snow (a) D_0 and (b) $\log N_w$ as a function of altitude relative to the melting layer (i.e., below the 0 ° level. The symbols are defined in 4.1.

For dry snow, a typical density of 0.1 g cm^{-3} was chosen while a larger density of 0.5 g cm^{-3} was selected for dry graupel, leaving only the fraction of air to calculate from (4.4). Slightly prolate spheroids were selected for the frozen particle shape with an axis ratio of 0.95, which will result in $K_{dp} < 0$. For melting hydrometeors, a water fraction ranging from 0.01 to 0.85 was estimated from the NAMMA data and a starting ice fraction was selected corresponding to the density of the particle prior to melting. As the hydrometeors melt, the shape will approach spherical or oblate raindrops, but to simplify the process a constant axis ratio of 1.05 was applied.

4.3.2 The dielectric constant of melting ice

The Maxwell Garnett (MG) mixing formula [Maxwell Garnett (1904)] is applied to compute the effective dielectric permittivity ϵ_{eff} given the fractional volumes of air, ice and water. Using the MG is one of the most common methods for modeling melting particles [Bohren and Battan (1980); Meneghini and Liao (1996); Olson et al. (2001)], but there are several drawbacks. Selection of the matrix and spherical inclusion materials must be made while considering that the maximum volume of spherical inclusions is approximately 0.63. Consider $\mathrm{MG}_{1,2}$ where the subscripts indicate that material 2 is included in matrix

material 1. Unfortunately, $\mathrm{MG}_{1,2} \neq \mathrm{MG}_{2,1}$ for the same fractional volume of material 1 meaning a discontinuity will occur when the matrix and inclusion materials switch at the 0.63 threshold. Figure 4.5 displays several solutions for calculating the effective dielectric constant given an air and ice mixture (Fig. 4.5a) and for melting ice with some air (Fig. 4.5b) at X-band. The curves forming the envelope are the Maxwell Garnett solutions. More complicated methods for modeling melting hydrometeors are available [Liao and Meneghini (2005); Yokoyama and Tanaka (1984); Olson et al. (2001)], but it is difficult to determine the "best" one due to the physical variety and complexity of melting ice crystals involved.

A mathematical solution proposed here that will allow a smooth transition from one extreme to the other (e.g., solid ice to all water) utilizes a sigmoid function. This expression written as a function of the variable fraction f of ice or water is

$$\nu(f) = \frac{2}{1 + \exp\left[-20n(f - z)\right]} - 1 \tag{4.5}$$

where n controls the slope and z determines the zero-crossing of the function. Hence, it is referred to as the NZ-sigmoid or NZS solution. The effect of these two parameters is shown as a set of curves for NZS in Fig. 4.6. Using NZS, the final expression for calculating ϵ_{eff} is

$$\epsilon_{eff}(f) = 0.5\{[1 - \nu(f)]\, MG_{1,2} + [1 + \nu(f)]\, MG_{2,1}\} \tag{4.6}$$

providing smooth transitions of the dielectric constant through the melting layer. Fig. 4.5 shows several NZS curves, two of which are close approximations to the Bruggeman solution (green lines with triangle markers). The values for these two curves are shown in the legend and are used for the estimation of ϵ_{eff} in the remainder of this thesis. The third curve (shown in cyan in Fig. 4.5b) indicates another possibility. Experiments would be needed, however, to determine values of n and z that result in realistic transitions of melting particle ϵ_{eff}. The simplicity and flexibility of (4.5) and (4.6) make the NZS method a formidable solution, albeit one that may not simulate the physical world depending on the values selected.

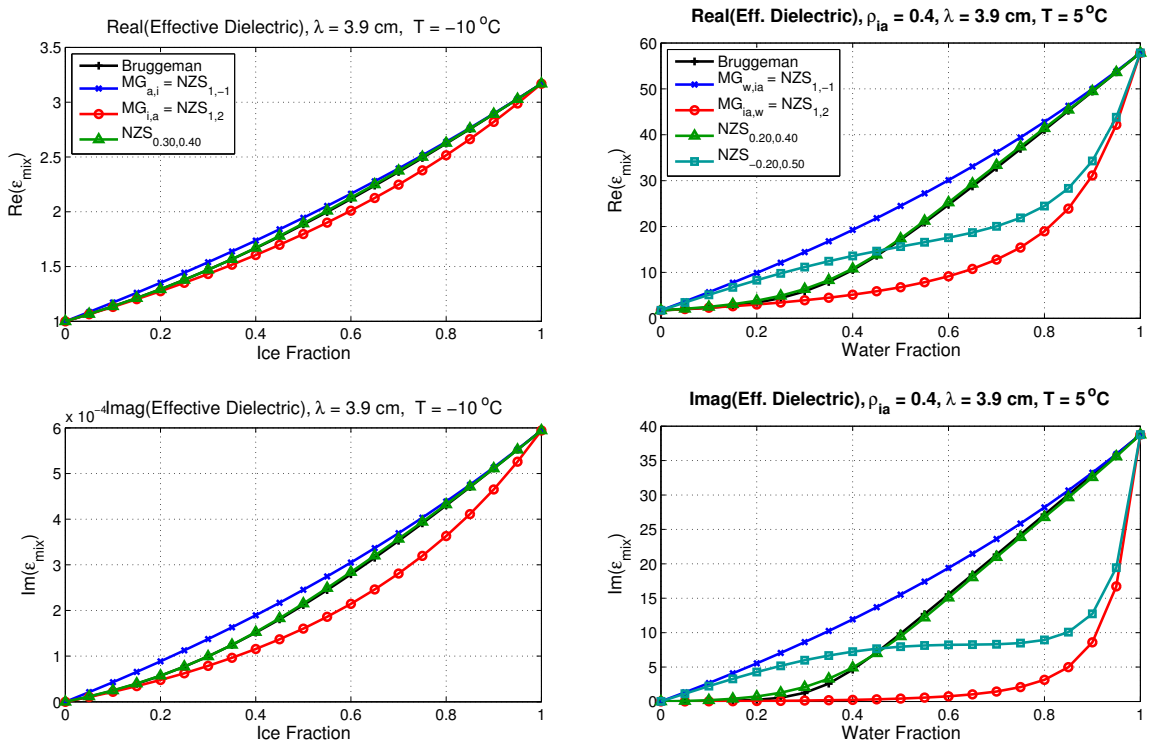

(a) (b)

Figure 4.5: The real (top panels) and imaginary (bottom panels) parts of the effective dielectric constant of an air, water and/or ice mixtures at a 3.9 cm wavelength. (a) Air and ice mixture dielectric versus an increasing ice fraction. The blue curves ('x' marker) represent the Maxwell Garnett ice inclusion within an air matrix, while the bottom red curves (circle marker) show the air in ice Maxwell Garnett solution. The black curve ('+' marker) is the Bruggeman solution, but it is almost completely covered by an equivalent NZ-sigmoid representation shown in green (triangle marker). The legend also shows the NZ-sigmoid values to represent the Maxwell Garnett solutions. (b) Similarly, these panels show the dielectric constant for melting ice versus water fraction from an initial air-ice density of 0.4 g cm^{-3} at 5 °C. Again, an NZ-sigmoid approximation for the Bruggeman solution is shown, plus an additional NZ-sigmoid possibility for a smooth transition shown in the cyan curve (square marker).

4.3.3 Frequency and Angle Conversion Models

Simulating the response at different frequencies and observation angles can be used to determine the relationship among them. For small particles such as snow and graupel, simple regression analysis techniques can be used to fit polynomial or exponential functions in order to convert from one set to another. Figs. 4.7 and 4.8 show the results of the scattering simulations for a horizontal S-band observation and an X-band elevation angle of 55° for dry and wet particles respectively at the altitudes comprising the extent of solutions.

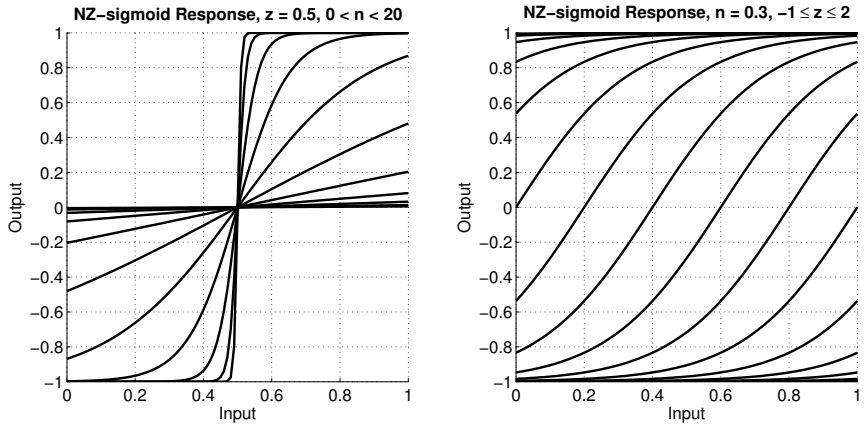

Figure 4.6: NZ-sigmoid response, clipped between 0 and 1, the plausible values for f in (4.6). (a) $z = 0.5$ keeps the zero-crossing constant while n defines the slope from 0 @ $n = 0$ to ∞ @ $n = \infty$. (b) $n = 0.3$ defines a slow transition while z is varied from -1 to 2.

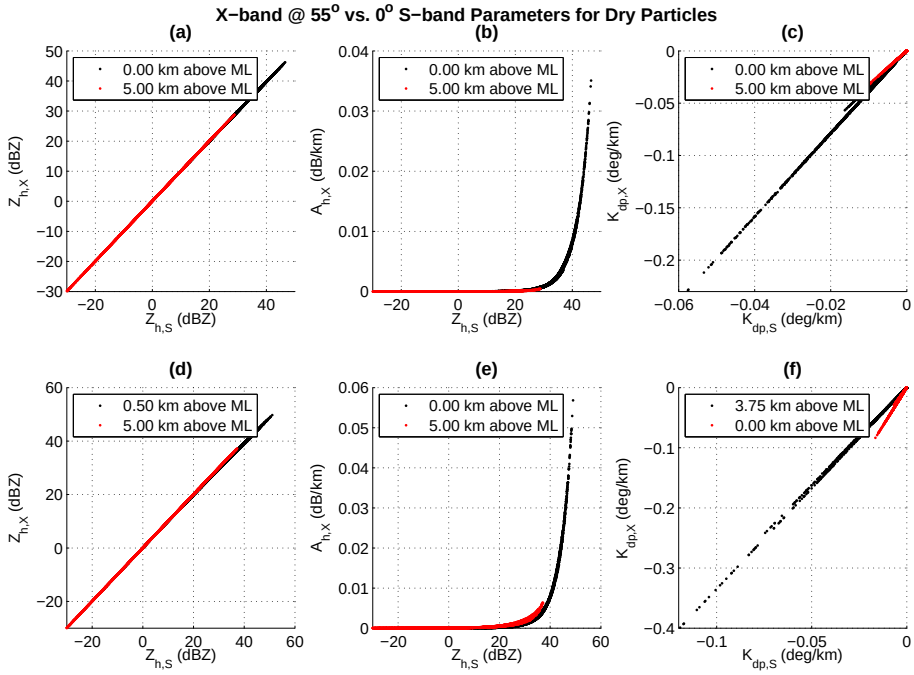

Figure 4.7: Scattergrams showing the relationship between S and X band parameters at the minimum and maximum levels for dry graupel (top row) and dry snow (bottom row). The S-band simulation assumes an antenna elevation angle of 0° while the X-band is pointed at 55°.

Dry graupel (Fig. 4.7a-c) and dry snow (Fig. 4.7d-f) show similar characteristics, while wet graupel (Fig. 4.8a-c) and wet snow (Fig. 4.8d-f) exhibit distinguishing characteristics. Due to the nearly spheroidal shape and densities involved, differential reflectivity, differential specific attenuation and linear depolarization ratio are very close to zero so they are not

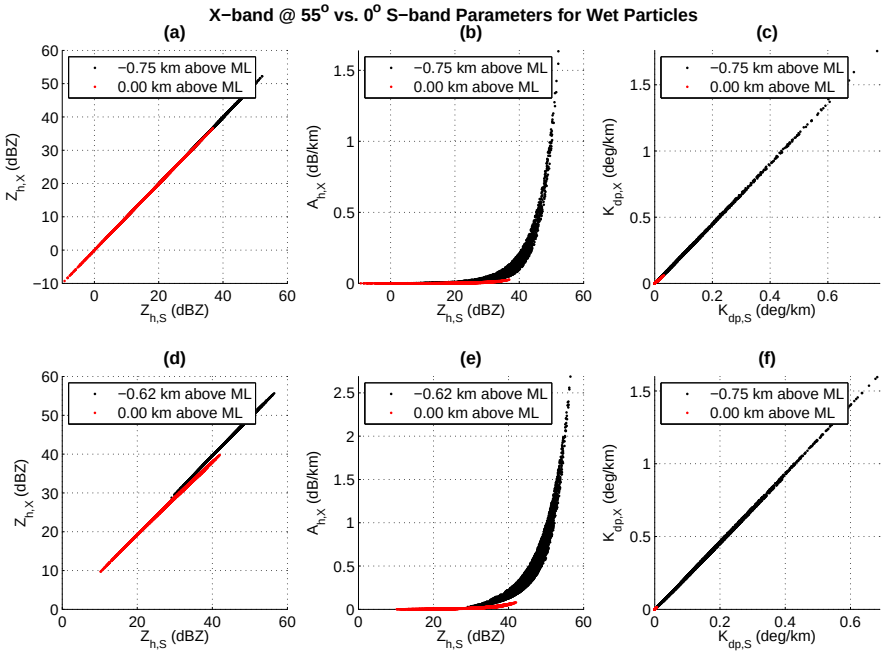

Figure 4.8: Scattergrams showing the relationship between S and X band parameters at the minimum and maximum levels for melting particles.The S-band simulation assumes an antenna elevation angle of 0° while the X-band is pointed at 55°.

shown. In each panel, scatter plots are depicted for the altitude with the minimum value in red and the maximum value in black. In most cases, Z_h, A_h and K_{dp} increase as altitude decreases. Panels (a) and (d) depict X-band reflectivity $Z_{h,X}$ versus S-band $Z_{h,S}$, specific attenuation at X-band $A_{h,X}$ versus $Z_{h,S}$ is shown in panels (b) and (e) while panels (c) and (f) display X-band versus S-band specific differential phase ($K_{dp,X}$ and $K_{dp,S}$ respectively).

Similarly, simulations were run to determine the relationship between horizontal S-band with Ku-band pointing at 65° as well as horizontal C-band with a 65° pointing X-band antenna. The S to Ku results are shown in Figs. 4.9 and 4.10. Attenuation is significantly higher in the melting snow case, as expected, but other parameters are similar. Given the size of the particles relative to the wavelengths used, there is not a significant difference in the C-band to X-band case as seen in Figs. 4.11 and 4.12. Both Z_h and K_{dp} exhibit a linear relationship with low variance. A power law relation exists to estimate $A_{h,X}$ from $Z_{h,S}$ in the form $\widehat{A}_{h,X} = a z_{h,S}^{b}$ where $z_{h,S}$ is reflectivity in linear units. Coefficients for these models are typically determined using a minimum LS error fit to the data which provides an excellent representation given the low variability at the frequencies analyzed.

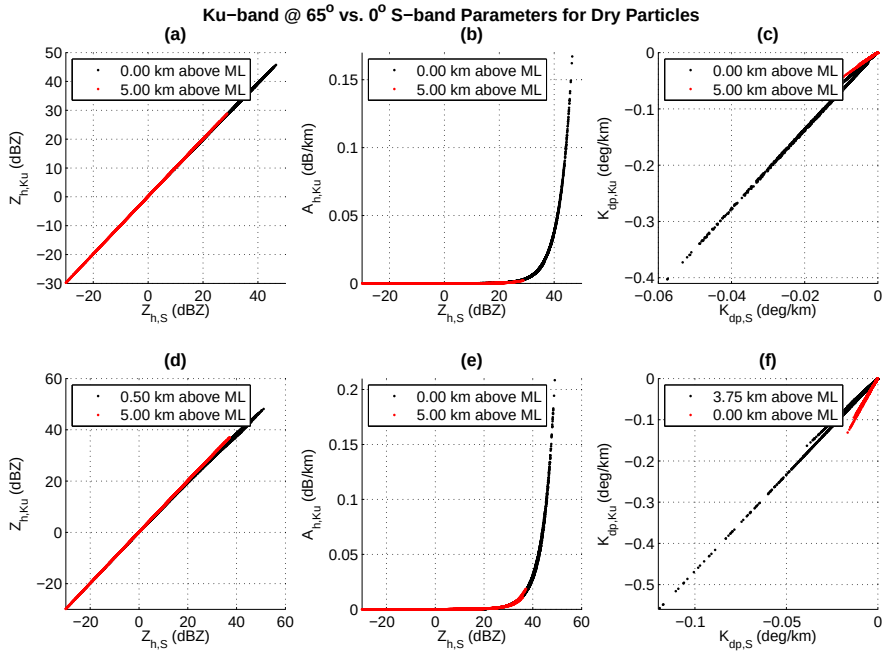

Figure 4.9: Scattergrams showing the relationship between S and Ku band parameters at the minimum and maximum levels for dry graupel (top row) and dry snow (bottom row). The S-band assumes an antenna elevation angle of 0° while the Ku-band is at 65°.

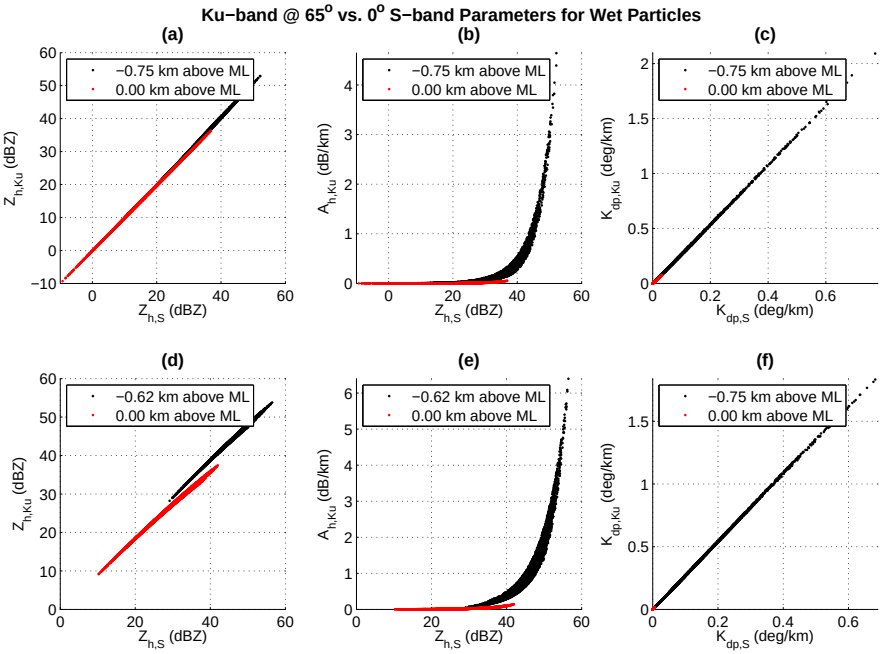

Figure 4.10: Scattergrams showing the relationship between S and Ku band parameters at the minimum and maximum levels for melting particles. The S-band assumes an antenna elevation angle of 0° while the Ku-band is at 65°.

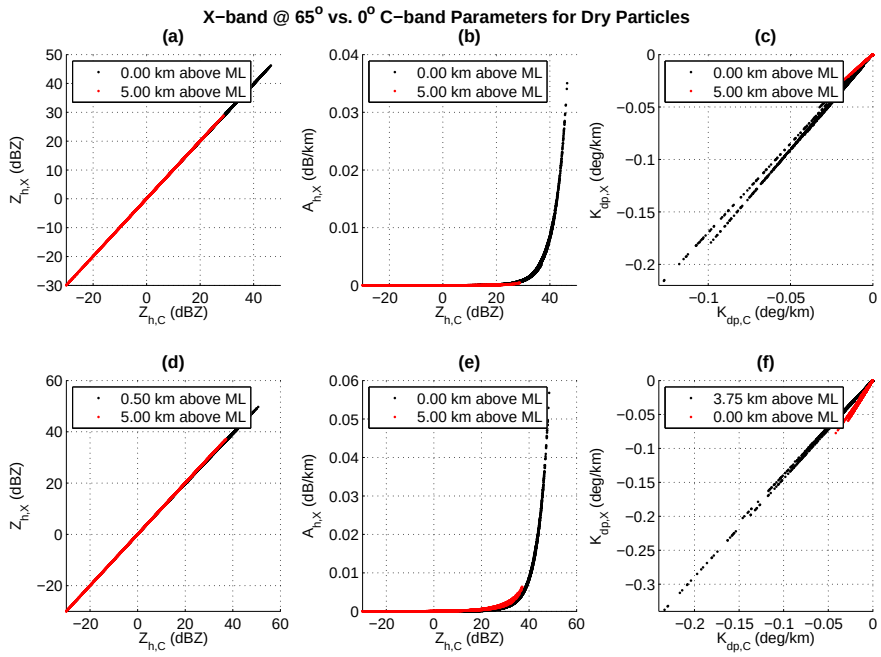

Figure 4.11: Scattergrams showing the relationship between C and X band parameters at the minimum and maximum levels for dry graupel (top row) and dry snow (bottom row). The C-band assumes an antenna elevation angle of 0° while the X-band is at 65°.

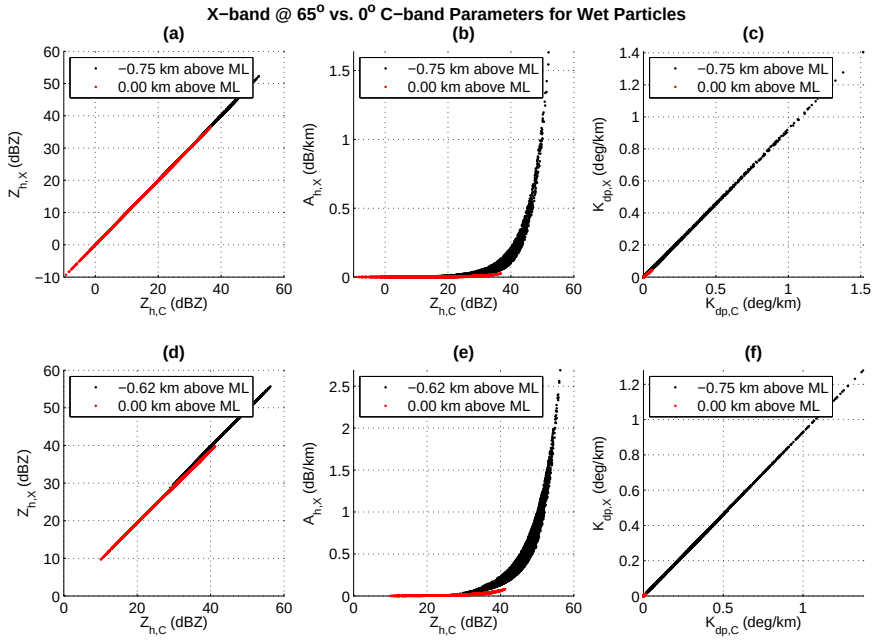

Figure 4.12: Scattergrams showing the relationship between C and X band parameters at the minimum and maximum levels for melting particles. The C-band assumes an antenna elevation angle of 0° while the X-band is at 65°.

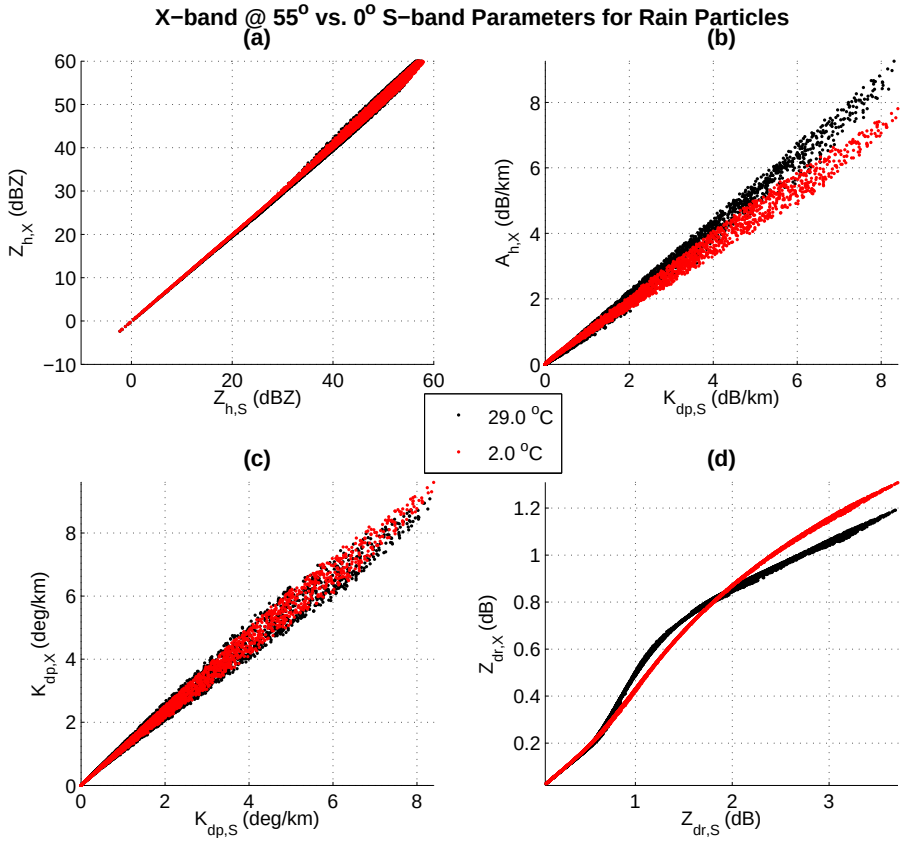

Figure 4.13: Scattergrams showing X-band at 55° versus horizontal S-band observables at 2.0 ℃ (red) and 29 ℃ (black). (a) $Z_{h,X}$ vs. $Z_{h,S}$ are almost identical and both exhibit a slight increase in variance above 35 dBZ as the canting distribution of more oblate particles becomes detectable. (b) $A_{h,X}$ vs. $K_{dp,S}$. At higher temperatures, and larger $K_{dp,S}$ levels, the attenuation noticeably decreases. (c)$K_{dp,X}$ vs. $K_{dp,S}$ where the change due to temperature is only visible at large values. (b) $Z_{dr,X}$ vs. $Z_{dr,S}$ where the curvature due to Mie scattering is exacerbated by temperature.

4.4 Rain

Simulations for rain at S, C, X and Ku bands at the same elevation angles (0° for S and C, 65° at X and Ku and 55° at X) provide the data necessary to design models for using real lower frequency ground rain observations to estimate higher frequency spaceborne measurements. For rain, the following standard PSD value ranges were used [Bolen and Chandrasekar (2003); Bringi and Chandrasekar (2001)]: $0.5 \leq D_0 \leq 2.5$, $3 \leq \log_{10}(N_w) \leq 5$ and $-1 \leq \mu \leq 4$ with a constraint of a rain rate less than 300 mm h^{-1} and $Z_h \leq 55$ dBZ for C-band ground radars and $Z_h \leq 60$ dBZ for S-band. In addition, the raindrop shape model combining the models of Andsager et al. (1999) and Beard and Chuang (1987) proposed by

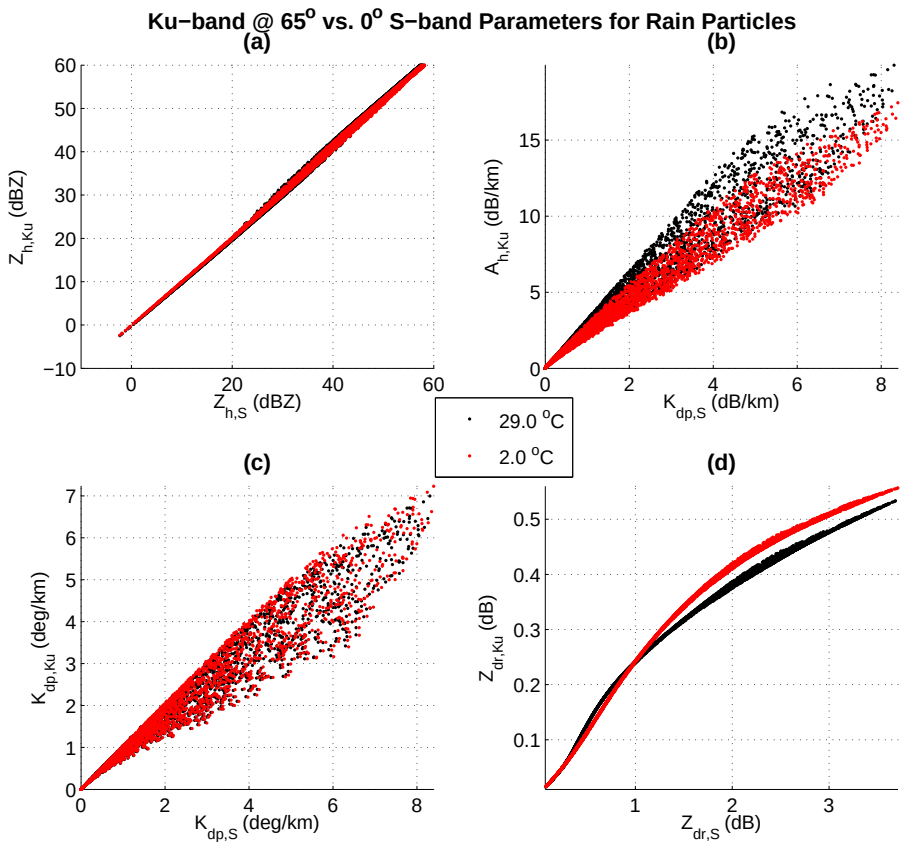

Figure 4.14: Similar to Fig. 4.13 except showing Ku-band at 65° elevation versus horizontal S-band observables at 2.0 ℃ (red) and 29 ℃ (black). Both A_h and K_{dp} exhibit increased variance as Mie scattering becomes more dominant. The Z_{dr} does not appear to change as much with temperature, however, the Ku-band values at this elevation angle are small.

Bringi et al. (2003) was selected with a canting angle standard deviation of 5°. Simulations were then run at temperatures ranging from near 2 ℃ (red) to 29 ℃ (black). Figs. 4.13, 4.14 and 4.15 display the results for the temperature extremes at three pairs of wavelength and elevation configurations. X-band at 55° versus horizontal S-band results are shown in Fig. 4.13, 65° Ku-band versus 0° S-band output is depicted in Fig. 4.14, while Fig. 4.15 shows 65° X-band versus horizontal C-band. In all panels, Mie scattering is evident in regions of curvature and increased variance. The horizontal attenuation and differential reflectivity in panels (b) and (d) respectively are the most impacted by temperature. Reflectivity is plotted in the (a) panels with virtually no temperature dependence except a slight increase in variance, while the (c) panels show K_{dp} with a mild affect at higher values.

Several different model types are typically used for rain. The most common model for fre-

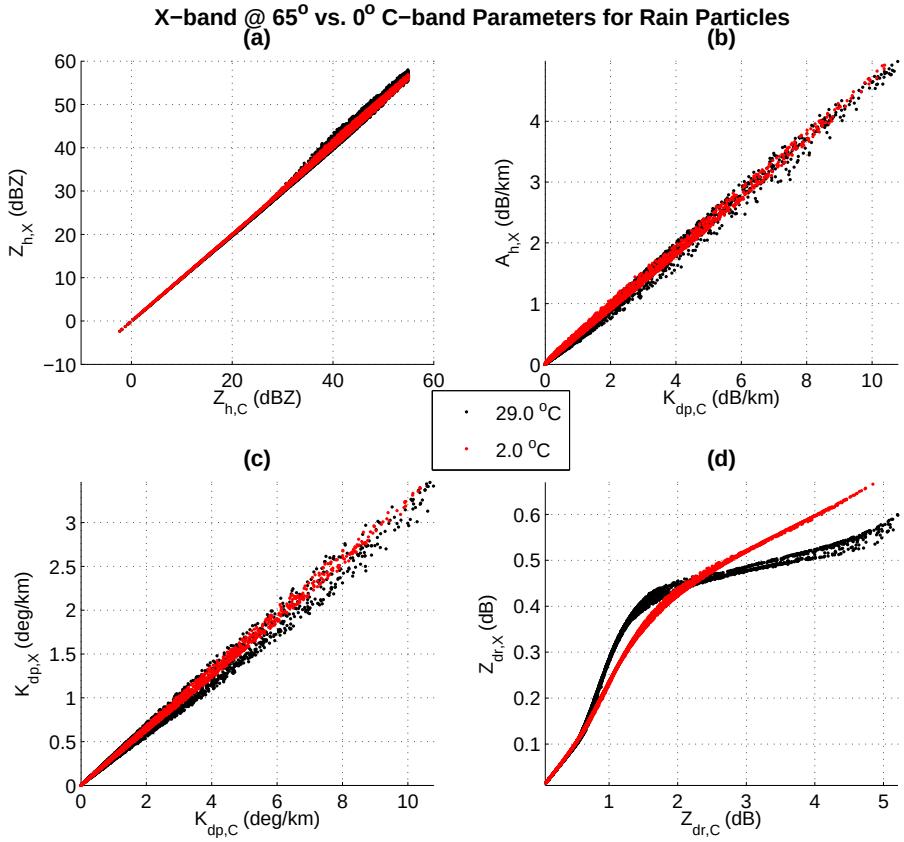

Figure 4.15: Similar to Fig. 4.13 except showing X-band at 25° incidence versus horizontal C-band observables at 2.0 °C (red) and 29 °C (black).

quency transformation of K_{dp} takes advantage of the linear trend when $K_{dp} > 0.5\,\mathrm{deg\,km^{-1}}$ [Bringi and Chandrasekar (2001)], although a second order polynomial accounts for the slight curvature when the lower frequency is in the S band. In some cases, a power law relation with Z_h and sometimes Z_{dr} is also applied depending on frequencies and expected real data quality. For Z_h, shown in (a) panels of Figs. 4.13, 4.14 and 4.15, a complex, but fairly accurate model is represented by

$$\hat{Z}_{h,H} = \begin{cases} c_1 Z_{h,L} + c_2 & Z_{h,L} \leq 25\,dBZ \vee Z_{dr,L} < 0.1\,dB \\ c_3 c_4^{Z_{h,L}} Z_{dr,L}^{c_5} & 25 < Z_{h,L} \leq 40\,dBZ \\ c_6 Z_{h,L}^{(c_7 + c_8/Z_{dr,L})} & 40 < Z_{h,L} \leq 50\,dBZ \\ c_9 Z_{h,L}^{(c_{10} + c_{11}/Z_{dr,L})} & 50 < Z_{h,L}\,dBZ \end{cases} \tag{4.7}$$

where coefficients $\mathbf{c}$ are found via least squares regression analysis, the subscript H is generic for the higher frequency and L for the lower frequency. To account for the curvature in the Z_{dr} relation, an 8^{th} order polynomial is used in $0.5 < Z_{dr,L} \leq 2.5$; otherwise, a linear

model is applied. At C-band, the Z_h, Z_{dr} relationship to horizontal attenuation is degraded as compared to S-band, so the K_{dp} linear model is usually applied to fit the data plotted in Fig. 4.15c. Weather radars in the C band are known to exhibit resonance in rain making Z_{dr} less reliable. From Fig. 4.14, however, we see that polynomial univariate models will be inadequate to characterize the variability of A_h and K_{dp}. One approach is to use a bivariate model such as

$$\hat{A}_{h,H} = c_1 z_{h,L}^{c_2} + c_3 K_{dp,L} \tag{4.8}$$

where $z_{h,L}$ is reflectivity in linear units. A new model is proposed in Section 4.7 that is comparable for simulated data, but considers a more complex interaction between the variables. In addition, it is capable of representing all rain relationships with the need to maintain a set of coefficients for every temperature unlike the LS curve fit models.

4.5 Hail

4.5.1 Overview of polarimetric radar hail scattering

Dual-polarized radars provide opportunities to study and characterize the electromagnetic scattering from hail and identify it in the presence of rain [Aydin et al. (1986); Aydin and Zhao (1990); Aydin et al. (1994); Balakrishnan and Zrnic (1990); Bringi and Chandrasekar (2001)]. As the hail diameter D approaches and then exceeds the wavelength (i.e., $\frac{\pi D}{\lambda} \approx 1$ where λ is the wavelength) scattering from hail falls within the Mie scattering regime, which obviously is more prevalent at higher frequencies. If the hailstone axis ratio is close to unity, or the canting angle distribution is nearly uniform, polarimetric variables Z_{dr}, LDR and K_{dp} will be close to zero. However, it is not unusual for $Z_{dr} < 0$ for larger hailstones that are oblate, indicating a 90° mean canting angle from vertical [Balakrishnan and Zrnic (1990); Bringi and Chandrasekar (2001)]. Previous studies have shown that polarimetric radar observables can be used to quantify a hail signature, and Aydin et al. (1986) defined a new parameter base on Z_{dr}:

$$H_{dr} = Z_h - \mathcal{F}(Z_{dr}) \tag{4.9}$$

where, at a frequency of 3 GHZ

$$\mathcal{F}(Z_{dr}) = \begin{cases} 27 & Z_{dr} \leq 0\,dB \\ aZ_{dr} + 27 & 0 < Z_{dr} \leq b \\ 60 & Z_{dr} > b. \end{cases} \tag{4.10}$$

Under the equilibrium axis ratio assumption, $a = 16.5$ and $b = 2dB$. Given the wide variation in hail size, shape, canting and density parameters that can be observed in different storms, the benefits of simulating all cases at once is likely to be small. However, simulating a few representative scenarios will provide output to handle most hail storms. Scattering oscillations described by the Mie solution in 2.1.3 also make modeling observations a challenge, but one that is tackled here.

When hail is mixed with rain, superposition can be used to model the covariance matrix of the mixture in the linear polarization basis assuming "mirror" reflection symmetry and polarization plane isotropy [Bringi and Chandrasekar (2001)]. In the BSA convention, the covariance matrix of the mixture can be expressed as

$$(\mathbf{C})_{\text{mix}} = (Z_e)_{\text{mix}} \begin{bmatrix} 1 & 0 & |\rho_{co}|_{\text{mix}} \\ 0 & 2(L)_{\text{mix}} & 0 \\ |\rho_{co}|_{\text{mix}} & 0 & 1/\left(z_{dr}\right)_{\text{mix}}) \end{bmatrix} \tag{4.11}$$

where

$$(Z_e)_{\text{mix}} = (Z_e)_{\text{hail}} + (Z_h)_{\text{rain}} \tag{4.12a}$$

$$(z_{dr})_{\text{mix}} = \frac{1 + [(Z_h)_{\text{rain}}/(Z_e)_{\text{hail}}]}{1 + [1/(z_{dr})_{\text{rain}}]\,[(Z_h)_{\text{rain}}/(Z_e)_{\text{hail}}]} \tag{4.12b}$$

$$(L)_{\text{mix}} = \frac{(L)_{\text{hail}} + (L)_{\text{rain}}\,[(Z_h)_{\text{rain}}/(Z_e)_{\text{hail}}]}{1 + [(Z_h)_{\text{rain}}/(Z_e)_{\text{hail}}]} \tag{4.12c}$$

$$|\rho_{co}|_{\text{mix}} = \frac{|\rho_{co}|_{\text{hail}} + |\rho_{co}|_{\text{rain}}\,[(Z_h)_{\text{rain}}/(Z_e)_{\text{hail}}]\,(z_{dr})_{\text{rain}}^{-0.5}}{1 + [(Z_h)_{\text{rain}}/(Z_e)_{\text{hail}}]\,(z_{dr})_{\text{mix}}^{-0.5}}. \tag{4.12d}$$

Note that the equivalent reflectivity factor $(Z_e)_{\text{hail}}$ is used for hail and this is the output from the T-matrix based simulation for hail.

4.5.2 PSD parameters and canting angle distributions

The PSD parameters and canting angle distributions for hail differ from rain [Cheng and English (1983); Bringi and Chandrasekar (2001)]. For rain, the size limits for the integration of the PSD are typically 0.1 to $\max(3D_0, 8)$ mm. A narrower set of limits

are used for simulations here by applying $D_0 \pm 0.02D_0$ and $5 \leq D_0 \leq 40$ mm to cover a broad range of hail sizes. Depending on the storm, hail shapes and canting parameters can vary widely. In order to produce a negative Z_{dr}, two configurations are designed: prolate spheroids with an axis ratio of 0.97 and oblate spheroids with a mean canting angle of 90° from vertical and an axis ratio of 1.07. A slight positive Z_{dr} is achieved using oblate spheroids with an axis ratio of 1.06, but with a canting distribution around the vertical axis. Rather than use a standard Gaussian PDF to describe the canting angle distribution, Fisher and axial distributions are applied. Limiting the Fisher distribution to be symmetric about the vertical axis, the mean angle from vertical is $\bar{\theta} = 0$. Assuming the second rotational angle, $\bar{\phi}$ is zero, the general Fisher PDF can be expressed as [Bringi and Chandrasekar (2001)]

$$g(\theta, \phi) = \frac{\kappa e^{\kappa \cos\theta}}{4\pi \sinh(\kappa)} \sin\theta. \tag{4.13}$$

Given the mean $\bar{\theta}$ of 90° used for the side canted oblate spheroids and a uniform distribution around the vertical axis, the axial distribution is described by

$$g_A(\theta) = \frac{1}{2\pi d(\kappa)} \exp\left(-\kappa \cos^2\theta\right) \sin\theta \tag{4.14}$$

where

$$d(\kappa) = 2\int_0^1 e^{-\kappa t^2} dt. \tag{4.15}$$

The width of both distributions is determined by κ, and a value of 2 was selected for all cases, providing a fairly large variability. PSD distributions for hail are described as exponential or as gamma distributions [Cheng et al. (1985); Balakrishnan and Zrnic (1990)], so the shape parameter is limited to $0 \leq \mu \leq 1$. The slope intercept parameter N_w is also smaller than that of rain, and here, we use $-2 \leq \log_{10} N_w \leq 3$. Combining all of these variables provides a simulation that covers a variety of hail conditions.

4.5.3 Simulation results: the effect of D_0 and density

Using the PSD parameters described in Section 4.5.2, T-matrix based scattering simulations were run for hail for 0° elevation S-band and 35° incident angle X-band and Ku-band

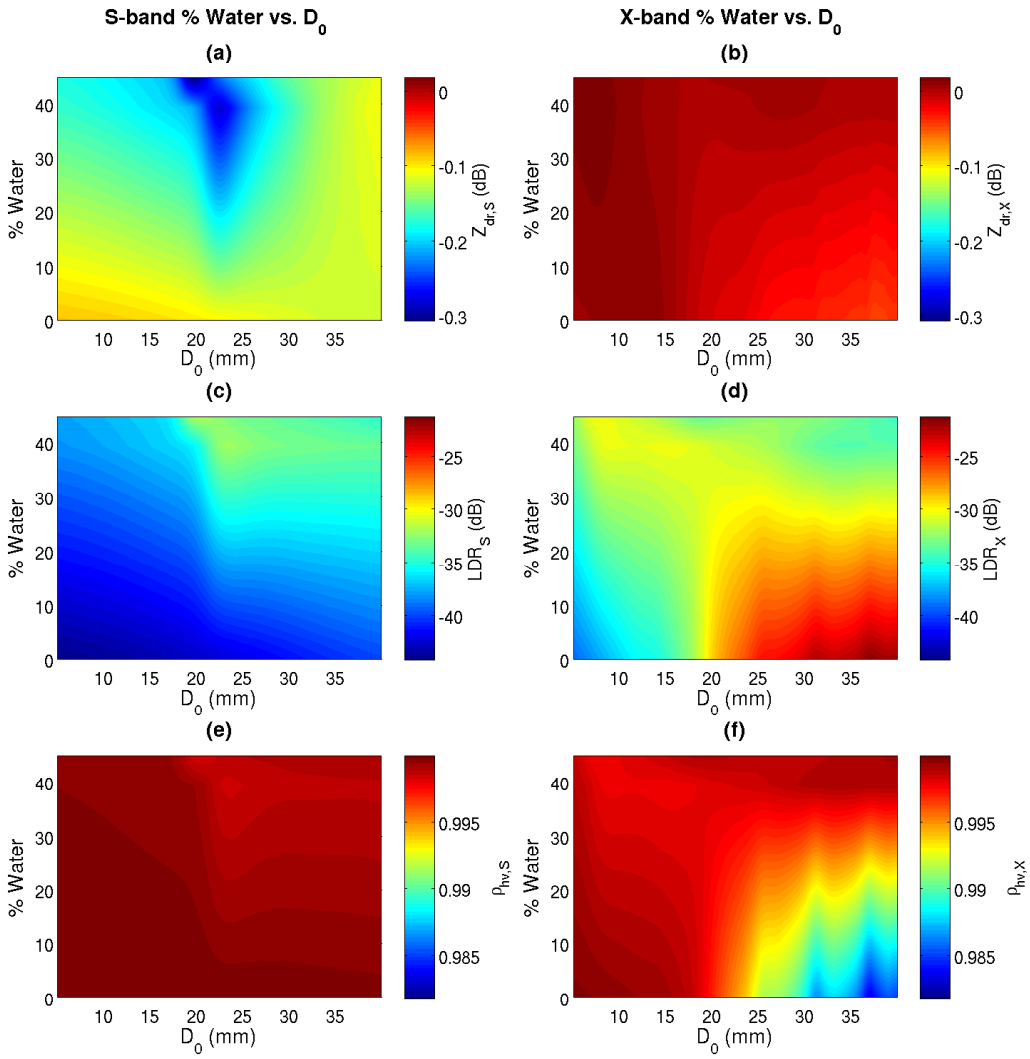

Figure 4.16: Behavior of 3 observables with water fraction (density) and median hail stone size at S-band (left panels) and 55° X-band (right panels) for oblate spheroids canted at 90°.

radars. Additional parameters consist of a constant temperature of -10 ℃ with ten water fraction levels increasing linearly from 0 to 0.45 corresponding to densities ranging from 0.917 to 0.954 g cm^3 according to (4.4) and based on some in situ observations by El-Magd et al. (2000).

Due to the oscillatory behavior in the Mie scattering regime, the polarimetric observations for radars at the same frequency can vary significantly. Three parameters, Z_{dr}, LDR and ρ_{hv} vary relatively smoothly with D_0 and water fraction. Fig. 4.16 displays these functions for the oblate spheroids canted at 90° where the left panels are S-band and the

right panels are X-band (35° incidence angle) and the scales for each variable are set to be identical for comparison. The top row (Figs. 4.16a and b) are for $Z_{dr}\,(dB)$, Figs. 4.16c and d in the middle depict $LDR\,(dB)$ while the bottom row (Figs. 4.16e and f) shows the unitless ρ_{hv}. Due to the use of (4.6), no discontinuity occurs as the water fraction increases. A similar depiction is shown for the oblate spheroids canted about the vertical axis in Fig. 4.17. The most notable difference is the increased range of values of Z_{dr} for the horizontal oblate spheroids that begins positive and turns negative around $D_0 = 15$ mm. The prolate spheroid result is similar except that Z_{dr} starts negative and turns positive. When the frequency is increased to the Ku band, the transition point occurs at a smaller D_0.

As Figs. 4.16 and 4.17 show, LDR is always below about -23 dB and ρ_{hv} is above 0.99 for almost all parameter sets. Both of these are not that realistic because the simulation program does not reproduce particle vibration and oscillation as mentioned previously. In addition, LDR is typically a very noisy parameter and as analysis with real data shows, these values are often much closer to 0 dB. Therefore, these two parameters will be excluded from the generation of spaceborne observations.

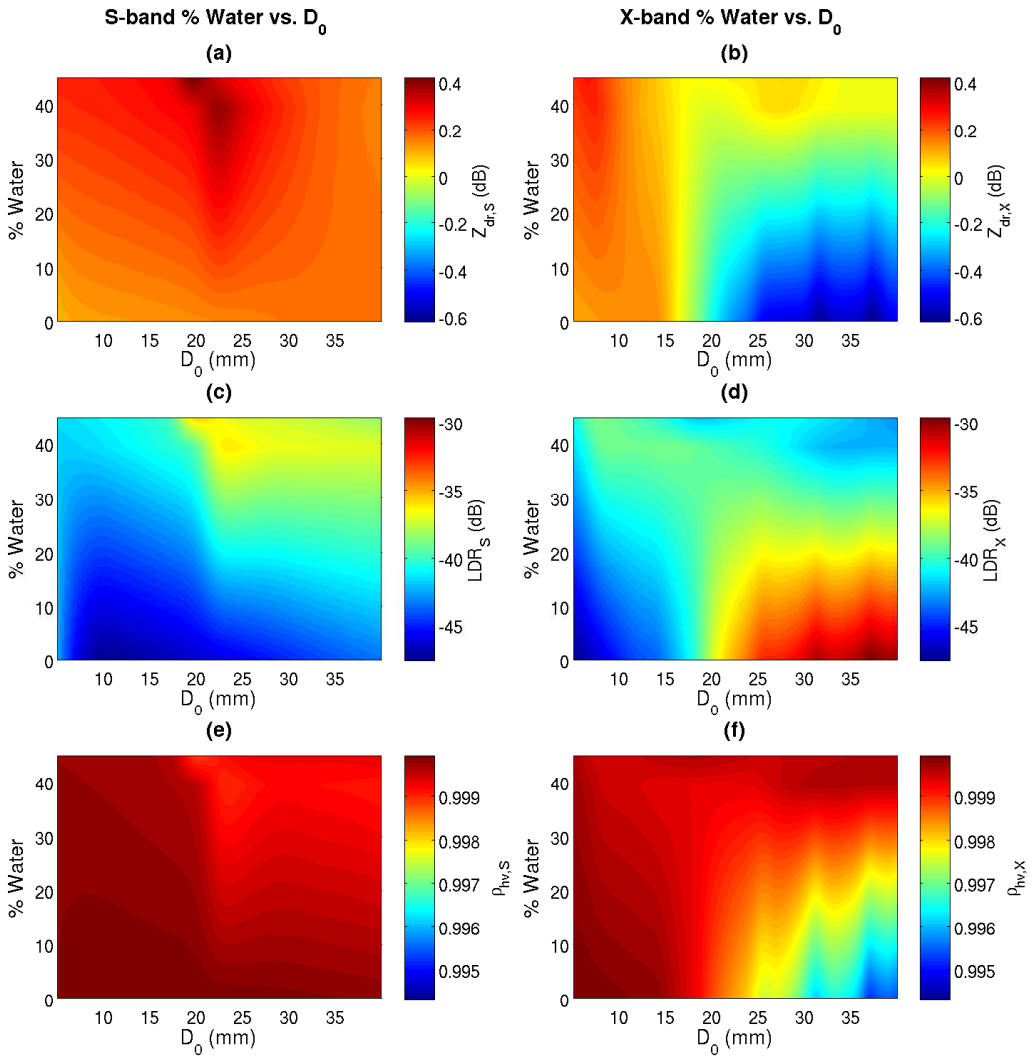

Figure 4.17: Behavior of 3 observables with water fraction (density) and median hail stone size at S-band (left panels) and 55° X-band (right panels) for oblate spheroids oriented about the vertical axis.

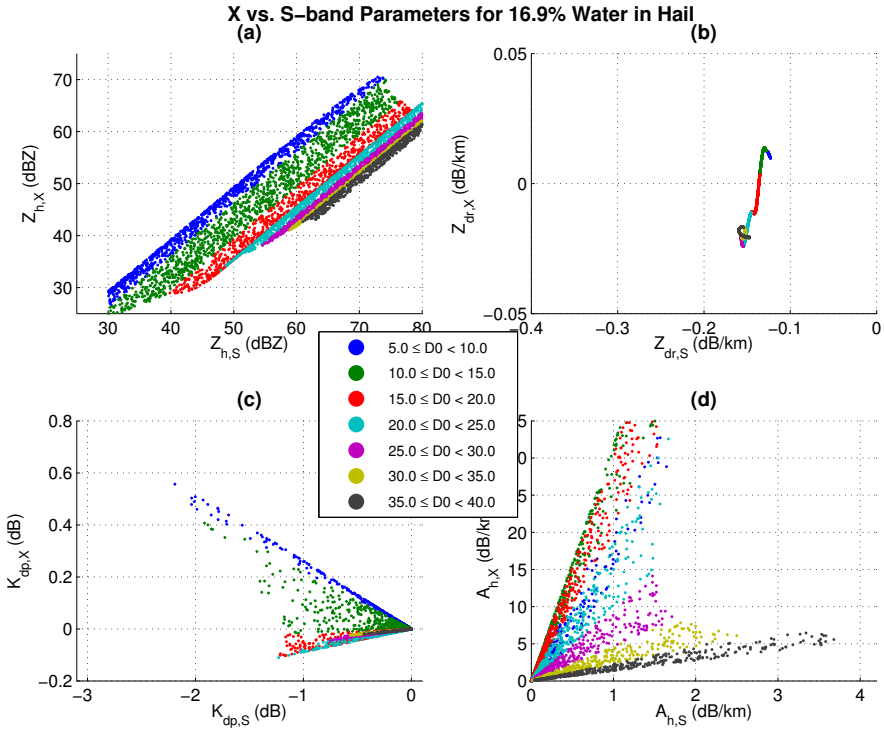

Figure 4.18: Scattergrams showing the relationship of 55° X-band parameters vs. S-band at a 17% water fraction and 90° canted oblate spheroids. (a) Z_h, (b) Z_{dr} (c) K_{dp} and (d) A_h

A more detailed look at the relationship of polarimetric observables between S and X band frequencies is given in Fig. 4.18 for a water fraction of about 17% and Fig. 4.19 at a 39% water fraction for the side canted oblate spheroids. The scattergrams are color coded by range of D_0 in 5 mm increments. Given random input values of the PSD parameters, it is possible to obtain unrealistic combinations, so to eliminate the *extreme* cases the simulation results were removed under the following liberal conditions for the plots: $Z_h < 35$ dBZ, $Z_h > 80$ dBZ and $A_{h,X} > 35$ dB. More stringent maximum values of 75 dBZ, 15 dB km^{-}1 for $A_{h,X}$ and 22 dB km^{-}1 for $A_{h,Ku}$ are used for model creation. By changing the particle canting orientation to be distributed about the vertical axis, Z_{dr} and K_{dp} change significantly while reflectivity and attenuation are virtually the same. These differences are depicted in Fig. 4.20 and Fig. 4.21 for the same two water fractions respectively.

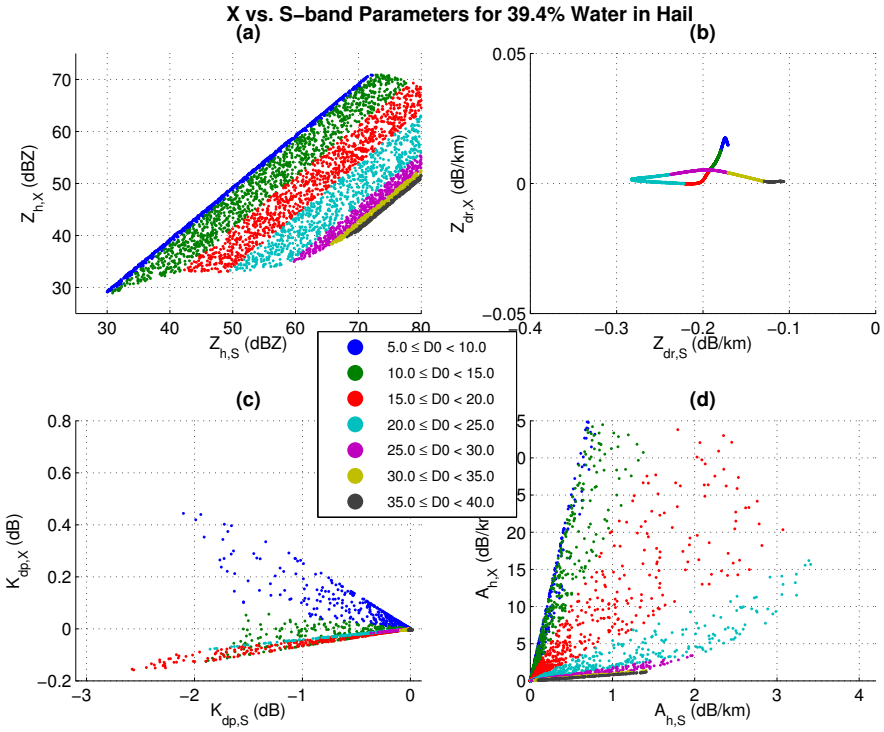

Figure 4.19: Similar to Fig. 4.18 except at a water fraction of 39%.

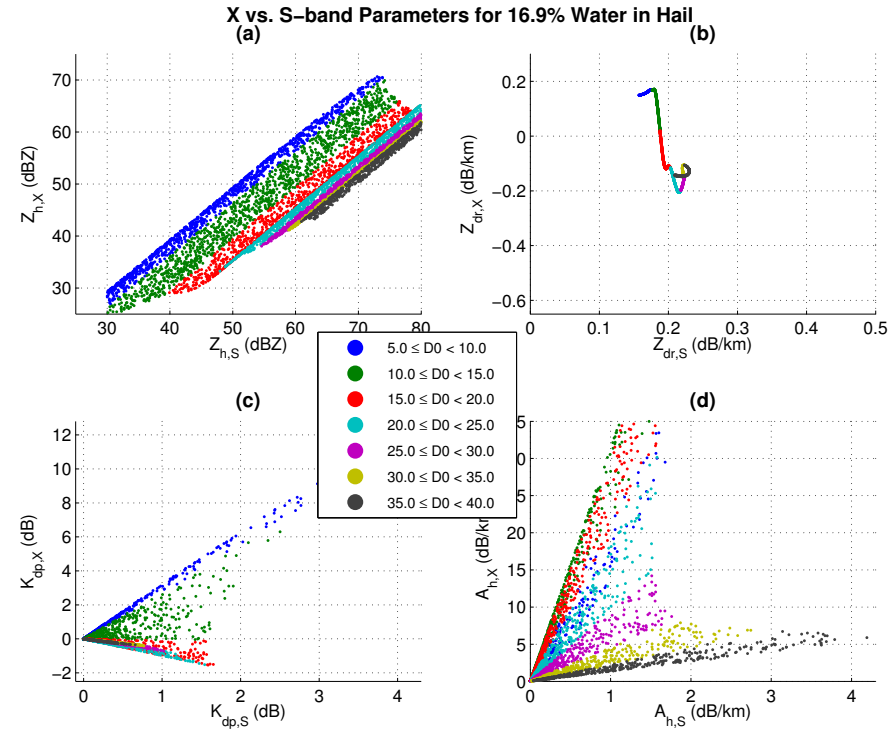

Figure 4.20: Scattergrams showing the relationship of 55° X-band parameters vs. S-band at a 17% water fraction and oblate spheroids canted about the vertical axis. (a) Z_h, (b) Z_{dr} (c) K_{dp} and (d) A_h

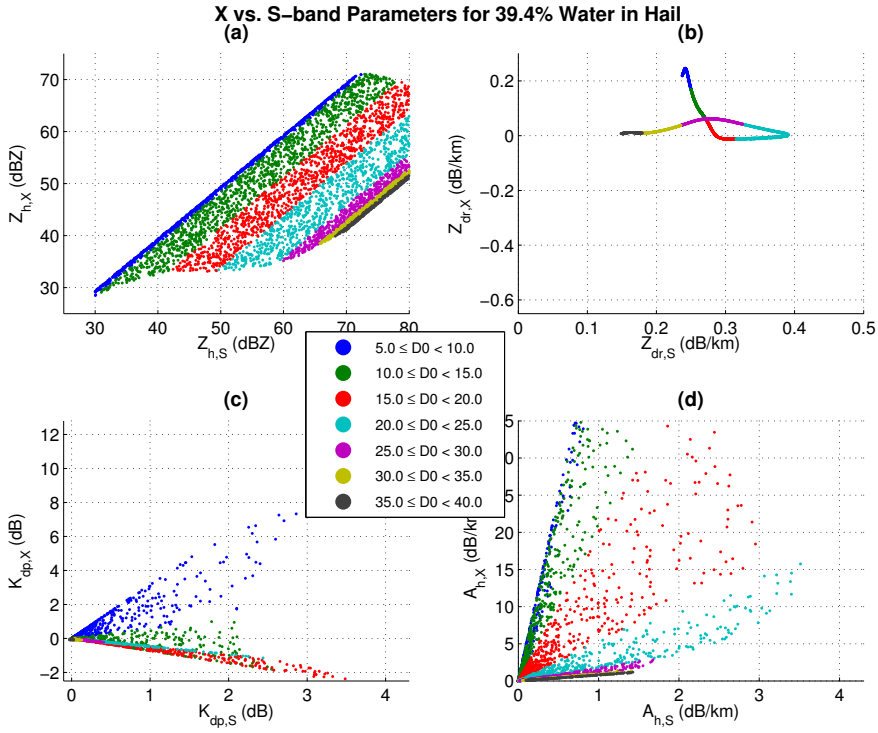

Figure 4.21: Similar to Fig. 4.20 except at a water fraction of 39%.

One prominent feature, that may be counterintuitive, is the *decrease* of higher frequency reflectivity and attenuation as the particle size increases, again related to Mie scattering. It is clear from these four figures that there is a strong dependence upon D_0 and density, but it is also clear that the non-linear relationship between wavelengths is quite complex. However, when the simulation results are viewed in three dimensions, a parametric relationship is revealed. Figure 4.22 depicts $Z_{dr,X}$ versus $Z_{h,S}$ and $Z_{dr,S}$ at a 34% water fraction and clearly shows the points lying on a 3D surface for both orientations of oblate spheroids. Thus, an ideal model to simulate one frequency from another would essentially fit a nonlinear hypersurface to the data.

4.6 Rain Hail Mixture

When the distributed scattering medium consists of hail only, the complex relationship between radar observables at different frequencies creates a modeling challenge. Even rain poses a problem, especially as the frequency increases above X-band where Mie scattering effects are even more prevalent. As hail falls below the freezing altitude and melting hail-

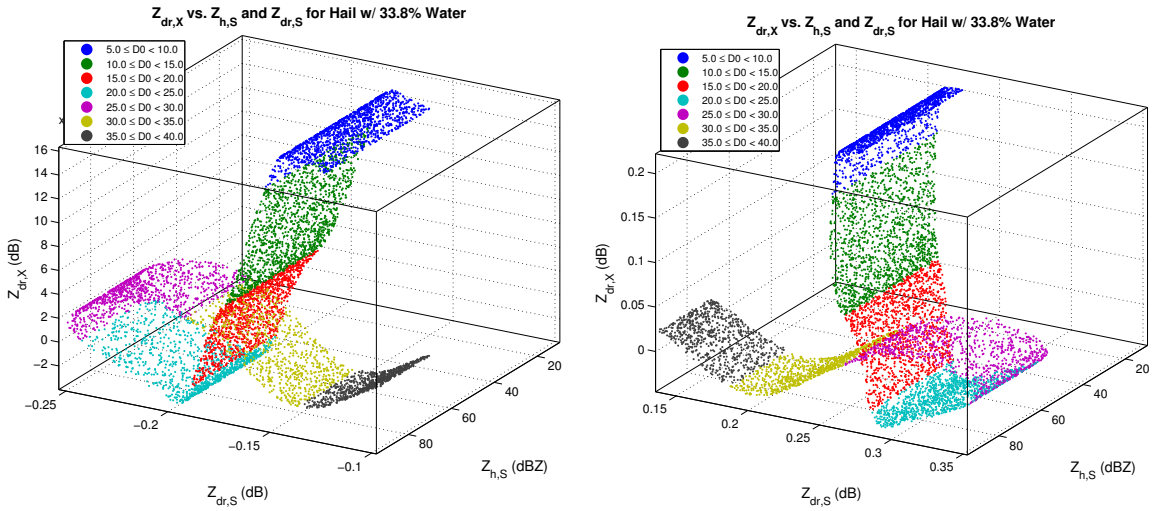

Figure 4.22: At 34% water, $Z_{dr,X}$ versus $Z_{h,S}$ and $Z_{dr,S}$ forms a complex 3D surface. (a) 90° canted oblate spheroid and (b) 0° canted oblate spheroid

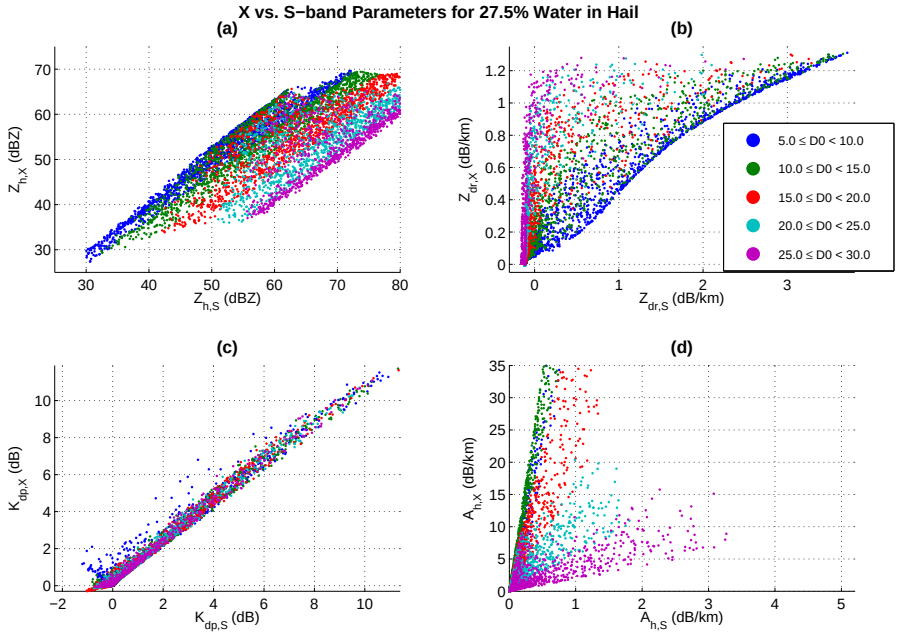

Figure 4.23: Scattergrams showing the relationship of 55° elevation X-band parameters vs. horizontal S-band for a mixture of rain and hail at a 28% water fraction for the hail using oblate spheroids canted about the horizontal axis.

stones morph into pure raindrops, the mixture of rain and hail provides a further challenge to extract meteorological variables from radar. Using the PSD parameters discussed previously for rain and hail (up to 30 mm hail D_0 and excluding water fractions below 10%),

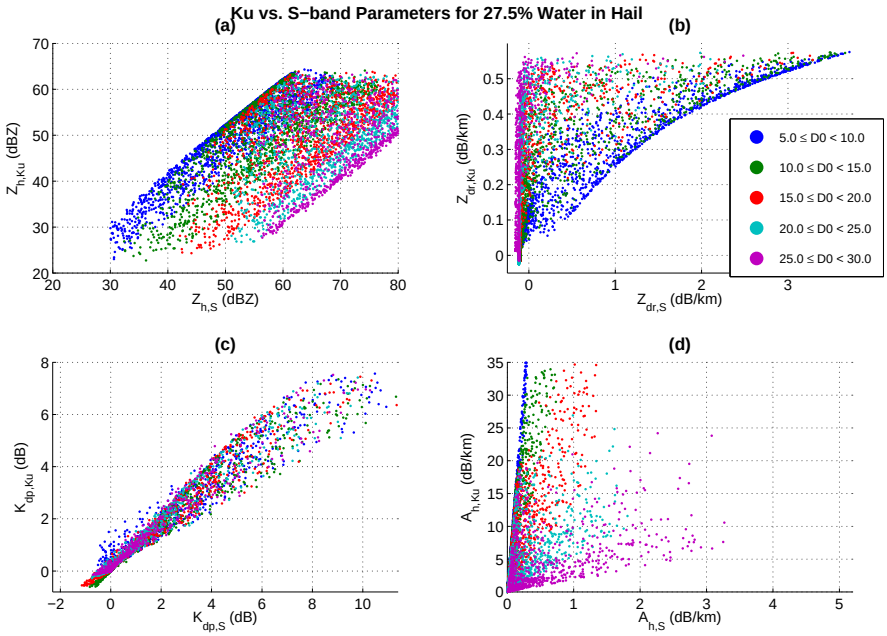

Figure 4.24: Scattergrams showing the relationship of 65° elevation Ku-band parameters vs. horizontal S-band for a mixture of rain and hail at a 28% water fraction for the hail using oblate spheroids canted about the horizontal axis.

simulations of the mixture generate results such as those seen in Figs. 4.23 and 4.24. There is still a multi-dimensional relationship among the observables, but the addition of rain increases the challenge to model higher frequency radar observations from real ground-based systems. In Fig. 4.24a, the reflectivity drops even further versus the ground measurement as compared to Fig. 4.23a. The structure of K_{dp} seen in Fig. 4.24c is also diminished. Horizontal attenuation in panel (d) appears to be similar, but this is primarily due to the fact that data with unrealistically high attenuation were removed from both results at the same threshold of 35 $dB\,km^{-1}$. Characterizing the multivariate nonlinear relationship is not, however, insurmountable and the next section presents a method to achieve the goal of modeling rain, hail and the mixture of the two for simulating spaceborne convective storm observations using real ground-based polarimetric radar measurements.

4.7 A Nonlinear Regression Model for Rain and Hail

Previous efforts to generate a model for simulating higher frequency radar observations from lower frequency ground data typically relied on fitting linear and nonlinear functions to scattering simulation results as discussed in previous sections [Chandrasekar et al. (2006);

Chandrasekar and Khajonrat (2009)]. The models can work very well as long as the variance of data due to Mie scattering effects is relatively small or highly correlated to another variable such as Z_{dr}. Curve fitting techniques also require a priori specification of the underlying function, which could be multivariate in nature. A new model is presented here based on a nonlinear regression technique of the scattering simulations implemented as an adaptive radial basis function neural network (A-RBFN) or generically written as an adaptive neural network (ANN).

Neural networks have been used in many nonlinear and pattern recognition applications including those related to weather radar such as rainfall rate [Bringi and Chandrasekar (2001); Xiao and Chandrasekar (1997)] PSD estimation [Vulpiani et al. (2006)] and attenuation correction [Vulpiani et al. (2005)]. An adaptive A-RBFN was also successfully applied to the rainfall rate estimation problem [Liu et al. (2001)], although it is more commonly used for real-time control systems, nonlinear dynamic system identification, and of course, pattern recognition [Campa et al. (2002); Li et al. (2000); Haykin (1999)]. The availability of unlimited simulated training sets and the inherent nonlinear relationship between polarimetric observables affected by Mie scattering (e.g., see Fig. 4.22) lends itself to an ANN solution if the simulation data are similar to the real data. If the real input data differs significantly from the training data, or if the ANN has been over fit, the output can oscillate wildly. Fortunately, the choice of the A-RBFN over other types of neural networks, such as the multilayer perceptron, reduces or eliminates this instability and overfitting problem.

A minimum resource allocation network RBFN is used to achieve the goal of simulating realistic high frequency spaceborne observations from real ground based C or S-band data. With that goal in mind, the ANNs are designed and trained such that a reasonable output occurred when real data is applied, as opposed to creating an optimal fit of purely simulated data. Once the network parameters are selected, the A-RBFs are trained using the learning algorithm outlined in Section 2.4. Several constant parameters for all ANNs are: pruning enabled, an overlap value of 0.4, an update radius of 1e10 (i.e., update all neurons), stabalizing factors set to 0, all limiters at 1e9 and a learning rate of 5×10^{-4} for all three basis function values. In addition, the windowed mean threshold is a constant 0.02 with

the linear filter pole at 0.5 which effectively averages the current and previous error value. For rain, the maximum number of neurons is set to 300 while it is set to 400 for the hail plus rain networks and 500 for D_0 due to the challenge of estimating D_0 from only radar observations. However, the input parameters are chosen to create a network with fewer nodes at least within the first several iterations.

Scaling of the data prior to the RBFN input port, as described in Section 2.4 and shown in Fig. 2.13, can have a signficant impact on the result. First, it prevents large values, such as reflectivity, from completely overwhelming the impact of small variables such as K_{dp}. However, setting the input limits larger than the expected range, so that the data are scaled to say $[-0.5, 0.5]$, reduces the impact noisy measurements have on the result. In addition, setting the target limits for horizontal attenuation such that the target is always between 0 and 1 practically eliminates negative attenuation values when real measurements are applied to the ANN. For example, if the simulated X-band attenuation values are in $[0, 10]$, the limits to the network are set to -10 and 10. Setting limits for other variables to accommodate real observations beyond the simulated values also aided in producing results close to the theoretical limits.

Ideally, presentation of one large set of training vectors would be adequate; however, that is not the case with this application. From the full set of simulated data vectors, 40-60,000 are selected for training, leaving about 5,000 for validation. Then, two rounds of training loops are run. The first sets the center distance parameters in (2.52) to $[d_{max}, d_{min}, gamma] = [0.5, 0.2, 0.9999]$ and runs the test vectors twice before checking the mean absolute error (MAE), randomly permutating the test vectors after the first run. The state (set of A-RBFN weights, centers and widths) is saved for the minimum error. At each loop iteration, the state is reset to zeros and continues until a maximum number of iterations is reached or until a specified number of consecutive increases of MAE occurs (10 in this case). For the second training loop, the state is not reset at each iteration, although the order of test vectors is randomized and the loop begins with lower d_{max}, d_{min} and possibly A-RBFN error threshold than the first training loop. The loop continues until either the MAE reaches a threshold MAE_{min}, or the average slope of MAE increases above $-\text{MAE}_{min}/100$. A least

squares fit of the previous P values of MAE (5 or 6) determines the slope, but if the MAE increases more than 5% in a single iteration, that state is discarded and a new iteration is started from the previous state. If the MAE increases more than 5% a second time, the training stops.

While it is possible to develop one network to estimate all desired outputs from radar observations, better performance is achieved by designing a network for each output. In addition, different sets of lower frequency observables produced slightly different results due to the varied relationships between them as seen in the previous sections. Table 4.7 shows the ground radar input variables for each output and hydrometeor type; the networks for rain plus hail were also used for "pure" hail so only two types are needed. In both cases, an additional input variable is used that is correlated to the change in output. For rain, it is temperature which can simply be determined from the distance to the melting layer estimated in the hydrometeor classification step [Lim et al. (2005)] or from actual profiles if available. Note that curve fitting models also need the temperature for minimum error. A lower error is also obtained for rain A_{dp} when linear reflectivity is input, while rain K_{dp} uses the logarithm of the input K_{dp}. In particular, the output is expressed as

$$K_{dp,out} = \exp\{\hat{y}\left([Z_{h,g}, \log|K_{dp,g}|]\right)\} \tag{4.16}$$

where $\hat{y}$ is the ANN output from (2.44) and the g subscript indicates ground radar input. The absolute value is only needed for real data where K_{dp} could be less than 0, but the corresponding outputs are also negated because $K_{dp} < 0$ is expected. The operation in (4.16) was not performed for the hail model, however, because even theoretical observations will be negative and are not necessarily symmetric about 0.

In the hail case, D_0 has a significant impact on radar observations as seen in Figs. 4.18 through 4.22. Hail diameter must be estimated, however, so another ANN is designed for that purpose and fed into the other ANNs. In this case, only direct radar observables, including LDR, and the secondary variable K_{dp} are used to train the ANN. The D_0 estimation networks are the most difficult to train and achieve low error values. Nonetheless, most output from subsequent networks still fell within reasonable values. Modifications necessary to achieve better outputs are discussed in Section 4.8.

Table 4.1: Ground radar input parameters for each spaceborne observation ANN in rain, and rain plus hail (T = temperature in ℃)

Output Parameter	**Ground Observable Inputs**	
	Rain	**Rain + Hail**
Z_h	Z_h, Z_{dr}, K_{dp}, T	Z_h, Z_{dr}, K_{dp}, D_0
Z_{dr}	Z_h, Z_{dr}, T	Z_h, Z_{dr}, D_0
K_{dp}	Z_h, $\log(K_{dp})$	Z_h, Z_{dr}, K_{dp}, D_0
A_h	Z_h, K_{dp}, T	Z_h, K_{dp}, D_0
A_{dp}	$10^{0.1Z_h}$, K_{dp}, T	Z_h, Z_{dr}, K_{dp}, D_0
D_0[a]	N/A	Z_h, Z_{dr}, K_{dp}, LDR

[a] estimated D_0 of hail for input to ANNs in hail regions

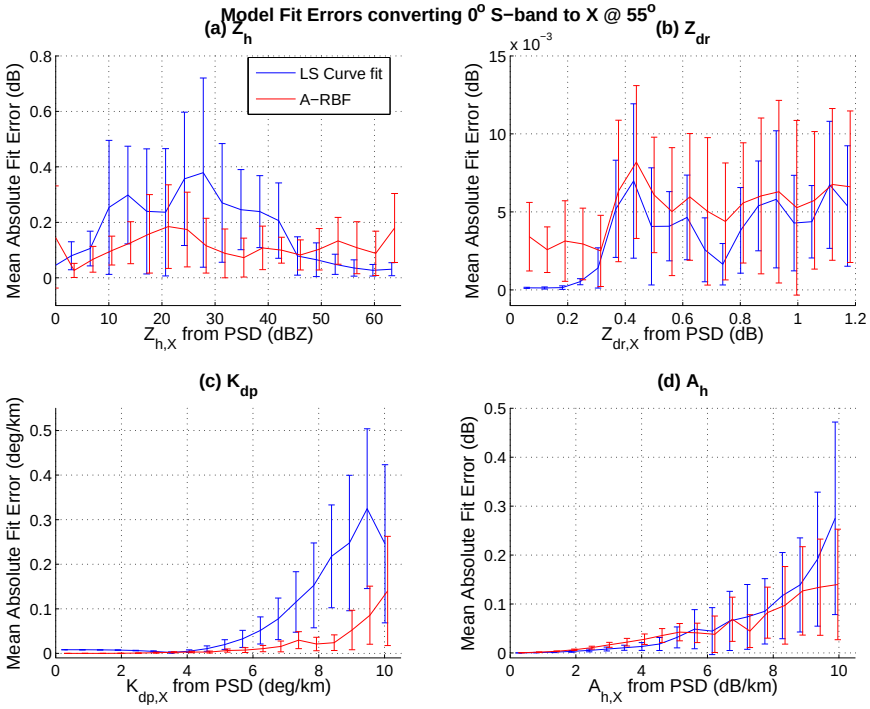

Figure 4.25: Mean absolute errors for existing curve fitting techniques (blue) and the adaptive RBFN (A-RBFN) model (red) for converting S-band to 55° X-band at 26 ℃ for (a) Z_h, (b) Z_{dr}, (c) K_{dp} and (d) A_h. The lines in the figure represent the mean over the interval between error bars, and the error bars indicate two standard deviations total.

4.7.1 Comparison of Model Fit Errors For Rain

Simulated data based on the PSD provides an opportunity to directly compare models because the desired output is known precisely. Figs. 4.25, 4.26 and 4.27 display the results of such a comparison between existing curve fit models described in Section 4.4 and the

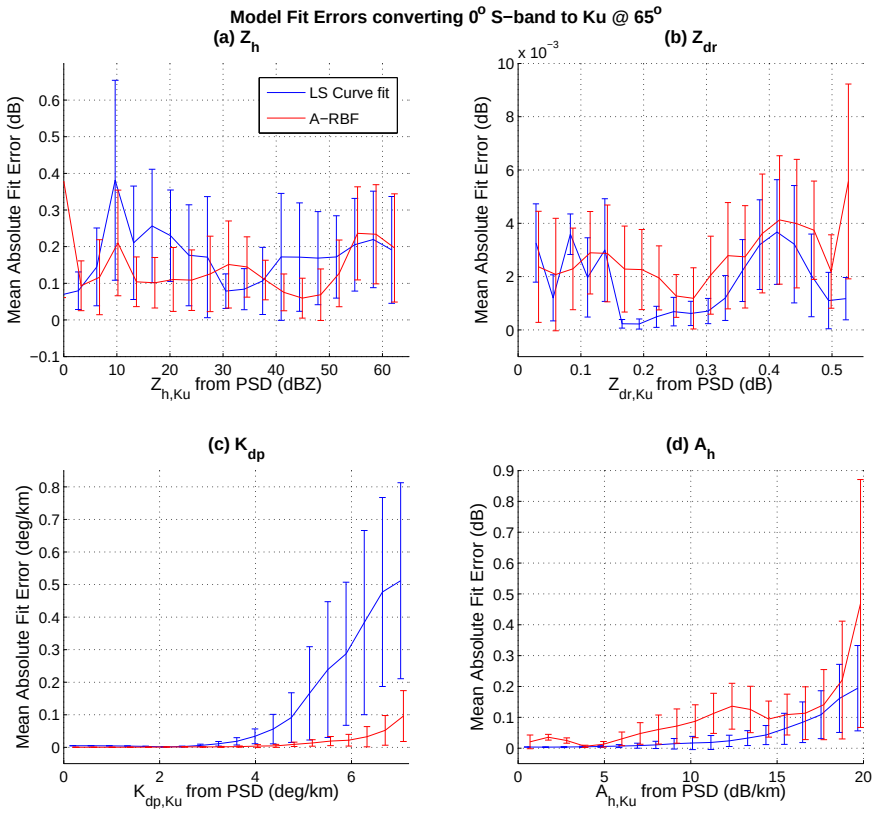

Figure 4.26: Mean absolute errors for existing curve fitting techniques (blue) and the ANN model (red) for converting S-band to 65° Ku-band at 29 °C for (a) Z_h, (b) Z_{dr}, (c) K_{dp} and (d) A_h. For attenuation, the Z_h, K_{dp} model performs well.

neural network model for the S-to-X, S-to-Ku and C-to-X conversions respectively. The lines in the figure represent the mean over the interval between error bars, and the error bars indicate two standard deviations total. With the exception of K_{dp}, there is virtually no difference between the models. From this, a potentially false conclusion could be drawn that the models will produce equivalent results. The ANN model used, however, was trained to provide the most reasonable results when applied to real data. Therefore, the errors depicted in these figures for the ANN model are higher than they would be if the ANN was trained to find the optimal fit to simulation only data. Nonetheless, the performance is either very close or better than the LS curve fits. An argument could be made that the additional complexity of the RBFN does not warrant its use in most cases; however, the ANNs characterize the complex relationship among multiple parameters and can be used to identify noisy or possibly mis-classified hydrometeors.

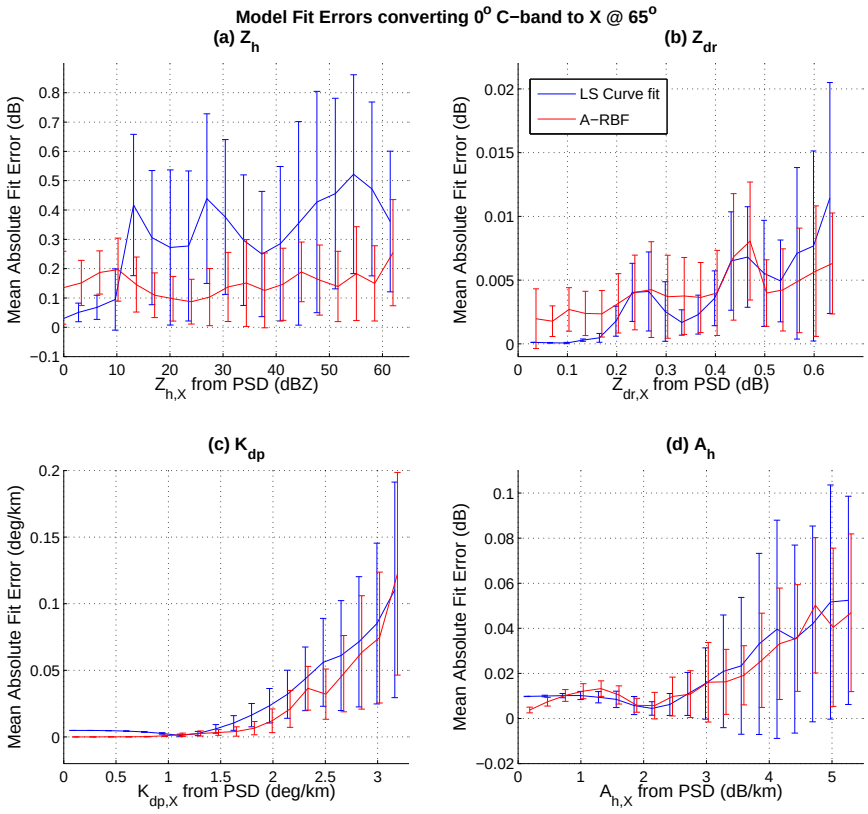

Figure 4.27: Mean absolute errors for existing curve fitting techniques (blue) and the ANN model (red) for converting C-band to 65° X-band at 29 ℃ for (a) Z_h, (b) Z_{dr}, (c) K_{dp} and (d) A_h.

The best way to convey the different performance between the two models on real data is to demonstrate it. Fig. 4.28 compares the two approaches for converting horizontal S-band data from CSU-CHILL during the STEPS experiment to Ku-band at a 25° incidence angle (see Section 4.8 for a more detailed description of the real data). The left panels show the 2D histogram of the curve fit model output while the right displays the A-RBFN model, both of which use a constant temperature of 23 ℃. Reflectivity in Fig. 4.28a using (4.7) exhibits a larger variance in the 25 to 40 dBZ region, but the ANN output clearly has reduced Z_h when the input Z_h is above 50 dBZ. This is actually due to low and even negative K_{dp} associated with this high reflectivity when the scattering simulations suggest it should be high. Theoretically, K_{dp} and Z_h are related via a power law similar to attenuation and reflectivity. For differential reflectivity in Fig. 4.28b and specific differential phase in Fig. 4.28c, we see that a univariate curve fit looks very clean (low variance) by definition.

However, this may not be an accurate representation because it does not consider other variables and their interrelation. For example, the $Z_{dr,Ku}$ values above the main curve (corresponding to $Z_{dr,S} < 0.6$) are from points with a higher $Z_{h,S}$ relative to the theoretical data. This larger $Z_{h,S}$ then increases the ANN output for $Z_{dr,Ku}$. Whether or not the influence is too strong is not easily determined without meticulous experiments. Finally, Fig. 4.28d shows the attenuation results and the only variable without a lower frequency version as input. The effect of the $K_{dp} < 0$, especially in higher Z_h regions, causes the model output to become negative for the curve fit model. The A-RBFN output, however, is able to at least prevent negative attenuation (gain), but it is clear that neither completely follow the power law relation with respect to Z_h.

Similar to Fig. 4.28, Fig. 4.29 shows the results applied to C-band data from the Bric della Croce radar operating in northern Italy after conversion to 25° incidence angle X-band. (More details about the storm and the radar are given in Section 6.3.) Between real values of 40 and 50 dBZ in Fig. 4.29a, many curve fit model outputs fall well below the theoretical expectation, probably due to Z_{dr} that was not completely attenuation corrected, ground clutter/side-lobe contamination or oscillations. This problem does not occur from the ANN model, but it does still produce lower Z_h when the input is above 50 dBZ. Z_{dr} and K_{dp} in Fig. 4.29b and 4.29c are similar in behavior to the S-to-Ku band results shown in Fig. 4.28. The attenuation response in Fig. 4.29d, however, shows that the ANN version is much better behaved than the curve fit output despite what Fig. 4.27d indicates. The negative K_{dp} is again the cause of negative attenuation, but this occurs for almost all Z_h values. Low values of K_{dp} at $Z_h > 45$ dBZ also reduce the attenuation output for the ANN model, suggesting that perhaps the 340 m range spacing of this radar might not be small enough to effectively capture higher K_{dp} gradients. Overall, the curve models might be realistic, but the ANN does a better job of representing the actual measurements even if they contain noise. The potential exists, then, to apply the ANN for data filtering improvements.

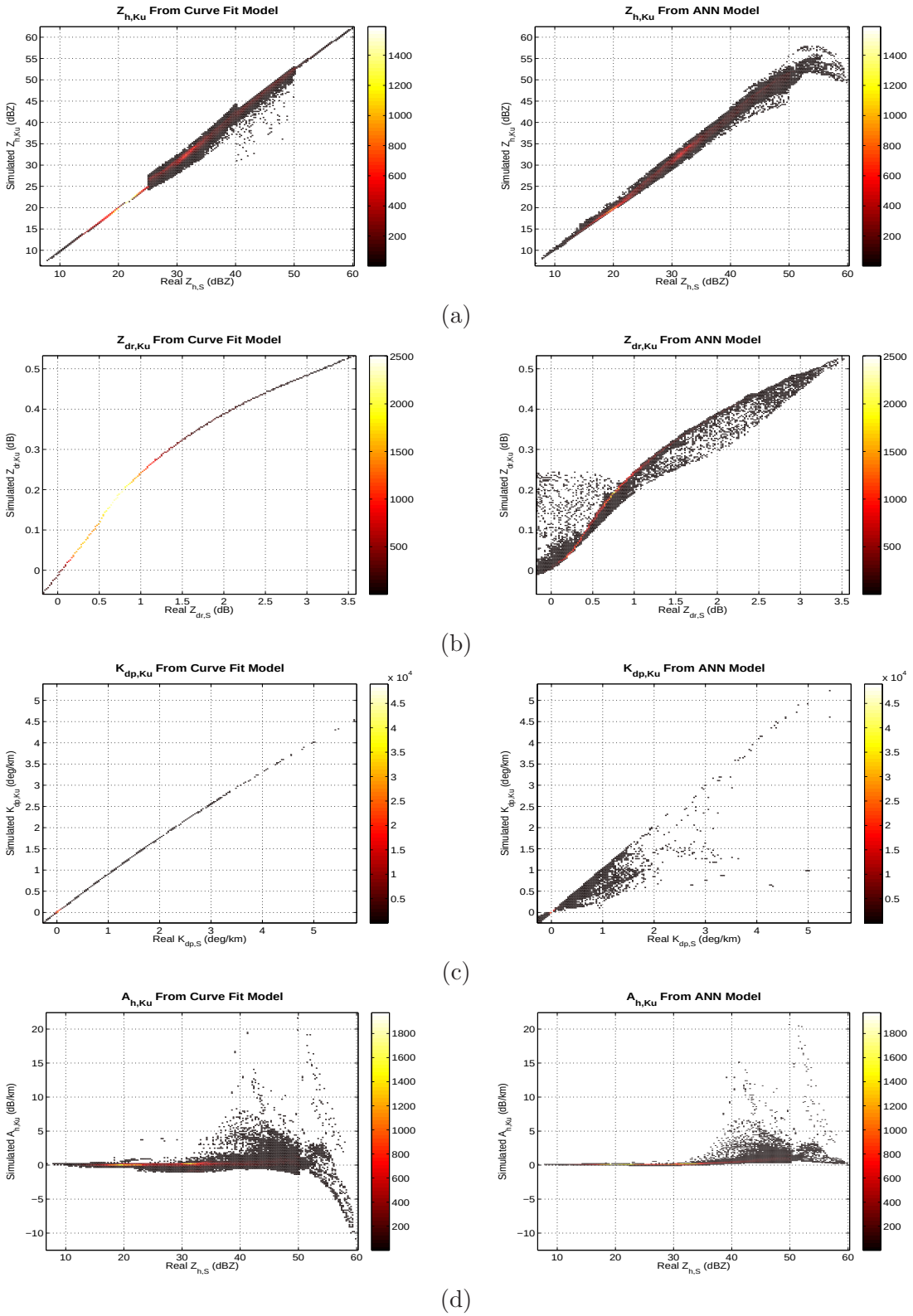

Figure 4.28: Curve fit model (left panels) and ANN models (right panels) from CSU-CHILL data to simulated Ku-band observations at 25° incidence angle for (a) Z_h, (b), Z_{dr} (c) K_{dp} and (d) A_h. Univariate models are "clean", but may not represent the actual data well.

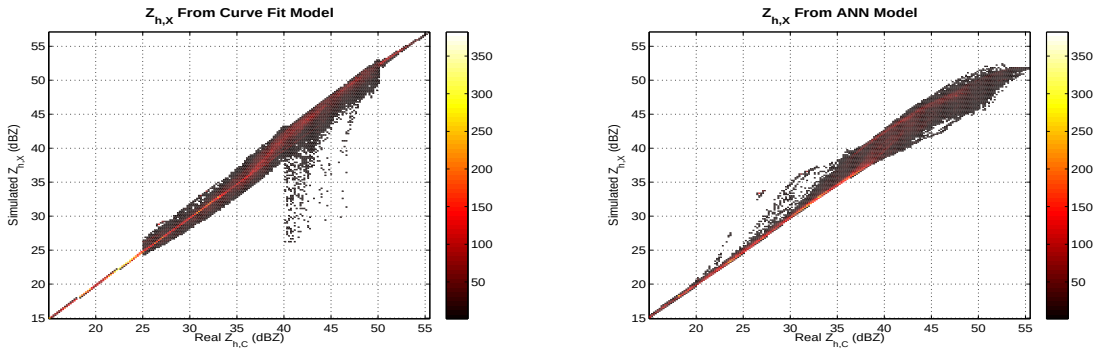

(a)

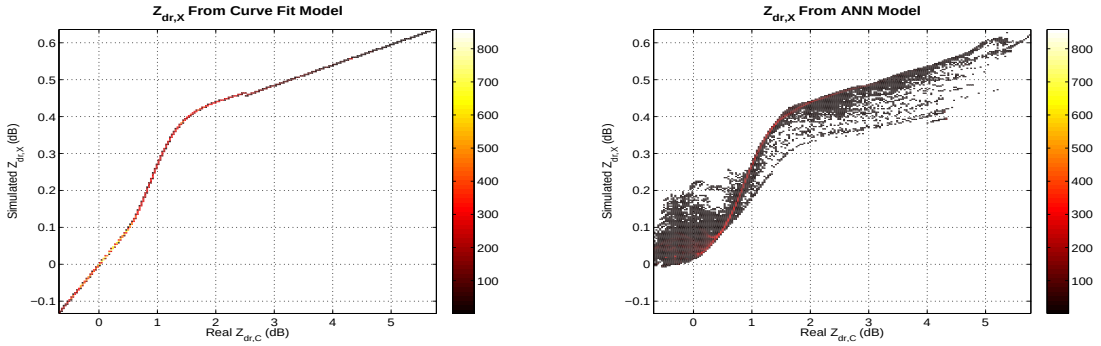

(b)

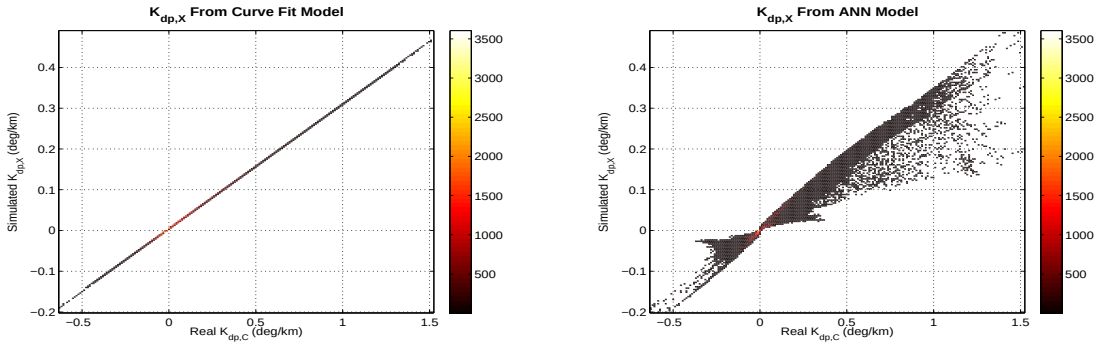

(c)

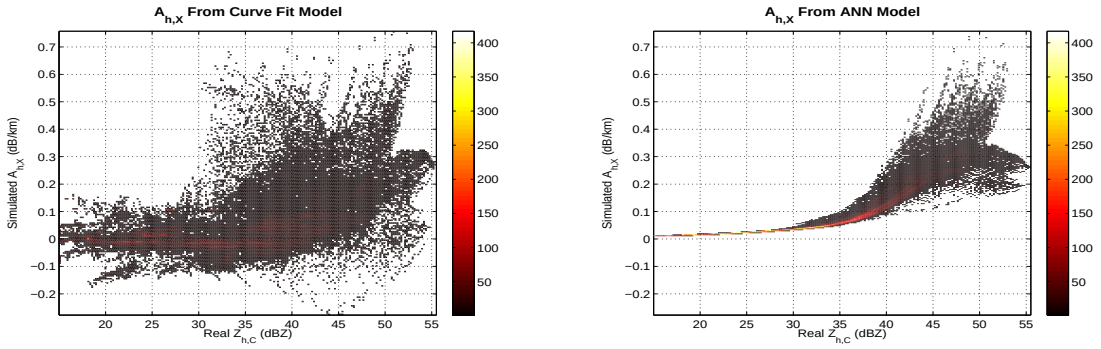

(d)

Figure 4.29: Curve fit model (left panels) and ANN models (right panels) from Bric della Croce C-band data to simulated X-band observations at 25° incidence angle for (a) Z_h, (b), Z_{dr} (c) K_{dp} and (d) A_h. Here, the curve fit A_h has a much larger variance and many negative values.

4.8 Results From Real Storm Measurements

The real test of model performance is the result of applying real ground based storm measurements. By comparing the output to the theoretical values, we can assess whether or not the model achieves the goal of simulating a realistic response from a spaceborne, higher frequency platform. A good model will also be robust in the sense that input values that are outside the vector space of training data still produce reasonable results. Real data are noisy, and estimated values such as K_{dp} depend highly on the quality of the direct measurements. The RBFN model provides such robustness, and can also indicate data that have abnormal components, either from noisy measurements or perhaps from the presence of other hydrometeor types or contamination. The following sections document the performance of the ANN model using two storms observed by the CSU-CHILL dual polarization S-band Doppler weather radar. One is from the STEPS experiment [Lang et al. (2004)] in eastern Colorado during a hailstorm on 29 June, 2000 (denoted as 000629) which was considered a classic supercell storm. A convective squall line on 2 August, 2001 (denoted as 010802) was used for an additional validation case. Both cases were converted to 55° X-band observations, and the second storm was also converted to simulate 65° Ku-band. Chapter 5 takes these results to the next stage to simulate data from a SAR platform and the full propagation effects.

Before applying the conversion models, pre-processing is needed to identify the rain and hail regions. First, an algorithm to estimate the forward scattering K_{dp} from the observed backscatter Φ_{dp} is applied [Wang and Chandrasekar (2009)]. A basic gridding method is then used to create an Earth-centric Cartesian grid of data that is subsequently smoothed with a 3D Gaussian kernel. From this grid of polarimetric variables, hydrometeor classification using the procedure described in Lim et al. (2005) generates seven classes of precipitation: drizzle, rain, melting ice, dry snow, dry graupel, hail and rain plus hail, although drizzle and rain are often combined as one.

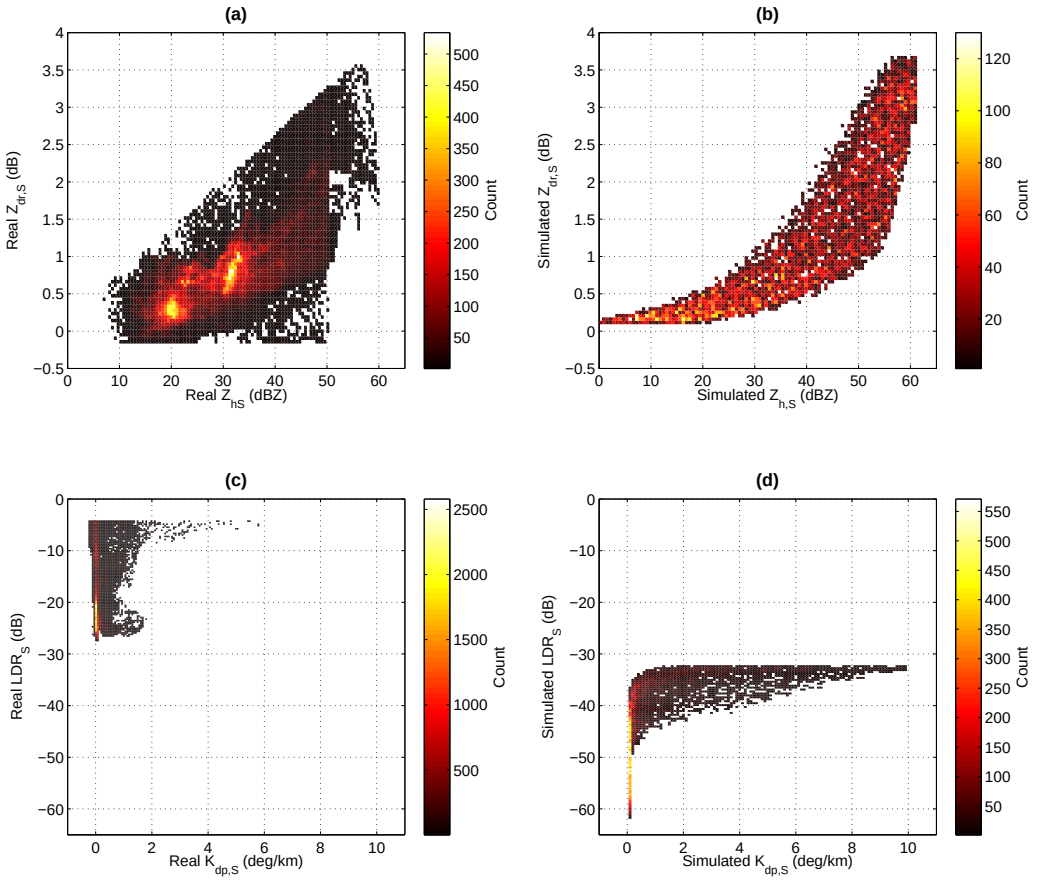

Figure 4.30: 2D histograms of rain from the 000629 data after gridding and filtering (left panels) and simulated S-band data used to train the ANN (right panels). This shows the similarities and differences among four polarimetric observations: (a) real Z_{dr} vs. Z_h, (b) simulatedZ_{dr} vs. Z_h, (c) real LDR vs. K_{dp} and (d) simulated LDR vs. K_{dp}.

4.8.1 Rain

4.8.1.1 STEPS Supercell

Fig. 4.30 shows 2D histograms of the real data after gridding and smoothing (Fig. 4.30a for Z_{dr} and Z_h and 4.30c for LDR and K_{dp}) compared to S-band observations simulated from the PSD parameters described in Sec. 4.6 (Fig. 4.30b and 4.30d). With the exception of LDR, considerable overlap of the histograms exists, although there are certainly regions that do not. Figure 4.30a also shows where an additional filter was applied to remove high Z_{dr} values at lower Z_h along a line that is roughly parallel to the theoretical set as well as $Z_{dr} < -0.2$ resulting in the "clipped-looking" results shown in Fig. 4.30. The disparity between simulation and reality for LDR is a primary factor for not using LDR to calculate

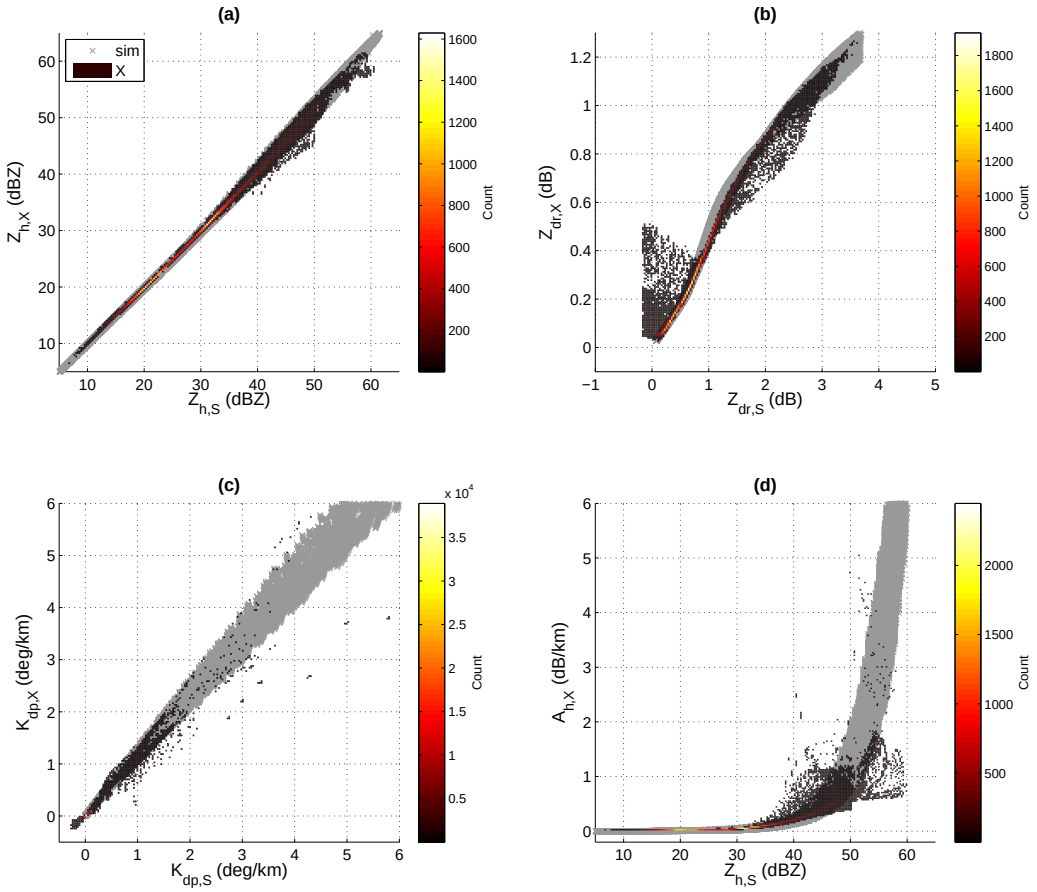

Figure 4.31: Simulated X-band observations of rain vs. real S-band 2D histograms of the 000629 storm overlaid on the pure simulation results (gray x's) (a) Z_h, (b) Z_{dr}, (c) K_{dp} and (d) A_h vs. $Z_{h,S}$. A vast majority of the result match the theoretical expectation.

other variables or to simulate it at the higher frequencies. In addition, many polarimetric ground radars operate in simultaneous or slant 45 mode meaning that they cannot produce a measure of LDR.

After training the ANNs on simulated S-band data, the results of applying the real data are plotted as 2D histograms shown in Figs. 4.31 and 4.32. The gray x's represent the theoretical X-band simulated from PSD directly. While some outliers do exist, a significant majority (over 99% in most cases) of the points lie within the theoretical region or continue the trend. All of the network outputs that are outside the theoretical bounds correspond to inputs that are outside the theoretical S-band values as seen in Fig. 4.30. For example, Fig. 4.31b shows some Z_{dr} output data which are higher than expected at S-band Z_{dr} values below 1. These data correspond to higher values of $Z_{h,S}$ that would theoretically produce

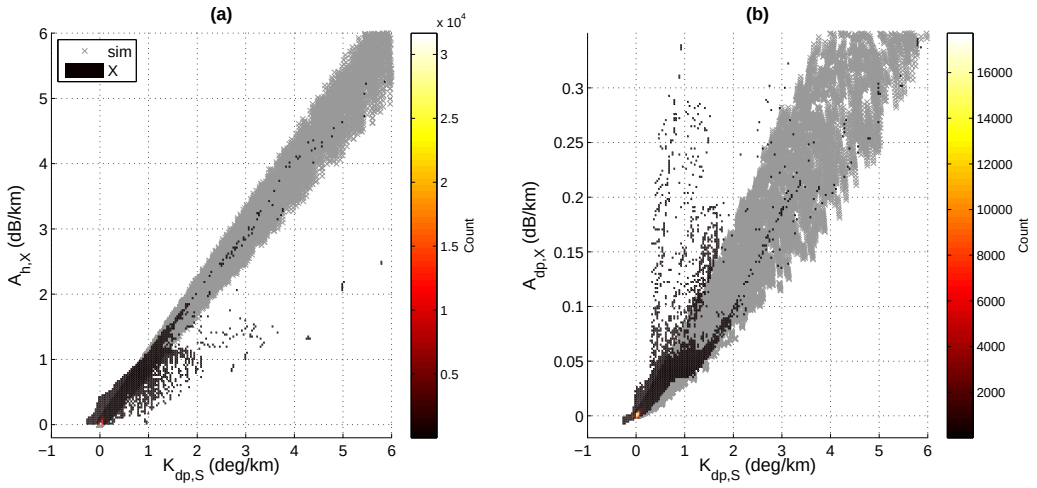

Figure 4.32: 2D histograms for simulated X-band specific attenuation vs. real S-band K_{dp} for rain from the 000629 storm over the pure simulation results (gray x's) (a) A_h and (b) A_{dp}.

higher differential reflectivity. Thus, we get an indication that the particles are either not pure rain or that the measured Z_{dr} is lower than expected. Theoretically, rain will not have $K_{dp} < 0$, but this condition exists in the real data possibly due to the presence of mixed phase hydrometeors near the melting regions or by an undershoot of the K_{dp} estimation algorithm. The ANN output, however, is also negative in these regions which was achieved by negating the output of these cells given that the scheme described in (4.16) will never produce a value less than 0.

For attenuation in Fig. 4.32 and Fig. 4.31d, the ANN result is still mostly within the expected values. Note that the color scale for Fig. 4.32a is multiplied by 10^4, so the percentage of points that seem to produce attenuation that is too low, most of which correspond to the points to the right of the attenuation versus reflectivity in Fig. 4.31d. Also, despite negative K_{dp} data, attenuation values are still positive which was partially achieved by setting the scaling limits of the RBFN such that the simulated target values all fell within 0-1. The differential attenuation shown in Fig. 4.32b also appears noisy, but again the percentage of values above the theoretical bound is very small.

4.8.1.2 2001 Squall Line

Fig. 4.33 shows 2D histograms of the real measurement from 2 August 2001 after gridding and smoothing. Z_{dr} and Z_h are shown in Fig. 4.33a for and Fig. 4.33c depicts LDR

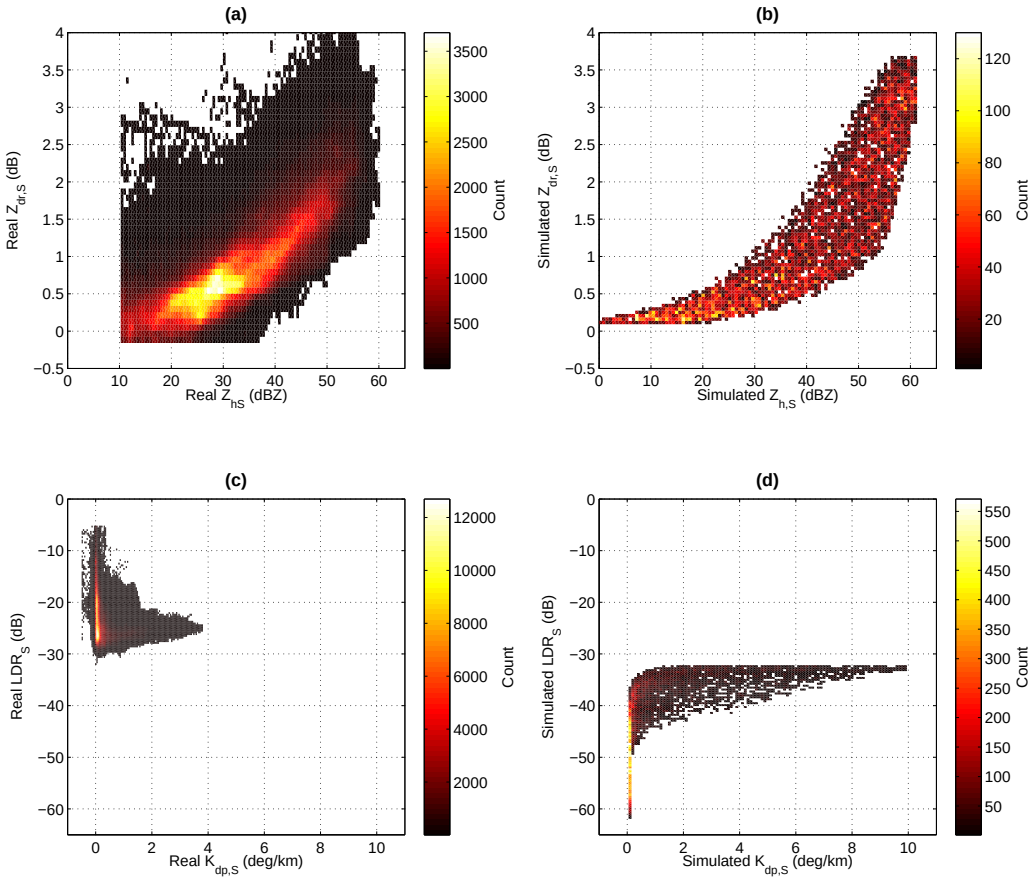

Figure 4.33: 2D histograms of rain from the 010802 data (left panels) and simulated S-band data used to train the ANN (right panels). This shows the similarities and differences among four polarimetric observations: (a) real Z_{dr} vs. Z_h, (b) simulatedZ_{dr} vs. Z_h, (c) real LDR vs. K_{dp} and (d) simulated LDR vs. K_{dp}.

and K_{dp}, with comparisons to S-band observations simulated from the PSD parameters described in Sec. 4.6 in Fig. 4.33b and 4.33d. As Fig. 4.33a shows, data with $Z_h < 10$ dBZ and $Z_{dr} < -0.2$ dB were removed before processing. The very low reflectivity potentially indicates frozen particles classified as rain. Higher Z_{dr} values above this, however, were not filtered as they were in the 000629 case. Again, a similar dispartity of LDR exists between reality and the simulation output, reaffirming the decision not to use it. Similar to Figs. 4.31 and 4.32, the ANN output for rain in the storm are plotted in Figs. 4.34 and 4.35. This storm is not as intense as the 000629 supercell, and the results indicate a better match to the theoretical values. Likewise, Figs. 4.36 and 4.37 demonstrate the capability of the A-RBFN to convert real S-band observations to realistic Ku-band.

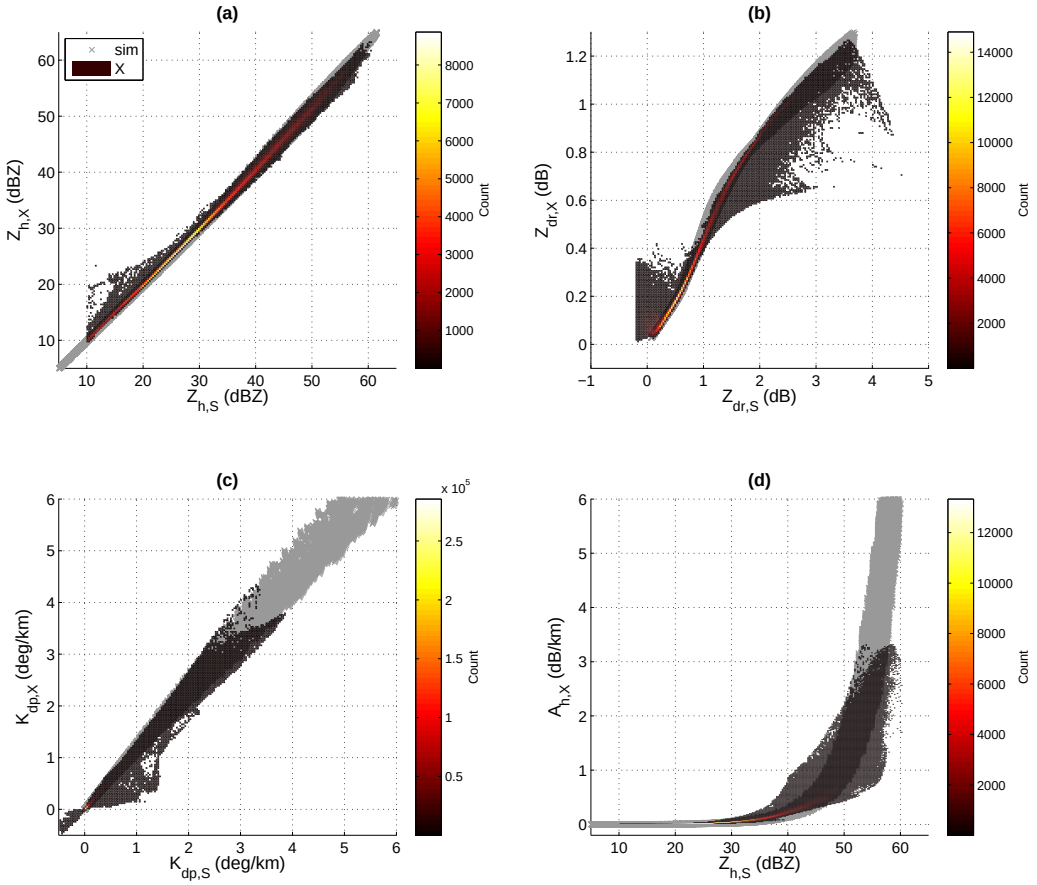

Figure 4.34: Simulated X-band observations of rain vs. real S-band 2D histograms of the 0108020 storm overlaid on the pure simulation results (gray x's) (a) Z_h, (b) Z_{dr}, (c) K_{dp} and (d) A_h vs. $Z_{h,S}$.

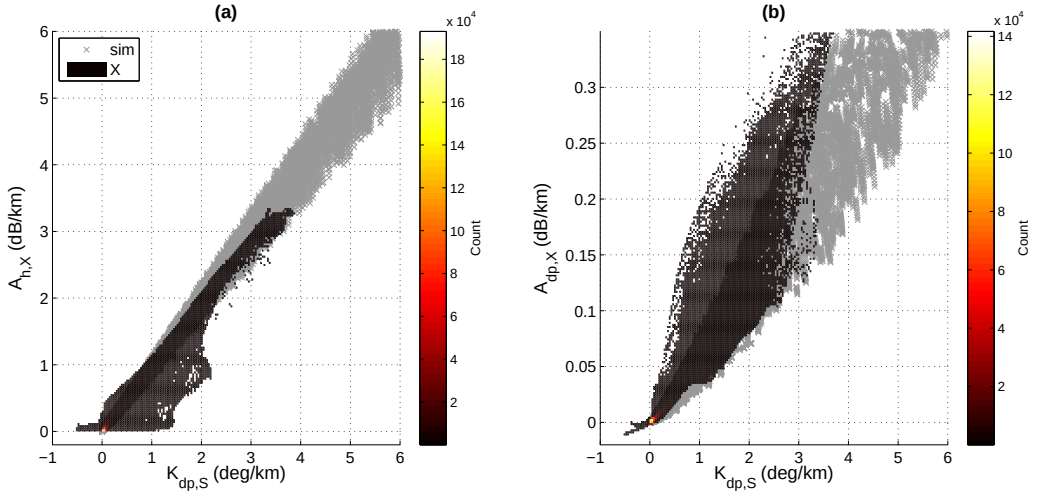

Figure 4.35: 2D histograms for simulated X-band specific attenuation vs. real S-band K_{dp} for rain from the 010802 storm over the pure simulation results (gray x's) (a) A_h and (b) A_{dp}.

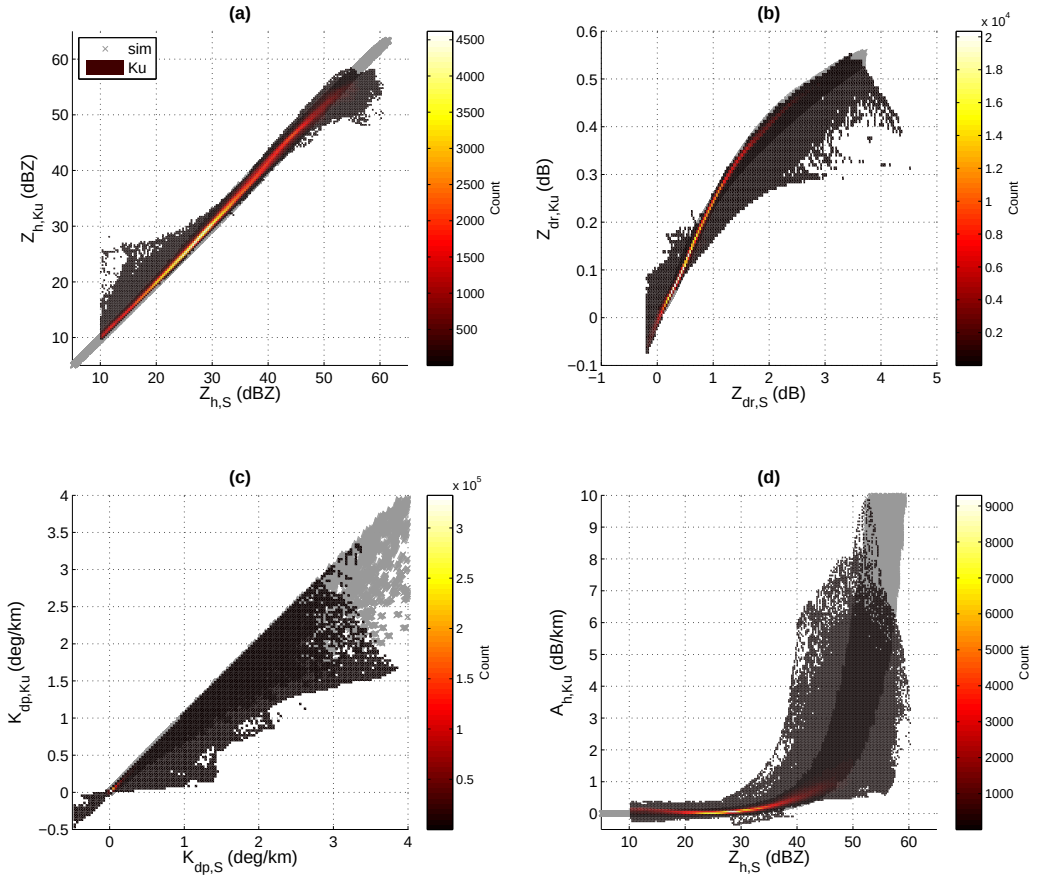

Figure 4.36: Simulated 65° Ku-band observations of rain vs. real S-band 2D histograms of the 0108020 storm overlaid on the pure simulation results (gray x's) (a) Z_h, (b) Z_{dr}, (c) K_{dp} and (d) A_h vs. $Z_{h,S}$.

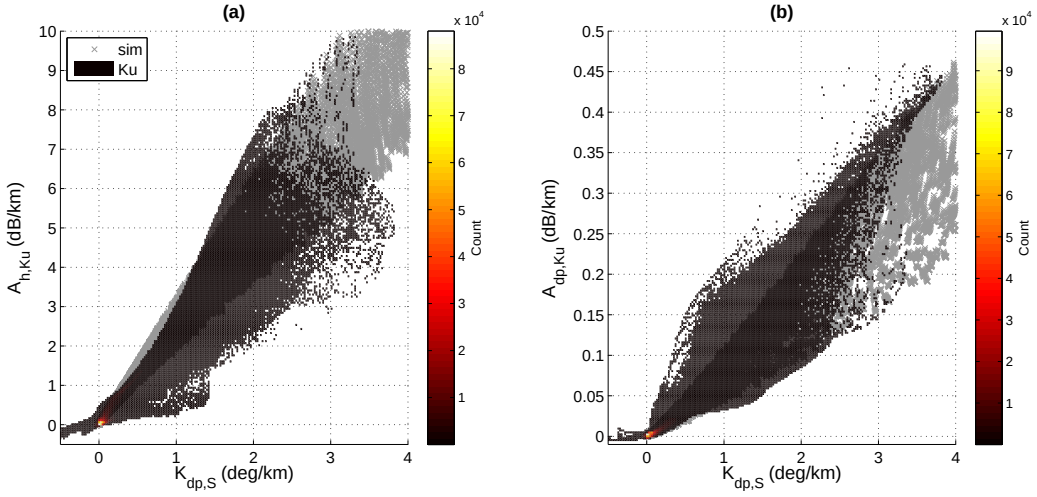

Figure 4.37: 2D histograms for simulated Ku-band specific attenuation vs. real S-band K_{dp} for rain from the 010802 storm over the pure simulation results (gray x's) (a) A_h and (b) A_{dp}.

4.8.2 Hail and Hail Mixed With Rain

Simulating high frequency radar observations of hail from real data presents several challenges, as alluded to by the discussion in Section 4.5. A method employed to improve the "realism" of the simulation data is to add a perturbation to the polarimetric variables. This helps to simulate measurement noise in addition to natural variation of hail canting and shape parameters. Without having a reasonable signal-to-noise (SNR) estimate in the gridded data, the perturbation model is made as a function of reflectivity in the form of a normal (Gaussian) distribution written as

$$\nu \sim N(0, \sigma^2), \qquad \sigma = \min\left(\frac{a_v}{Z_h}, b_v\right). \tag{4.17}$$

Table 4.2 contains the values of a_v and b_v for the variables to which the Gaussian noise is added.

Table 4.2: Noise variance parameters in (4.17)

Parameter	**S-band Variable**		
	Z_{dr}	K_{dp}	LDR
a_v	1.5	5	6
b_v	0.5	0.2	2

4.8.2.1 STEPS Supercell

Two dimensional histograms of the 000629 storm resolution cells containing hail compared to simulated S-band distributions are displayed in Fig. 4.38, similar to Fig. 4.30. In Fig. 4.38a we see an indication of a range of hailstone sizes as Z_{dr} decreases with increased Z_h. The majority of Z_{dr} values are also negative, indicating some level of vertical orientation, hence the choice of horizontally canted oblate and vertically oriented prolate spheroids in the simulation. K_{dp} also appears to be fairly close to the theory, although the real measurements tend to be slightly less than the theoretical ones. In addition to the fact that the simulations were run at a small number of discrete densities, the comparison to real data here indicates that simulation parameters might be too simplistic, but are fairly close. With the inclusion of the noise discussed above, the ANN can better accommodate the expanded input space of measurements.

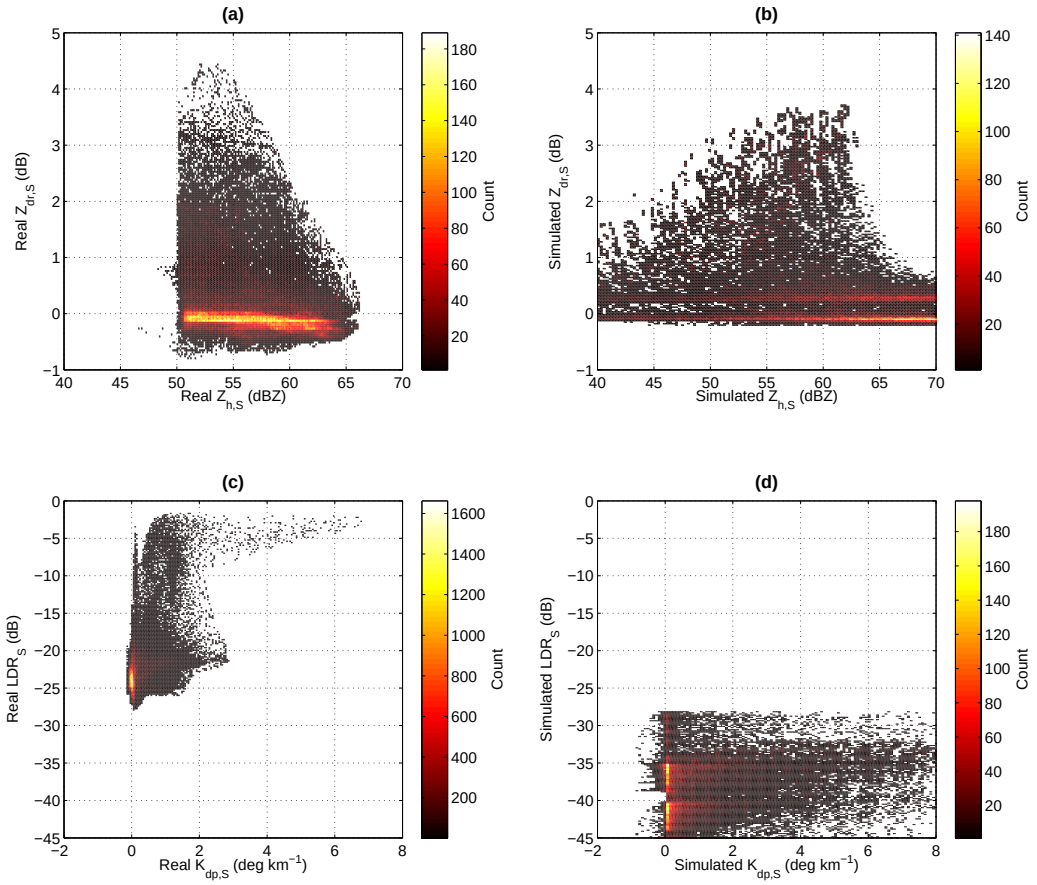

Figure 4.38: Same as Fig. 4.30 except for hail and rain plus hail within the 000629 storm. The theoretical values in panels (b) and (d) show the multiple hail canting configurations discussed in Section 4.5.2.

The neural networks for hail, however, do not perform well without the addition of a D_0 value as input when they are applied to the real data. Therefore, the first step is to estimate D_0 from observable parameters. As Table 4.7 indicates, LDR is used here, but in order to account for the large difference between reality and the simulation 20 dB was added to the simulated LDR prior to training the ANN. The histogram in Fig. 4.39 is the result of this effort, which tends to be the most difficult estimation in terms of minimizing error. Given the magnitude of this storm, and that 1.75 inch hailstones were reported [Lang et al. (2004)], the result seems reasonable. This output allowed the remaining ANNs to produce the results within theoretical bounds as exhibited in Figs. 4.40 and 4.41. The distribution shown in Fig. 4.39 also contains multiple modes, the largest of which corresponds mostly to the hail only regions. Unfortunately, it is unclear how well this matches reality or if it is

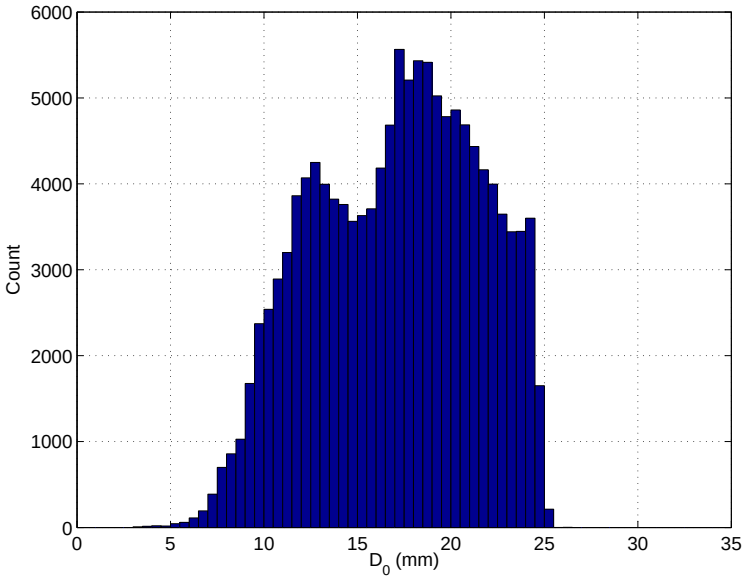

Figure 4.39: Histogram of D_0 estimated from 000629 hail and rain plus hail observations using the ANN with Z_h, Z_{dr}, K_{dp} and LDR.

a result of trying to make the data match the simulation.

Similar to Figs. 4.31 and 4.32, 2D histograms of the simulated X-band model output are plotted over the theoretical values in Figs. 4.40 and 4.41. All reflectivity estimates are within the theoretical space, and if we assume Fig. 4.39 is correct, this is the output we should expect. When real S-band Z_{dr} observations lie beyond the theoretical values, e.g., $Z_{dr,S} < -0.4 \vee Z_{dr,S} > 3.5$, there is no clear trend so the modeled response shown in Fig. 4.40b in this region could be reasonable. The $K_{dp,S}$ result shown in Fig. 4.40c is fairly representative of the expectation from simulation, and attenuation results seen in Fig. 4.40d and Fig. 4.41 are also within expected values except for a very few locations seen in Fig. 4.41a. Even the typically noisy differential attenuation produced realistic estimations.

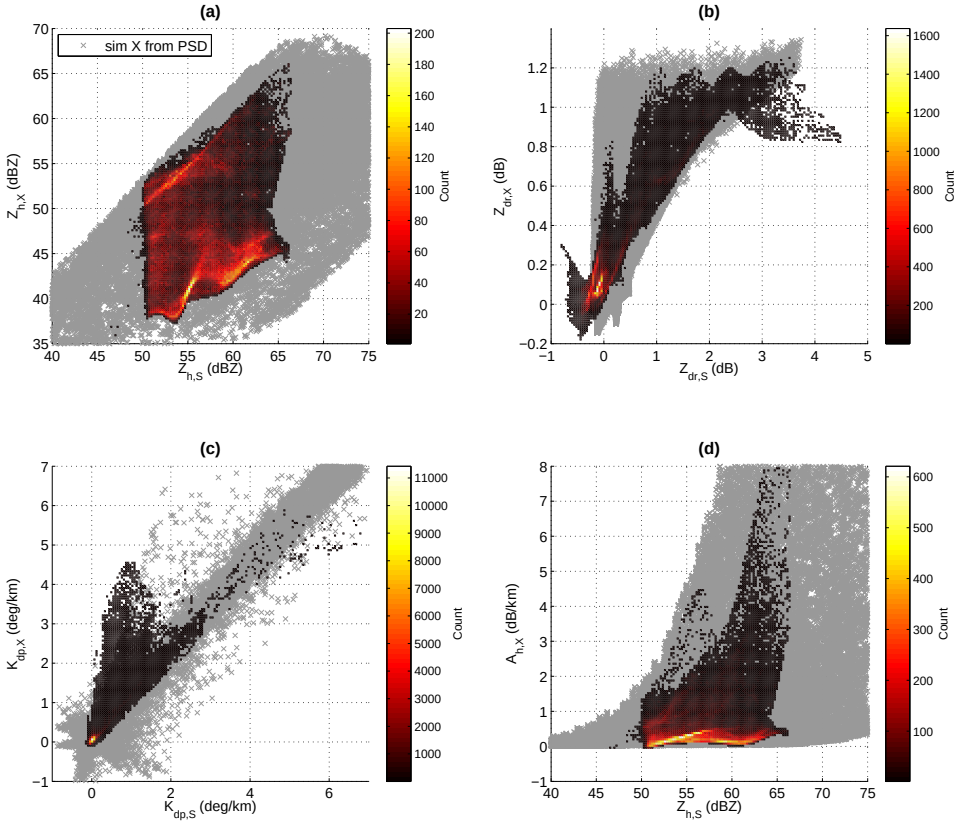

Figure 4.40: Simulated X-band observations of rain plus hail vs. real S-band 2D histograms of the 000629 storm overlaid on the pure simulation results (gray x's) (a) Z_h, (b) Z_{dr}, (c) K_{dp} and (d) A_h vs. Z_h.

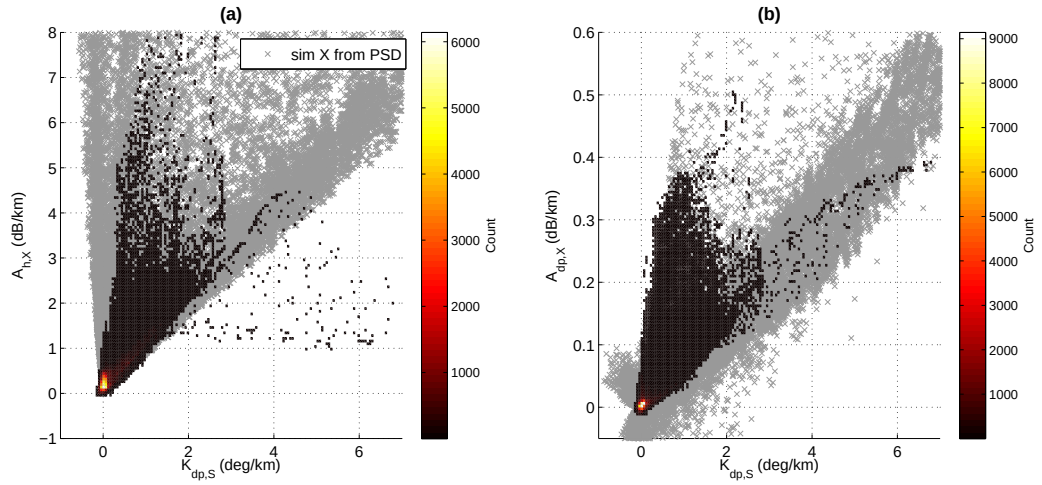

Figure 4.41: 2D histograms for simulated X-band specific attenuation vs. real S-band K_{dp} for rain plus hail from the 000629 storm over the pure simulation results (gray x's) (a) A_h and (b) A_{dp}.

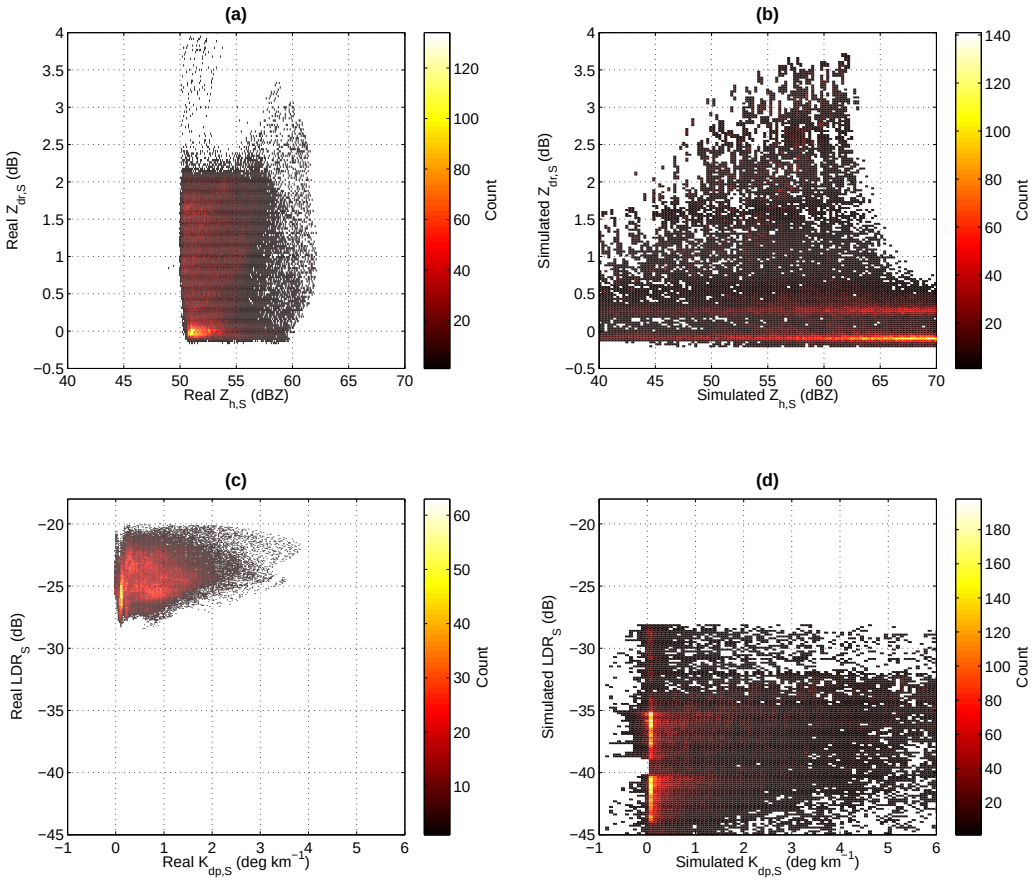

Figure 4.42: Same as Fig. 4.30 except for hail and rain plus hail within the 010802 storm. The theoretical values in panels (b) and (d) show the multiple hail canting configurations discussed in Section 4.5.2.

4.8.2.2 2001 Squall Line

With the success of the model applied to a classic supercell, another good test of robustness is to apply it to a different type of storm. The August 2, 2001 squall line observed by the CSU-CHILL radar provided this data, and the variables within resolution cells classified as hail or hail plus rain are depicted in Fig. 4.42. No additional filtering was applied as the data quality is quite good. Even LDR is much closer to the simulated range of values, but it was still only used for the D_0 estimate. Both Z_{dr} and K_{dp}, however, appear to have more variability than simulations suggest. Despite this, a very reasonable estimate of the D_0 distribution was made, as displayed in Fig. 4.43. A squall line is expected to have smaller hailstone sizes than a supercell, which is exactly what the figure suggests, showing a fairly narrow peak around 10 mm. In this particular case, almost all hail was melted

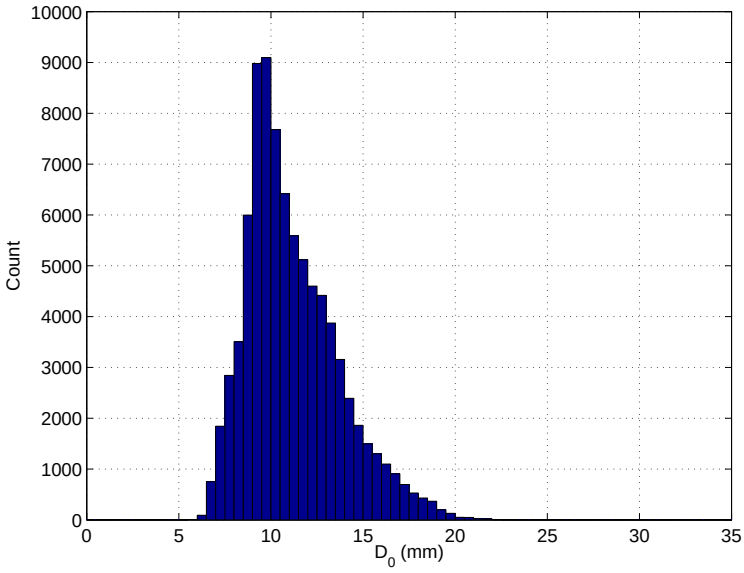

Figure 4.43: Histogram of D_0 estimated from 000629 hail and rain plus hail observations using the ANN with Z_h, Z_{dr}, K_{dp} and LDR.

before hitting the ground, as will be shown in Section 5.4.2.

With the estimate of D_0 being very reasonable, the model converted the S-band measurements to 55° X-band observations quite well. These results are shown in Figs. 4.44 and 4.45. Smaller hail stone sizes should result in higher reflectivity estimations, which is exactly what Fig. 4.44a indicates. The Z_{dr} output is also mostly within the theoretical bounds, as is the K_{dp} estimation. Data seen in Fig. 4.44(b and c) that are outside this region correspond to the same points where a large differential reflectivity (above 2.5) had an associated small differential phase shift around 0.5. The output of the model then became a reduced Z_{dr} and an increased K_{dp}. Given that K_{dp} is not measured directly, it is possible that it was underestimated. As expected based on the model output for observable variables, attenuation is also well within realistic expectations as seen in Fig. 4.44a relative to reflectivity and in Fig. 4.45. All A_h values are positive, and most A_{dp} values are where negative output corresponds to the small amount of negative Z_{dr}.

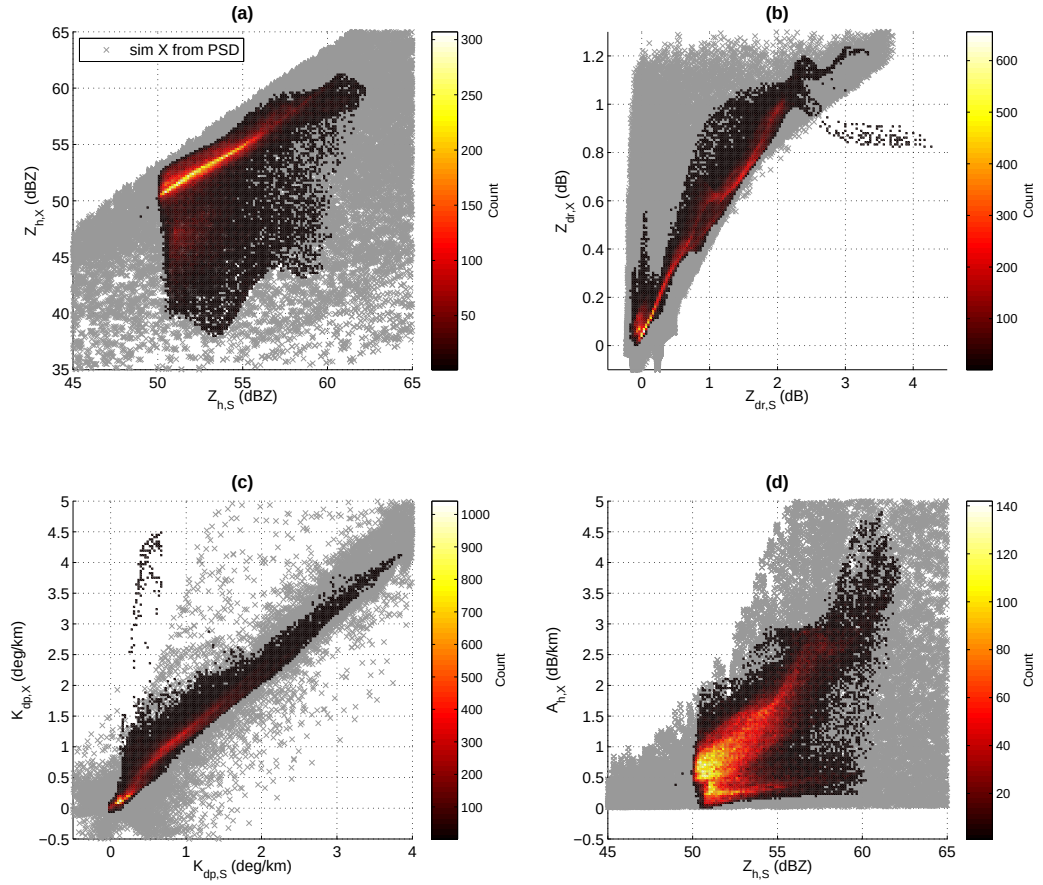

Figure 4.44: Simulated X-band observations of rain plus hail vs. real S-band 2D histograms of the 000629 storm overlaid on the pure simulation results (gray x's) (a) Z_h, (b) Z_{dr}, (c) K_{dp} and (d) A_h vs. Z_h.

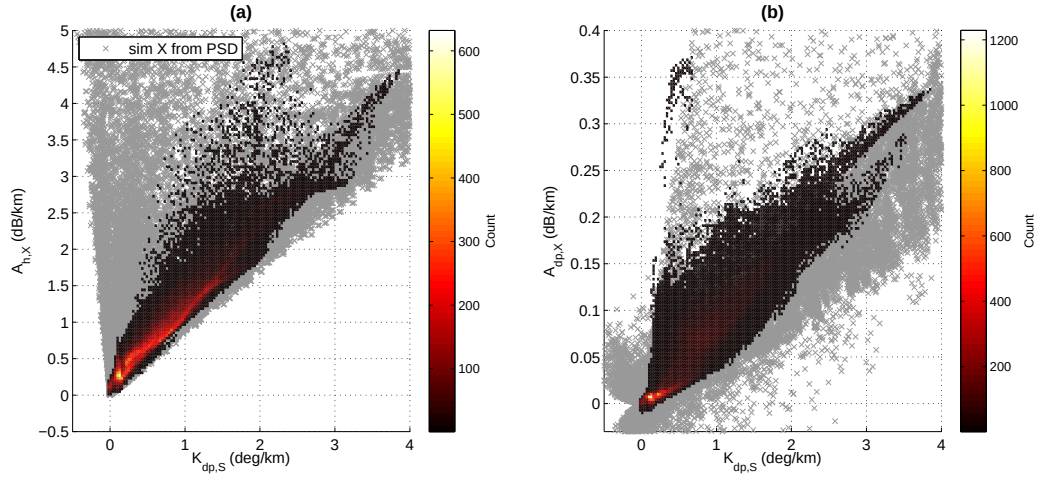

Figure 4.45: 2D histograms for simulated X-band specific attenuation vs. real S-band K_{dp} for rain plus hail from the 000629 storm over the pure simulation results (gray x's) (a) A_h and (b) A_{dp}.

4.9 Summary

Simulating the observations of a short wavelength spaceborne off-nadir radar from lower frequency ground data is the primary goal of this research. In order to reach this goal, electromagnetic scattering simulations are utilized given realistic PSD parameters for various hydrometeor types. For particles in the Rayleigh scattering size region, these parameters were derived from in situ observations and numerous experiments. The parameters for hail are also based on field observations; however, only a simple shape and three simple canting configurations are used to cover the essence of the real behavior. Following scattering simulations for horizontally pointing S and C-band radars and high elevation X and Ku-band radars, models are presented to transform the former to the latter. For rain and hail, a nonlinear regression model implemented with radial basis function neural networks is presented and performance documented from real S-band observations. The model for rain is also compared with an existing curve-fit model, but there is no current model for hail with which to compare. Nearly all model results lie within theoretical limits, thus achieving the primary goal. These results are then used directly for simulating X-band SAR observations discussed in subsequent chapters.

The neural network models produce excellent results, although they have cons as well as pros. On the one hand, the oscillations due to Mie scattering can be handled for a large variety of hail sizes and ice fractions, a lookup table of coefficients is not necessary and the error when applied to rain is comparable to existing models. The network is also adaptive to the input, so a complete redesign is not necessary to model different scenarios. On the other hand, training the ANNs so that they produce reasonable results with real input observations is challenging. This may be solved by a better optimization algorithm than the gradient descent method used. For the most part, the lower the mean absolute error, the better the results when applied to real radar measurements, so there is no overfitting problem that can occur with implementations such as the multi-layer perceptron [Fritz and Chandrasekar (2010a)]. However, values in real data that may be noisy, caused by unusual circumstances or mis-classification in the hydrometeor identification stage, can lead to erroneous results such as reflectivity that is too low. It is conceivable that results

like this could then aid an improved filter algorithm, but for now they must be accounted for by removing insidious data or providing an explanation for the results.

There are several possible improvements to the ANN models for future research. One is to improve the training sets in order to better match realistic observations. While it is not reasonable to simulate every case, better models of measurement noise could be helpful. Another possibility is to take advantage of the adaptability of the A-RBFN design when applied to real data. Although the target value may be unknown, the estimations will not deviate too much from adjacent grid cells. If the data are processed by incrementing through the grid, beginning with higher altitude values underneath snow or graupel, an error can be presented to the ANN if the output value is beyond a threshold, e.g., from the median value of adjacent cells that have already been computed. Thus, large spatial gradients can be reduced.

CHAPTER 5

SIMULATION OF SAR PRECIPITATION OBSERVATIONS

A scientific truth does not triumph by convincing its opponents and making them see the light,but rather because its opponents eventually die and a new generation grows up that is familiar with it.

- Max Planck

5.1 Introduction

Meteorological investigations from spaceborne SAR platforms are becoming possible given recent and upcoming launches of higher frequency systems. To date, however, limited work has been done to create models for simulating the effect of precipitation on short wavelength SAR and almost no prior research involves polarimetric observations. A methodology is presented here that is capable of simulating X-band polarimetric SAR observations of convective storms containing hail based on real data from a ground-based S-band polarimetric radar. This methodology involves a model and scattering simulations to transform the longer wavelength observations to shorter wavelengths at higher elevation angles, using a neural network for rain and hail, hydrometeor classification of the real data and spatial modeling of the SAR viewing geometry in order to compare the simulated storm to real SAR observations. Results using data from the CSU-CHILL radar of a supercell storm and a squall line are shown and the simulated storm is added to TerraSAR-X data collected over Florida in 2008.

5.2 SAR Precipitation Spatial Model

The spatial distribution and geometric model for SAR through precipitation has been presented by several previous works including Pichugin and Spiridonov (1985), Moore et al.

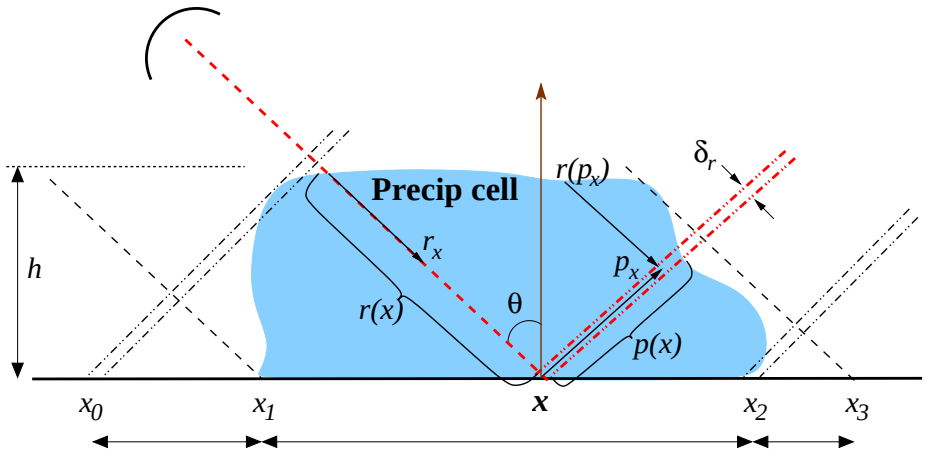

Figure 5.1: A schematic of SAR planar wavefronts through a rain cell. x is the cross-track ground range, with various transition points between attenuation or backscatter (or both) are indicated. r_x is the radial vector while p_x is the perpendicular (ideal wavefront) vector. Thus, $r(x)$ is the range through the precipitation cell to surface location x, $p(x)$ represents the backscatter component of the precipitation affecting the observation at x and $r(p_x)$ is the attenuation of the precipitation backscatter as it is integrated along p_x.

(1997) and Weinman and Marzano (2008) is described with the aid of Fig. 5.1. This cross track vertical slice depicts a precipitation cell (blue region), the direction of the incident radar beam and the plane wave approximations to the range-time samples ($\delta_r = c\tau/2$ where τ is the compressed pulse width). The cell could contain frozen, melting and liquid layers.

When the SAR beam passes through a precipitation cell, the observed NRCS can be expressed as the sum of volume and surface cross sections as seen in Fig. 5.1 [Pichugin and Spiridonov (1985); Melsheimer et al. (1998); Moore et al. (1997); Weinman and Marzano (2008)]. This sum is given by

$$\begin{aligned} \sigma_{obs} &= \sigma_{sp} + \sigma_{vp} \\ \sigma^0_{obs}\alpha_{srf} &= \sigma^0_{sp}\alpha_{srf} + \eta_{vp}V_{eff}, \end{aligned} \tag{5.1}$$

where $\alpha_{srf} = \delta_a\delta_r$ is the surface area within the SAR resolution cell, η_{vp} is the volumetric backscatter cross section ($\mathrm{m}^2\ \mathrm{m}^{-3}$) and V_{eff} is the effective volume of precipitation backscatter [Moore et al. (1997)] that incorporates the turbulent velocity dependent azimuth resolution described in Atlas and Moore (1987). The *obs* subscript indicates the observation while the *srf* subscript represents the surface component. Dividing through by this surface area leaves $\sigma^0_{obs} = \sigma^0_{sp} + \eta_{vp}a_{eff}$ where a_{eff} is the remaining effective area. In

general, the volume and surface components are scaled based on how much of the sampled beam volume travels through the precipitation volume ($r(x)$ in Fig. 5.1), or resides in this volume along the transverse dimension ($p(x)$). At the cross track range where the beam reflects the surface, x, with a no-rain NRCS σ^0_{NR} is expressed as

$$\sigma^0_{sp} = \sigma^0_{NR} l_{r(x)}(r) \tag{5.2}$$

where $l_{r(x)}(r)$ is defined by (2.29) integrated over $r(x)$, and

$$\eta_{vp} a_{eff} = \sin\theta \int_{p(x)} \eta(p_x) l_{r(p_x)}(r) dp_x \tag{5.3}$$

where $l_{r(p_x)}(r)$ is defined by (2.29) integrated over $r(p_x)$. Similarly, the differential reflectivity contains surface and volume components expressed as

$$Z^{obs}_{dr} = Z^{srf}_{dr} + Z^{vol}_{dr} - 2\int_0^R A_{dp}(r) dr \tag{5.4}$$

where A_{dp} is defined in (2.33) and the *vol* superscript indicates the contribution of the hydrometeor volume. The last term in reveals the differential attenuation for a target at range R.

If the precipitation cell were a perfect rectangle, basic trigonometry can be used to precisely calculate the integration parameters $r(x)$, $p(x)$ and $r(p_x)$ [Pichugin and Spiridonov (1985); Marzano and Weinman (2008)]. However, realistic values are not so easy to determine, especially when the edges of the storm are not well defined. The ground-based radar reflectivity corresponding to visible artifacts in the SAR images are most likely convective cells due to the high reflectivity values and sharp gradients [Steiner et al. (1995)] (this is discussed further in Sections 6.2.2 and 6.2.3). Over the regions that would be classified as stratiform, effects on the SAR observations are negligible. Despite the ambiguity, however, the ground radar reflectivity volume provides estimates for comparison. Further details on the impact of convective and stratiform precipitation cells are given in the following sections.

5.3 Data Processing

5.3.1 Overview

There are a number of steps involved to simulate storm observations of an X-SAR from ground-based polarimetric radar. An unavoidable consequence of multiple steps is the introduction of noise starting with the ground radar observations, hence the careful application of smoothing filters at various stages without degrading true gradients and peaks. The following is a list of the major stages.

1. *K_{dp} estimation.* As described in (2.31), K_{dp} is a forward scattering phenomena. Therefore, it cannot be observed directly from a monostatic radar and must be estimated from the backscatter Φ_{dp} (see (2.32)). The algorithm used for this purpose is detailed in Wang and Chandrasekar (2009), and in the process, low signal-to-noise ratio (SNR) data are removed.

2. *Attenuation correction.* If the ground based radar is subject to attenuation, for example C-band radars, attenuation correction should be applied at this stage. The algorithm used will depend on the specific conditions, but most are based on K_{dp} as it is not affected by attenuation [Testud et al. (2000)]. A consequence, however, is that the correction will be underestimated if K_{dp} is underestimated, which will propagate to the final result.

3. *Gridding.* Using standard interpolation techniques with a range dependent window, the original radial data are resampled to form an earth-centric Cartesian grid, i.e., the vertical axes indicates constant altitude based on the geolocation of the radar and the horizontal axes correspond to latitude and longitude. This process inherently filters the data, and some remaining artifacts can be smoothed further by applying a three-dimensional Gaussian kernel to average adjacent samples. In addition, manual removal of spatial outliers can be applied.

4. *Hydrometeor classification.* In order to apply the correct PSD based model to transform observations to those of a different wavelength, the hydrometeor types need to

be identified. This is a challenging process, met with a high degree of success using the fuzzy logic approach described in Lim et al. (2005). Part of this process involves an estimation of the melting layer from the dual-polarization observations, which can then provide an estimation of temperature if no sounding data is available. Membership functions have been fine tuned since the publication, as well as threshold values. In addition, a spatial processing algorithm was added in the course of this research to avoid cases where a grid cell is determined to contain frozen/melting particles while the 3×3 grid array above it contains only liquid particles because the original method does not consider spatial relationships except distance to the melting layer.

5. *Transform frequency and look angle.* Following hydrometeor classification, the models discussed in Chapter 4 are applied to simulate the observations of the storm from a higher frequency spaceborne radar with an off-nadir look angle. These observables include Z_h, Z_{dr}, K_{dp}, A_h and A_{dp}. The emphasis here is to generate realistic storm observations and not necessarily the true observations of the specific storm from the simulated platform, although that is the ultimate goal when coincident observations from polarimetric SAR and ground radars are available. Field experiments will be necessary, of course, to validate the simulation results.

6. *Geometric resampling.* At this point, the georeferenced volume of simulated polarimetric radar observations is resampled with the geometry of the SAR. Fig. 5.1 shows the essence of the process while Fig. 5.2 provides a more detailed look at the implementation showing discrete sample spacing. Slant angle resampling is described in more detail below.

7. *Integration to SAR observations.* Given the range independent parameters generated in the previous step, the final stage is to integrate them to simulate the propagation effects from the storm onto a SAR ground observation, namely providing solutions for (5.1) through (5.4) using real SAR observations without precipitation present. Ultimately, the full covariance matrix can be generated incorporating real surface measurements with simulated propagation effects.

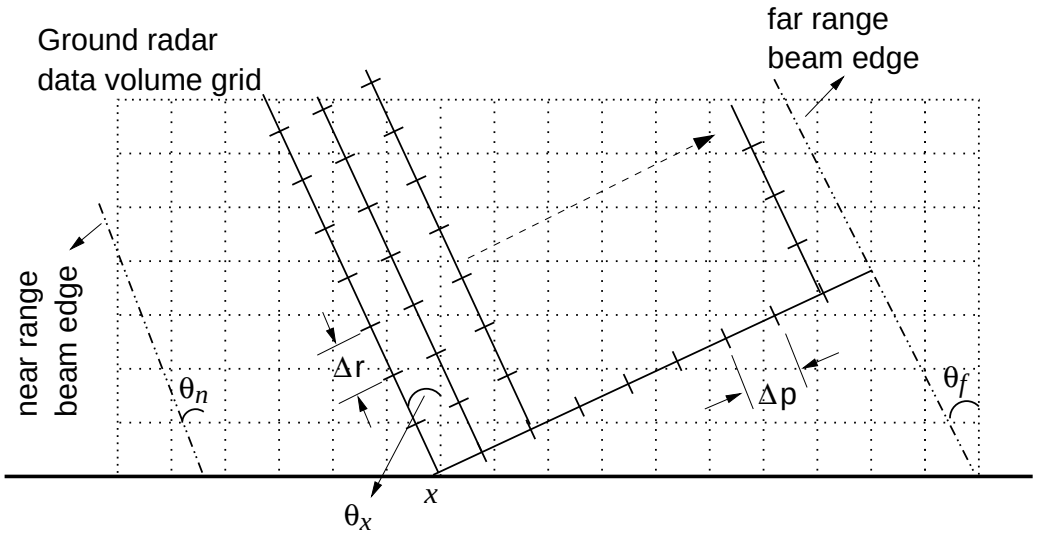

Figure 5.2: A more detailed look at the calculation of volumetric parameters given a grid of ground radar data shown. The incidence angle at each ground location x is θ_x where $\theta_n \leq \theta_x \leq \theta_f$, i.e., between the near-range and far-range angles. Along the slant path, the sample resolution is Δr, while the resolution in the transverse direction, representing a single range bin of SAR data, is Δp. For each x there are N_x slant path samples and M_x transverse samples.

5.3.2 Resampling and Integration

Fig. 5.2 provides a more detailed look at the implementation of the theory discussed in Section 5.2. The grid shown is generated in Step 3 in Section 5.3.1 and can represent any observation variable. Incidence angles of the SAR beam start at θ_n at the near-range side of the swath and end at θ_f along the far-range edge. Shown are the sample lines representing the slant range and plane wave beam approximation at ground location x ($\theta_n \leq \theta_x \leq \theta_f$). Along the transverse line, there are M_x samples at a resolution of Δp from the surface to the far beam edge. At the i^{th} sample along the transverse line is a slant line containing N_{xi} samples at a resolution of Δr. Thus, the i^{th} sample of measured (i.e., attenuated) horizontal reflectivity associated with x is

$$Z_{h,xmi} = Z_{h,xi} + L_{h,r(x)} = Z_{h,xi} - 2\Delta r \sum_{k=1}^{N_{xi}} A_{h,ik} \tag{5.5}$$

where $A_{h,ik}$ is the k^{th} sample of specific attenuation (see (2.28)) along the path to the i^{th} transverse sample. The estimation of path integrated attenuation (PIA) affecting the

surface return is the same as that affecting the volume at the surface where $i = 1$, i.e.,

$$L_{h,r(x)} = -2\Delta r \sum_{k=1}^{N_{x1}} A_{h,1k}. \tag{5.6}$$

Similarly, the differential reflectivity is determined by

$$Z_{dr,xmi} = Z_{dr,xi} + L_{dp,r(x)} = Z_{dr,xi} - 2\Delta r \sum_{k=1}^{N_{xi}} A_{dp,ik} \tag{5.7}$$

where $A_{dp,ik}$ is the k^{th} sample of specific differential attenuation (see (2.33)) along the path to the i^{th} transverse sample.

Before continuing with the conversion to NRCS, reflectivity is converted to volumetric radar cross section η_h using (2.26) in units of $\mathrm{m}^2\,\mathrm{m}^{-3}$. Then the volume contribution of the horizontal channel of the SAR observation can be written as

$$\eta_{h,x} = \Delta p \sum_{i=1}^{M_x} \eta_{h,xi} = b\Delta p \sum_{i=1}^{M_x} 10^{0.1\left(Z_{h,xi} - 2\Delta r \sum_{k=1}^{N_{xi}} A_{h,ik}\right) - 18} \tag{5.8}$$

where $b = \pi^5 |K_w|^2/\lambda^4$ and the '-18' exponent is from the conversion from mm^6 to m^6. The PIA at the ground location ($l_{r(x)}(r)$ in (5.2)) is the same as the second term in (5.5) at $i = 0$ before conversion to linear units. Complex SAR data is usually delivered in terms of β^0 rather than σ^0 where the two are related by (2.39). Therefore, it is simpler to calculate β_{obs} which removes the $\sin\theta$ term in (5.3). The final result for estimating the observed radar brightness for both co-polar channels is

$$\beta_{hhObs} = \beta^0_{hhNR} l_h + \eta_h \tag{5.9}$$

$$\beta_{vvObs} = \beta^0_{vvNR}\,(l_v) + \eta_v \tag{5.10}$$

where losses are in linear units, the subscript references to r and x have been dropped to simplify notation, $l_v = l_h/l_{dp}$ and η_v is calculated similar to (5.8) using $Z_v = Z_h - Z_{dr}$.

The co-polar correlation in (2.34) can also be estimated and provides the means to construct a 2×2 covariance matrix from the scattering vector consisting of the co-polar terms (i.e., $[S_{hh} \;\; S_{vv}]$). Propagation and volumetric backscatter affect the complex product term, $S_{hh}S^*_{vv}$, similar to the intra-polarization terms, so the correlation magnitude can be estimated in terms of β^0 by

$$|\widehat{\rho}_{obs}| = \frac{S_{hh}S^*_{vv}\sqrt{l_h l_v} + 0.5\,(\eta_h + \eta_v)}{\sqrt{\beta_{hhObs}\beta_{vvObs}}} \tag{5.11}$$

where $S_{hh}S_{vv}^{*}$ indicates the surface only response. This implies $\beta_{xx}^{0} = S_{xx}S_{xx}^{*} = |S_{xx}|^{2}$. Similar to attenuation, phase is also accumulated along the path of the propagating radar wave as described in (2.32), but consideration of the phase change along the entire wavefront must be made. Using K_{dp} and a similar approach used to determine volumetric backscatter attenuation in (5.8) the observed co-polar differential phase can be calculated. At the surface location x, the total phase due to precipitation is the sum of backscatter and averaged integrated specific phase:

$$\Psi_{dp,x} = \phi_{co,x} + \Phi_{dp,x} \tag{5.12}$$

where $\phi_{co,x} \simeq 0$ when the scattering is within the Rayleigh limits. For a SAR image without precipitation in the beam, $\Phi dp, x \simeq 0$ and the copolar phase shift from the surface backscatter is represented by $\phi_{co,x}$. To compute $\Phi_{dp,x}$, the specific phase K_{dp} is first integrated along the slant path to each transverse sample, resulting in multiple Φ_{dp} estimates along this constant range bin. Combining these differential phase values is accomplished considering that the estimate for a single resolution cell is calculated by taking the argument of the lag 0 covariance $R_{co}[0] = \langle V_{hh}V_{vv}^{*}\rangle$, where V_{vv} and V_{hh} are the measured voltages from vertical and horizontal polarization respectively. The overall calculation is represented by

$$\widehat{\Phi}_{dp} = \arg\left\{R_{co}[0]\right\} = \arg\left\{\frac{1}{N}\sum_{n=1}^{N} V_{hh}[n](V_{vv}[n])^{*}\right\}. \tag{5.13}$$

Given that samples of Φ_{dp} have been estimated along a constant SAR range bin, these must be coherently summed. The total differential phase due to precipitation becomes

$$\Phi_{dp,x} = \arg\left\{\sum_{i=1}^{M_x} \mathrm{e}^{j\Phi_{dp,xi}}\right\} \tag{5.14}$$

where

$$\Phi_{dp,xi} = 2\Delta r \sum_{m=1}^{N_x} K_{dp,xm}. \tag{5.15}$$

Then (5.14) is substituted into (5.12) and added to the copolar phase of the surface for the final estimation of differential phase at the ground location x. Combining all of these components provides a mechanism to simulate X-band SAR observations of a storm starting with real polarimetric S-band ground observations.

5.4 Case Studies

Data from the Severe Thunderstorm Electrification and Precipitation Study (STEPS) experiment [Lang et al. (2004)] during a hailstorm on 29 June, 2000 (denoted as 000629) and measurements of a squall line on 02 August 2001 (denoted 010802) are used to validate the model results. These observations were made by the CSU-CHILL S-band dual-polarization Doppler weather radar. Using the procedure detailed in Section 5.3, observations are simulated to match parameters of the TerraSAR-X X-band SAR operating with a 35° incidence angle in stripmap co-polarization mode where only S_{hh} and S_{vv} are measured. Real TSX scenes captured over Orlando, Florida in August 2008 are then used as the SAR data to which the simulated storms are added with a comparison to real storms observed in a prior overpass. This procedure neglects changes to the surface due to an active storm, which will provide insight into surface changes when comparing to real storms.

5.4.1 STEPS Supercell

In order to demonstrate the model, two cases are analyzed where hypothetical SAR swaths run in the north-south direction with different east-west positions relative to the storm - one on each side. For the east side swath, the storm is effectively rotated 180° so that the look direction will be the same allowing both to be added to a single real SAR image. Meanwhile, the swath on the west side simulates the SAR observations through the core of the storm.

Figs. 5.3 through 5.6 provide an overview of the storm being processed. In Fig. 5.3, three orthogonal slices of reflectivity indicate the intensity of the storm, identified as a supercell with copious amounts of hail and a strong updraft near the region where reflectivity above 60 dBZ extends from the surface at 1.5 km above Mean Sea Level (MSL) to about 12 km MSL. Detecting rain at such a high altitude, however, may in fact be caused by strong gradients in the horizontal versus vertical returns, which in turn may skew Z_{dr}. When the antenna is pointing toward the top of the storm, significant backscatter could be detected from the hail shaft via the sidelobes. Hydrometeor classification results using the Lim et al. (2005) procedure are shown in Fig. 5.4 along the same 3 slices. Hail is indicated by the

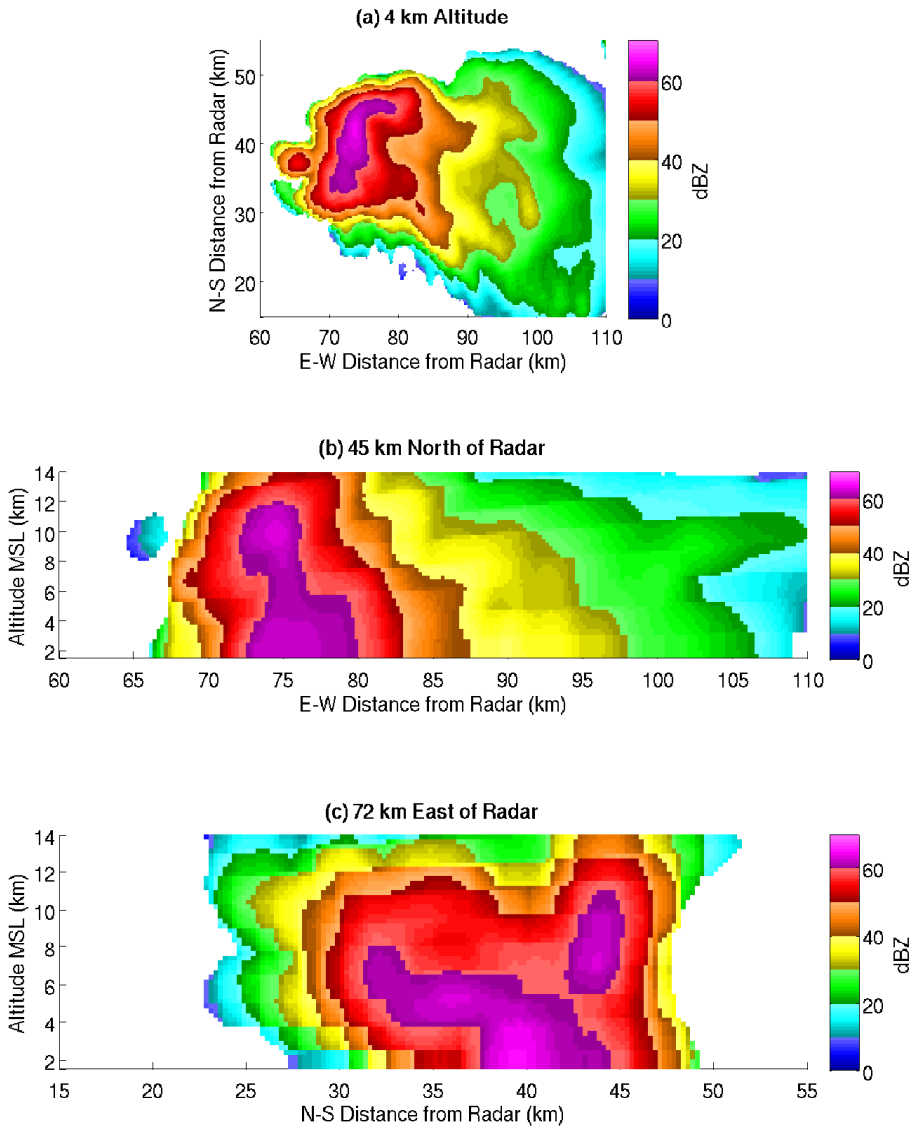

Figure 5.3: Slices of reflectivity observed by CSU-CHILL during the 000629 storm. (a) A horizontal slice at 4 km MSL. (b) A vertical slice at 45 km north of the radar. (c) A vertical slice at 72 km east of the radar. Some gridding effects are visible in this slice.

magenta color and hail mixed with rain by green. An estimation of the melting layer is depicted in Fig. 5.5 which clearly shows a strong updraft to the west of a downdraft. The horizontal slices of differential reflectivity displayed in Fig. 5.6 help confirm the presence of the updraft. Once Z_{dr} becomes positive from the storm top, hydrometeors have changed from oriented ice crystals to oblate raindrops [Bringi and Chandrasekar (2001)].

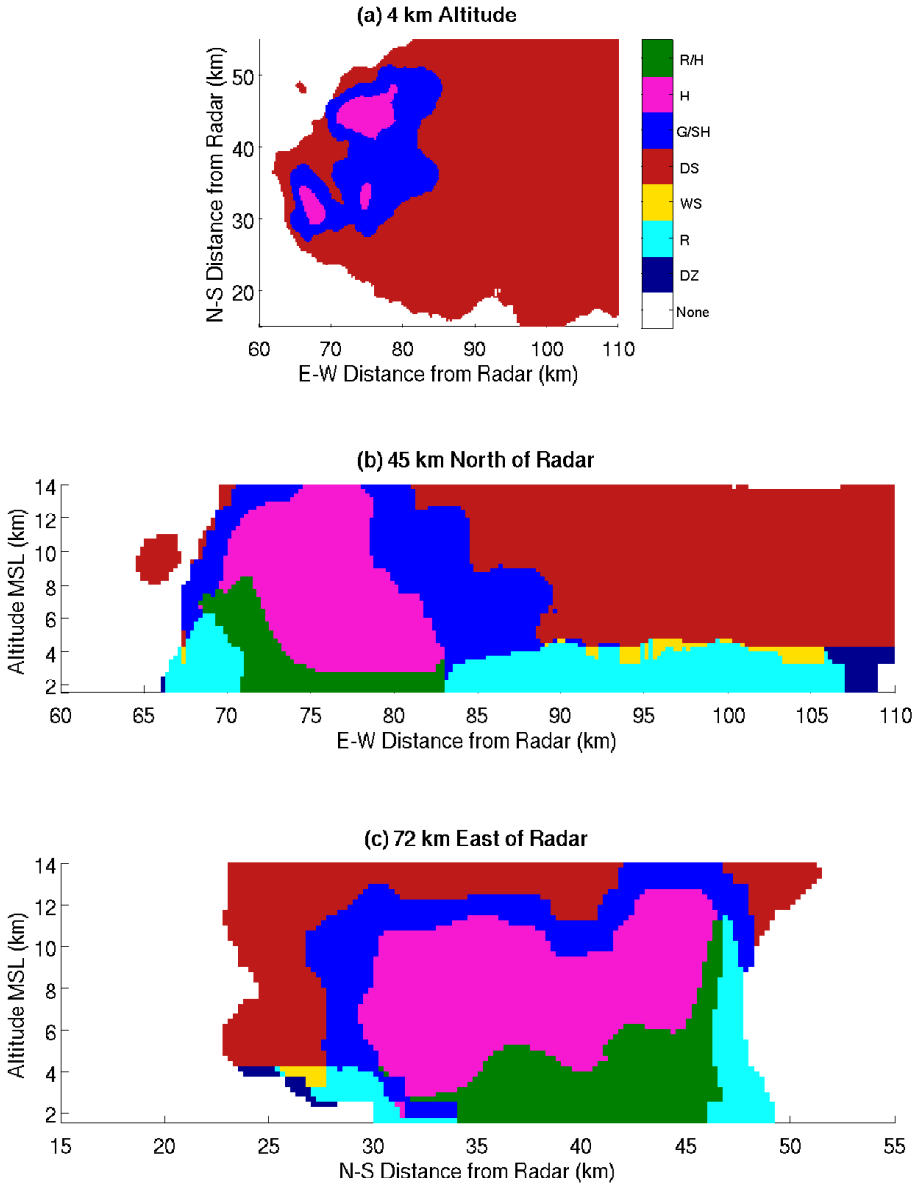

Figure 5.4: Slices of hydrometeor classification results at the same locations as the reflectivity slices in Fig. 5.3. (a) A horizontal slice at 4 km MSL. (b) A vertical slice at 45 km north of the radar. (c) A vertical slice at 72 km east of the radar. The color codes are as follows: R/H = rain plus hail, H = hail, G/SH = graupel or small hail (includes melting), DS = dry snow, WS = wet snow, R = rain and DZ = drizzle or light rain.

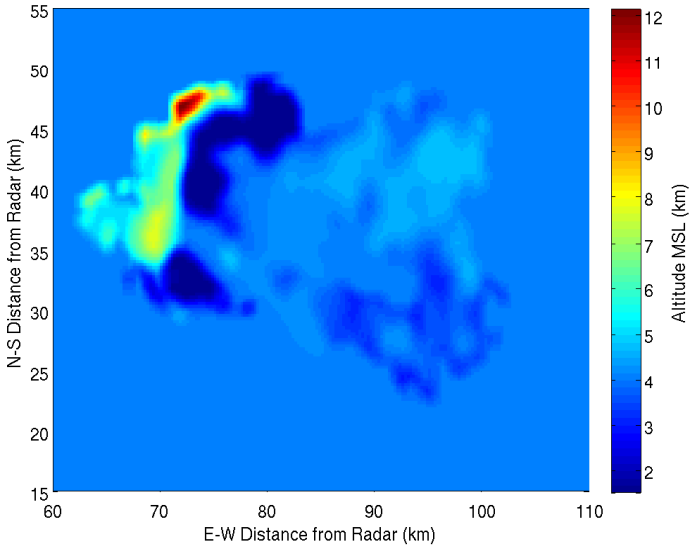

Figure 5.5: The melting layer height in km above MSL estimated during hydrometeor classification. The ground level is approximately 1.5 km. Around 72 km east of CSU-CHILL and 47 km north, a strong updraft is indicated by a very high melting layer. This may actually be above the freezing level, but indicate super-cooled raindrops. These raindrops then become hailstone embryos.

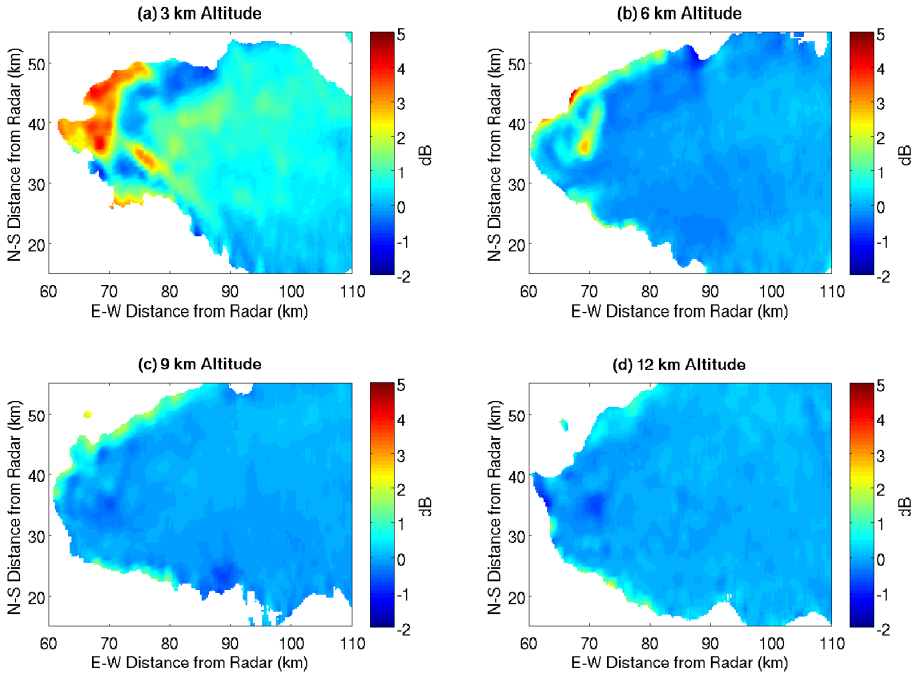

Figure 5.6: Horizontal slices of differential reflectivity observed by CSU-CHILL during the 000629 storm at (a) 3 km MSL (b) 6 km MSL (c) 9 km MSL and (d) 12 km MSL.

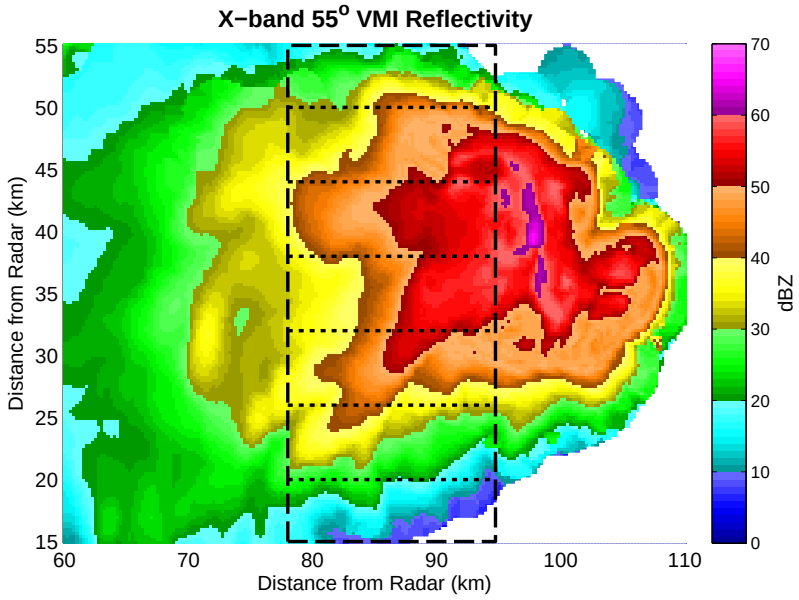

Figure 5.7: Vertical Maximum Intensity (VMI) of simulated X-band reflectivity from the 000629 storm (rotated 180°) with the location of the hypothetical SAR swath indicated by the dashed lines and vertical cross-track slice locations by the dotted lines.

5.4.1.1 Stratiform to Convective

A majority of the June 29 storm is clearly convective; however, the region on the east side possesses more stratiform characteristics. These characteristics include lower reflectivity, a relatively flat melting layer and, in general, more homogeneity, although the stratiform region in this storm does not exhibit a significant bright band. Frozen hydrometeor types in stratiform storms are typically snow crystals, including those within the melting region, unlike convective storms that contain higher density ice such as graupel and hail. Fig. 5.7 displays a Vertical Maximum Intensity (VMI) image of the rotated storm after being transformed to X-band. The figure also indicates the position of the SAR swath with vertical cross-track slice locations indicated by the dotted lines.

A better view of the storm structure within the SAR beam is given by Fig. 5.8 that shows vertical cross-track slices of reflectivity at the locations marked in Fig. 5.7 (where 0 km along-track = 15 km north of the ground radar). Lines in each panel indicate the slant path of the beam at six locations and the corresponding transverse planar wavefronts. Figs. 5.8a and 5.8b contain light precipitation toward the edge of the storm; negligible radar returns are indicated by white color. Much higher reflectivity values are shown in

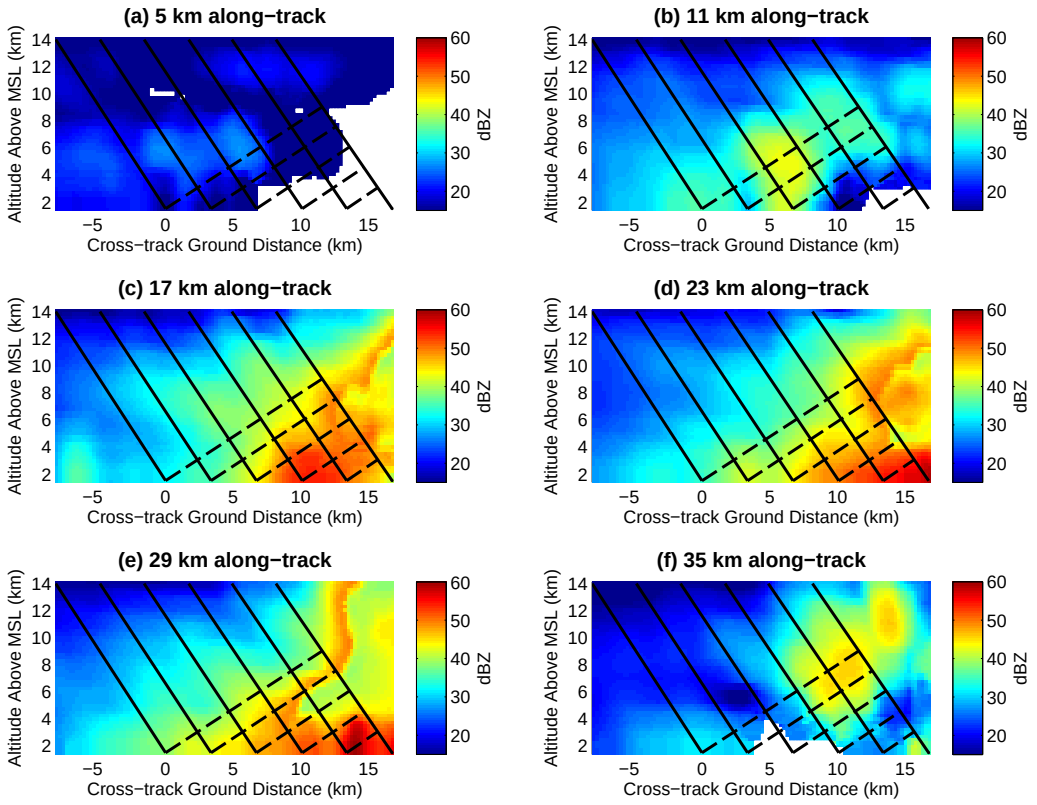

Figure 5.8: Six vertical cross-track slices of horizontal reflectivity $Z_{h,X}$ (see 5.7). The solid lines indicate several slant paths including the ideal beam boundaries and the dashed lines indicate transverse (constant range) values. The slices are at (a) 5 km (b) 11 km (c) 17 km (d) 23 km (e) 29 km and (f) 35 km along-track, offset from the ground radar by 15 km.

Figs. 5.8c-e where a gradient is visible along the edge of regions containing hail. Mie scattering within the hail cell is likely to cause a decrease in observed reflectivity, and the 2D histograms of this storm shown previously in Fig. 4.40 along with the D_0 in Fig. 4.39 confirms this.

Vertical cross-track slices of the X-band specific attenuation at the same six locations are depicted in Fig. 5.9. Although there is not a one-to-one correspondence between high reflectivity and attenuation, hydrometeor volumes resulting in high reflectivity, which are usually rain or melting particles, tend to cause higher attenuation at higher frequencies such as in X band. The resulting PIA within the SAR scene calculated from (5.6) is shown in Fig. 5.10 where we see a more complete picture of the high attenuation between 18 and 33 km along-track. Fig. 5.10a shows the PIA in horizontal polarization while Fig. 5.10b depicts the path integrated differential attenuation.

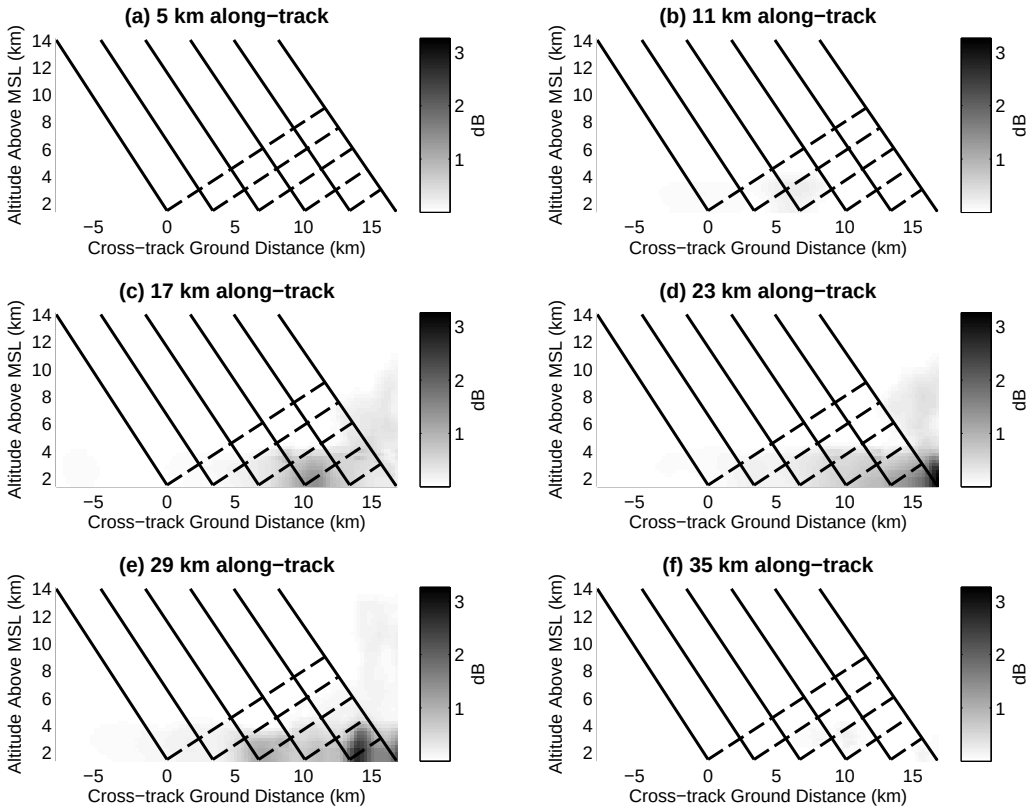

Figure 5.9: Six vertical cross-track slices of specific attenuation $A_{h,X}$ similar to Fig. 5.8 (see also 5.7). The slices are at (a) 5 km (b) 11 km (c) 17 km (d) 23 km (e) 29 km and (f) 35 km along-track, offset from the ground radar by 15 km.

In the absence of surface reflections, the volumetric radar cross-section η within the SAR swath is shown in Fig. 5.11. Without attenuation, the integrated horizontal RCS η_h in Fig. 5.11a is relatively high. By applying (5.8), much of the RCS above -10 dB is attenuated as seen in Fig. 5.11b. Toward the outer edge of the storm, the result is negligible even though the signal passes through regions around 30 dBZ. This is consistent with real observations [Danklmayer et al. (2009); Fritz and Chandrasekar (2010b)]. Fig. 5.11c depicts the difference between the attenuated η_h and η_v to show the differential reflectivity change, where the near-range area that is below zero corresponds to the similar differential attenuation in Fig. 5.10b.

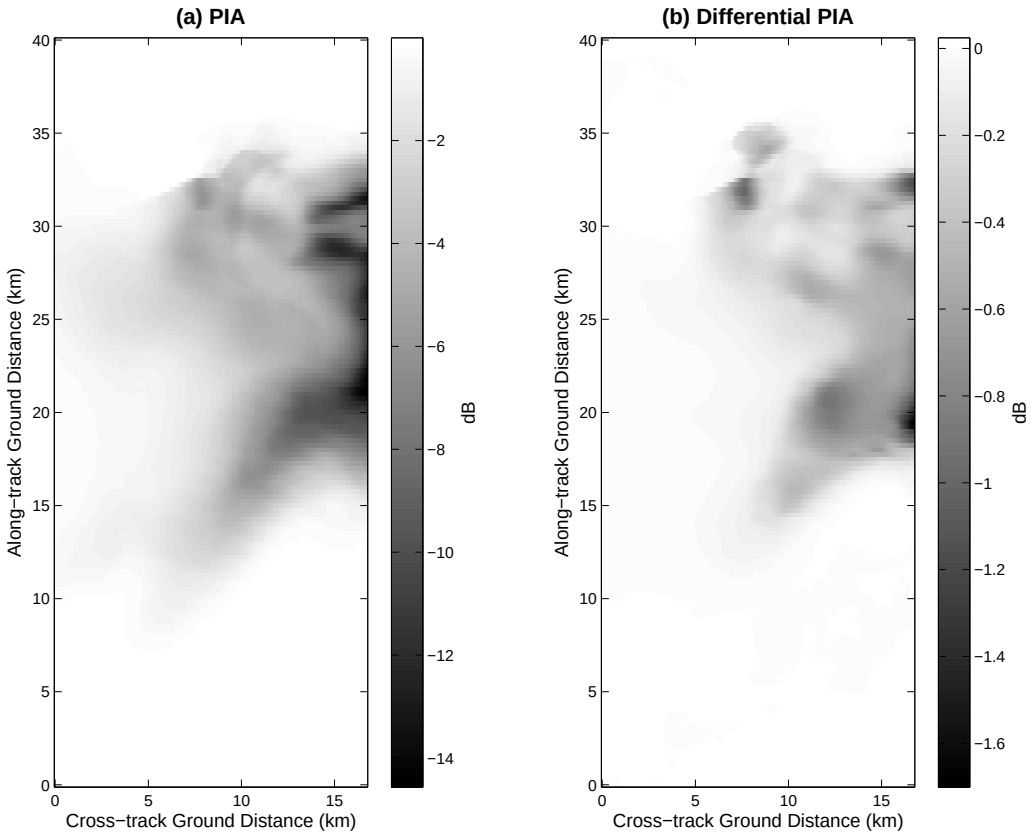

Figure 5.10: (a) The simulated total slant path integrated attenuation (PIA) from a SAR swath indicated in Fig. 5.7 (b) The differential PIA for the same SAR swath.

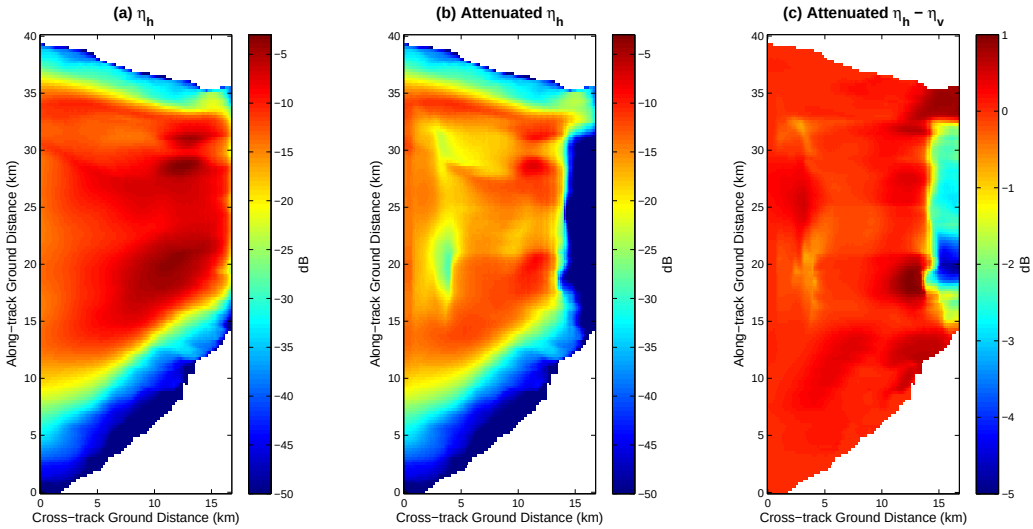

Figure 5.11: (a) The simulated volumetric radar cross section η_h from SAR swath indicated in Fig. 5.7. (b) The attenuated η_h for the same swath. (c) The attenuated $\eta_h - \eta_v$.

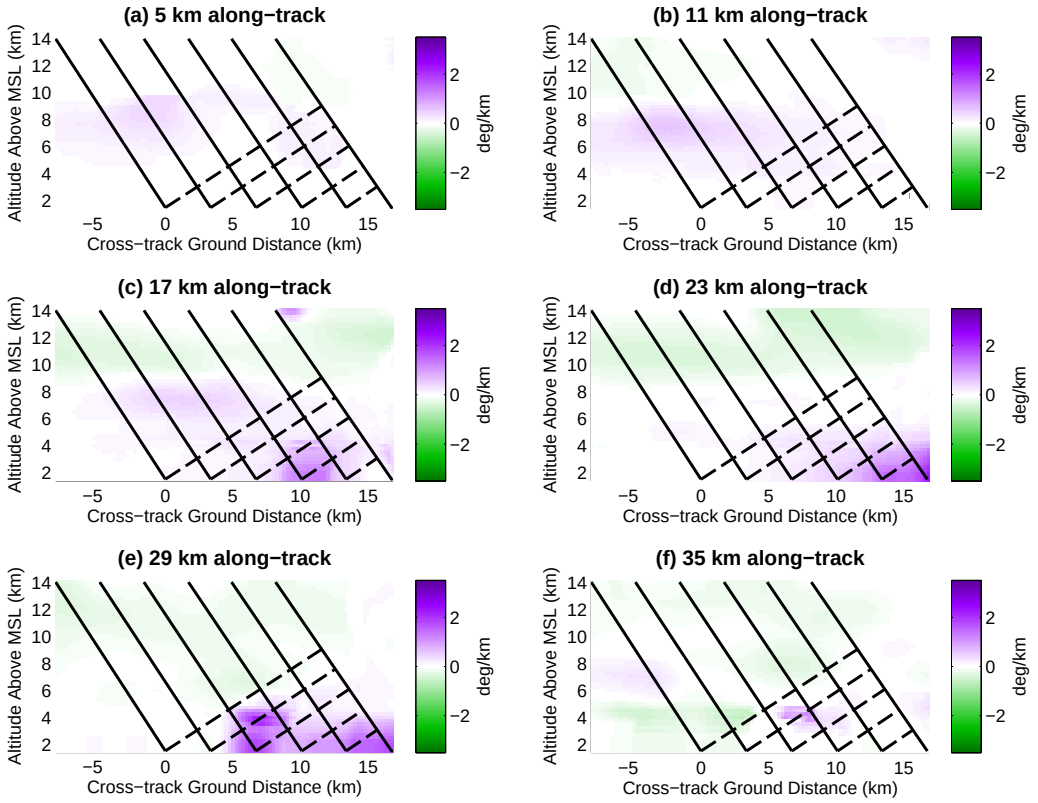

Figure 5.12: Six vertical cross-track slices of specific differential phase $K_{dp,X}$ (see 5.7). The slices are at (a) 5 km (b) 11 km (c) 17 km (d) 23 km (e) 29 km and (f) 35 km along-track, offset from the ground radar by 15 km.

Similar to attenuation, six vertical slices of specific differential phase are shown in Fig. 5.12. Some regions with high K_{dp} will not result in high Φ_{dp} on the surface due to negative K_{dp} above it and/or small values along the planar wavefront. The projection onto the SAR slant range plane is discussed below in Section 5.4.1.3. Differential phase, however, is not affected by attenuation like signal strength [Bringi and Chandrasekar (2001)].

5.4.1.2 Convective Supercell Storm

In Section 5.4.1.1 the simulation of SAR observations demonstrated the impact from light precipitation with part of the hypothetical SAR beam within the convective region to show backscatter and more significant attenuation. A more rigorous test of the simulation and modeling is needed to cover the hail shaft of the supercell. The neural network based models are more predominant in this area in order to transform the real S-band data to X-band slant angle observations given substantial Mie scattering effects caused by the large

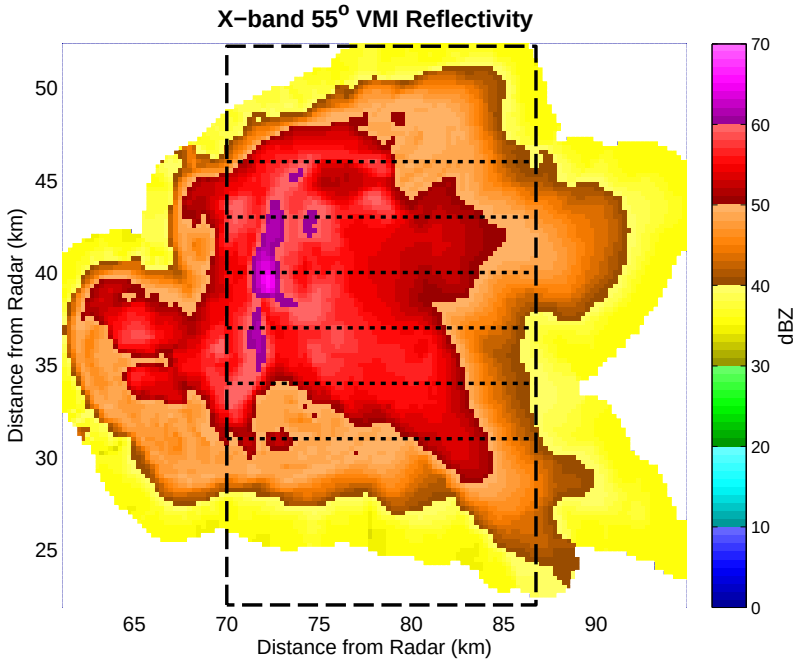

Figure 5.13: Vertical Maximum Intensity (VMI) of simulated X-band reflectivity in the convective region of the 000629 storm with the location of the hypothetical SAR swath indicated by the dashed lines and vertical cross-track slice locations by the dotted lines.

hailstones. Fig. 5.13 depicts the VMI of the X-band version in this convective region with a different hypothetical SAR swath indicated. Vertical slices of reflectivity at the indicated cross-track locations are shown in Fig. 5.14 providing a look at the transformation result. Along some of the boundaries of volumes classified as hail or rain plus hail with pure rain or graupel, a fairly sharp gradient exists. Again, if the estimation showing a large median diameter is correct, the result in Fig. 5.14 is expected; however, it is also possible the hydrometeor classification boundary is not perfect. An improvement may be to allow for a transition zone from graupel to hail. Despite this feature, the final result still exhibits reasonable values for attenuation and backscatter and is a good starting point for further research.

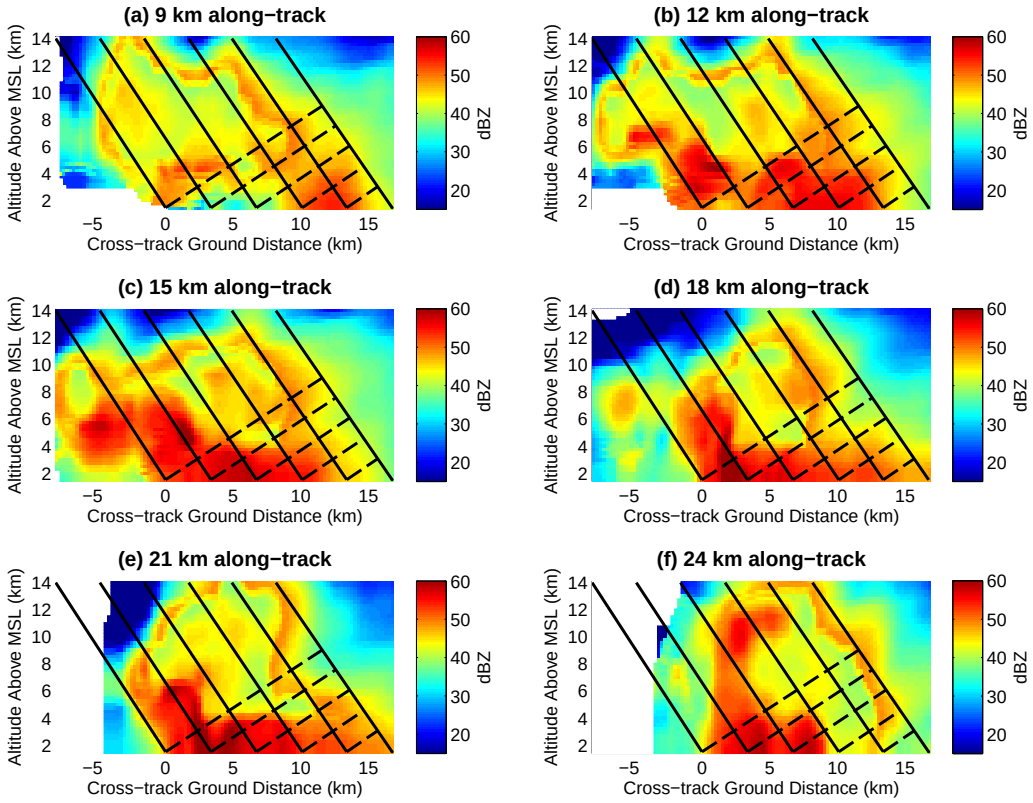

Figure 5.14: Six vertical cross-track slices of horizontal reflectivity $Z_{h,X}$ (see 5.13). The solid lines indicate several slant paths including the ideal beam boundaries and the dashed lines indicate transverse (constant range) values. The slices are at (a) 9 km (b) 12 km (c) 15 km (d) 18 km (e) 21 km and (f) 24 km along-track, offset from the ground radar by 22 km.

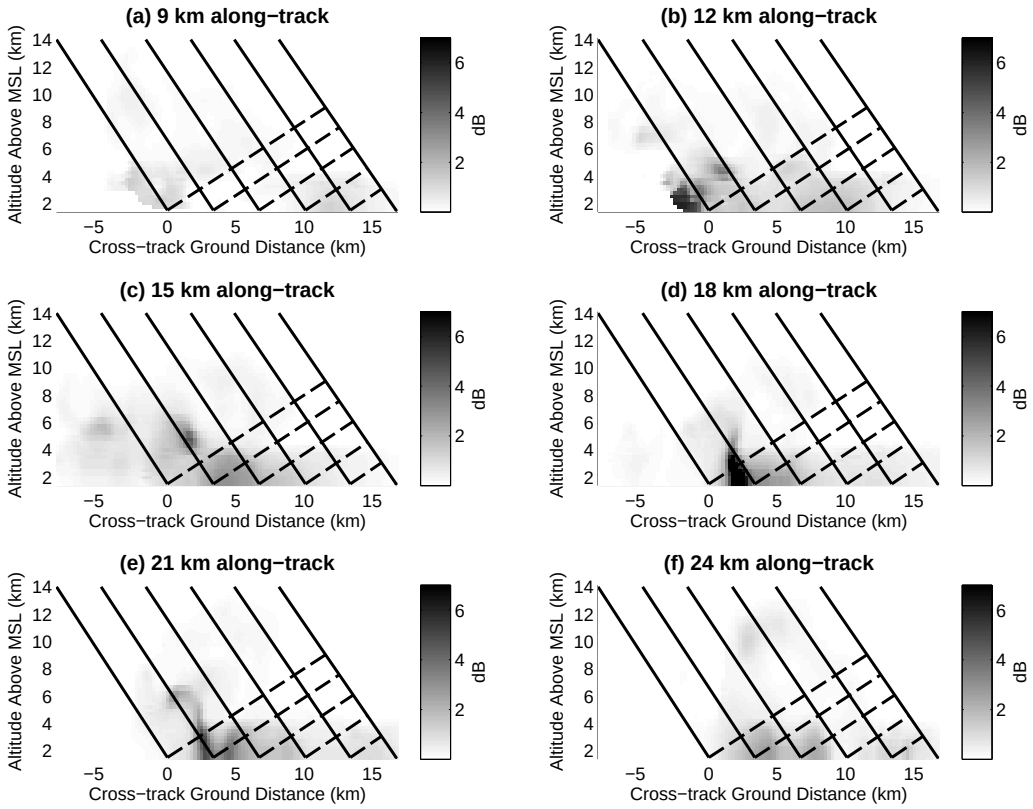

Figure 5.15: Six vertical cross-track slices of horizontal specific attenuation $A_{h,X}$ (see 5.13) with beam lines. The slices are at (a) 9 km (b) 12 km (c) 15 km (d) 18 km (e) 21 km and (f) 24 km along-track, offset from the ground radar by 22 km.

Results of the transformation to X-band and the conversion to two-dimensional SAR observations for attenuation, volumetric RCS and specific differential phase are displayed in Figs. 5.15 through 5.18. As expected, the attenuation through the storm core shown in Figs. 5.15 and 5.16a is more severe than in the propagation through the stratiform region that only begins to cover the convective core. The differential attenuation seen in Fig. 5.16b is also almost twice that of Fig. 5.10b, which is not surprising given the concentration of $Z_{dr} < 0$ seen in Fig. 4.40. Radar backscatter is also expected to be high, as Fig. 5.17a shows for horizontal polarization, with the attenuated version in Fig. 5.17b from (5.8). As the radar wave propagates through much of the storm cell, almost every region exhibits attenuation. Fig. 5.17c similarly depicts the difference between the attenuated η_h and η_v to show the differential reflectivity change. Transmission of the wave through the storm accumulates differential phase as depicted in Figs. 5.18.

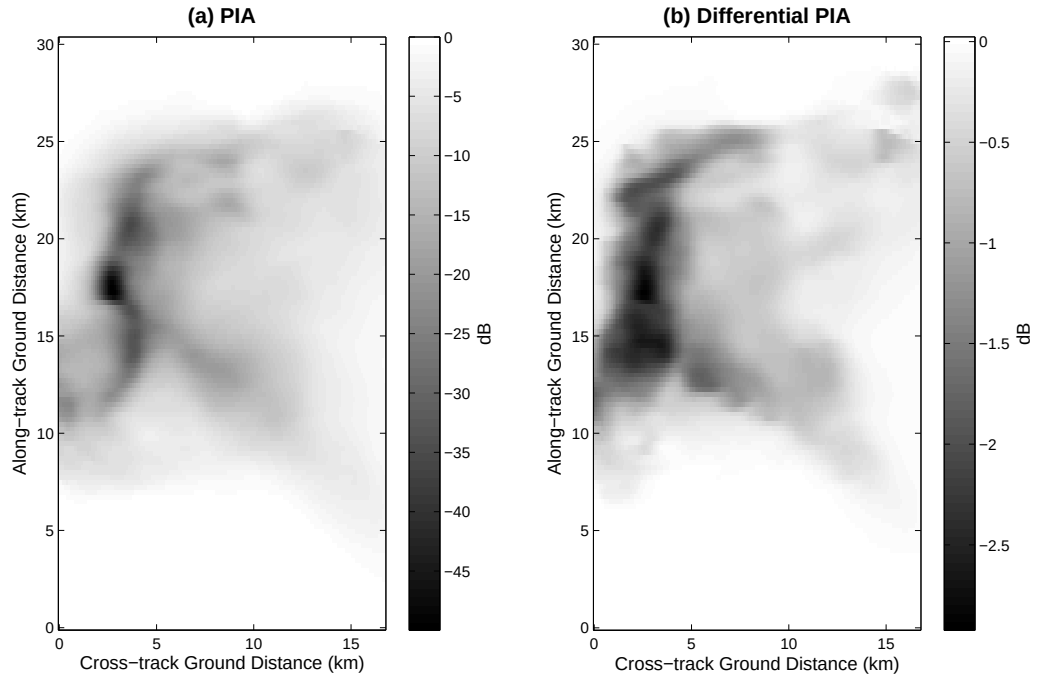

Figure 5.16: (a) The simulated total slant PIA from an X-SAR with swath indicated in Fig. 5.13 (b). The differential PIA for the same SAR swath.

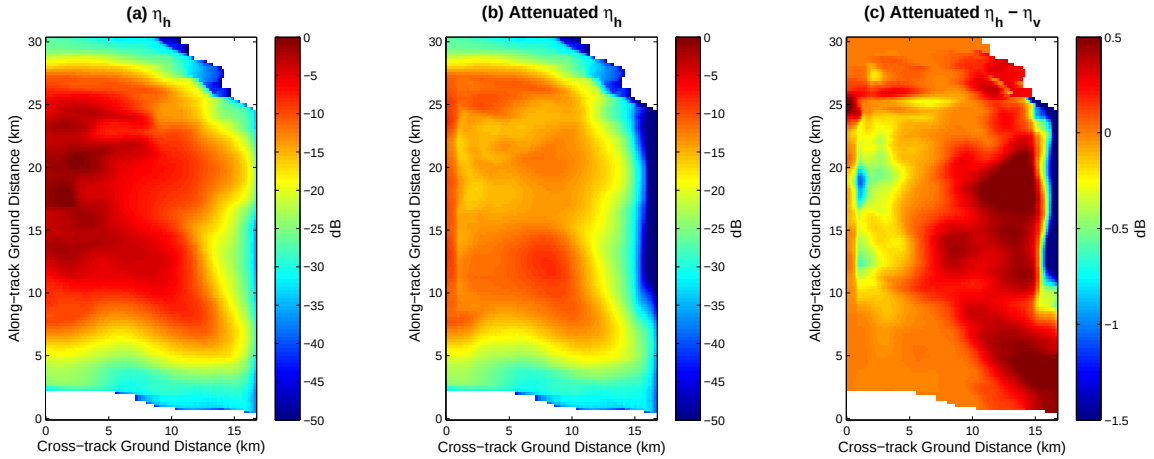

Figure 5.17: (a) The simulated volumetric radar cross section η_h from SAR with swath indicated in Fig. 5.13. (b) The attenuated η_h for the same swath. (c) The attenuated $\eta_h - \eta_v$.

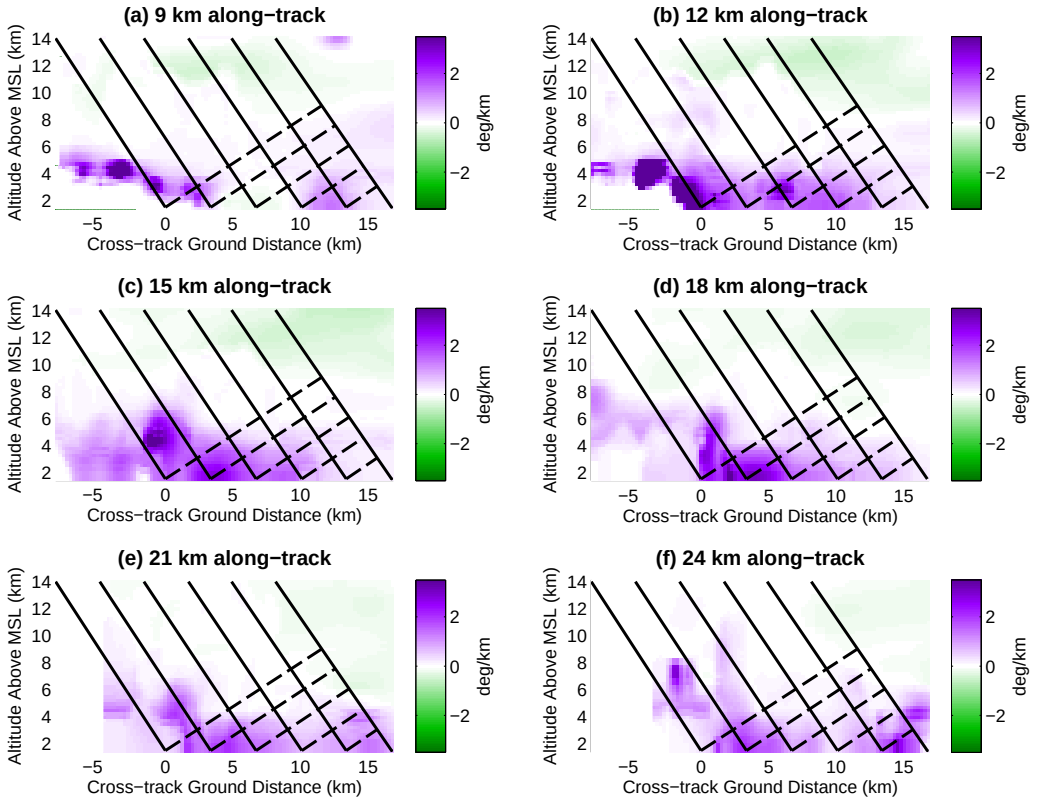

Figure 5.18: Six vertical cross-track slices of specific differential phase $K_{dp,X}$ (see 5.13). The slices are at (a) 9 km (b) 12 km (c) 15 km (d) 18 km (e) 21 km and (f) 24 km along-track, offset from the ground radar by 22 km.

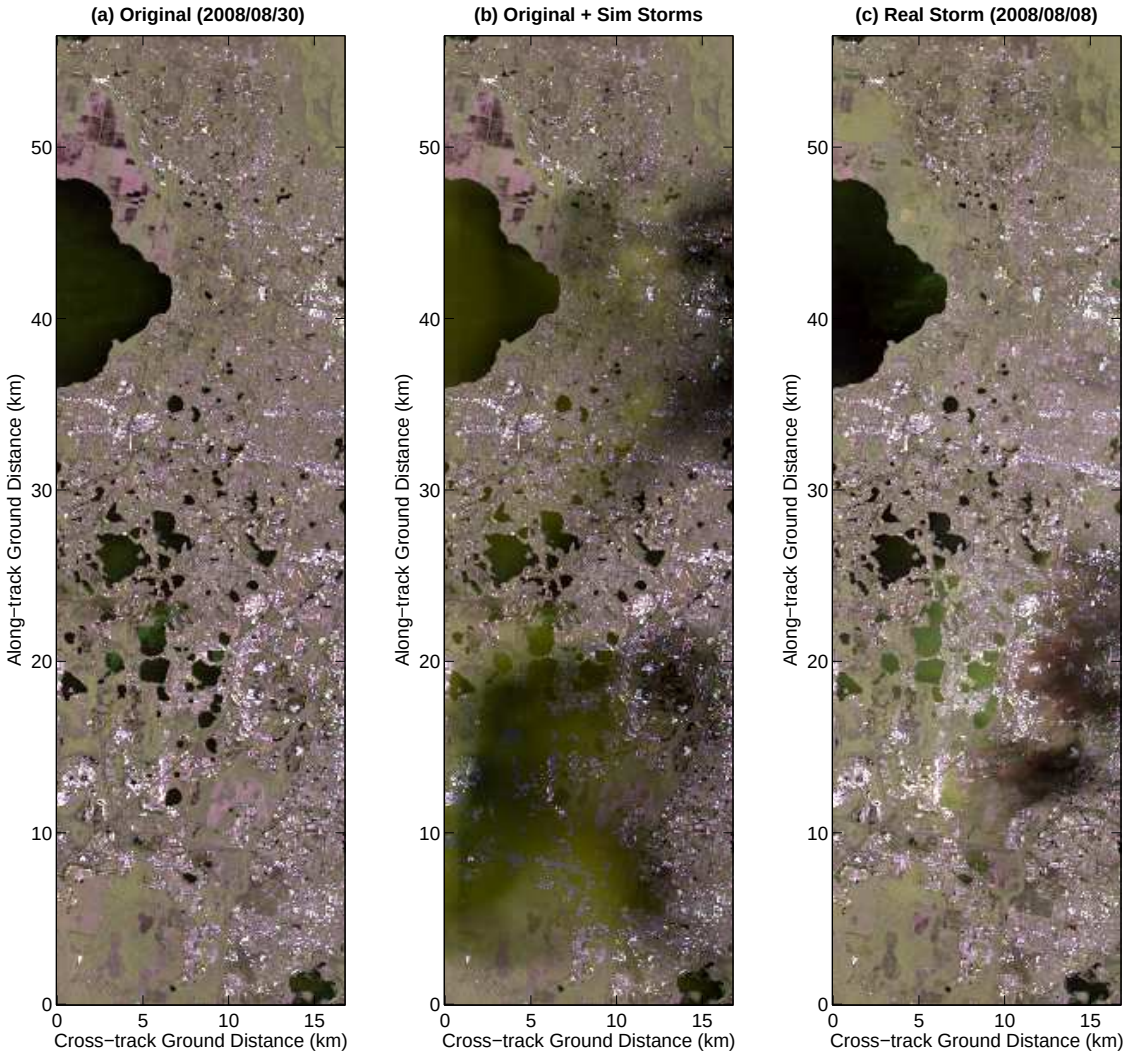

Figure 5.19: (a) Original TerraSAR-X image over Orlando, Florida 30 August 2008. The image is an RGB composite where Red $= |S_{hh}|^2$, Green $= |S_{vv}|^2$ and Blue $= 2^{-.5}|S_{hh} - S_{vv}|^2$ from the coherency matrix in (2.25). (b) The same data as (a) with the simulated storm shown in Fig. 5.7 added to the top half and the storm in Fig. 5.13 added to the bottom half. The greenish color indicates higher VV backscatter from the vertically oriented hail. (c) A previous TSX swath on 8 August 2008 with a real convective storm (squall line) for comparison. Here, a reddish color is noticeable on the near range side, indicating backscatter from oblate hydrometeors. Raindrops and wind perturbing water surfaces produce a higher VV backscatter that shows up as green.

5.4.1.3 Simulated SAR Observations

The final stage of the simulation process is to incorporate the simulated X-SAR observations detailed in Sections 5.4.1.1 and 5.4.1.2 with real X-SAR data without precipitation. TerraSAR-X data collected on 30 August 2008 over Orlando, FL is used for this purpose.

Fig. 5.19 displays the final result of (5.9) - (5.12) with the original image on the left and the simulated storm added to Fig. 5.19b. Matching the 100 m resolution of the weather radar data was achieved by a 60×40 boxcar style multilooking from the original TSX ground spacing of approximately 1.6 m in range (cross-track) and 2.4 m azimuth (along-track) followed by linear interpolation of the weather data at the reduced TSX resolution. While the correlation coefficient was modified via (5.11) and differential phase via (5.12) the volumetric backscatter appears as a yellowish-green color indicating slightly stronger backscatter in the vertical polarization (VV) channel. This is to be expected as the previous analysis and the original S-band data suggest hail stones with a vertically oriented tendency. Surface change due to precipitation, such as roughening of water bodies, however, has not been included. Around 23 km along-track and 0 to 6 km cross-track in Fig. 5.19a is a minor real storm signature where the water shows up as green due to raindrops impinging the surface [Contreras et al. (2003)]. Figure 5.19c depicts a real convective storm (squall line) over the same region 22 days prior, which allows for qualitative comparisons. Significant VV scattering is visible on the lakes, while the near range side of the attenuation regions is reddish (HH). Oblate hydrometeors will exhibit increased HH backscatter, so this is expected. In the simulated storm, it is possible that the hail backscatter overwhelms that of the oblate raindrops.

Figs. 5.20 through 5.21 provide more insight into the simulation result. While Fig. 5.19 provides information about the relationship between channels, it is only qualitative. The span image created by summing the diagonal elements of the covariance matrix and converted to dB as displayed in Fig. 5.20a is more quantitative along with the span ratio in Fig. 5.20b. The ratio indicates exactly how much the overall power changes due to the simulated storm, with the lower limit clipped at -25 dB (below the actual noise floor of the SAR data which is $\sim$ -20 dB). Although some backscatter is visible in Fig. 5.20a, near 7 km along-track and 4-9 km cross-track for example, the power change did not increase above the original observation except over water bodies. A decrease in the co-polar power ratio Z_{dr} is also evident as shown in Fig. 5.20c. The shift is toward the Z_{dr} of the precipitation from the that of the surface, which in this case is higher. Histograms of the co-polar

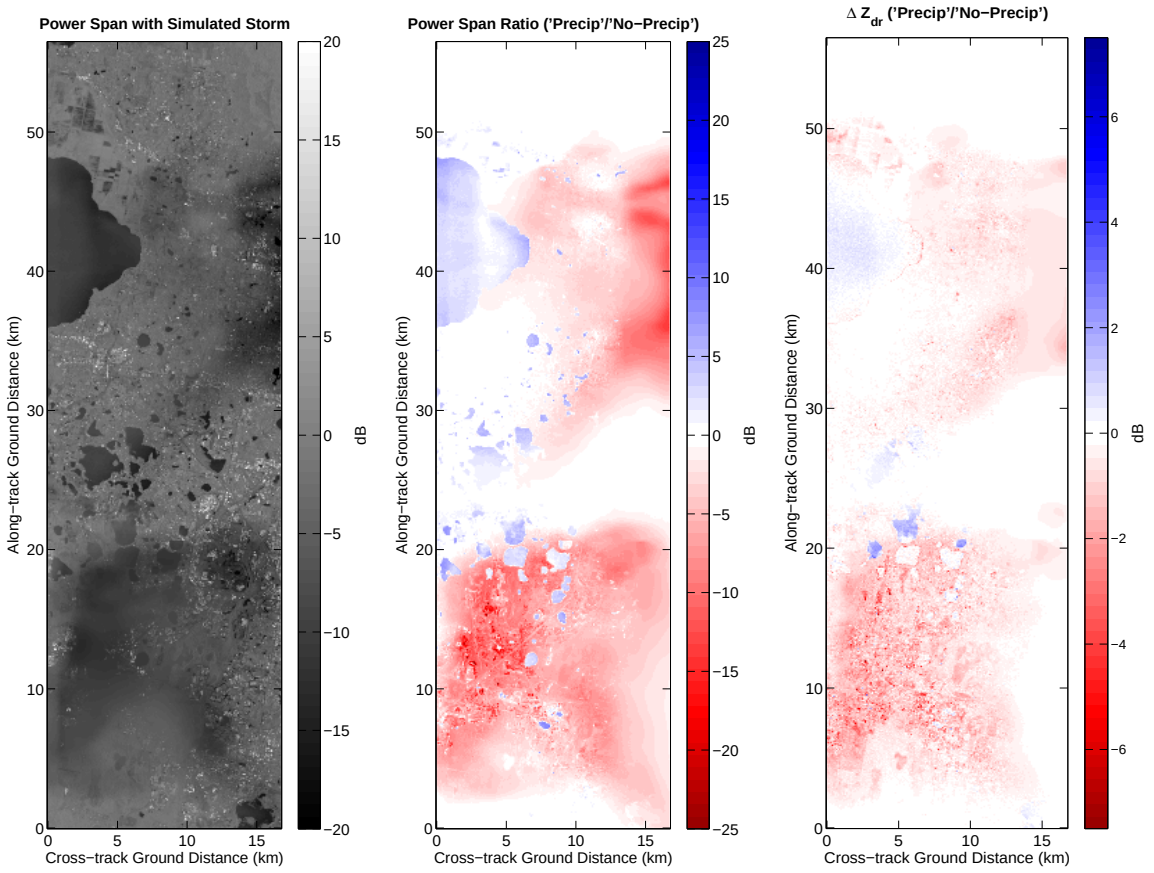

Figure 5.20: (a) The span $(10\log_{10}\left(|S_{hh}|^2+|S_{vv}|^2\right))$ image with the simulated storm. (b) The span ratio with the original data indicating power increase (blue) due to backscatter or decrease(red). Increased power is mostly over water bodies where the original power was low due to pseudo-specular reflection, but it is not necessarily visible in (a) or Fig. 5.19. (c) The ratio of the Z_{dr} with the simulated storm to the original Z_{dr}. In general, the simulated storm increases Z_{dr} by several dB which is expected due to the radar wave interaction with raindrops as described by (5.4).

correlation coefficient are shown in Fig. 5.21 and show a distinct increase in correlation. This is expected because scattering from rain and other hydrometeors is highly correlated as seen in Fig. 6.19b. All of these results are reasonable when compared to analysis of real storms in TSX scenes detailed in Chapter 6 [Fritz and Chandrasekar (2010b)]. Specifically, see Figs. 6.17-6.20

Fig. 5.22 depicts the simulated differential phase shift from the storm, the surface backscatter differential phase and the combination of the two. The resulting projection of Φ_{dp} from applying (5.14) is shown in Fig. 5.22a. This projection appears as expected given

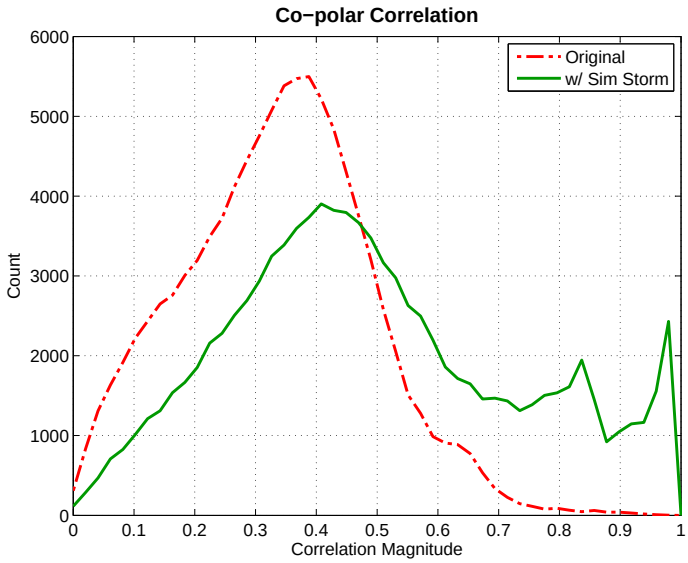

Figure 5.21: Histograms of the co-polar correlation coefficient ρ_{co} for the original SAR data (red) and the data with simulated storms (green). A distinct increase in correlation is present, which is to be expected as precipitation generally has correlation magnitudes above 0.9.

the K_{dp} slices in Fig. 5.12 for the top half and Fig. 5.18 for the bottom half. Considering the path length and wavefronts through the upper regions with negative K_{dp}, especially for the hail core, the overall Φ_{dp} is reduced. Along the near range edge beyond 35 km along-track, however, a positive Φ_{dp} due to prolate ice crystals at the upper layers of the storm is shown. Fig. 5.22c depicts the copolar phase change ϕ_{co} of the surface backscatter and Fig. 5.22b is the result of applying (5.12) to the data in the other two panels. Given the $\pm 180°$range when combined with the surface differential phase, the additional propagation effect is subtle, although some pixels that are close to 180°will wrap around to $-180°$. This simulation, of course, does not account for surface changes in ϕ_{co} that may occur during a real storm, which will be discussed in 6.2.5.

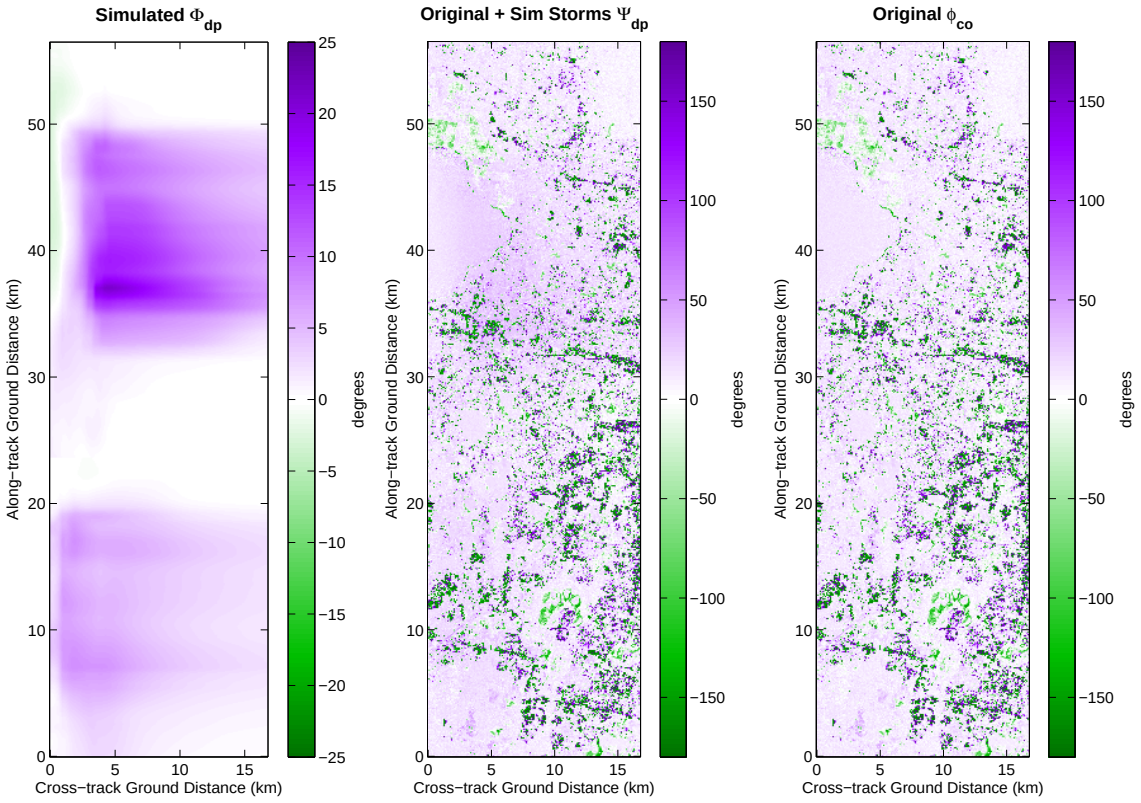

Figure 5.22: (a) Simulated propagation differential phase Φ_{dp} from the 000629 storm (both renditions). (b) The original surface backscatter copolar phase shift plus the simulated propagation shift, $\Psi_{dp} = \Phi_{dp} + \phi_{co}$. Some values wrap as the sum exceeds $\pm 180°$. (c) The original SAR copolar phase difference ϕ_{co}.

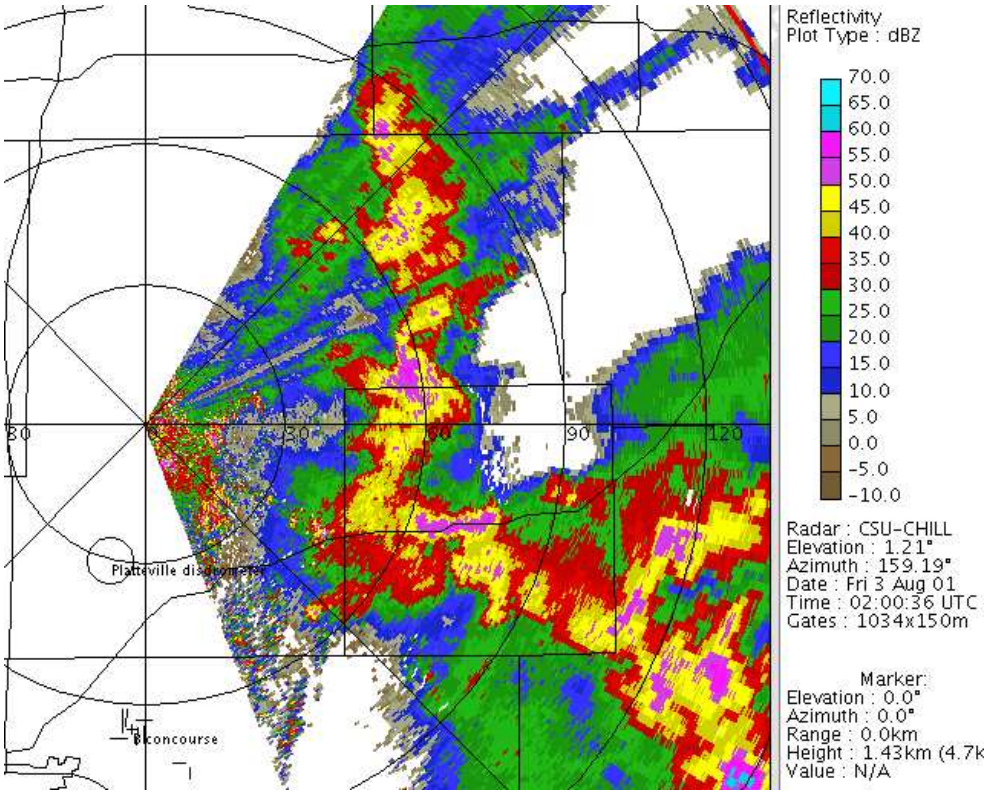

Figure 5.23: A single scan of reflectivity at 1.2° elevation from CSU-CHILL on 010802. The storm cell of interest is around 60 km (each range ring is 30 km).

5.4.2 2001 Squall Line

In order to demonstrate the effectiveness of the simulation based model for a variety of meteorological conditions, another storm was selected. On August 2, 2001 a convective squall line passed through the domain of the CSU-CHILL radar in Greeley, Colorado at an altitude of approximately 1700 m MSL. A scan of the reflectivity data is shown in Fig. 5.23 at an elevation angle of about 1.2°. The portion of the storm aligned with north around 60 km due east of the radar was selected to simulate spaceborne data. Fig. 5.24 depicts horizontal and vertical slices of reflectivity over a slightly smaller sub-region, cutting through a hail cell at 6.8 km MSL and 58 km east of CSU-CHILL. The hail region can be seen in the slices of hydrometeor classification, at the same locations, in Fig. 5.25. As this figure indicates, almost all hail is melted by the time they reach the ground; therefore, it is not likely that the hailstones are large. A distribution of relatively small hail was confirmed by the RBFN estimation of D_0 shown in Fig. 4.43. In addition, there is no indication of

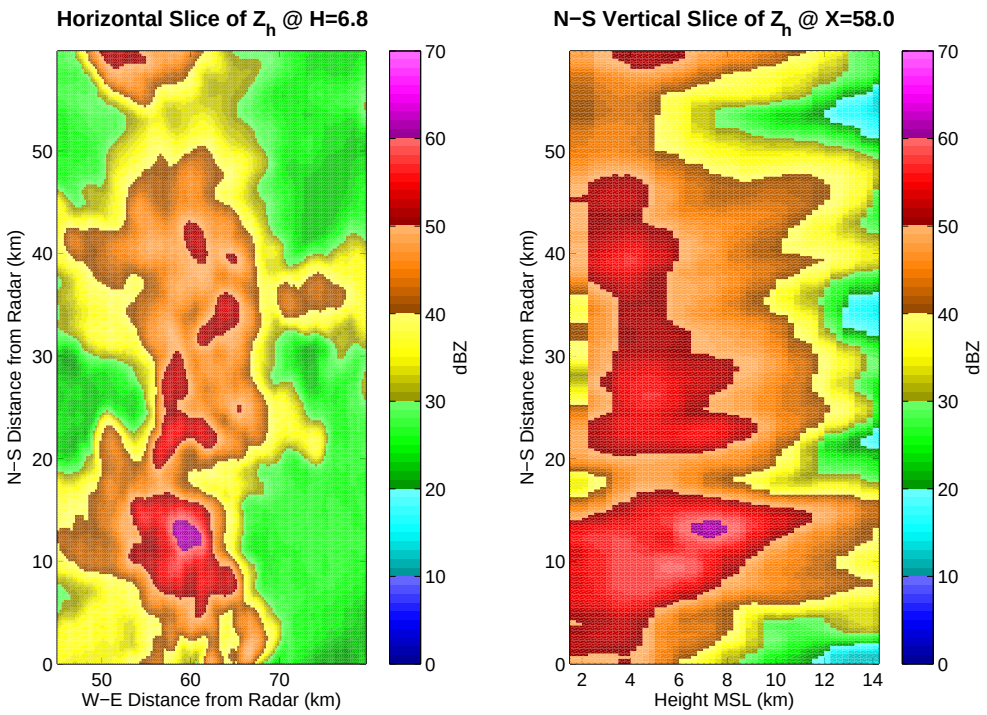

Figure 5.24: Slices of reflectivity observed by CSU-CHILL during the 010802 storm, trimmed to the region of interest. (a) A horizontal slice at 6.8 km MSL. (b) A vertical slice at 58 km east of the radar. Some gridding effects are visible in this slice.

a flat melting layer containing wet snow, adding more evidence of this being a convective storm. The melting layer estimated from data is shown in Fig. 5.26. Strong updrafts, which lead to the hail shafts, effectively push the melting layer height upwards from the average of around 4.7 km MSL (3 km above ground level). The differential reflectivity shown in Fig. 5.27 at 4 altitude levels was used to detect the updrafts at locations where it is positive even at 6.5 km MSL.

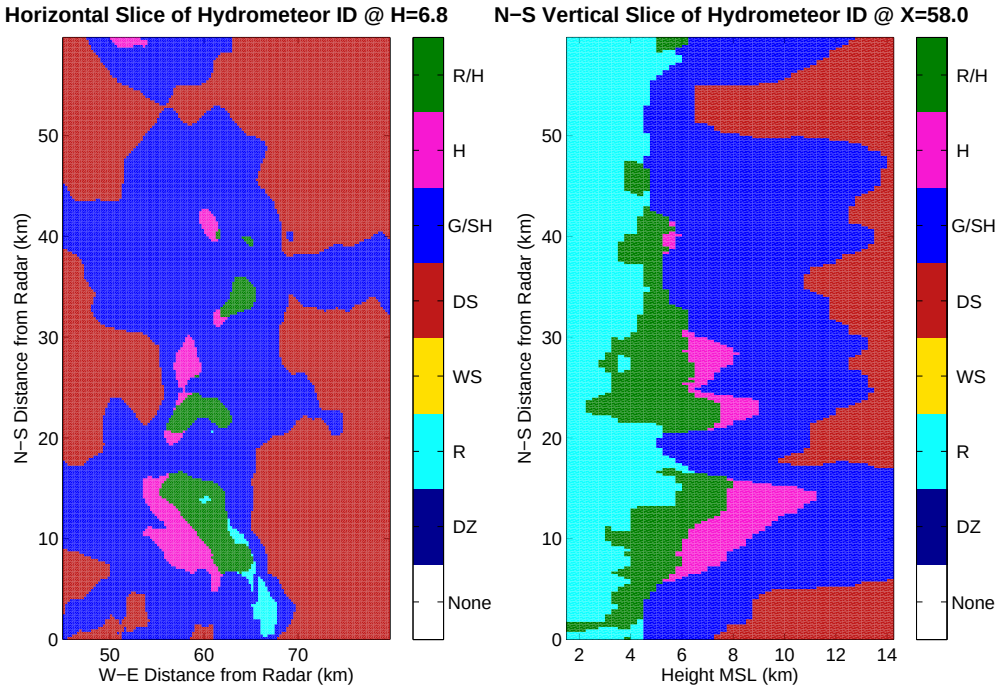

Figure 5.25: Slices of hydrometeor classification results at the same locations as the reflectivity slices in Fig. 5.3. (a) A horizontal slice at 6.8 km MSL. (b) A vertical slice at 58 km east of the radar. Note that almost all rain plus hail becomes all rain at the ground level.

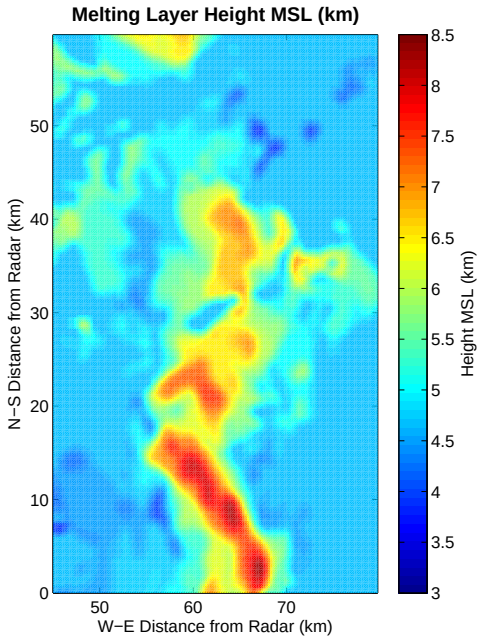

Figure 5.26: The melting layer height in km above MSL estimated during hydrometeor classification. The ground level is approximately 1.7 km. Strong updrafts indicated by a very high melting layer estimate indicate super-cooled raindrops that become hailstone embryos.

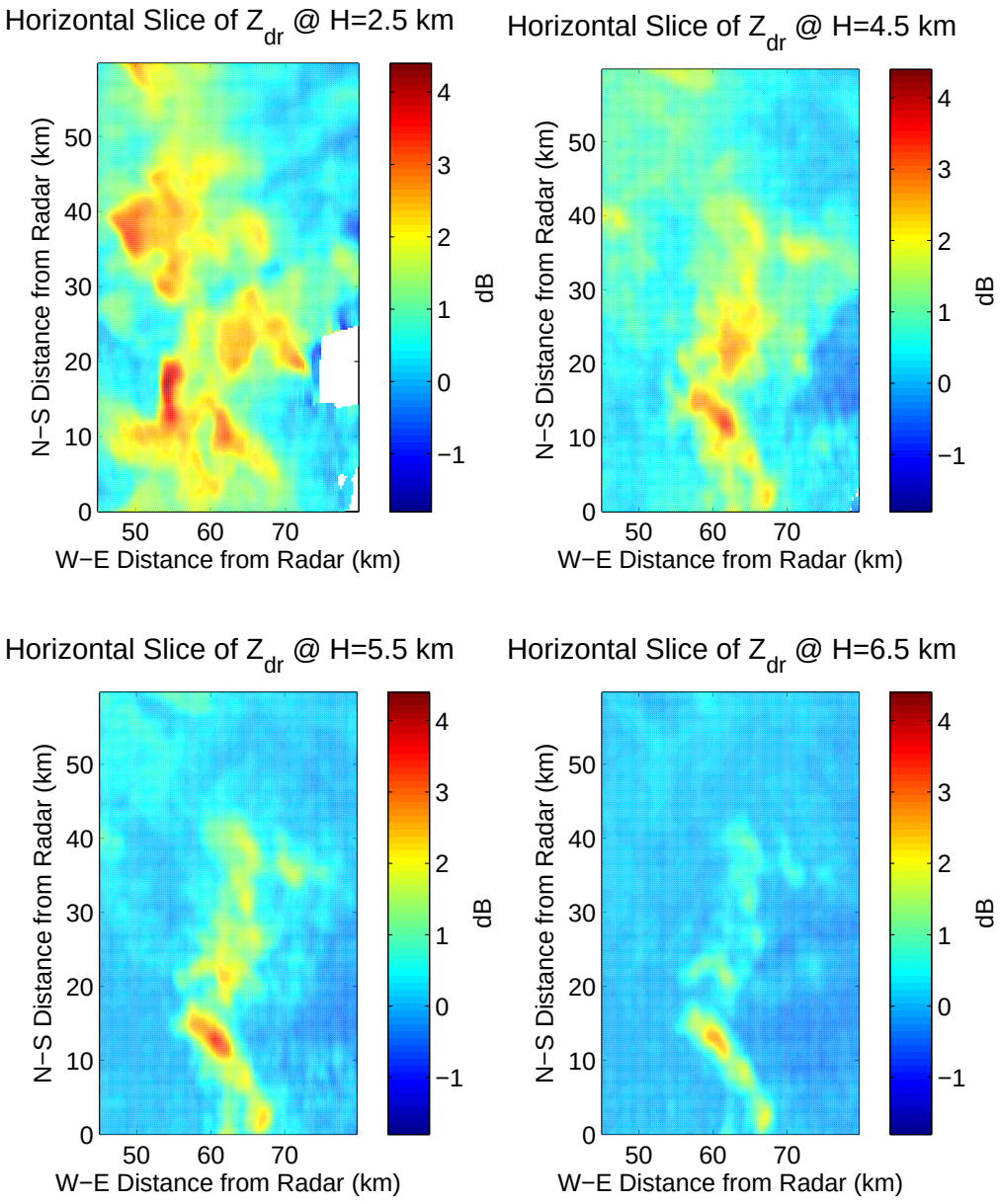

Figure 5.27: Horizontal slices of differential reflectivity observed by CSU-CHILL during the 000629 storm at (a) 2.5 km (b) 4.5 km (c) 5.5 km and (d) 6.5 km MSL. Positive Z_{dr} at higher altitudes can indicate updrafts where larger raindrops are blown above the actual freezing level to eventually become hailstones.

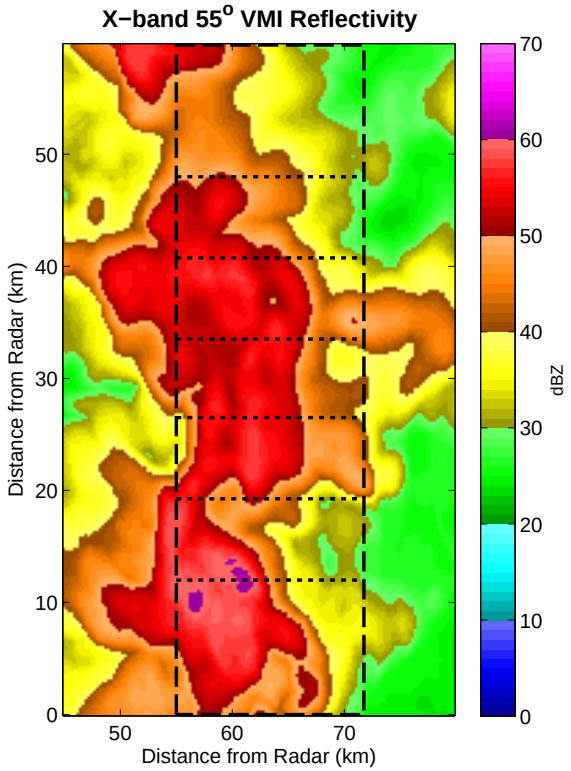

Figure 5.28: Vertical Maximum Intensity (VMI) of simulated X-band reflectivity from the 000629 storm (rotated 180°) with the location of the hypothetical SAR swath indicated by the dashed lines and vertical cross-track slice locations by the dotted lines.

After all the storm data are interpolated on the georeferenced Cartesian grid and hydrometeor classification is determined, the data can be transformed from the horizontal S-band to X-band observations at a 35° incidence angle. A hypothetical SAR image swath was determined and is drawn over an image of vertical maximum intensity (VMI) reflectivity displayed in Fig. 5.28 as the long dashed lines. The short dashed horizontal lines in Fig. 5.28 indicate locations where vertical slices of transformed data are displayed in the figures that follow. The bottom of the image is due east of CSU-CHILL. In Fig. 5.29, the X-band reflectivity provides an indication of the volumetric backscatter to the SAR, in lieu of attenuation. At 12 km, the hail only region is most clearly seen because the reflectivity drops due to Mie scattering. The next 4 slices (Fig. 5.29b-e) indicate the presence of reflectivity levels above 50 dBZ. The corresponding specific attenuation at these same vertical slice locations is shown in Fig. 5.30. As expected based on the Z_h plots, the highest attenuation occurs at 12 km (Fig. 5.30a), although the remaining slices still indicate A_h above 1 dB km^{-1}.

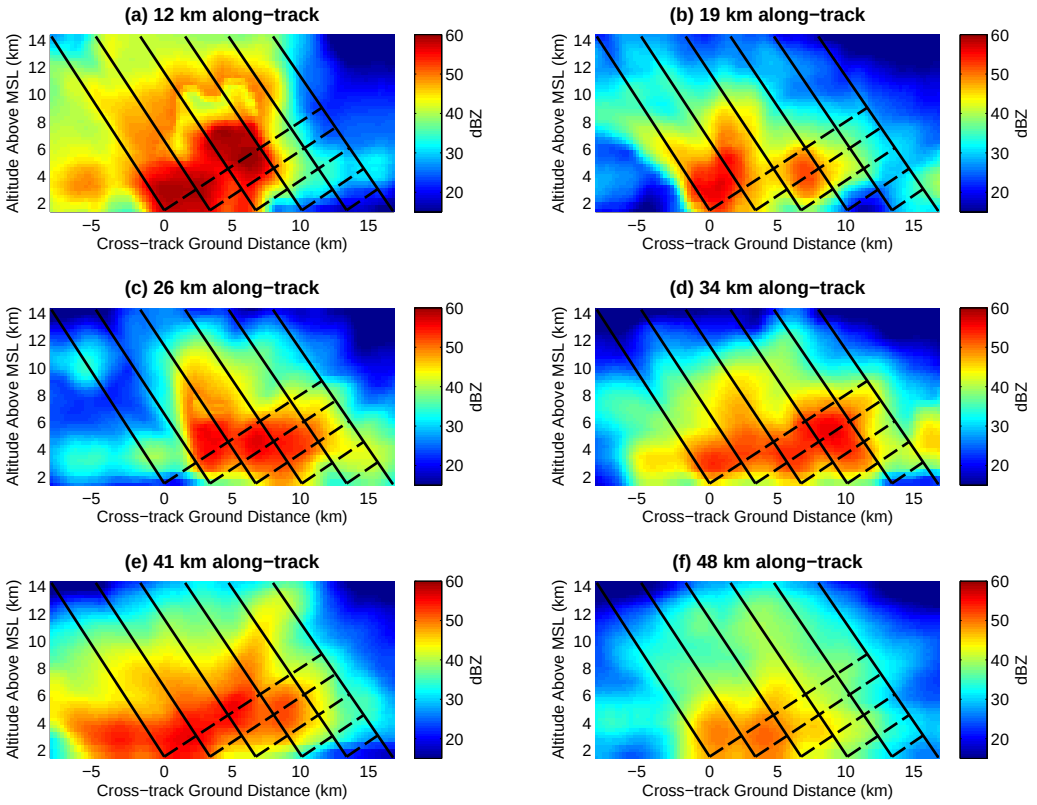

Figure 5.29: Six vertical cross-track slices of horizontal reflectivity $Z_{h,X}$ (see 5.28). The solid lines indicate several slant paths including the ideal beam boundaries and the dashed lines indicate transverse (constant range) values assuming ideal plane waves. The slices are at (a) 12 km (b) 19 km (c) 26 km (d) 34 km (e) 41 km and (f) 48 km along-track in both the SAR and ground radar reference frame.

Similarly, vertical slices of specific differential phase are plotted in Fig. 5.31. As expected, K_{dp} tends to be high in areas where Z_h and A_h are also high. Almost the entire volume responds with positive values indicating horizontally oriented oblate spheroids including the hail.

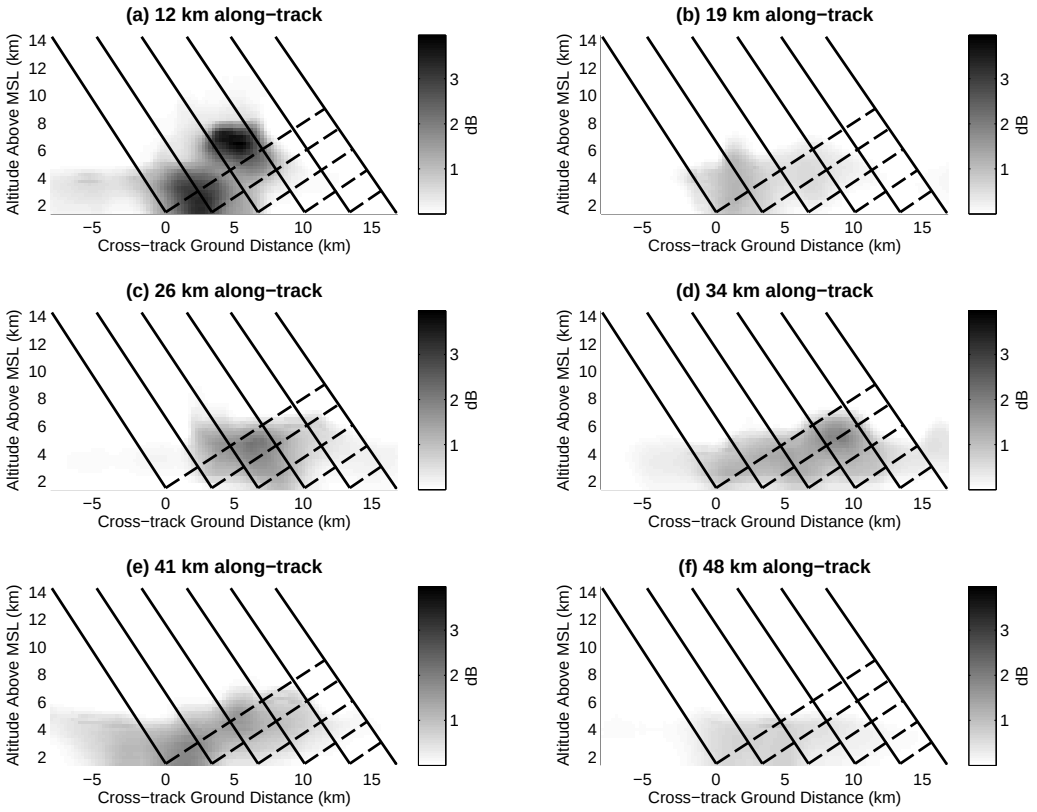

Figure 5.30: Six vertical cross-track slices of specific attenuation $A_{h,X}$ similar to Fig. 5.29 (see also 5.28). The slices are at (a) 12 km (b) 19 km (c) 26 km (d) 34 km (e) 41 km and (f) 48 km along-track.

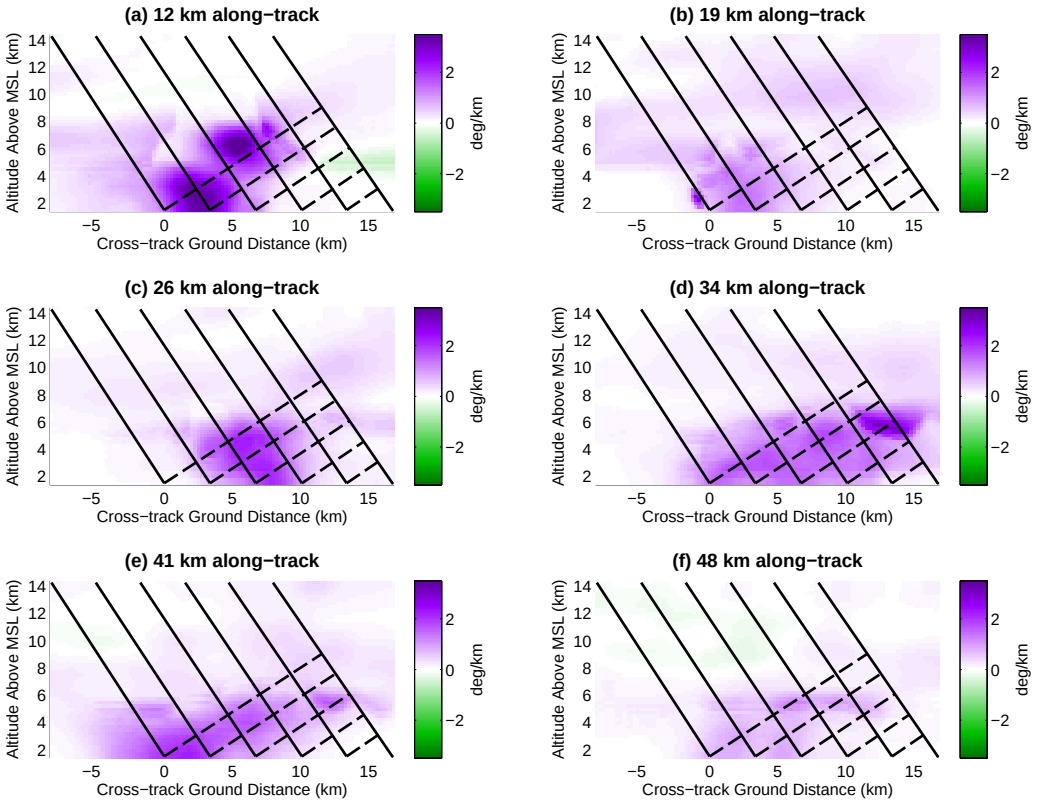

Figure 5.31: Six vertical cross-track slices of specific differential phase $K_{dp,X}$ (see 5.28). The slices are at (a) 12 km (b) 19 km (c) 26 km (d) 34 km (e) 41 km and (f) 48 km along-track.

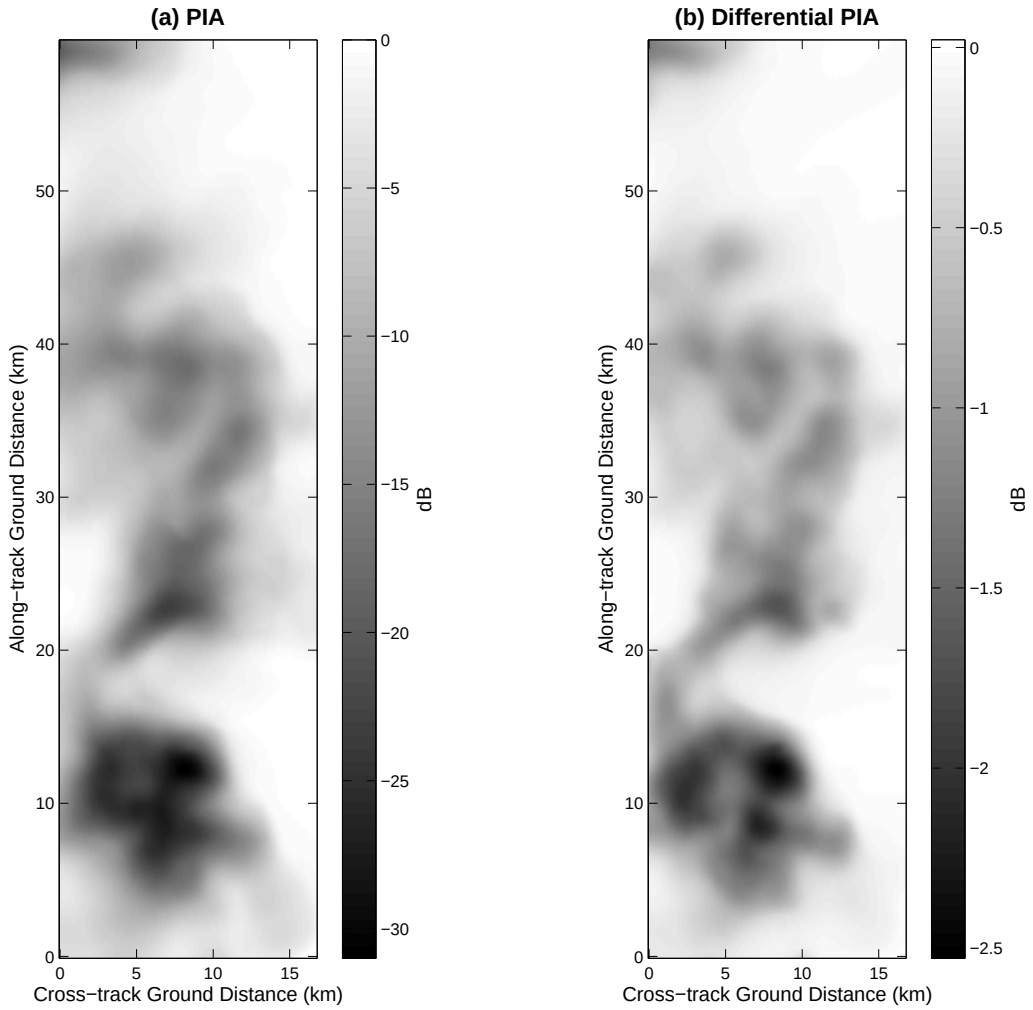

Figure 5.32: (a) The simulated total slant path integrated attenuation (PIA) from a SAR swath indicated in Fig. 5.28 (b) The differential PIA for the same SAR swath.

Given a glimpse of what the radar beam propagates through, the full projection onto the ground can be calculated via the procedure outlined in Section 5.3.2. The full path integrated attenuation (PIA) is depicted in Fig. 5.32a along with the corresponding differential PIA. Around the 12 km along-track slice seen in previous figures, the attenuation results in more than a -25 dB signal loss with horizontal polarization about 2 dB below that of vertical. Other parts of the storm are attenuated at a more moderate level of 10 to 15 dB, although this can still be severe for SAR, especially at the beam edges where the noise floor is higher. The horizontal volumetric backscatter without attenuation is plotted in Fig. 5.33a with the attenuated version in Fig. 5.33b. Similar to the supercell storm discussed in Section 5.4.1.2, peak backscatter is above 0 dB before attenuation is considered. Very

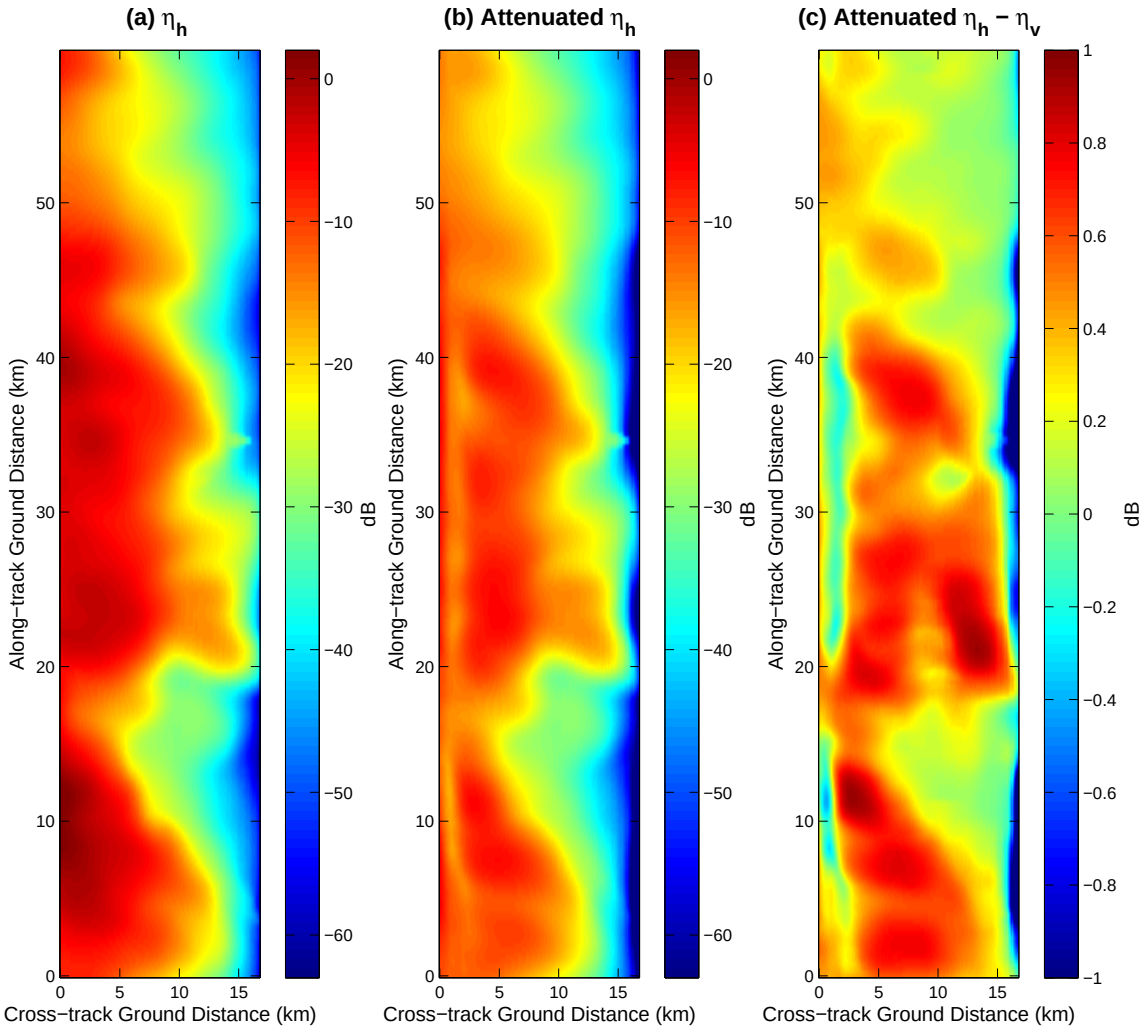

Figure 5.33: (a) The simulated volumetric radar cross section η_h from SAR swath indicated in Fig. 5.28. (b) The attenuated η_h for the same swath. (c) The attenuated $\eta_h - \eta_v$.

little backscatter occurs at the far range side considering that the volume of the storm along constant range lines diminishes to zero. Fig. 5.33c depicts the difference between the attenuated η_h and η_v to show the differential reflectivity change.

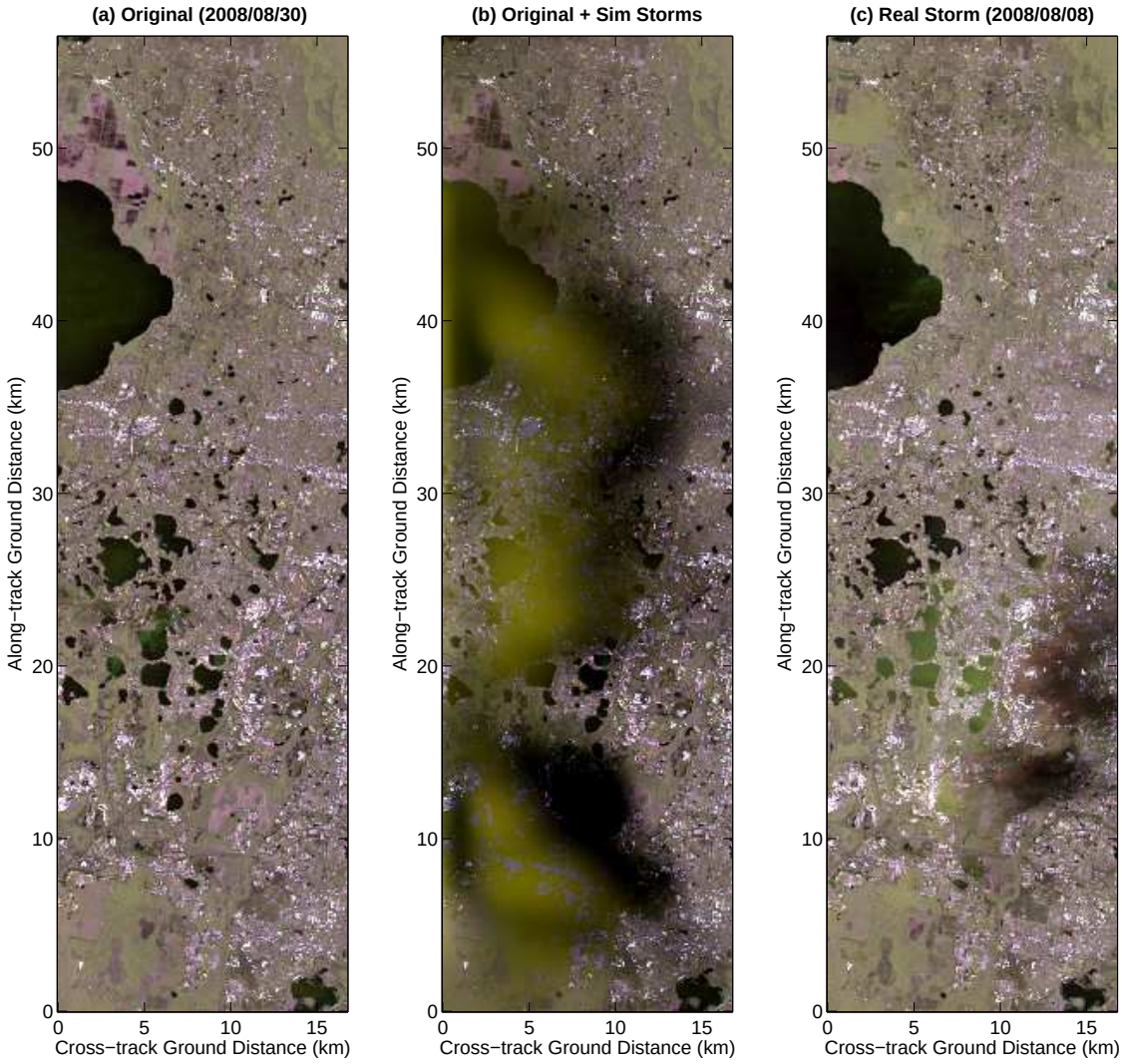

Figure 5.34: (a) Original TerraSAR-X image over Orlando, Florida 30 August 2008. The image is an RGB composite where Red $= |S_{hh}|^2$, Green $= |S_{vv}|^2$ and Blue $= 2^{-.5}|S_{hh} - S_{vv}|^2$ from the coherency matrix in (2.25). (b) The same data as (a) with the simulated storm shown in Fig. 5.28 added. The backscatter is seen on the near-range side. (c) A previous TSX swath on 8 August 2008 with a real convective storm (squall line) for comparison. Here, a reddish color is noticeable on the near range side, indicating backscatter from oblate hydrometeors. Raindrops and wind perturbing water surfaces produce a higher VV backscatter that shows up as green.

5.4.2.1 Simulated SAR Observations

The culmination of simulating high frequency SAR observations from the real ground-based S-band radar measurements of the 010802 squall line is displayed in Fig. 5.34b in between the original "no-rain" case (Fig. 5.34a) and a real squall line observation (Fig. 5.34c). Backscatter is very prominent in the simulated storm along the near-range side

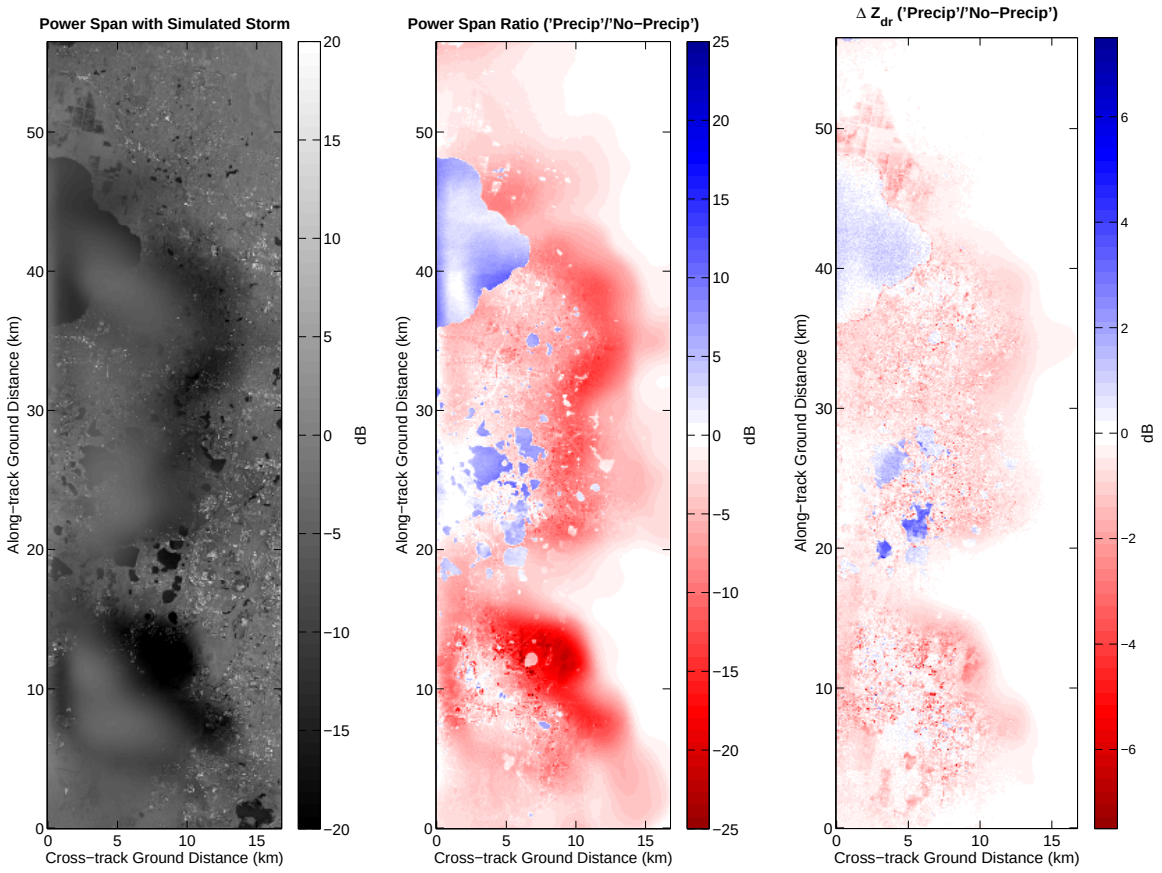

Figure 5.35: (a) The span $(10\log_{10}\left(|S_{hh}|^2+|S_{vv}|^2\right))$ image with the simulated storm. (b) The span ratio with the original data indicating power increase (blue) due to backscatter or decrease(red). Increased power is mostly over water bodies where the original power was low due to pseudo-specular reflection, but it is not necessarily visible in (a) or Fig. 5.34. (c) The ratio of the Z_{dr} with the simulated storm to the original Z_{dr}. In general, the simulated storm increases Z_{dr} by several dB which is expected due to the radar wave interaction with raindrops as described by (5.4).

and the hail core around 5 to 15 km along track. From a qualitative perspective, the attenuation appears to be fairly close to the real observations. Some of the stronger targets from man-made structures are still visible through the attenuation as they are in Fig. 5.34c and would provide locations for future analysis. Within the hail core region, some of these structures show up in a blue color indicating that $2^{-.5}|S_{hh}-S_{vv}|^2$ is stronger than $|S_{hh}|^2$ and $|S_{vv}|^2$ individually. Considering the horizontally oriented hail stones and raindrops below as determined by the ground radar Z_{dr}, this is expected. Figs. 5.35 and 5.36 provide a more qualitative analysis.

The power span and power span ratio images displayed in Fig. 5.35 indicate overall power level changes measured in decibels. From the power span image, the backscatter regions are around 10 dB, although from the ratio image we see that in most areas there is still a slight decrease in received power except over water bodies. In the hail core region, some attenuation is visible from rain just to the west of the near-range edge as seen in Fig. 5.29a before the beam begins reflecting from the hail. Beyond this, the power is reduced by as much as -25 dB. The attenuation and backscatter are not as strong to the north, but are significant. In Fig. 5.35b, attenuation is measured approaching -5 dB which is not readily noticeable in the composite image of Fig. 5.34b without very close inspection. Increased power from the lake reflections can increase 5 to 10 dB and is similar to real observations seen in Fig. 5.34c and analyzed quantitatively in Section 6.2.3.

The differential reflectivity change after adding the simulated storm also shows interesting effects as seen in Fig. 5.35c. With a few exceptions in the hail core region, Z_{dr} from land backscatter decreases indicating a general shift to lower horizontal polarization returns. This should be taken in the context of the fact that SAR surface Z_{dr} is typically higher than weather radar rain Z_{dr} with a much higher variance. Thus, as precipitation returns begin to overcome surface returns, Z_{dr} decreases. Around 20 km along track, two lakes exhibit a sizable increase in Z_{dr} in a region where fairly strong simulated backscatter overlaps real storm effects seen in Fig. 5.34a from much lighter precipitation that changes surface characteristics. In both Fig. 5.35b and Fig. 5.35c, surface features are clearly visible providing an indication that even when surface changes are not simulated they impact the resulting data as expected from (5.1).

Similar to Fig. 5.21 from the supercell simulation case, the propagation through the storm increases co-polar correlation as shown in Fig. 5.36. In this case, however, the increase is more significant because the storm cells cover more area. This provides further validation of the results seen from the real storm analyzed in Section 6.2.5. For the simulation, however, the low resolution of the weather data impacts more pixels and hence, increases this effect.

Differential phase shifting caused by the storm are display in Fig. 5.37 similar to Fig. 5.22. In Fig. 5.37a the Φ_{dp} is concentrated along the near range side due to the coherent

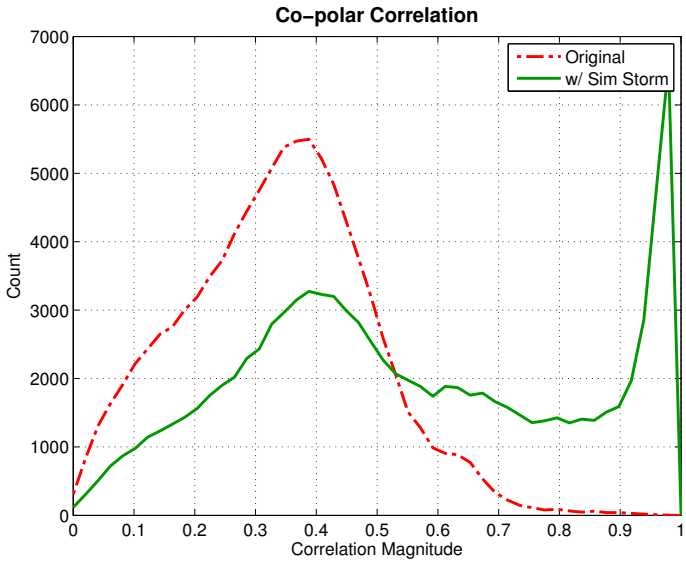

Figure 5.36: Histograms of the co-polar correlation coefficient ρ_{co} for the original SAR data (red) and the data with simulated storms (green). A distinct increase in correlation is present, which is to be expected as precipitation generally has correlation magnitudes above 0.9.

sum of integrated K_{dp} along the constant range wavefronts as shown in Fig. 5.31. Most of the values are positive and below 15° except around 4−12 km cross-track and 13−17 km along-track. Again, the result after combining with the surface ϕ_{co} is subtle give the 360° span of values, but it is visible. During the two real storms observed where HH and VV were coherent, the histograms tend to become narrower, but do not exhibit significant shifts in mean value. This will be discussed further in Section 6.2.5.

5.5 Summary

A multi-stage modeling approach is presented here that builds on previous research into simulating higher frequency radar observations from real lower frequency data and hydrometeor classification. The methodology for converting polarimetric ground-based data to polarimetric spaceborne SAR observations is presented in detail with simplifying assumptions such as ideal beam patterns and planar wavefronts. Results are then presented for the novel method of using neural networks to simulate rain and hail observations at X and Ku bands from real C and S band data of a supercell storm and a squall line, accounting for Mie scattering. Two hypothetical SAR swaths with three storm cells are examined in detail showing attenuation, backscatter and co-polar phase shifts due to various storm parameters.

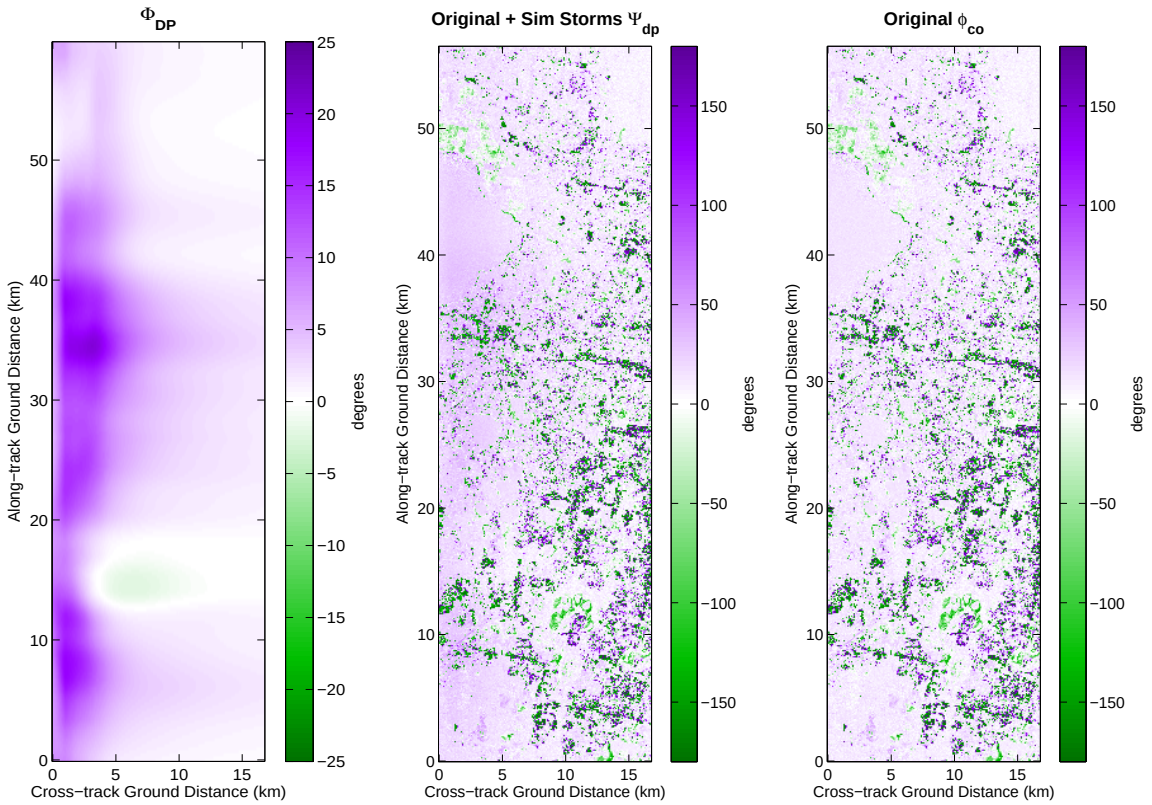

Figure 5.37: (a) Simulated propagation differential phase Φ_{dp} from the 010802 storm. (b) The original surface backscatter copolar phase shift plus the simulated propagation shift, $\Psi_{dp} = \Phi_{dp} + \phi_{co}$. Some values wrap as the sum exceeds $\pm 180°$. (c) The original SAR copolar phase difference ϕ_{co}.

Finally, the hypothetical observations are added to real SAR data from TerraSAR-X, validating the overall methodology and modeling components because they are similar to real observations accounting for the simplifications and ground radar resolution. Considering the complexity of the process and the possible introduction of errors at most stages, the results show promise while also revealing problematic areas. The assumption of an ideal beam pattern is likely to cause an increase in backscatter as seen in Fig. 5.19 and especially in Fig. 5.34. This is because the calculation integrates across the beam front (5.3) where the beam edges are weighted the same as the beam center versus a real beam that rolls off from boresight. An enhancement of the result can be achieved by obtaining a real SAR antenna pattern to weight the values as the real system would. In addition, some SAR systems provide an estimate of the noise floor, which increases from the beam center, which

can be used to determine where simulated attenuation will result in complete signal loss.

Changes to the observed phase difference between HH and VV were also simulated from the storms alone and when combined with a SAR acquisition without precipitation. Due to the coherent sum along a constant range slicing through the precipitation volume, the resulting phase shifts are subtle when combined with the surface returns that span $-pi$ to π radians. However, overall shifts of 20 degrees are feasible given an intense storm. More data is needed to analyze the polarimetric differential phase shift due to precipitation.

CHAPTER 6

QUANTITATIVE ANALYSIS OF POLARIMETRIC X-BAND SAR STORM OBSERVATIONS

What most experimenters take for granted before they begin their experiments is infinitely more interesting than any results to which their experiments lead.

- Norbert Wiener

6.1 Introduction

The focus of this chapter is to analyze and characterize real observations of storms by multi-polarization X-band SAR and simultaneous ground weather radar. Ideally, both the SAR and the ground radar will by fully polarimetric allowing for the calculation of the full covariance matrix and the many benefits that come with polarimetric observations. Unfortunately, very few radars exist that are fully polarimetric, so it becomes more difficult to obtain such conditions. Two such cases are discussed here. One involves dual-polarimetric (HH and VV) TerraSAR-X (TSX) observations of storms with HH only measurements from ground radars in central Florida, USA. The second benefits from a polarimetric C-band ground radar, but the spaceborne SAR is the COSMO-SkyMed (CSK) system where the HH and VV data are not coherent (see Section 2.3.5). In both cases, the storms occur over heterogeneous land adding more challenges to the problem of characterizing the propagation effects. Backscatter from the ground to the C-band radar also reduces the capability considering this radar is not as sofisticated as say the CSU-CHILL system. Nonetheless, these two cases provide a fundamental step towards fully characterizing storms from spaceborne SAR.

Table 6.1: Coefficients to convert $Z_{h,S}$ to X-band parameters in the form $aZ_{h,S}^{b}$

X-band Parameter	**a**	**b**
k_h	1.4E-4	0.80
A_{dp}	8.4E-7	0.93
K_{dp}	1.6E-4	0.75

6.2 TerraSAR-X Over Florida

By using data from two National Weather Service (NWS) Weather Surveillance Radar, 1988, Doppler (WSR-88D) S-band systems, in conjunction with microphysical and spatial distribution models, the observed backscatter and attenuation in the TSX images can be explained. The two NWS radars used were KMLB in Melbourne, Florida and KTBW in Tampa Bay, Florida. In addition, multiple TSX acquisitions were scheduled at the same location allowing temporal analysis of surface backscatter through different atmospheric conditions. One of the consequences of using strip-map dual-pol TSX data, is a reduction in swath width to only 15 km. However, the very high resolution may still provide some insight into storm structure. Various parameter specifications for the two radar systems during the data acquisitions analyzed in this chapter are given in Tables 2.2 and 2.4.

6.2.1 Microphysical simulation from horizontal polarization ground radar

In order to analyze the precipitation effect due to storms, simulations are utilized based on the microphysical representation to simulate X-band observations give horizontal polarization S-band ground radar data. Similar to Bolen and Chandrasekar (2003), the PSD is represented by a normalized gamma distribution in (4.2).

The PSD in (4.2) provides the framework for simulating the relationship between polarimetric X-band parameters and S-band horizontal reflectivity. For rain cells, the following standard value ranges are used (Bolen and Chandrasekar (2003); Bringi and Chandrasekar (2001)): $0.5 \leq D_0 \leq 2.5$, $3 \leq \log_{10}(N_w) \leq 5$ and $-1 \leq \mu \leq 4$ with a constraint of a rain rate less than 300 $\mathrm{mm\,h^{-1}}$. In addition, the Beard and Chuang (1987) drop shape model was used with an S-band radar elevation angle of 2° and 56° for X-band (corresponding to a 34° incidence angle) at a temperature of 10 ℃. Fig. 6.1 shows the results as scattergrams

with non-linear curve fits shown in red. The relationship between horizontal reflectivity is nearly linear, i.e.,

$$Z_{h,X} = \left(2.1 \times 10^{-3}\right) Z_{h,S}^2 + 0.91 Z_{h,S} + 0.51 \tag{6.1}$$

while the other parameters follow a power law relationship. Table 6.1 gives the coefficient values for the power law equations in the form $p = aZ^b$ where p is the parameter of interest and Z is the S-band reflectivity in linear units. Because the TSX data contains HH and VV polarizations, the co-polar differential scattering ratio can be determined (Z_{dr}); however, the relationship between X-band differential reflectivity at a 34° incidence angle and horizontal pointing S-band reflectivity is not always well defined as seen in Fig. 6.2. The differential reflectivity does increase in general with reflectivity due to oblate particles, but it is close to 0 dB.

6.2.2 Multi-temporal SAR Acquisitions

Estimation of the attenuation caused by precipitation requires an estimation of the surface return without rain - the basis for the TRMM Surface Reference Technique (SRT) in Meneghini et al. (2000). For a homogeneous surface, the observations of nearby rain-free regions is generally adequate (Meneghini et al. (2000); Marzano and Weinman (2008)). Over land, this criterion is typically found only in rain forests or deserts. Unfortunately, this is not usually adequate for heterogeneous surfaces, but SAR systems can take advantage of accurate repeated orbits to use temporally adjacent samples. The short, 11 day repeat cycle of TSX orbits helps to reduce temporal decorrelation due to land cover changes; however, consideration of backscatter change due to soil moisture and near surface water should be considered, especially in a region such as Florida with numerous lakes and easily saturated soil (Ulaby et al. (1986); Fritz and Chandrasekar (2009a)).

In August 2008, several TSX acquisitions over the Florida peninsula were requested by the author with the express goal of capturing precipitation signatures in the data. By requesting acquisitions suitable for interferometry, better temporal comparisons can be made without concern for fluctuations due to different viewing geometries or beam modes. Success was achieved on multiple overpasses using the same operational mode. Specifically,

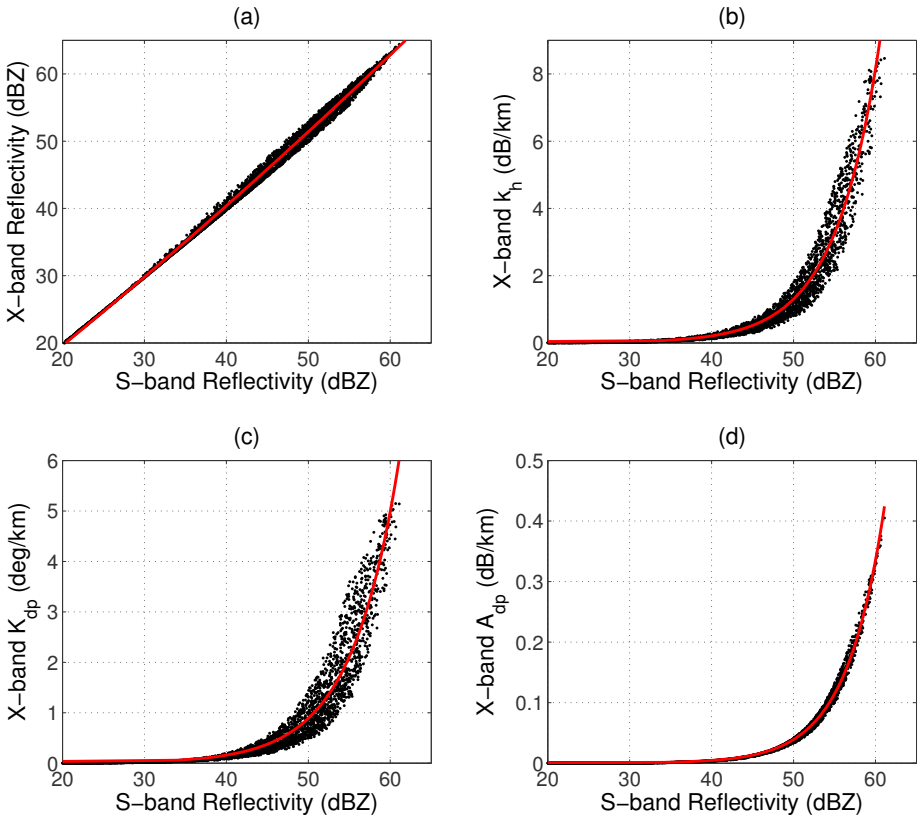

Figure 6.1: Scattergrams of X-band polarimetric observables vs. S-band horizontal polarization reflectivity using the PSD model (4.2): a) horizontal reflectivity, b) specific attenuation, c) specific differential phase and d) specific differential attenuation. The S-band radar is set at a 2° elevation angle while the X-band is at 56°, corresponding to a 34° incidence angle with a temperature of 10 ℃. The parameters for the curve fits are given in Table 6.1.

data acquired in the dual-polarimetric strip-map mode over the Orlando and Kissimmee regions captured a strong storm on 8 August (080808) seen from the NEXRAD KTBW radar in Fig. 6.3a. Given the sharp reflectivity gradients and high values, this storm is mostly convective (Steiner et al. (1995)) and may even be classified as a squall line. In mid-August, Tropical Storm Fay (TS Fay) swirled over the state for several days dumping up to 700 mm of rain near Melbourne, FL with sustained winds over 100 km h^{-1} (Stewart and Beven (2009)). During this time, the TerraSAR-X satellite acquired a dual-polarization data just south of Orlando, FL on 19 August 2008 (080819) as shown over the NEXRAD KMLB radar reflectivity in Fig. 6.3b. The third acquisition was captured during a virtually rain free time period 11 days later on the 30 August (080830). Each SAR swath is broken into multiple products known as frames and the two southernmost are analyzed in this work

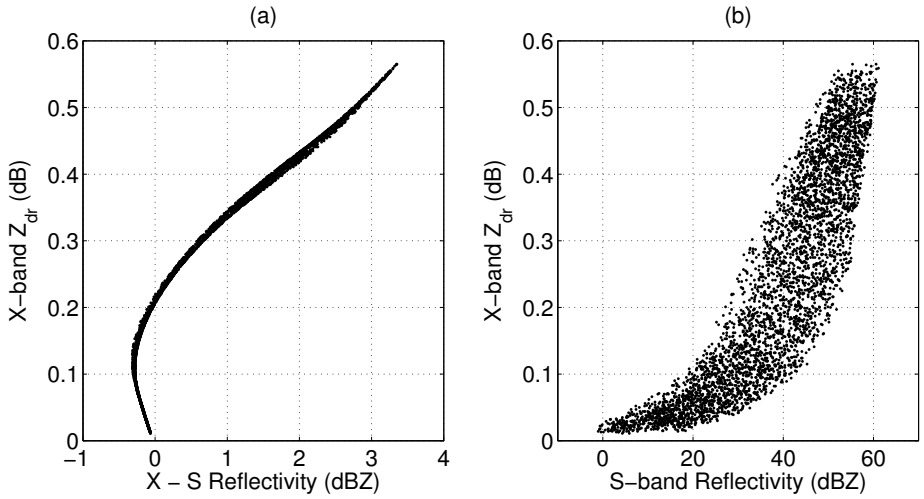

Figure 6.2: Scattergram from the theoretical model showing (a) the difference between X and S band reflectivity vs. X band differential reflectivity $Z_{dr,X}$ and (b) $Z_{dr,X}$ vs. $Z_{h,S}$, with the same radar alignment as Fig. 6.1. When the X minus S band reflectivity difference drops below 0 dBZ, the a 1:1 correspondence with $Z_{dr,X}$ no longer exists due primarily to Mie scattering. There is also high variability in the differential reflectivity when only knowing $Z_{h,S}$, but at an elevation angle of 56° $Z_{dr,X}$ is close to 0 dB.

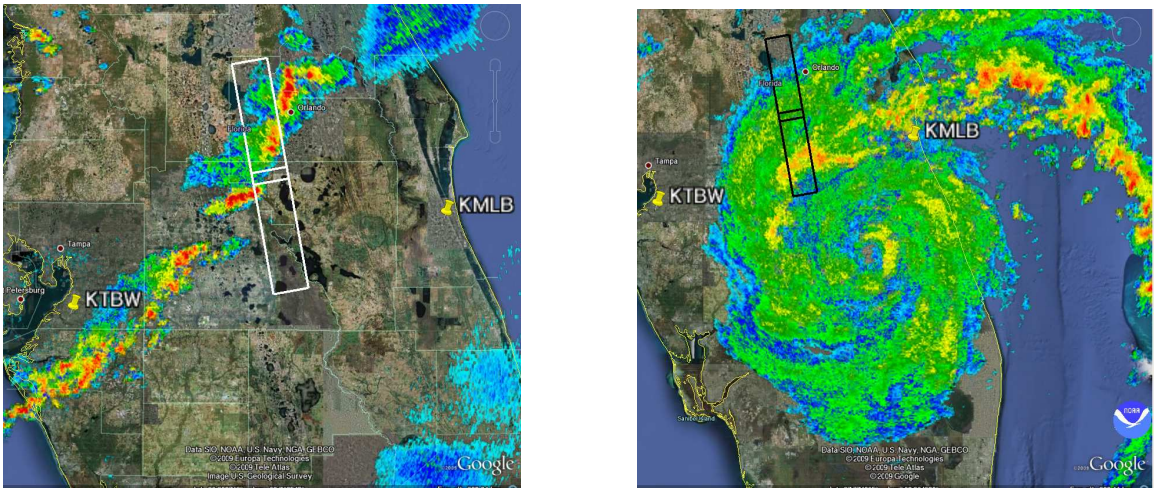

(a) (b)

Figure 6.3: WSR-88D reflectivity scans over Google Earth image of Florida, USA. (a) Convective storm front reflectivity from the KTBW radar on 8 August 2008 at an elevation of 1.5°. (b) Tropical Storm Fay reflectivity on Aug. 19, 2008 from the KMLB radar at an elevation of 0.5°. The SAR image frames are outlined in (a) white and (b) black with the NEXRAD locations indicated.

(i.e., six products/images were purchased from DLR under the TSX science program).

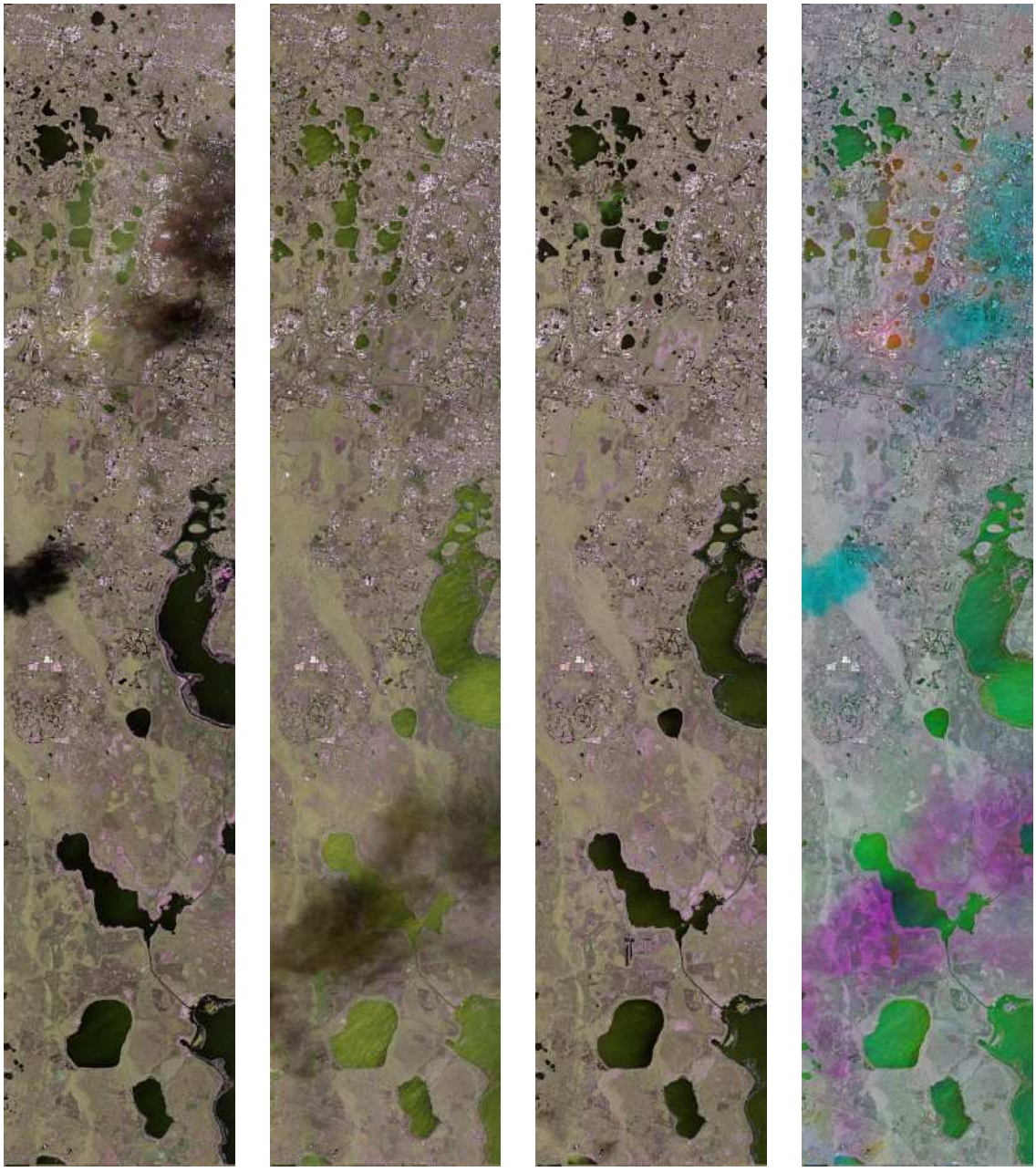

(a) (b) (c) (d)

Figure 6.4: Three TSX HH, VV acquisitions on (a) 080808 (b) 080819 and (c) 080830. The truecolor composite images are comprised of 2 β^0 frames of $|HH|$ (red) $|VV|$ (green) and $\sqrt{T_{22}}$ (blue) in dB and are co-registered with respect to each other. (d) depicts $\sqrt{T_{11}}$ where the RGB consists of 080808, 080819 and 080830 respectively (see text). The flight direction is bottom to top looking right.

Fig. 6.4 depicts color composite multi-looked β^0 images of all three acquisitions where the two frames have been mosaicked together. The first three images consist of the $|HH|$ and $|VV|$ channels assigned to the red and green while the blue color is $2^{-.5}|HH - VV|$ (i.e., $\sqrt{T_{22}}$ in (2.25)). For qualitative comparison and visualization, the histogram tails are clipped at the same values ($\pm 0.5\%$ with respect to the 080830 data) after conversion to decibels. The fourth image, Fig. 6.4d, consists of T_{11} from 080808 (red), 080819 (green) and 080830 (blue). This provides a clear indication of the different power from each acquisition even with only an 11-day separation. For example, cyan indicates attenuation from the 080808 storm, red marks backscatter from that storm, whereas magenta and green identify where TS Fay increased attenuation and VV reflectivity over water surfaces.

There are several interesting features to point out that are relative to the investigation of storms. Obviously, the storms during the first two acquisitions caused severe attenuation and appear like black clouds. Without further knowledge, a conclusion might be reached that these storms cells were isolated, but the analysis in Section 6.2.3 shows that is not the case. These images do give an indication, however, that the storm cells on 8 Aug. were more severe than on 080819 because they appear to have higher attenuation. In Fig. 6.4a a higher (reddish) HH return is visible on the near-range side, indicating the precipitation backscatter here is stronger than the attenuated surface returns (i.e., the volume term in (5.1) dominates). As shown in Section 6.2.3, this region corresponds to the high reflectivity gradient on the western side of the convective cell. Figs. 6.5-6.7 show the storm regions in more detail and indicate zones that will be used for a more detailed analysis and comparison to the weather radar data in Section 6.2.3 and polarimetric investigations in Section 6.2.5. The colors shown in these images are created by using $|HH|$, $|VV|$, and $\sqrt{T_{22}}$ from 080808, 080819, and 080830 respectively only to indicate the attenuation region while still revealing surface features that would otherwise be obscured by the precipitation.

Two other storm related effects visible in the TSX images are related to surface water. One is the higher VV return from the water bodies due to the wind and rain resulting in a significant increase in Bragg scattering at the TSX incidence angle, which is typically stronger in VV polarization (Contreras et al. (2003)). In the 080808 image, rain is more

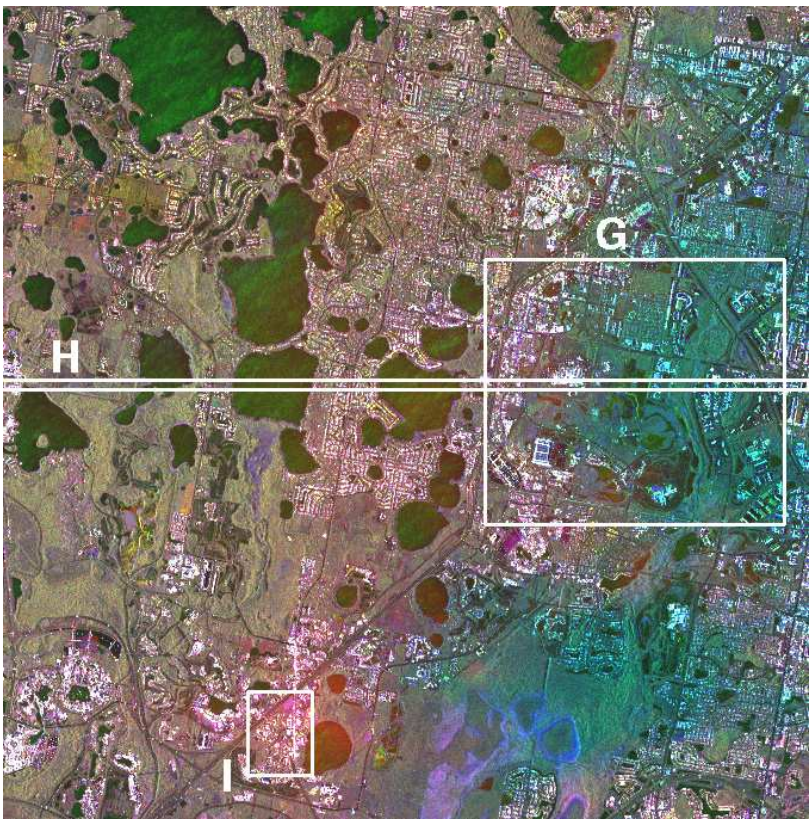

Figure 6.5: Close-up of the 080808 storm region over Orlando with analysis zones marked. The RGB image is formed by using $|HH|$ from 080808, $|VV|$ from 080819, and $\sqrt{T_{22}}$ from 080830 respectively only to indicate the attenuation region while still revealing surface features. Attenuation here is indicated by the cyan color (green + blue) while backscatter is more red.

likely the cause, but the pattern on the water surfaces in the 080819 image suggests that the high winds might be more dominant. The other effect is due to near surface water and soil saturation. Some of these regions become visible in the composite image of Fig. 6.4d and are discussed briefly in the next two sections. There is significant agriculture in this region and the sandy soil is easily saturated.

6.2.3 Comparison to Ground Radar

Weather data from ground based radar are used to quantify the observations from TSX acquisitions. The goal is to demonstrate that features in the reflectivity data align with features in the SAR data, followed by a more quantitative analysis in the regions indicated in Figs. 6.5-6.7. Considerable overlap exists between the two NEXRAD radars, ie., KMLB in Melbourne, FL and KTBW in Tampa Bay, FL, and provides the capability to estimate

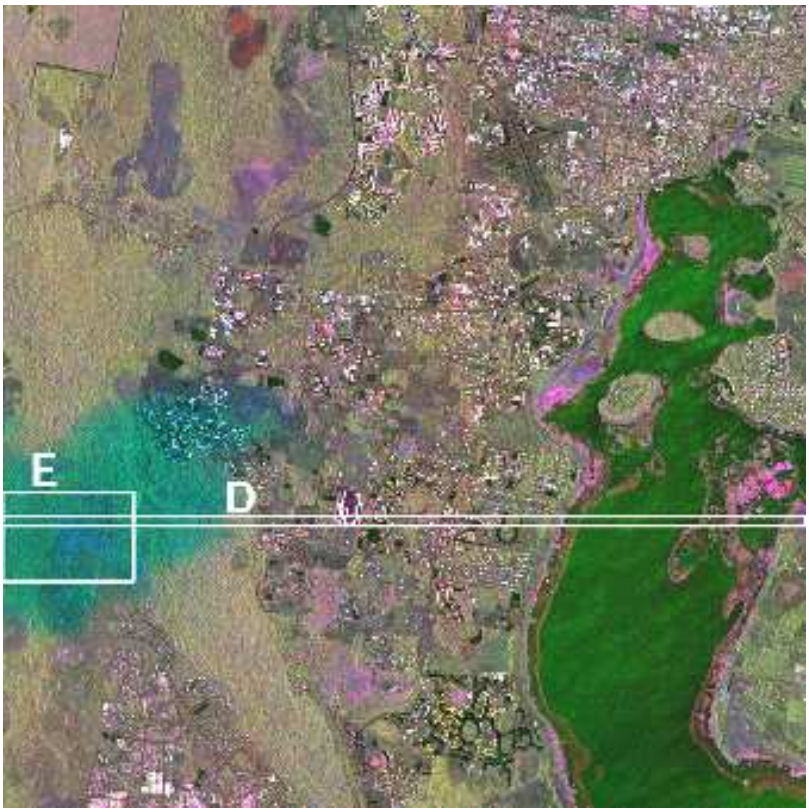

Figure 6.6: Close-up of the 080808 storm region near Kissimmee with analysis zones marked. The RGB channels are the same as in Fig. 6.5. Again, the attenuation from the 080808 storm shows up as cyan.

the reflectivity volume by combining observations. KMLB is the closest radar to the TSX acquisition frames at roughly 78 and 92 km to the center of each frame while KTBW is approximately 105 and 119 km.

The merging process is complicated by the fact that the two radars are not synchronized and sometimes have very different volume coverage patterns (VCPs). For example, during TS Fay KMLB scanned a volume in 4.5 min. whereas KTBW took about 6 min., with different pulse repetition frequencies (PRFs), scan rates and elevation angles (see Table 2.2). Fortunately, these differences are addressed in the Warning Decision Support System - Integrated Information (WDSS-II) and the merging algorithms contained within Lakshmanan et al. (2006) and Lakshmanan et al. (2007). The 3D grid from WDSS-II is georeferenced allowing for spatial comparisons with the SAR acquisitions. A Gaussian weighted 3D low-pass filter is then applied for additional smoothing. WDSS-II can also estimate advection, which is especially important when the precipitation cores of the TS Fay were moving over

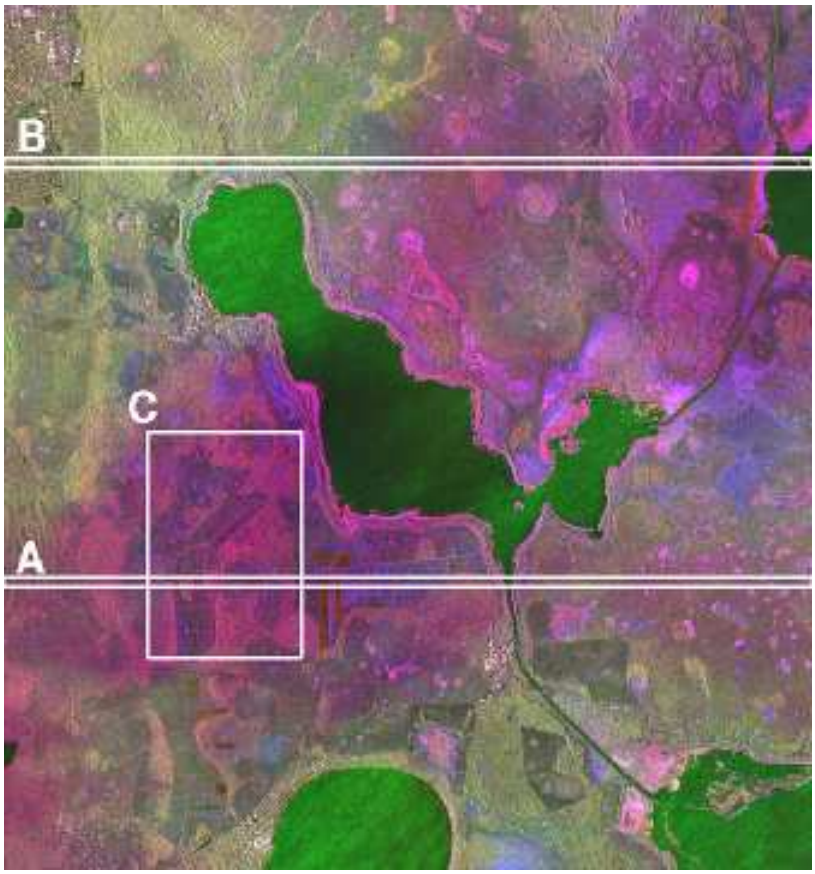

Figure 6.7: Close-up of the 080819 storm region with analysis zones marked. The RGB channels are the same as in Fig. 6.5. In this case, the attenuation caused by the 080819 tropical storm is magenta (red + blue) with higher backscatter in bright green.

22 ms^{-1}; however, there is still a fair amount of uncertainty and selection of the best algorithm is not straightforward. Prior to experimenting with advection estimation, adjusting the time period of the output volumes can provide a reasonable snapshot of the storm during the TSX acquisition, within the limitations of the radar VCPs. The grid resolution is 0.0015° latitude and longitude (approximately $150 \times 150\,\mathrm{m}^2$), by 250 m vertically. After the 3D volume of reflectivity is gridded, it can be sliced at any angle to reveal what the SAR beam would pass through and illuminate. The path integrated reflectivity at S-band can then be used to estimate the attenuation seen by the X-band SAR at each resolution cell using the model presented in Section 6.2.1. Coregistration and orthorectification of the TSX data was accomplished using the Doris SAR interferometry software (Kampes and Usai (1999)).

6.2.3.1 Case 1: 8 August 2008

Fig. 6.8 clearly shows a strong relationship between the ground radar reflectivity and the precipitation signature in the orthorectified SAR image. To get a better sense of the 3D volume in a 2D image, the reflectivity plot is the maximum value within the vertical column at each grid location to capture the most intense portions within the storm, also known as Vertical Maximum Intensity (VMI). Smoothed contours of this maximum reflectivity field at 29, 36 and 43 dBZ are drawn over the SAR image. With an incidence angle of about 35°, it appears that the visible backscatter and attenuation in the TSX data is around 45 dBZ in this case. Selection of this threshold will be explored in the subsequent quantitative analysis below, and it is likely that the threshold level depends on many variables. Several factors contribute to the challenge of accurately aligning ground-based weather radar observations to SAR images. A major factor is the 4 to 6 minute volume update time of the NEXRAD radars versus the nearly instantaneous SAR acquisition. Another factor is horizontal cross-track storm motion which can induce a Doppler shift resulting in along-track displacement. It is also clear from Fig. 6.8a that it was raining over the lakes to the west of the convective cell causing stronger backscatter in the vertical polarization. Although it is not visible at the scale of the images in this document, a small amount of attenuation is also present in the data around 28.6° latitude and -81.45° longitude, corresponding to the small region that is close to 40 dBZ in Fig. 6.8b. Around 28.2° latitude, the cell with reflectivity > 55 dBZ to the west of the TSX swath results in nearly complete signal loss from the SAR. This is described in Fig. 6.9c-d and the accompanying text and is also shown in Fig. 6.16c where the copolar phase is almost uniformly distributed. The outline of the TSX images in Fig. 6.8b also indicate the overlap of the frames.

As aforementioned, the advantage of having a gridded volume of reflectivity from multiple ground radars is that it can be sliced to examine what the SAR beam encounters as the radar wave propagates through the lower troposphere. Fig. 6.9a shows a slice from Zone H in Fig. 6.5 where lines indicating the cross-track ground range of the SAR image and the ideal beam edges and planar wavefronts are also shown for reference. White regions in all of the reflectivity images indicate no data is available even after smoothing. Because it is

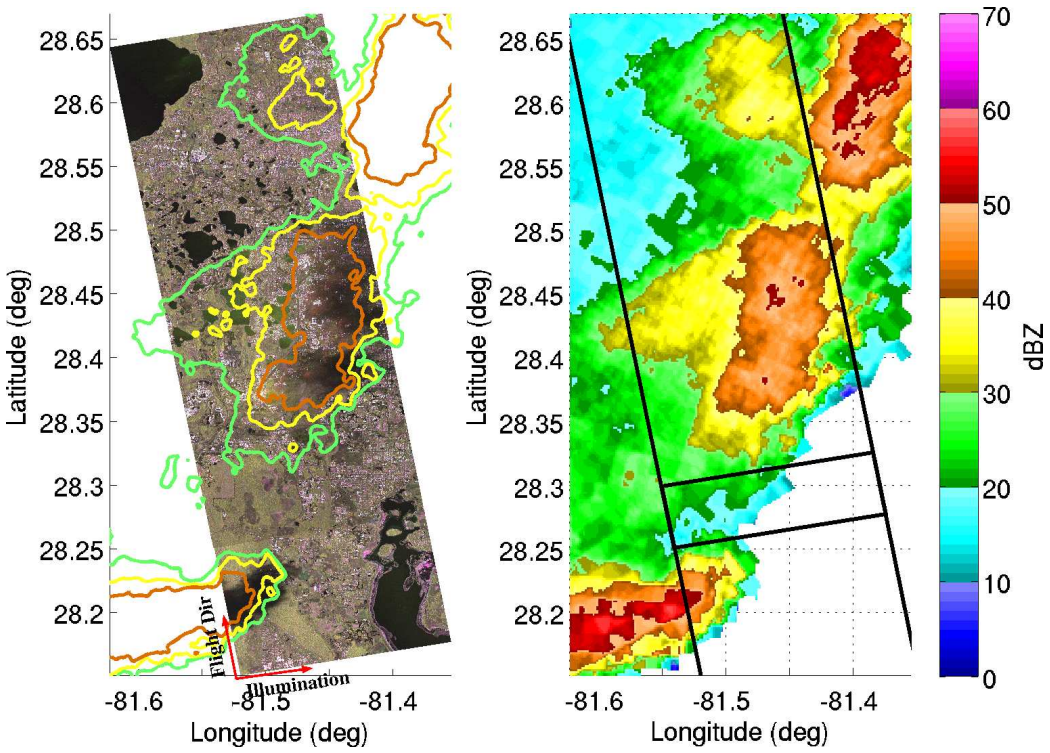

Figure 6.8: (a) The orthorectified 080808 TerraSAR-X RGB composite compared to (b) the same region in the vertical maximum of the merged WSR-88D reflectivity. Contours of this maximum field are drawn on the TSX image at 29, 36 and 43 dBZ. This clearly shows correspondence between the high reflectivity region and the high attenuation in the SAR image and provides a visual indication of the horizontal displacement due to viewing geometry described in Sec. 5.2. Portions of the 2 SAR image frame boundaries are shown in (b).

unlikely that the reflectivity changes significantly from the lower edge shown in Fig. 6.9a and the ground, the values were repeated to 0 km AGL (Above Ground Level) to fill in the bottom portion of the slice. The reflectivity slice is then interpolated at a resolution of 75 m (half of the grid resolution) along the ideal beam path calculated from the known incidence angles at the near and far ranges.

From the SAR data at multiple dates, an estimate of the storm induced attenuation can be calculated as shown in Fig. 6.9b for both HH and VV. The full cross-track zones selected for analysis are 62 lines wide in the azimuth direction and averaged at 96 pixels in range yielding speckle reduced samples of approximately the same horizontal resolution as the gridded reflectivity volume (150 m^2).

Overall, the trend in $\Delta\beta^0$ in Fig. 6.9b shows an increase in radar brightness followed

by a trough, and is typical of a precipitation cell signature in side-looking radar images (Pichugin and Spiridonov (1985); Melsheimer et al. (1998); Weinman and Marzano (2008)). This increase is not immediately apparent in the SAR images, e.g., Fig. 6.4a. Fig. 6.9b also shows the change in β^0 between 080808 and the subsequent acquisitions, where the higher intensity backscatter from the rain roughened water surfaces that are not present in the 080830 image is clearly seen as three large peaks. Nonetheless, noticeable attenuation starts at roughly 10 km from the near range side, well into the storm cell. However, it appears that only the more intense convective core impacts the SAR observations. In addition, the two plots in Fig. 6.9b reveal differences in the behavior of HH vs. VV over the same region, 11 days apart. Around 12 km, there are indications of higher HH backscatter on both no-rain days, possibly due to a larger PSD in the convective core on August 8. This comparison also provides more insight to the impact of precipitation on various terrain types.

In addition to the SAR data differences, Fig. 6.9b also shows the theoretical path integrated attenuation (PIA) indicated by the dash-dot blue line. The PIA is calculated from the reflectivity in Fig. 6.9a using the k-Z relation discussed in Section 6.2.1 and the values in Table 6.1. The curve only accounts for the attenuation term in (5.2), so it will never rise above 0 dB. The blue dash-dot curves in Fig. 6.9b show there is strong agreement between the observed attenuation and the theoretical attenuation. As discussed above, the 3D reflectivity volume relies on 4 to 5 min. unsynchronized volume scans which may explain the quicker recovery of the theoretical curve versus the observations. Additional investigations are necessary.

An example of severe attenuation due to the 080808 storm is explored in Zones D and E. Just on the near range side of the image at roughly 5 km AGL, reflectivity values close to 60 dBZ were observed from the ground radars as seen in Fig. 6.9c, although no hail was reported in the region. However, it is likely that hail was aloft based on studies of convective storms with polarimetric radar (Bringi and Chandrasekar (2001)) and considering that the reflectivity is higher above 4 km (this could indicate a melting layer of approximately 4 km). This induces a signal loss from the surface of nearly 15 dB relative to the two other acquisitions as shown in Fig. 6.9d. Absolute values in this region were close to -20 dB which

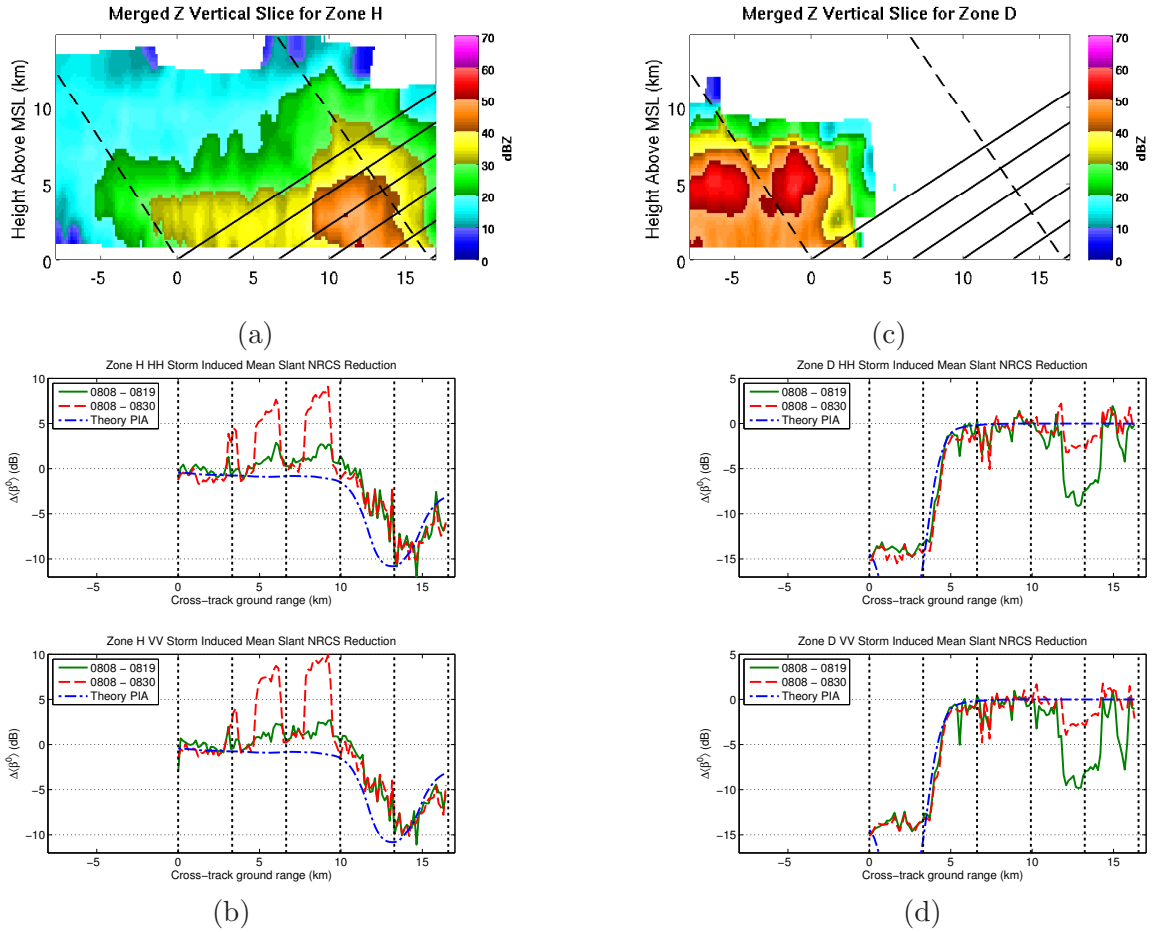

Figure 6.9: (a) Vertical slice of the merged reflectivity volume at zone H (see Fig. 6.5) with ideal beam boundaries and 5 planar wavefronts indicated. (b) The HH (top) and VV (bottom) averaged slant range NRCS (β^0) change from 080808 to both 080819 (green line) and 080830 (red line). The blue line indicates the theoretical path integrated attenuation at each ground point give the reflectivity slice in (a) (see text for details). (c) Vertical slice of the merged reflectivity volume at zone D (see Fig. 6.6) with ideal beam boundaries and 5 planar wavefronts indicated. (d) The HH (top) and VV (bottom) averaged slant range NRCS (β^0) change from 080808 to both 080819 (green line) and 080830 (red line). The blue line indicates the theoretical path integrated attenuation at each ground point give the reflectivity slice in (c) (see text for details).

is lower than the semi-specular reflections observed from smooth water surfaces indicating that many observations are likely to be close to the system noise floor before averaging. Near and far range pixels are farthest from the beam center, meaning the system noise floor is higher in these regions. Theoretically, however, the attenuation in this region should go down to −22 dB if the system were sensitive enough and the hydrometeors were all liquid water. The theoretical PIA plotted in Fig. 6.9d does match fairly well with the signal

recovery after passing beyond the storm cell at approximately 5 km. Because there is no precipitation beyond about 5 km cross-track ground range, the differences observed from 080808 to 080819 and 080830 can be attributed to surface backscatter changes and some precipitation effects caused by TS Fay discussed in Section 6.2.3.2.

6.2.3.2 Case 2: 19 August 2008 - TS Fay

Tropical Storm Fay provides another case to explore the impact of precipitation on X-band SAR. Fig. 6.10 depicts the spatial relationship between ground radar reflectivity and TSX signal attenuation on 080819, similar to Fig. 6.8. In this case, however, it is evident that rain is falling over the entire region, but mostly at rates too low to noticeably attenuate the TSX data. The threshold for attenuation appears to be closer to the 43 dBZ contour line shown in Fig. 6.10a, but there are numerous differences between this tropical storm and the convective storm on 080808. Aside from physical differences, the KTBW radar was operating with a 6 min. VCP. With estimated storm motion in this region of 22 $\mathrm{m\,s^{-1}}$ even the shorter 4 min. VCP for KMLB will have difficulty capturing the horizontal storm structure.

Using the same analysis and processing discussed in Section 6.2.3.1, comparisons between the ground-based reflectivity from two NEXRAD radars are compared with the TSX data during TS Fay. Cross-track vertical slices of the WSR-88D reflectivity at the Zone A and B along-track ranges shown in Fig. 6.7 correlate spatially with the SAR parameters in those regions. The vertical slice of the S band reflectivity volume shown in Fig. 6.11a verifies that attenuation should be apparent from the near-range edge. The observed disparity between TSX radar brightness on this date relative to 080808 and 080830 results in a decrease of about 3 dB to begin with, dropping to about -7 dB at both polarizations as seen in Fig. 6.11b. A larger discrepancy between the acquisitions is also more apparent in HH polarization mode; however, surface changes resulting from the tropical storm may play a considerable role in this natural ground cover region. Fig. 6.11b also shows a fairly close match with the theoretical PIA, although features do not line up in range as well, most likely due to a temporal gap in the lower elevation NEXRAD coverage. Close examination

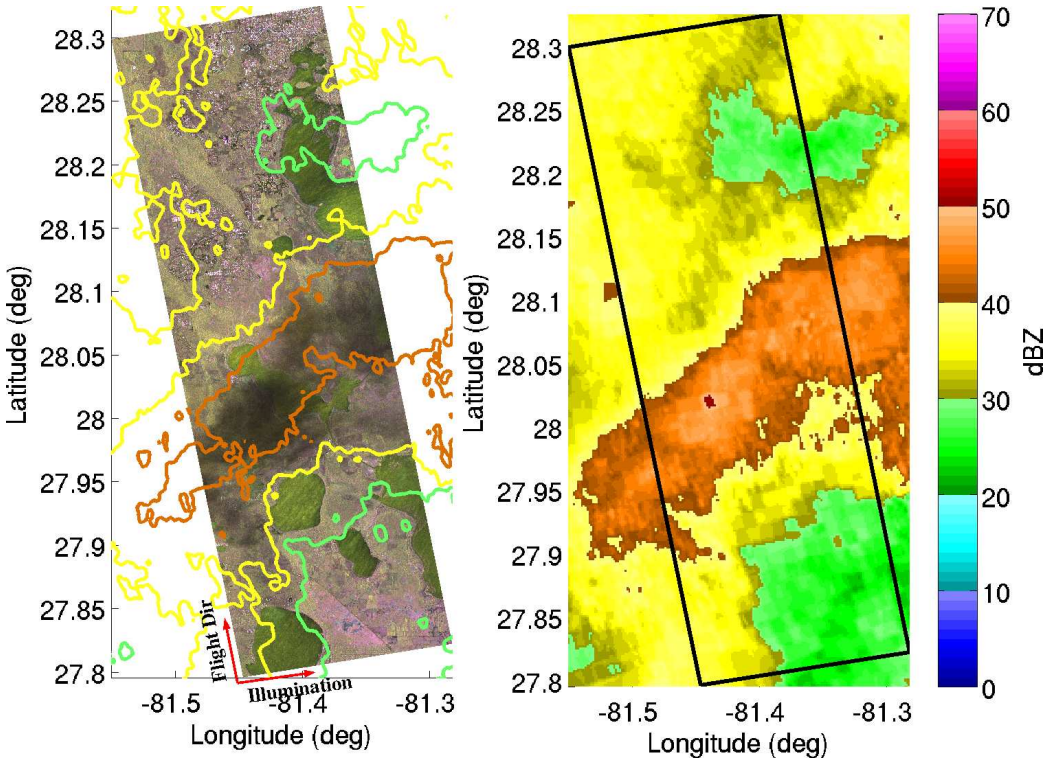

Figure 6.10: (a) The orthorectified 080819 TerraSAR-X RGB composite compared to (b) the same region in the vertical maximum of the merged WSR-88D reflectivity. Contours of this maximum field are drawn on the TSX image at 29, 36 and 43 dBZ.

of the sharp changes with respect to 080830 reveal flooded regions and other water surfaces that exhibit low backscatter.

Analysis of Zone B, depicted in Fig. 6.11c-d, shows a slightly different behavior of the observations relative to Zone A. However, these are more similar to the 080808 case where the attenuation is preceded by backscatter despite the fact that it is not visually noticeable. Compared to the theoretical PIA curve in Fig. 6.11d, the backscatter term in (5.1) appears to dominate the attenuation plus the wet surface may have enhanced reflectivity. Again, the trend in the theoretical curve does not quite line up with the observations, but they are within a few decibels. The SAR data, however, appears to pick up a sharper gradient that is beyond the resolution of the WSR-88Ds. Similar to the Zone A response, the HH return relative to 080808 is larger, but storm induced surface alteration is suspected because no rain was present in this area on either of the adjacent acquisition dates. The drastic spike at the far range is caused by SAR interaction with the lake surface.

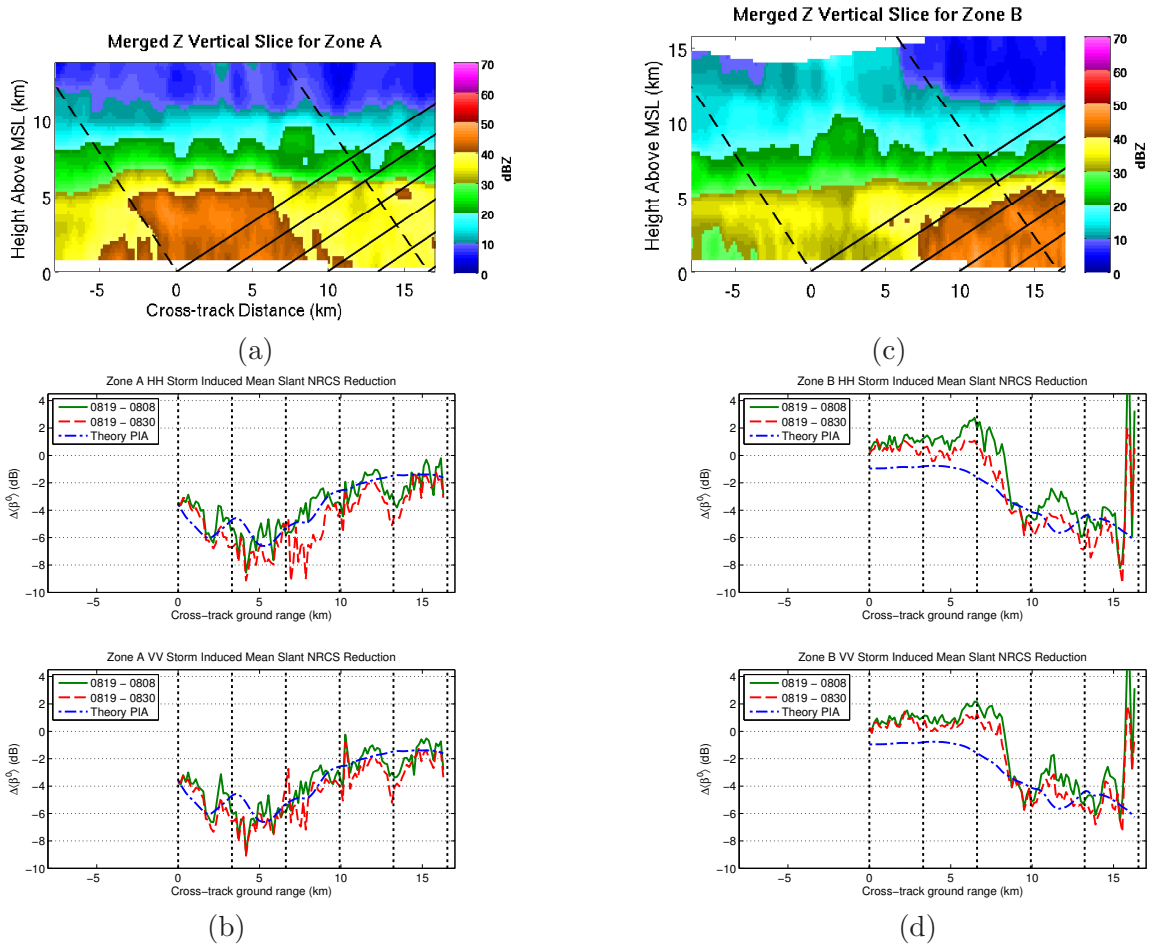

Figure 6.11: (a) Vertical slice of the merged reflectivity volume at zone A (see Fig. 6.7) with ideal beam boundaries and 5 planar wavefronts indicated. (b) The reduction in slant range NRCS (β^0) from both 080808 and 080830 in Zone A (see Fig. 6.7 for zone indications) with ΔHH on the top and ΔVV on the bottom. This shows the total NRCS change from each of the two adjacent passes indicating that potentially significant surface change resulted from the storm. (c) Vertical slice of the merged reflectivity volume at zone B (see Fig. 6.7) with ideal beam boundaries and 6 planar wavefronts indicated. (d) The reduction in radar brightness (β^0) from both 080808 and 080830 in Zone B with HH on the top and VV on the bottom. This shows the total β^0 change from each of the two adjacent passes indicating that potentially significant surface change resulted from the storm.

6.2.4 Summary of Ground Radar Comparison

The overall relationship between the path integrated slant range reflectivity and change in radar brightness compared to the no-rain cases for *all* cross-track zones is displayed in Fig. 6.12. Drastic changes due to roughened water surfaces were removed and differences between the no-rain data were averaged. Accumulating reflectivity with range is unconventional, but it is analogous to PIA using a directly observable parameter. Significant backscatter can still

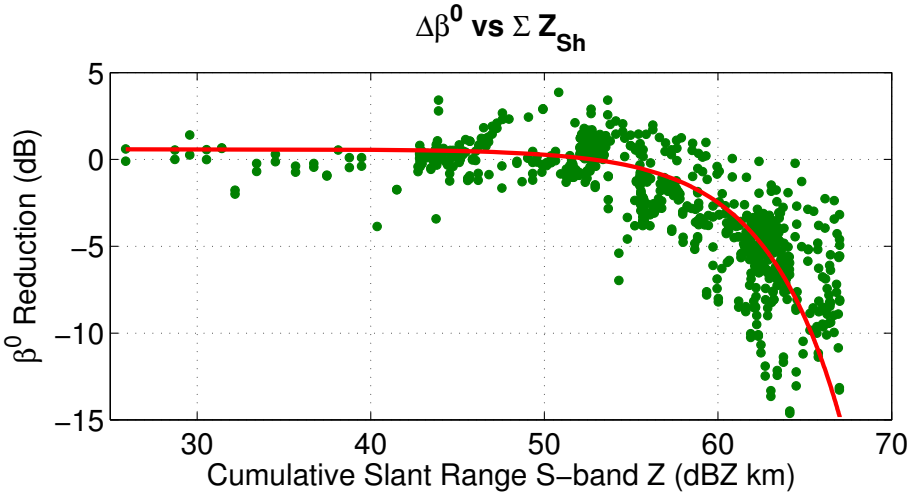

Figure 6.12: Differential radar brightness from rain cases versus path integrated S-band reflectivity for all cross-track zones (A, B, D, F and H) at both polarizations. Observations from roughened water are removed and differences between no-rain values are averaged. The solid line is an exponential least squares fit.

be present up to an accumulated 55 dBZ, but at that point it drops sharply. Accumulated values above 68 dBZ, which did not decrease the signal beyond the noise floor, were also removed. An exponential recursive least squares fit of the form $\hat{y} = ae^{bx}$ (in linear units) where $a = 1.144$ and $b = -7.065 \times 10^{-7}$ is plotted as the black line in Fig. 6.12. In general, this is similar to the expression for PIA in (2.29).

6.2.5 Polarimetric effect

The previous section analyzed the attenuation and backscatter caused by the storms. Now we investigate the effect of the precipitation on signal polarization. There are three parameters we can investigate with the two available copolar channels. Two of these parameters are represented by (2.34): 1) the copolar correlation coefficient magnitude $|\rho_{co}|$, and 2) the copolar phase ϕ_{co}. The third parameter is the copolar ratio Z_{dr} (differential reflectivity) from (2.35). While weather radars measure these parameters directly, in the absence of ground clutter, SAR must rely on detecting the deviation from the polarimetric properties of the surface scattering. Unfortunately, this may not be conclusive because polarimetric SAR is also valuable as a surface property change analyzer. Despite this uncertainty, however, pure attenuation of the surface reflections will not change the polarimetric properties.

Given a constant return from the surface, this change can only occur due to propagation effects that are polarization dependent, such as nonspherical oriented hydrometeors Bringi and Chandrasekar (2001).

Several observations about polarimetric effects of precipitation can be made from the scatter plots in Section 6.2.1 and literature on the subject (Bringi and Chandrasekar (2001)). Differential reflectivity and attenuation will be 0 dB for perfectly spherical hydrometeors and increase as liquid drops increase in size and become oblate. Lighter rain, and most hail, tend to be very correlated between polarizations, decreasing as the raindrop size, and corresponding oblateness, increases. The oblateness increase is usually associated with an increase in horizontal reflectivity coupled with an higher attenuation in this polarization. However, Figs. 6.1d and 6.2b indicate that the impact on Z_{dr} and A_{dp} are minimal at a surface incidence angle of 34°. Likewise, the copolar phase change will be close to zero until particles become more nonspherical and oriented. As the EM wave propagates through a volume with non-spherical oriented hydrometeors, the phase change accumulates as shown in (2.31) and Fig. 6.1c conveys the level of propagation phase shift relative to S-band Z_h at the viewing geometries analyzed.

Histograms of the three polarimetric parameters for Zone C (Fig. 6.5) are shown in Fig. 6.13 for all three acquisitions. The solid green line is 080808, the dash-dot blue line is 080819 and the dashed red line is 080830. Parameters from 19 August during TS Fay clearly stand out from the others. For Z_{dr}, however, the difference is not statistically significant because over this natural cover area, the mean copolar ratio is approximately 0 dB. On the other hand, the 080819 $|\rho_{co}|$ histogram shown in the middle panel indicates higher copolar correlation with an increase in the mean of 0.04 and 0.06 from the other two. This is indicative of the precipitation affecting the observed signals. A more significant divergence of the TS Fay data is seen in the bottom panel for ϕ_{co}. The mean phase difference decreases by 14.4° and 11.1° from the other dates with a $14° - 20°$ decrease in standard deviation. Additional discussion of copolar phase change due to TS Fay, including pooling surface water, can be found in Fritz and Chandrasekar (2009b).

Figure 6.14 provides some insight into the polarimetric changes that occurred in Zone C due to the storm. For these images, data from 080830 were selected as the no-rain

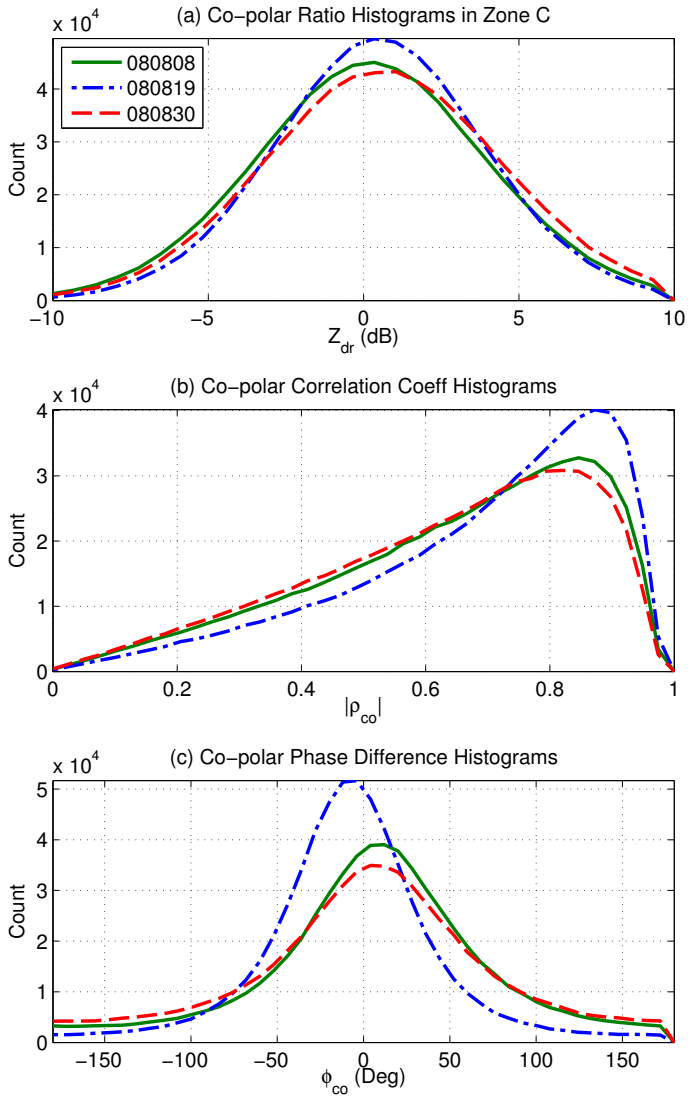

Figure 6.13: Histograms of polarimetric parameters from Zone C for all three acquisitions. 080808 is the green solid line, 080819 is the blue dash-dot line and 080830 is the red dashed line. (a) Z_{dr}, (b) $|\rho_{co}|$, (c) ϕ_{co}.

estimate of surface returns considering the fact that changes occur even without rain. The complex copolar difference power (T_{22} from (2.25)) on 080830 is depicted in Fig. 6.14a. Limited dihedral scattering results in relatively low power. TS Fay, however, caused a drastic decrease in this parameter of about 10 dB as seen in Fig. 6.14b, where the linear power ratio between 080819 and 080830 determines the change prior to decibel conversion. A drop of this magnitude is not likely from pure surface change in 11 days. Fig. 6.14c displays the increase in copolar correlation ($|\rho_{co}^{080819}| - |\rho_{co}^{080830}|$) seen in the Fig. 6.13b

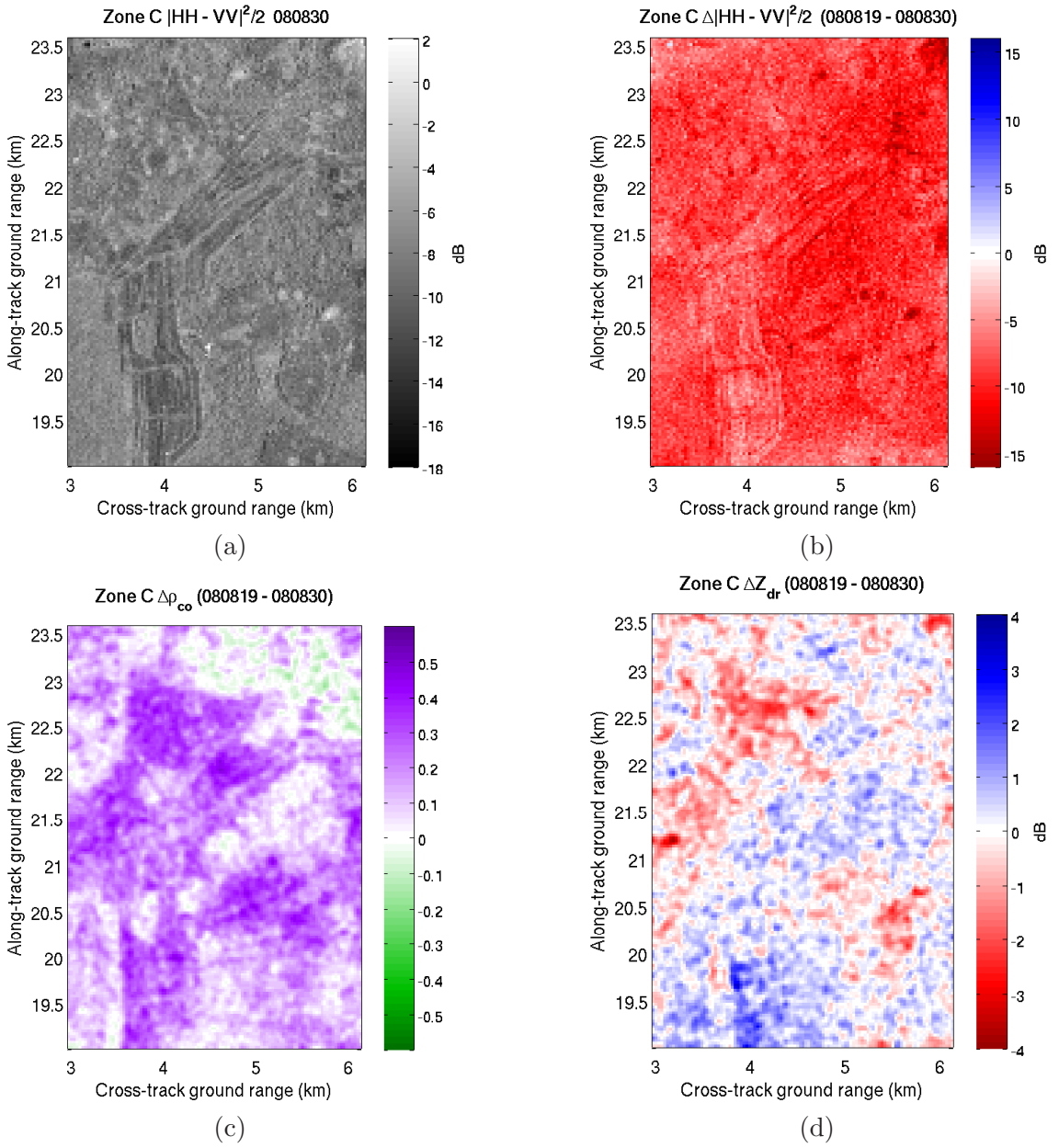

Figure 6.14: Polarimetric changes in Zone C. (a) T_{22} in dB on 080830 (the no-rain date). (b) The difference (in dB) of T_{22} from 080819 to 080830. (c) The smoothed difference of ρ_{co} from 080819 to 080830, where $\Delta\rho_{co} \in [-1, 1]$. (d) The smoothed difference (in dB) of Z_{dr} from 080819 to 080830. In both cases, smoothing is performed by a 2D Gaussian kernel with $\sigma = 0.9$.

histogram. Comparing this to Fig. 6.14a does reveal some correspondence with ground features, but the increase over most of the region points to propagation effects. The change in Z_{dr} from 080819 to 080830 is shown in Fig. 6.14d (again the linear power ratio was calculated prior to decibel conversion). Here we can see that while shifts on the order of

±3 dB have occurred in this zone, the balance does not drastically change the histogram in Fig. 6.13a. Unfortunately, the impact of the last two terms of (5.4) is inconclusive here without better ground truth. Due to the inherent noise of Z_{dr} and $|\rho_{co}|$, a 2D Gaussian filter kernel with $\sigma = 0.9$ was applied to better reveal the spatial trend.

Moving up to Zone E where the largest signal attenuation was detected during the 080808 storm, we find a different polarimetric effect. The histograms are plotted in Fig. 6.15 in the same fashion as Fig. 6.13. In this region and time, the Z_{dr} histograms are almost identical and centered close to 0 dB. In this case, though, hydrometeors appear to have had the opposite effect on $|\rho_{co}|$ indicating more decorrelation as shown in the middle plot of Fig. 6.15. In the bottom plot it is apparent that ϕ_{co} has a nearly uniform distribution. This provides additional support to the statement in Section 6.2.3.1 that the rain attenuated the signal down to the system noise floor.

Figure 6.16 also provides more insight into the polarimetric response, similar to Fig. 6.14, except that the reference date is 080808. The change in T_{22} is again drastically reduced as Fig. 6.16b shows, with the average drop more than 12 dB down from the 080830 observations. Unlike the observations in Zone C, though, the copolar coefficient magnitude shown in Fig.6.16c is decreased almost everywhere, in agreement with Fig. 6.15b and the assessment that the signal quality is low on 080808. Fig. 6.16d depicts a more widespread decrease in Z_{dr} at the far-range, possibly indicating a nonnegligible third term of (5.4). Again, however, the no-rain Z_{dr} in this natural land cover zone makes it challenging to draw conclusions on propagation effects to differential reflectivity.

In contrast to the Zones discussed above, Zones G and I exhibit noticeably discernible Z_{dr} during the 8 August storm, but the differences in co-polar correlation are similar to Zone C. The histograms are depicted in Figs. 6.17 - 6.19. One key difference is that the land cover is primarily urban which tends to exhibit less fluctuation over time. The positive shift seen in mean Z_{dr} can be explained by backscatter and attenuation from oblate hydrometeors. This interaction also increases the $|\rho_{co}|$ as shown in the middle plot of both Fig. 6.17 and Fig. 6.19. Furthermore, the copolar phase difference exhibits similar behavior to that of Zone C in that it trends towards 0° as seen in the bottom plot of Figs. 6.17 and 6.19. The

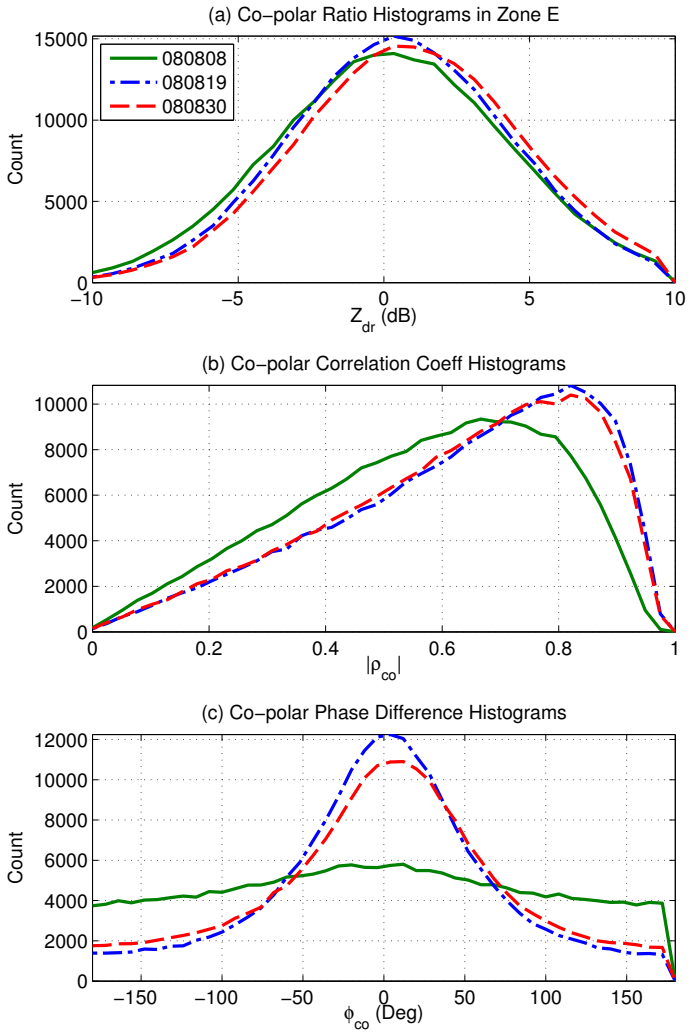

Figure 6.15: Histograms of polarimetric parameters from Zone E for all three acquisitions with the same color/line representations as Fig. 6.13. (a) Z_{dr}, (b) $|\rho_{co}|$, (c) ϕ_{co}.

mean ϕ_{co} is slightly above 0° for the 080808 case, but the tails of the distribution are lower than the ones from 080819 and 080830.

Again, plots of changes to polarimetric variables across the zone, seen in Figs. 6.18 and 6.20. Both Fig. 6.18a and 6.20a indicate much stronger dihedral scattering mechanisms from man-made structures on 080830. These are also visible in Fig. 6.18b which also provides a much clearer indication of propagation induced attenuation of T_{22} within the storm core. In Fig. 6.18c we see where the increased copolar correlation occurs: at the near-range side of the storm, meaning that it is probably caused by precipitation backscatter. Significant overlap exists between this area of increased correlation and increased Z_{dr} seen in Fig.

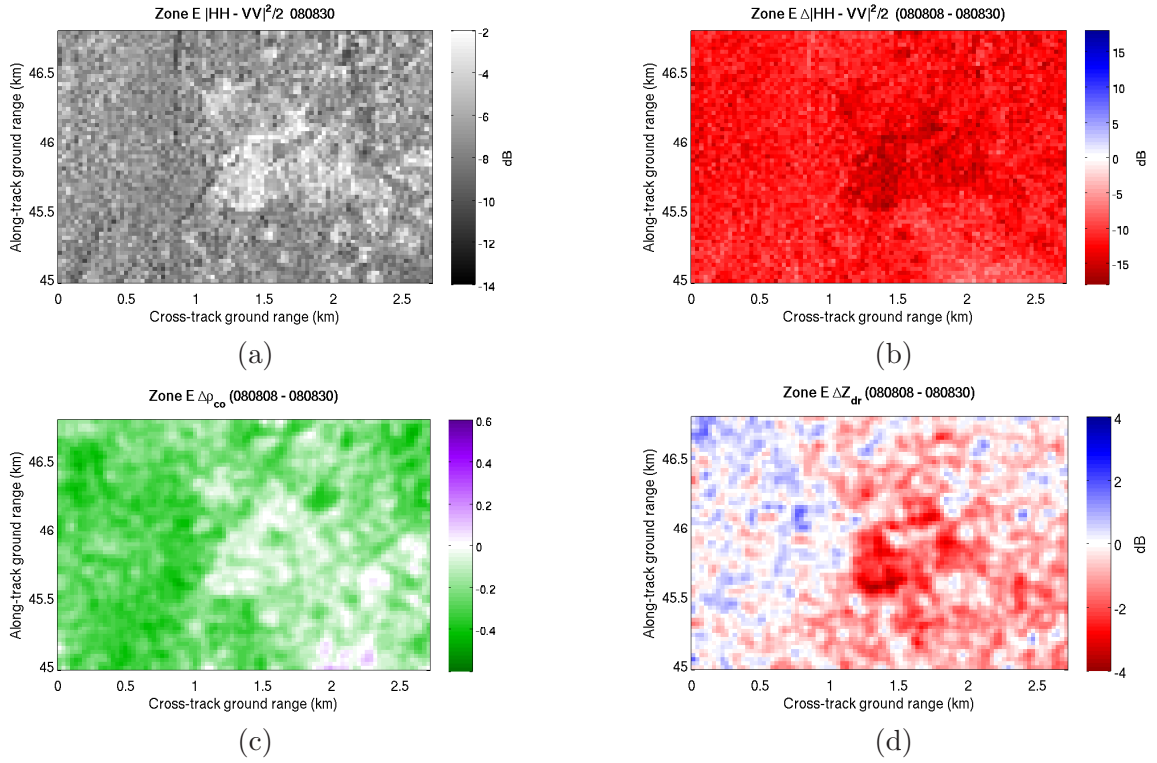

Figure 6.16: Polarimetric changes in Zone E. (a) T_{22} in dB on 080830 (the no-rain date). (b) The difference (in dB) of T_{22} from 080808 to 080830. (c) The smoothed difference of ρ_{co} from 080808 to 080830, where $\Delta\rho_{co} \in [-1, 1]$. (d) The smoothed difference (in dB) of Z_{dr} from 080808 to 080830. In both cases, smoothing is performed by a 2D Gaussian kernel with $\sigma = 0.9$.

6.18d. While this is not conclusive of reflectivity from large rain drops, it is encouraging. In Zone I, where precipitation backscatter was visible in the power images (Fig. 6.4), T_{22} is slightly elevated and Fig. 6.20c agrees with Fig. 6.19b in indicating increased co-polar correlation. The change in Z_{dr}, however, is not consistent except over the lake edge as Fig. 6.19 shows.

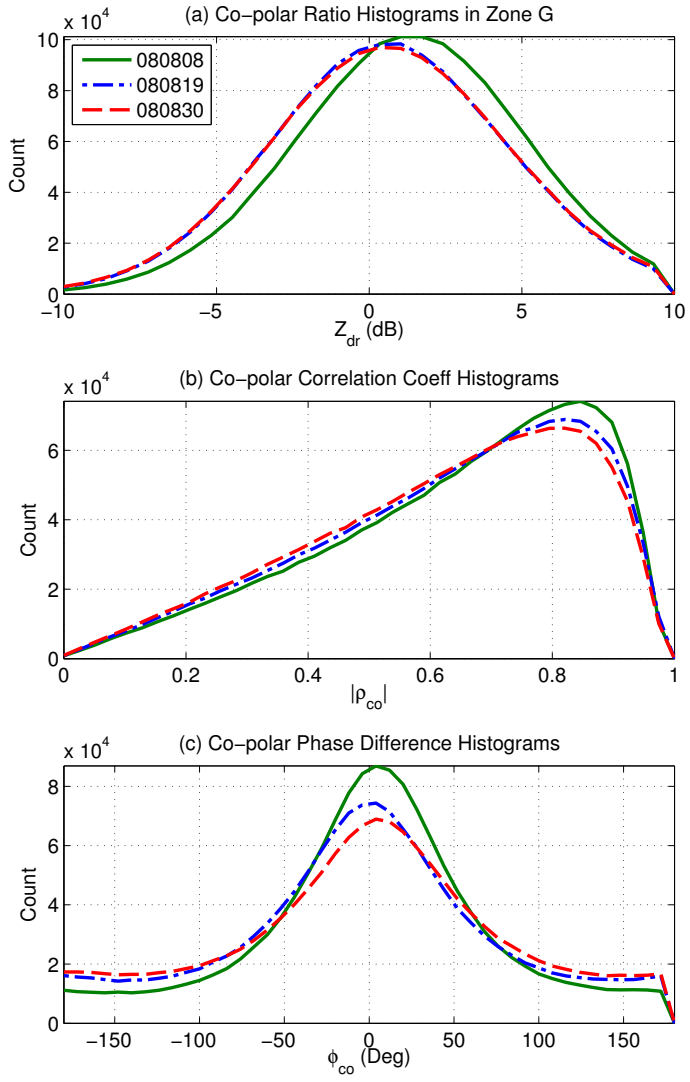

Figure 6.17: Histograms of polarimetric parameters from Zone G for all three acquisitions with the same color/line representations as Fig. 6.13. (a) Z_{dr}, (b) $|\rho_{co}|$, (c) ϕ_{co}.

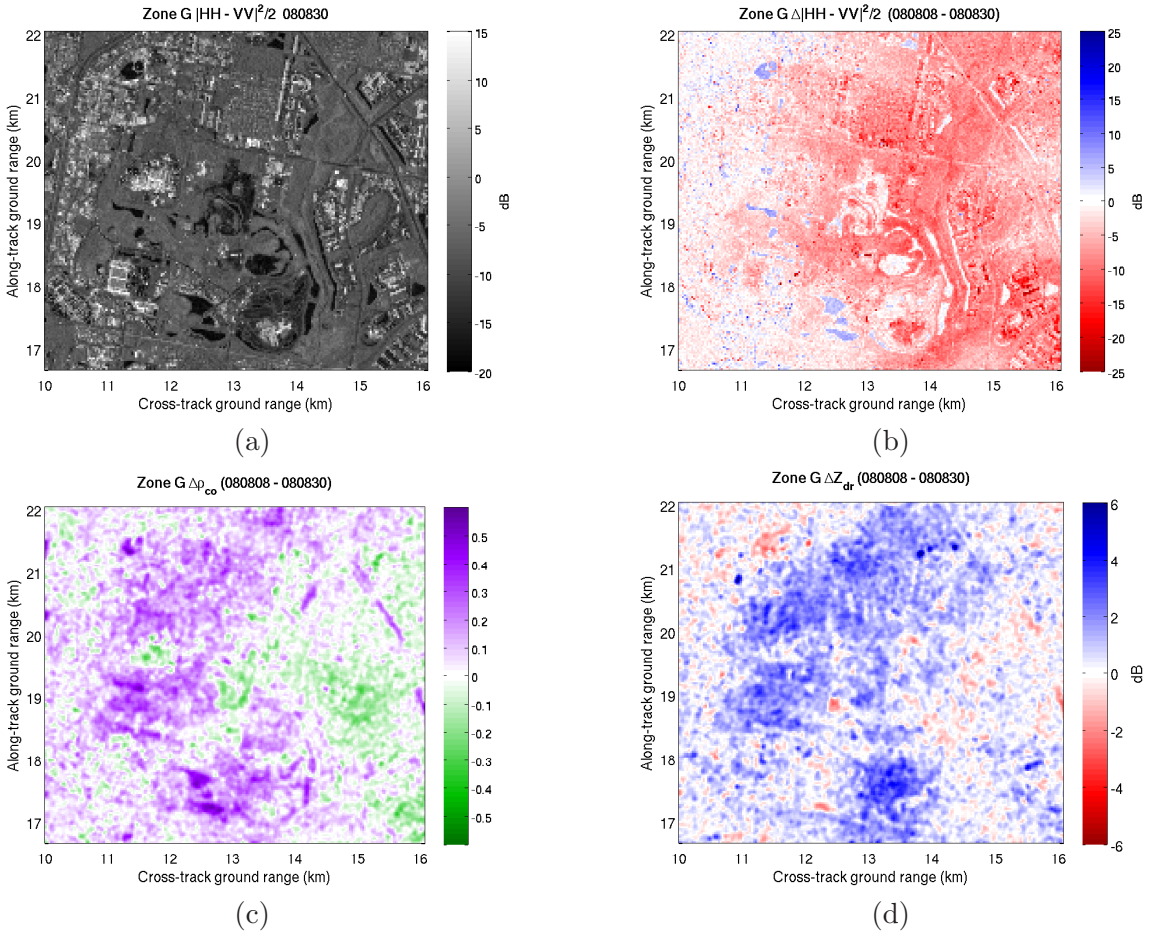

Figure 6.18: Polarimetric changes in Zone G. (a) $2^{-.5}|HH - VV|$ in dB on 080830 (the no-rain date). (b) The difference (in dB) of $2^{-.5}|HH - VV|$ from 080808 to 080830. (c) The smoothed difference of ρ_{co} from 080808 to 080830, where $\Delta\rho_{co} \in [-1, 1]$. (d) The smoothed difference (in dB) of Z_{dr} from 080808 to 080830. In both cases, smoothing is performed by a 2D Gaussian kernel with $\sigma = 0.9$.

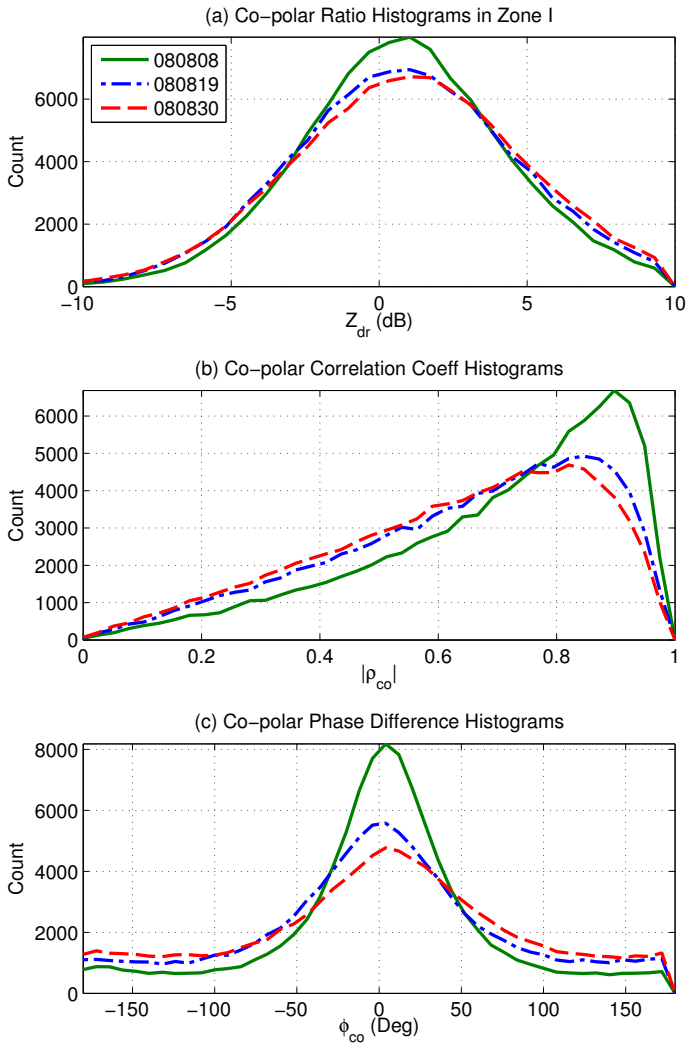

Figure 6.19: Histograms of polarimetric parameters from Zone I for all three acquisitions with the same color/line representations as Fig. 6.13. (a) Z_{dr}, (b) $|\rho_{co}|$, (c) ϕ_{co}.

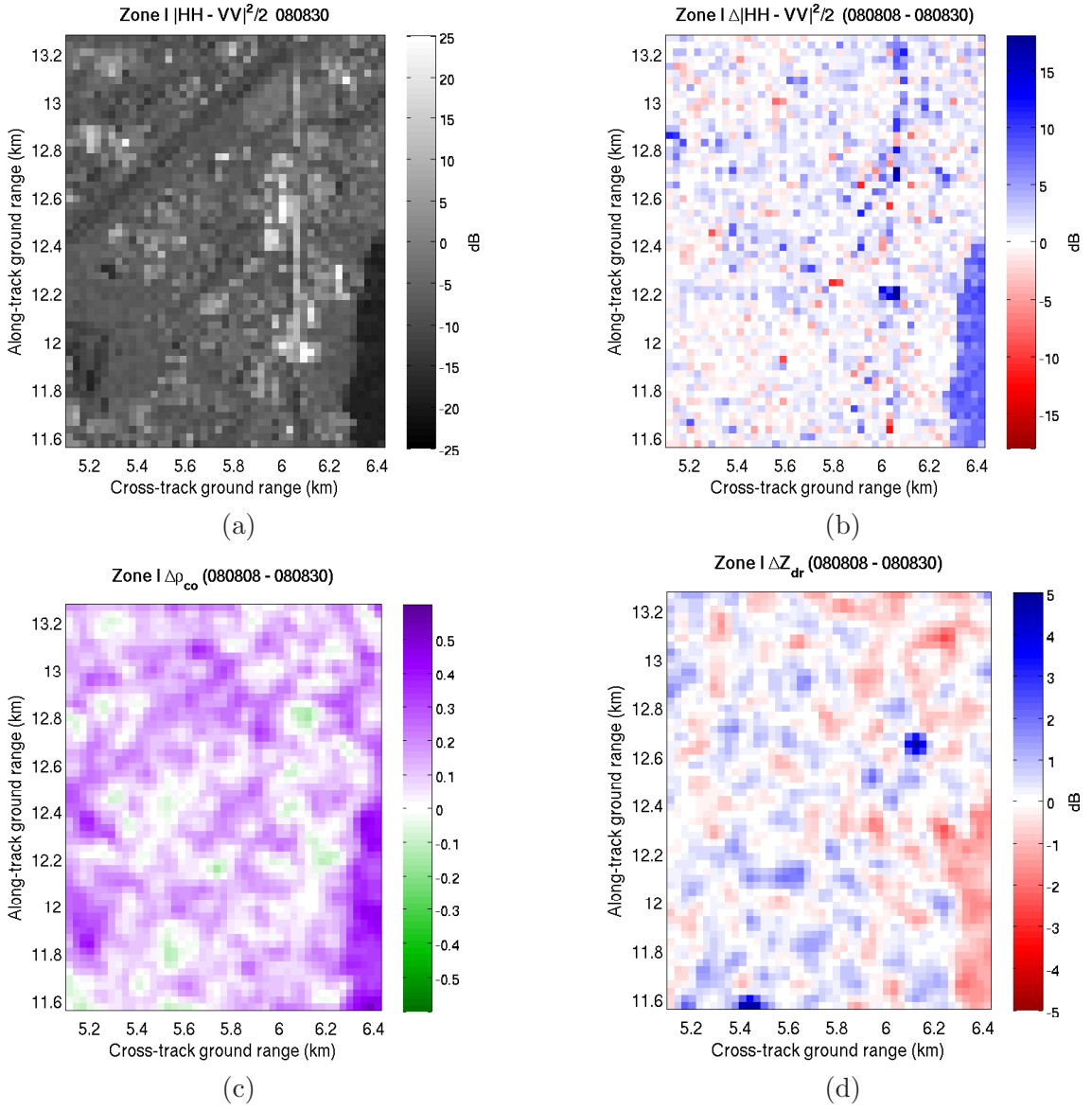

Figure 6.20: Polarimetric changes in Zone I. (a) T_{22} in dB on 080830 (the no-rain date). (b) The difference (in dB) of T_{22} from 080808 to 080830. (c) The smoothed difference of ρ_{co} from 080808 to 080830, where $\Delta\rho_{co} \in [-1, 1]$. (d) The smoothed difference (in dB) of Z_{dr} from 080808 to 080830. In both cases, smoothing is performed by a 2D Gaussian kernel with $\sigma = 0.9$.

6.2.5.1 Storm induced differential phase shift

The co-polar phase shift observed by TerraSAR-X in several small rectangular zones shown in Figs. 6.13c, 6.17c, 6.15c and 6.19c indicate that storms effect the phase between HH and VV. Simulation results of the propagation phase shift caused by precipitation were shown in Sections 5.4.1.3 and 5.4.2.1, but comparisons to real observations were not made. However, both showed only slight phase changes relative to the 360° range of values. In Figs. 6.21 and 6.22, the ϕ_{co} values in the two storm regions are shown for all three acquisition dates to provide a qualitative comparison. These representations are averaged with the 15×10 boxcar filter in order to reduce the speckle phenomena which is very prevalent in phase data.

Within the attenuation region caused by TS Fay displayed in Fig. 6.21, the surface is comprised of mostly agriculture, sub-tropical forest and lakes. During the storm, the observed ϕ_{co} seen in Fig. 6.21b exhibits an overall decrease to negative values compared to Figs. 6.21a and 6.21c, and it also appears to partially obscure surface features. Zone C falls completely within this region, and the histogram in Fig. 6.13c also shows the negative mean and reduction of large phase changes as a narrower distribution. According to the theory and simulations discussed previously, K_{dp} should also be negative, although the lack of polarimetric ground radar measurements prevents verification of this. By the 30th of August, much of the co-polar phase response in this region returns to the pre-storm levels except around many of the numerous lakes and water filled pits to the east of Lake Hatchineha in the center of the scene. As documented by Fritz and Chandrasekar (2009a), the trees surrounding these water bodies create dihedral scattering resulting in a 180° co-polar phase shift and is a surface effect unique to this type of terrain.

Contrary to the effect of the tropical storm, Fig. 6.22 depicts the change in co-polar differential phase near Orlando during and after the August 8, 2008 squall line. In this region of urban and mixed used ground cover, the storm affects are more difficult to discern. Comparing Fig. 6.22a to the 6.22b and 6.22c, it appears that there is a slight increase in ϕ_{co} and a similar obscuring of surface features. Many urban structures seen where ϕ_{co} is close to 180° are still visible; however, shifts closer to -180° indicated by darker green in Figs.

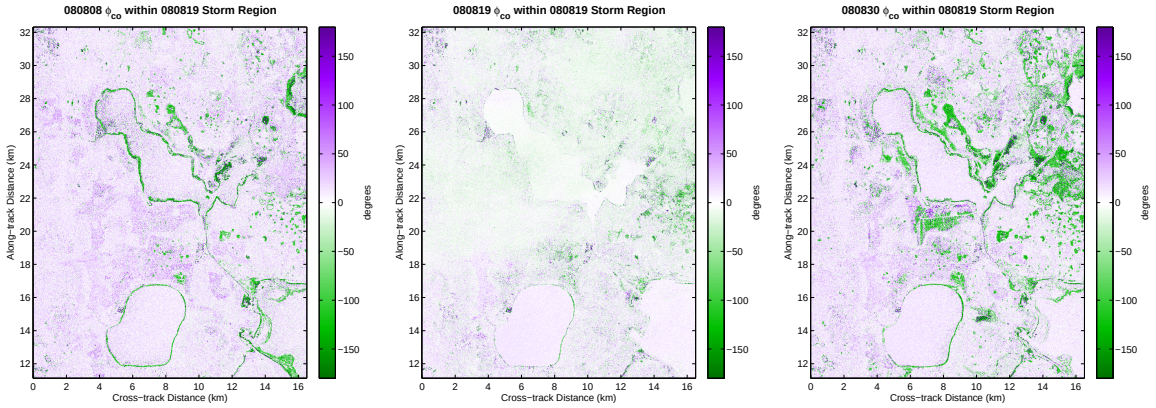

(a) (b) (c)

Figure 6.21: The differential phase shift ϕ_{co} observed by TSX in the region most affected by Tropical Storm Fay (approximately the area shown in Fig. 6.7) from acquisitions on (a) 2008/08/08 (b) 2008/08/19 and (c) 2008/08/30. Note the overall decrease in ϕ_{co} to negative values during the storm in addition to reducing the visibility of surface features. The significant increase of phase near $-180°$ in (c) occurs around lakes and pits that filled with water and have trees around them, creating a dihedral return to the radar.

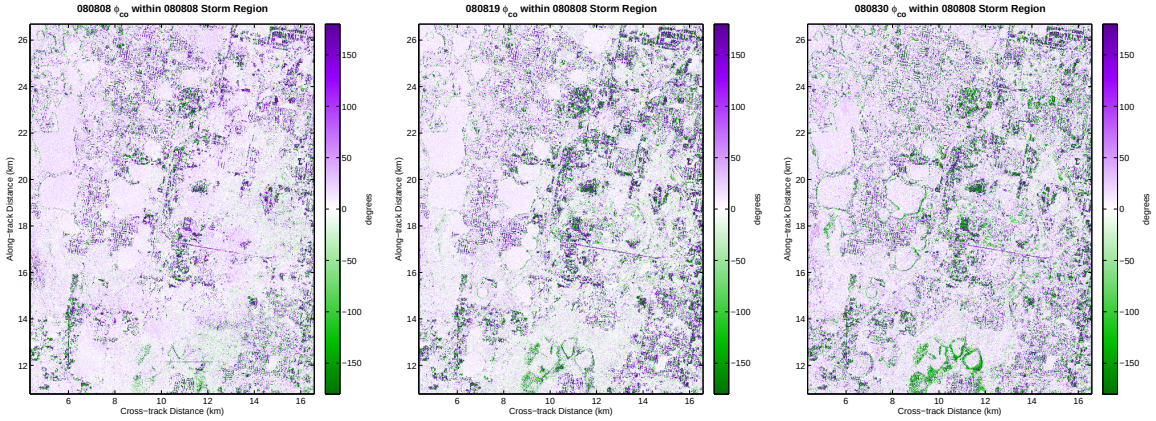

(a) (b) (c)

Figure 6.22: The differential phase shift ϕ_{co} observed by TSX in the region most affected by the August 8 squall line (approximately the right 2/3 of the area shown in Fig. 6.5) from acquisitions on (a) 2008/08/08 (b) 2008/08/19 and (c) 2008/08/30. In this case, the far-range portion seems to have a slight increase in ϕ_{co} seen in (a), although it still has the affect of obscuring surface features.

6.22b and 6.22c are not. Without a detailed analysis of this phenomena with coincident observations by a polarimetric ground radar, the main conclusion that can be reached is that the storm definitely impacts the co-polar phase shift, part of which may be due to surface changes.

6.3 COSMO-SkyMed Over Northern Italy

On June 29, 2010 satellite number two of the COSMO-SkyMed X-band SAR constellation acquired HH and VV images over the Pavia region of northern Italy capturing a convective storm. Meanwhile, the Bric della Croce C-band polarimetric radar, operated by ARPA Piemonte, observed the same storm from its location near Turino. This upgraded Gematronik 400C radar, however, only has a range resolution of about 350 m with azimuth spacing at 1°. With the storm observation at approximately 80−100 km, the spatial resolution limits detection of small scale features. Having multiple polarizations, though, allows for hydrometeor classification to improve the conversion of ground measurements to those spaceborne SAR. Thus, the models and methodology developed in Chapters 4 and 5 can be deployed, although complexities induced by the real world environment require some simplifications.

The first two steps of the procedure to simulate the SAR observations from ground data detailed in Section 5.3.1 are K_{dp} estimation and attenuation correction. C-band weather radars suffer from attenuation, and are notorious for oscillations in Z_{dr} due to Mie effects, so the correction is necessary here. In addition, ground backscatter can adversely impact the measurements as seen in the lower two elevation scans in Fig. 6.23 for reflectivity. The part of the storm cell imaged by the CSK is seen in Fig. 6.23d, within the approximate SAR acquisition swath in pink, after applying a basic clutter filter and attenuation correction algorithm from K_{dp} estimates [Testud et al. (2000)]. Fig. 6.23a shows the level of ground clutter visible to the radar at the lower left of the image pointing at -0.1° from its perch near Turino, with the filtered version in Fig. 6.23c. Considering that most of the storm cell of interest was removed by the filter, this scan was discarded in processing, and data were projected to the surface from the lowest level available. Attenuation correction was still needed for differential reflectivity, although only modest increases were realizable.

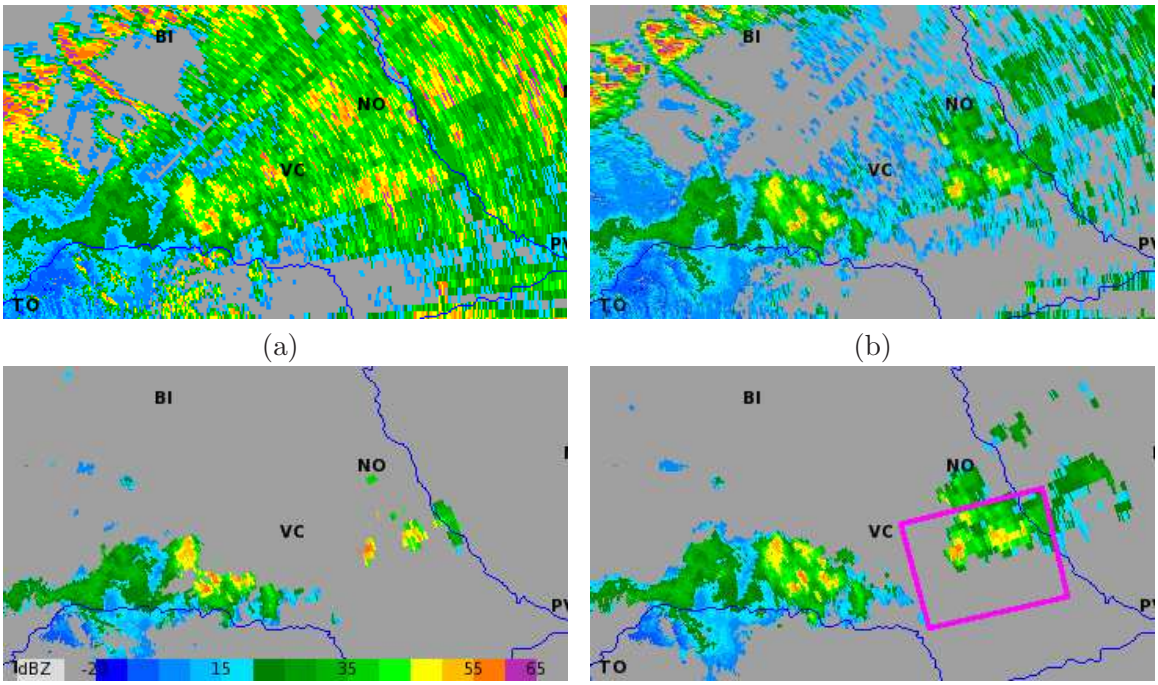

Figure 6.23: Reflectivity of the June 29, 2010 storm as observed and processed by the Bric della Croce C-band weather radar located in the lower left corner of the panels. (a) At the lowest possible elevation angle (-0.1°), ground clutter overwhelms the precipitation returns. (b) Ground clutter subsides a lot at the next elevation (0.5°), but is still present. (c) Much of the ground clutter is removed and reflectivity corrected for attenuation, but there is not much left of the storm cell in the right half that is within the SAR swath. (d) The storm cell on the right is now visible after clutter filtering and attenuation correction, but there is still a chance of over-filtering and under-correcting from the close-range cell effects. The pink square shows the approximate boundaries of the CSK image frame.

6.3.1 Multi-temporal SAR Acquisitions

Before continuing to simulate SAR precipitation observations from the ground radar data, it is helpful to examine the SAR data itself. In an effort to capture data containing precipitation and take advantage of multiple satellites in the same orbit, all satellites were scheduled to collect HH and VV data over the same region in Pavia. Two of the satellites can repeat an acquisition within 24 hours, which could provide a rain versus no rain pair if one imaged a storm. Unfortunately, data was not collected at the requested interval for an undisclosed reason.

Five acquisitions did occur, however, on May 13, May 20, May 28, June 21 and June 29, 2010 as seen in Fig. 6.24 at an incidence angle of approximately 25°. After obtaining the data, all channels were converted to radar brightness (β^0) from the digital number (DN) format followed by co-registration to the May 28 data. Theoretically, direct comparisons of power can be made between the HH and VV data if the calibration parameters supplied are accurate. The images in Fig. 6.24 were created from the HH, VV and complex difference β^0 channels, but because the HH and VV channels are not coherent, the images lack much color. The histograms for all channels and images have the same limits, allowing for a qualitative comparison of relative power changes between horizontal and vertical polarization overall. From the first date of May 13 to the last of June 29 there appears to be a monotonic increase in received power, with a slightly higher increase in the HH channel. It turns out this region of Italy is reknowned for growing rice, hence the low backscatter from flooded fields in mid-May to a significant increase by late June as the rice grew. The urban areas seen in Fig. 6.24, on the other hand, maintain a relatively constant power level as expected. The consequence of data acquired from this region is that a "no-rain" average backscatter image can not be created, exacerbating the challenge of evaluating the storm impact seen in Fig. 6.24e.

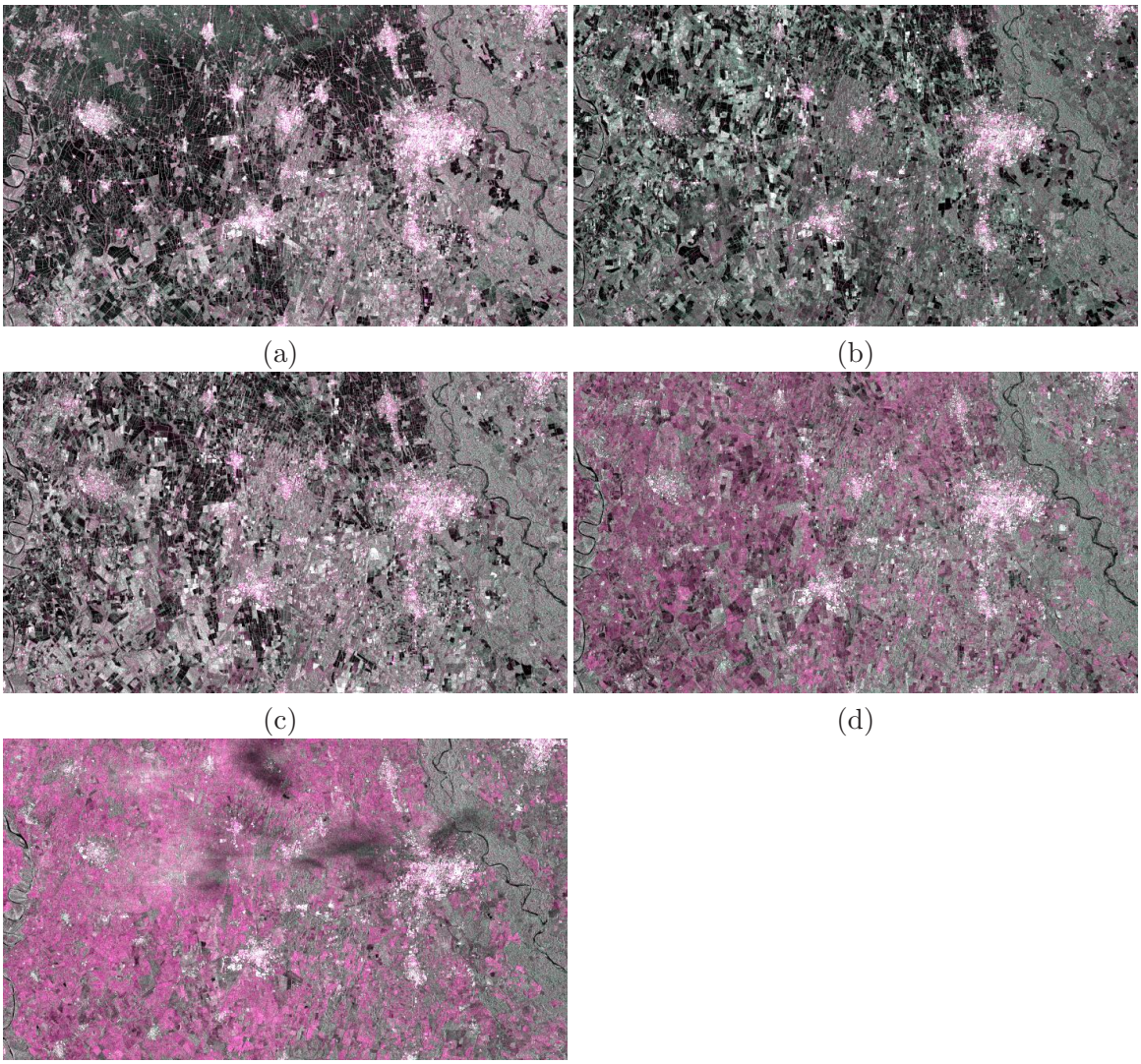

Figure 6.24: The northern half of the CSK acquisitions in Pavia shown as composite RGB images created from $|HH|$, $|VV|$, and $\sqrt{T_{22}}$ of the slant range NRCS (β^0) co-registered data. There is not much color due to lack of coherence between HH and VV. All of these images were created with identical histogram limits for every channel in order to compare relative power levels from colors. The reason for such a drastic change is because the region is home to Italy's reknowned rice patty fields that began flooded and became nearly full grown. The acquisition dates are (a) 2010/05/13 (b) 2010/05/20 (c) 2010/05/28 (d) 2010/06/21 and (e) 2010/06/29.

6.3.2 Simulation of SAR Observations from Ground Radar Data

Two dimensional histograms of the three observed variables, Z_h, Z_{dr} and K_{dp}, are shown in Fig. 6.25a and 6.25d for rain. This radar operates in a simultaneous H and V transmission mode, as opposed to alternating polarizations on each pulse, meaning that the linear depolarization ratio LDR is not available. Simulated data histograms are shown in Fig. 6.25b and 6.25d for comparison. In general, the real data has the same trend as the theoretical parameters, but the figure shows that a lot of Z_{dr} is negative as well as some K_{dp} despite attempts to correct for attenuation. Due to the resolution of the radar and the fairly large spatial gradients in Z_h, it is likely that the K_{dp} estimates were not able to capture the true features evident when they decreased to 0 at Z_h levels above 45 dBZ. Therefore, K_{dp} values in these regions were recalculated using the following power law relation [Wang and Chandrasekar (2009)]:

$$K_{dp} = aZ_h^b \tag{6.2}$$

where the coefficients are estimated from the theoretical relationship shown in 6.25d.

6.3.2.1 Gridding and hydrometeor classification

In order to eliminate one resampling step, the data were resampled on a georeferenced Cartesian grid that was aligned to the CSK swath rather than compass directions. The ascending orbit direction was approximately 349° pointing slightly NNW. Thus, a vertical slice corresponding to lines of the SAR image is simply one row at all depths in this weather radar data volume. The storm reflectivity and corresponding hydrometeor classification results at three slice planes within this gridded volume are shown in Fig. 6.26. Constant altitude slices at 2.5 km MSL are shown in Figs. 6.26a-b while Figs. 6.26c-d depict vertical slices at 78.5 km cross-track range and Figs. 6.26e-f are vertical slices at 16.5 km along-track range. Of particular interest are the lower two high intensity "cells" within 20 km from the radar in the northerly direction and 75 to 95 km toward the east. These resulted in the attenuation visible in the SAR image. Parts of the eastern cell were classified as hail plus rain, but below the melting layer is almost all rain. The empty region seen in Fig. 6.26c-d

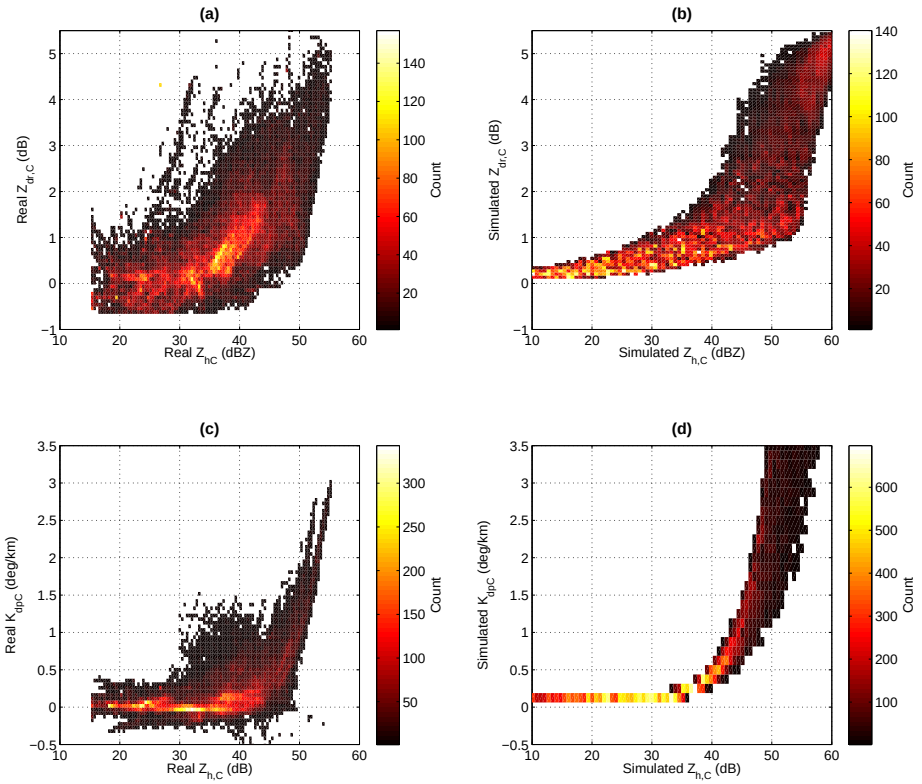

Figure 6.25: 2D histograms of rain from the 100629 data (left panels) and simulated C-band data used to train the NN (right panels). This shows the similarities and differences among three polarimetric observations: (a) real Z_{dr} vs. Z_h, (b) simulatedZ_{dr} vs. Z_h, (c) real K_{dp} vs. Z_h and (d) simulated K_{dp} vs. Z_h. The BRIC radar transmits simultaneous H and V, so LDR is not available.

near 20 km was filtered out due to $\rho_{HV} < 0.88$ which was probably influenced by ground clutter.

Similarly, Fig. 6.27 depicts Z_{dr} and the recalculated K_{dp} at the same slice locations as Fig. 6.26. The areas of high Z_{dr} and K_{dp} correspond well with the high Z_h regions in Fig. 6.26. The associated melting layer estimation is depicted in Fig. 6.28. Due to $Z_{dr} < 0$ near the surface as seen in Fig. 6.27c and 6.27e, which could be caused by attenuation, ground clutter or resonance, the algorithm determined the melting layer went down to the ground in some locations. This is highly unlikely in late June on the plains of northern Italy, so the melting layer was clipped at 3.5 km MSL (about 2.75 km AGL).

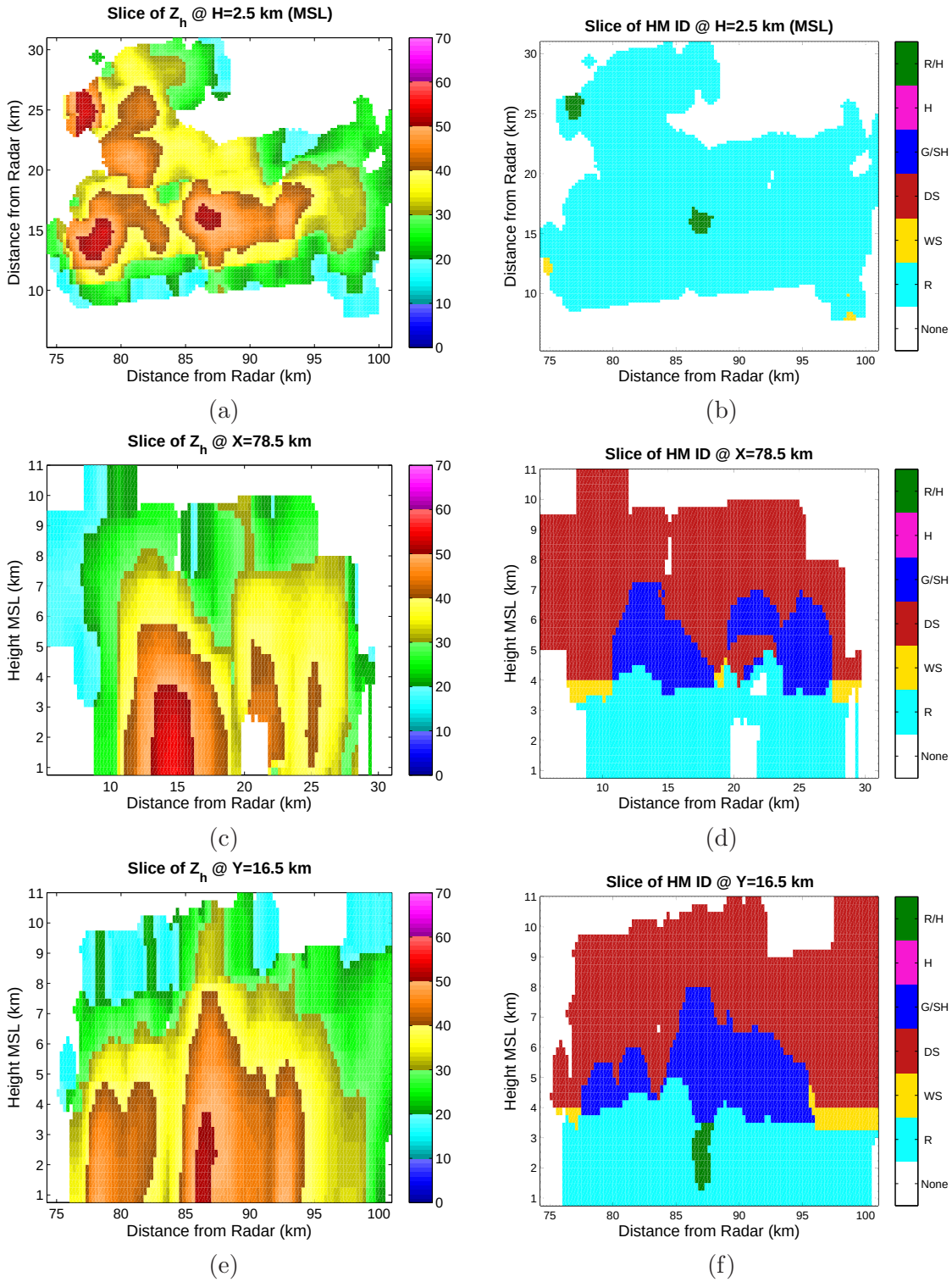

Figure 6.26: Reflectivity slices (left column) and hydrometeor classification (right column) for the gridded 100629 storm observed by the Bric della Croce C-band radar with the grid aligned to the COSMO-SkyMed swath. (a) and (b) are horizontal slices at 2.5 km MSL, (c) and (d) are northerly slices at 78.5 km from the radar and (e) and (f) are easterly slices at 16.5 km from the radar.

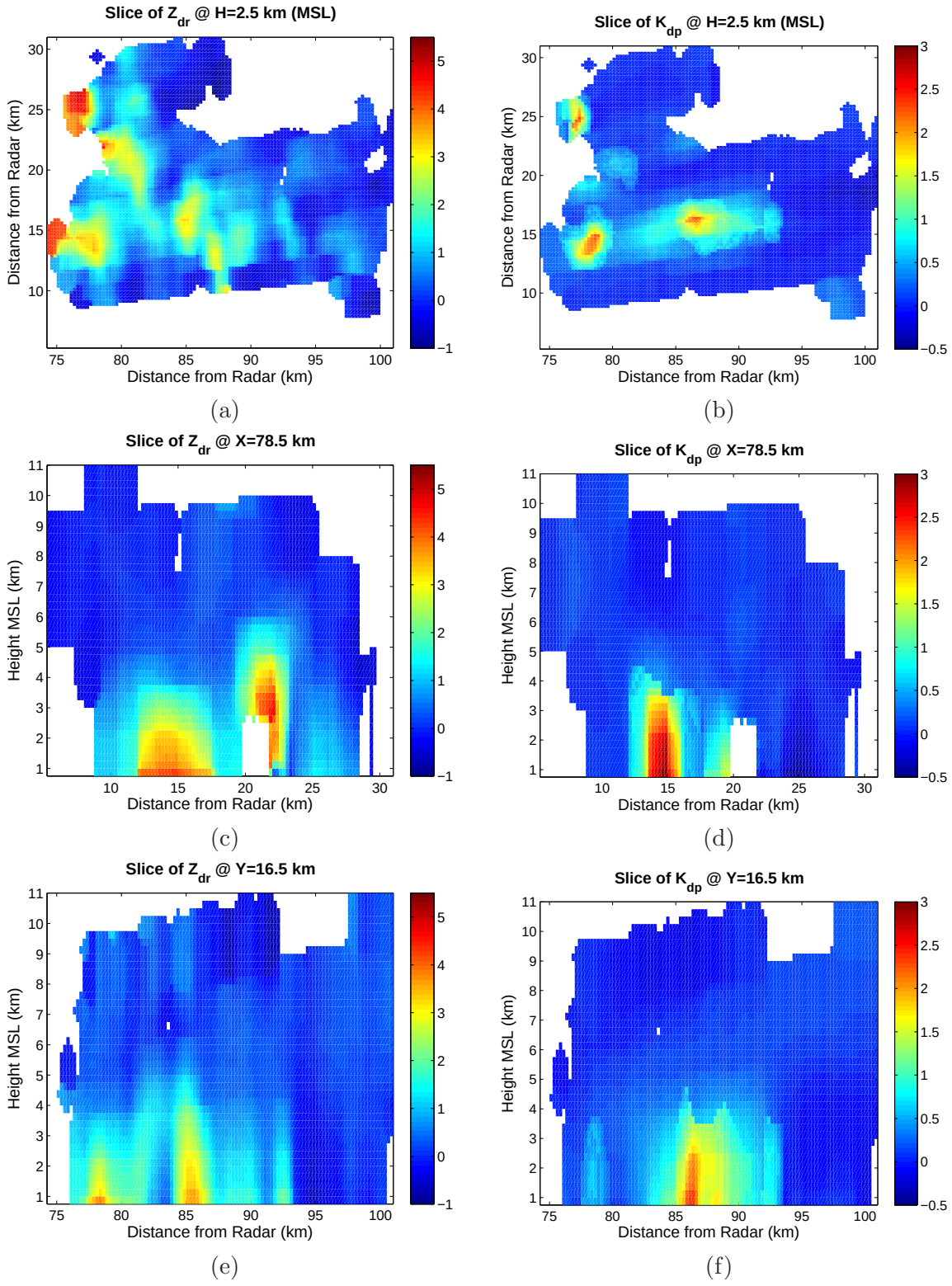

Figure 6.27: Z_{dr} (left column) and K_{dp} slices (right column) for the gridded 100629 storm observed by the Bric della Croce C-band radar with the grid aligned to the COSMO-SkyMed swath. (a) and (b) are horizontal slices at 2.5 km MSL, (c) and (d) are northerly slices at 78.5 km from the radar and (e) and (f) are easterly slices at 16.5 km from the radar.

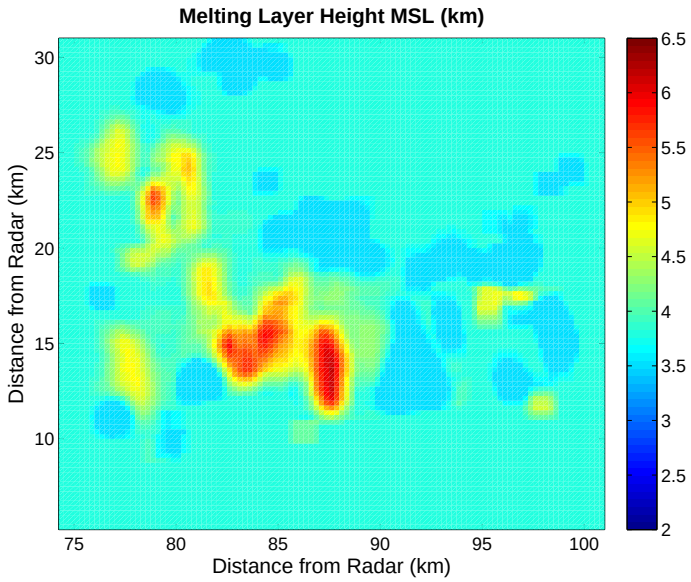

Figure 6.28: The melting layer height measured above MSL. The original output had the melting layer at ground level (0.75 km MSL), which was clipped to 3.5 km as shown.

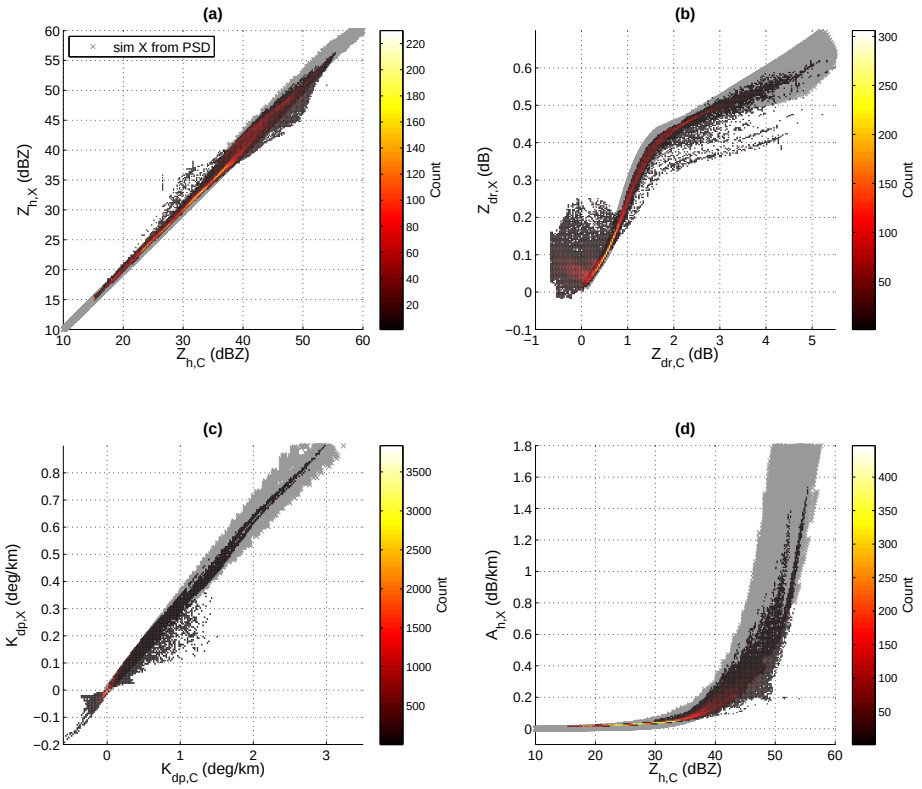

Figure 6.29: Simulated 25° incidence angle X-band observations of rain vs. real horizontal C-band 2D histograms of the 100629 storm overlaid on the pure simulation results (gray x's) (a) Z_h, (b) Z_{dr}, (c) K_{dp} and (d) A_h vs. $Z_{h,S}$.

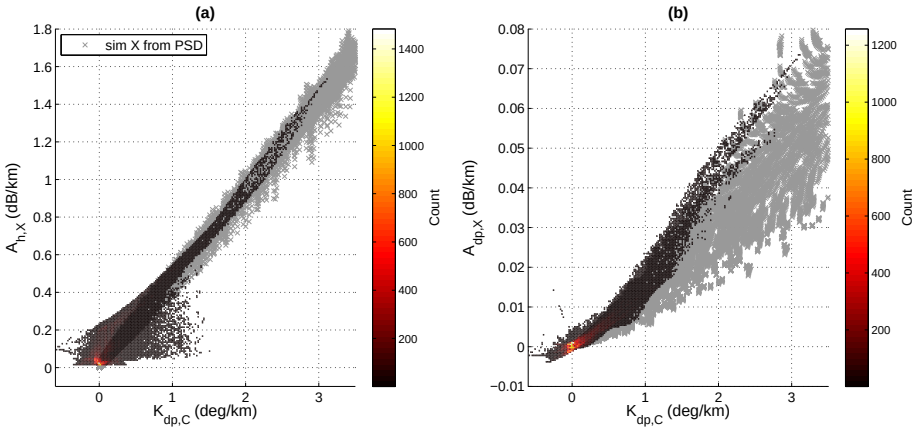

Figure 6.30: Simulated 25° incidence angle X-band attenuation due to rain vs. real horizontal C-band 2D histograms of the 100629 storm overlaid on the pure simulation results (gray x's) (a) A_h, (b) A_{dp}

6.3.2.2 Conversion to X-band

In order to convert the C-band ground observations into expected X-band spaceborne data, models of the relationship are applied depending upon the hydrometeor type. For frozen and melting particles, excluding hail, a simple least squares regression will determine coefficients for polynomial or power law models detailed in Chapter 4. For both hail and rain, a novel adaptive radial basis function neural network (A-RBFN) model was developed (see Section 4.7), and the output for the rain portion of this storm are shown in Figs. 6.29 and 6.30. These figures show 2D histograms of the A-RBFN output overlaid on the pure simulation output, and they show areas where some noisy input data results in noisy results. More importantly, however, Figs. 6.29d and 6.30a indicate that the specific attenuation is below 1 $\deg\,\mathrm{km}^{-1}$ for most data. This is due mostly to low estimation of K_{dp} as seen in Fig. 6.29c. Following the data conversion via the models, theoretical SAR observations are generated by resampling the converted volume in the reference frame of the CSK satellite.

6.3.2.3 Simulated X-band SAR

Using the models defined in Chapter 4, the conversion to 25° incidence angle X-band (Step 5 in Section 5.3.1) can be performed. Fig. 6.31 displays the reflectivity VMI after conversion, plus the border of the overlapping portion of the CSK swath. The dotted lines simply indicate six locations of vertical slices to use for analysis and validation. Fig. 6.32 shows the corresponding SAR image with white lines marking the same slice locations. While the high intensity portions of the storm as seen by the ground radar do have a spatial correspondence to the SAR attenuation, the eastern part of the storm seems to be slightly further south in the SAR image. There are many reasons for this that include advection, alignment errors and resolution. The issues surrounding the differences will be discussed in the subsequent sections.

Fig. 6.33 through Fig. 6.35 depict the vertical slices of the resulting simulated X-band data for reflectivity, specific attenuation and specific differential phase with lines indicating the SAR observation beam. From Fig. 6.33, the highest reflectivity observed from the SAR should occur around 9 and 10 km along-track, although stronger returns should be seen near 12 km as well. Referring to Fig. 6.32, the faint whitish cloud between 8 and 10 km

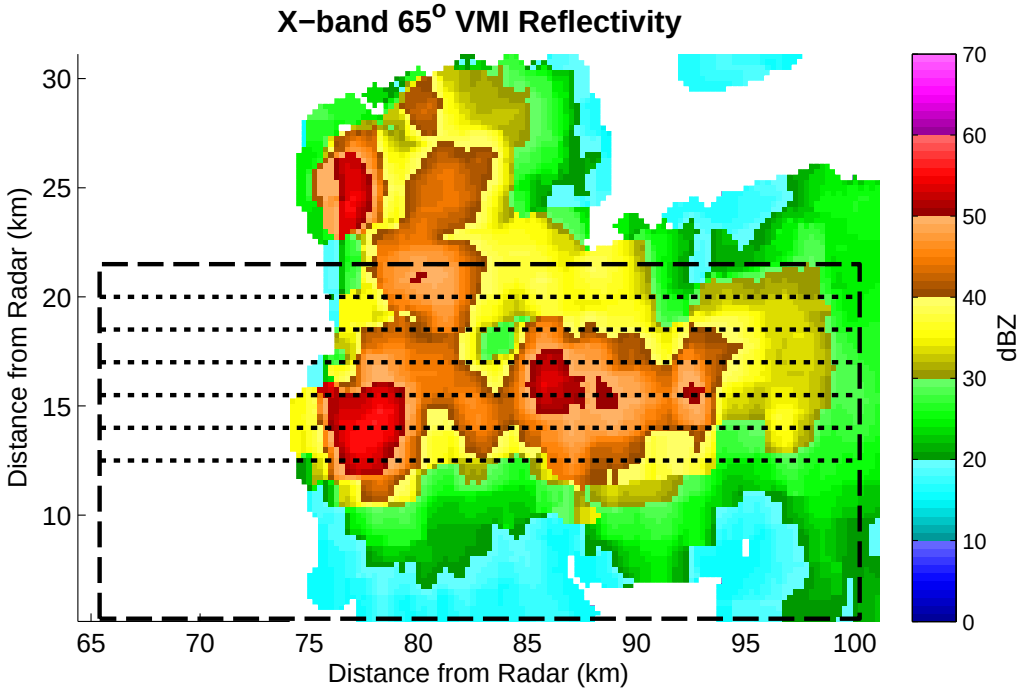

Figure 6.31: The Vertical Maximum Intensity (VMI) image showing the outline of the overlapping SAR acquisitions and 6 cross-track slices for analysis.

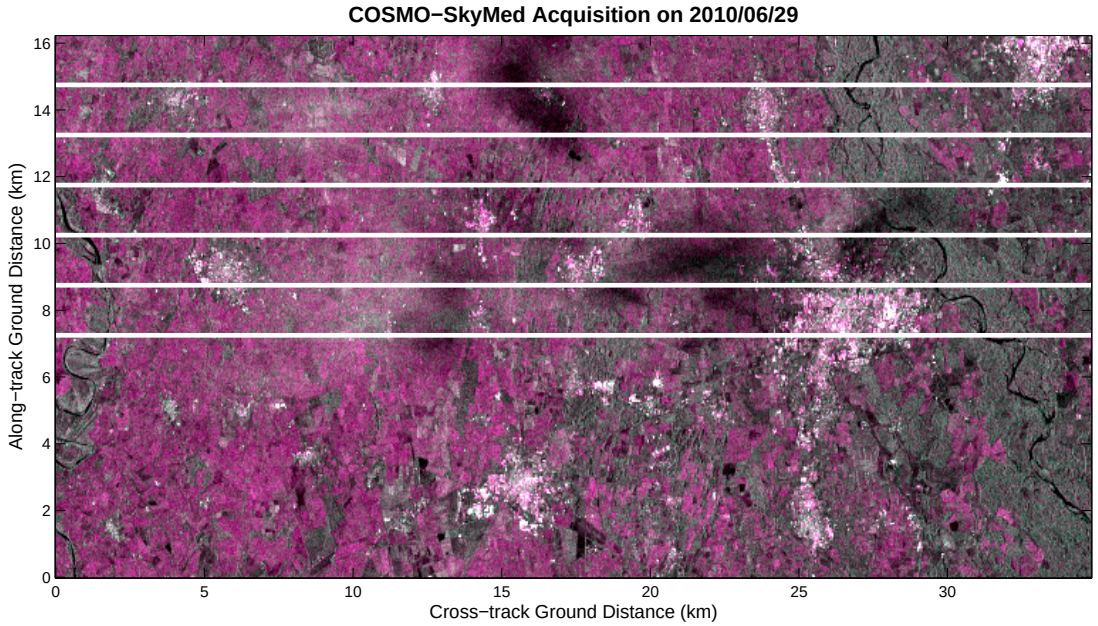

Figure 6.32: The region of the 100629 storm within the weather radar grid showing dimensions in km. The white lines indicate the cross-track slices shown in Fig. 6.31.

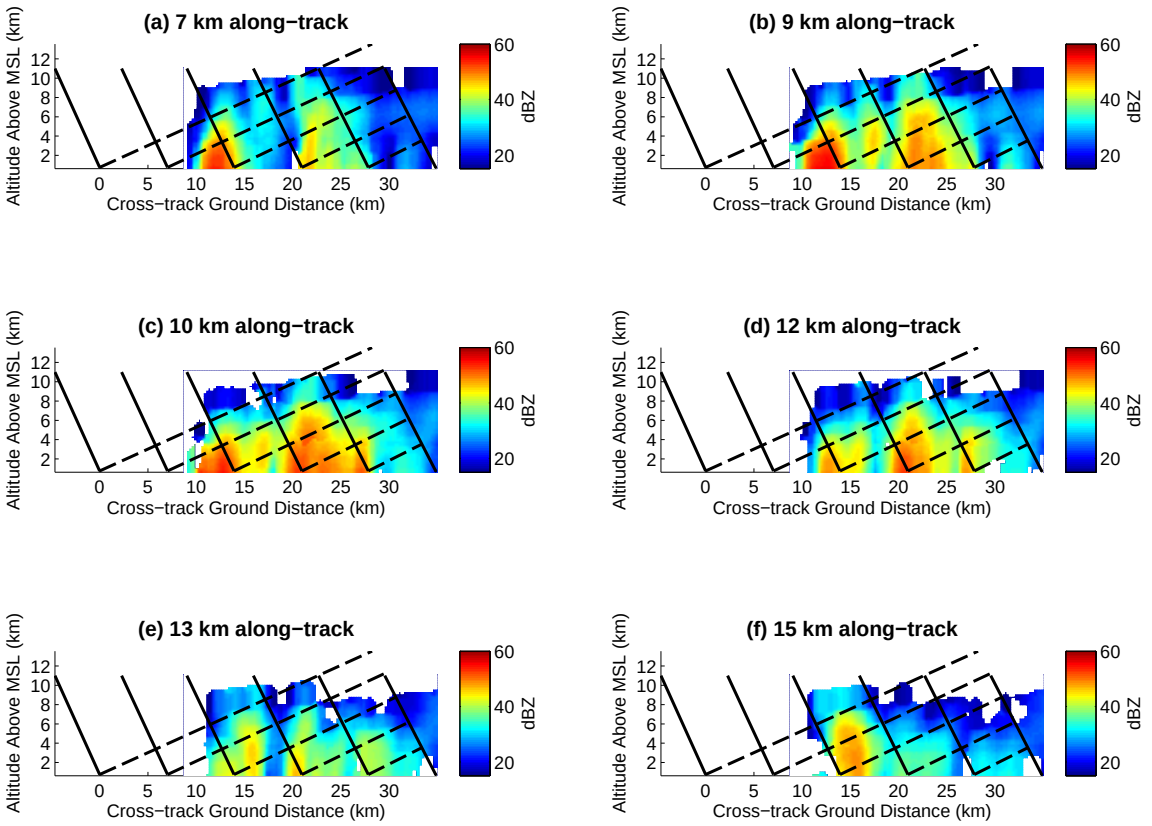

Figure 6.33: Simulated X-band reflectivity at the 6 slice locations of Fig. 6.32.

along-track and 10 km cross-track gives an indication that this is correct. Likewise, the A_h seen in Fig. 6.34 shows that higher attenuation should be detectable in these regions as well. Fig. 6.34f does not indicate the high attenuation seen in Fig. 6.32, but this issue will be discussed below. Finally, the K_{dp} that the SAR should see is depicted in Fig. 6.35. The values are relatively low except in panel (b). Also visible in the figure is the boundary between several hydrometeor classes. While the models may be fairly accurate in and of themselves, Fig. 6.35 provides evidence that the overall model should consider transition boundaries and constrain the results to be continuous across them.

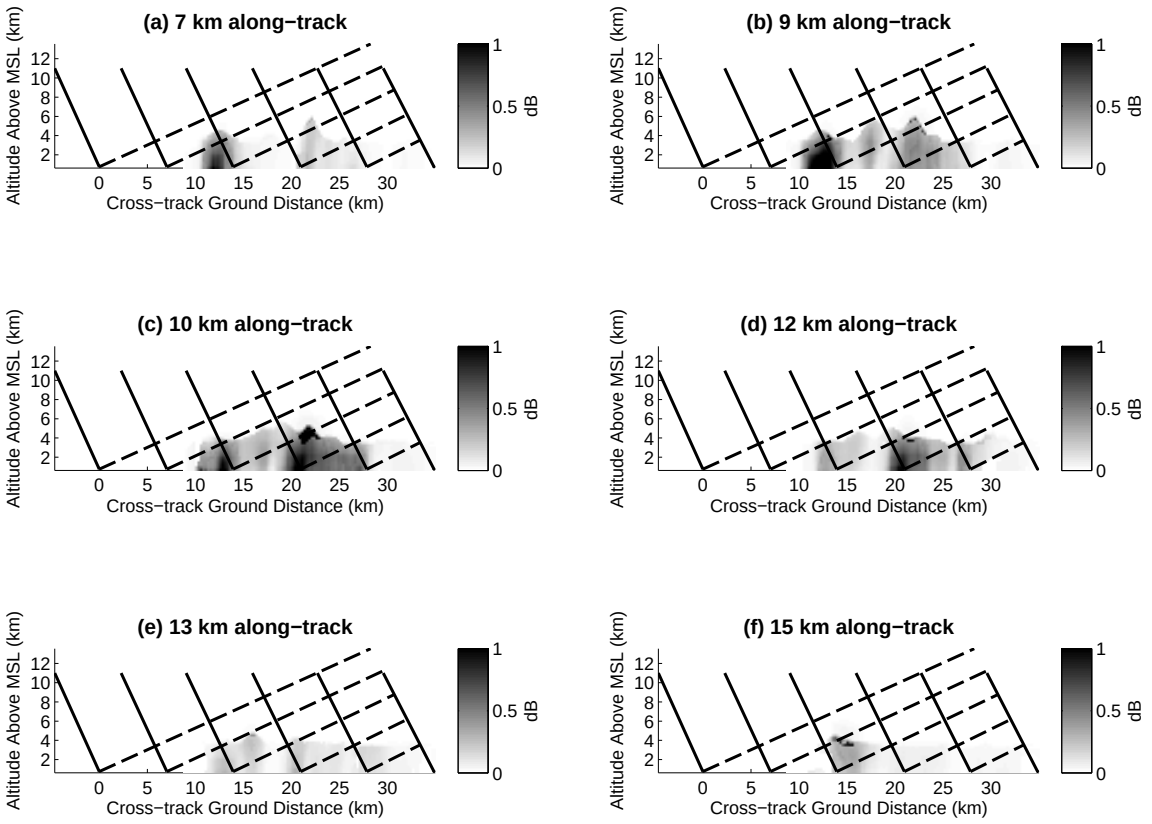

Figure 6.34: Simulated X-band horizontal attenuation at the 6 slice locations of Fig. 6.32.

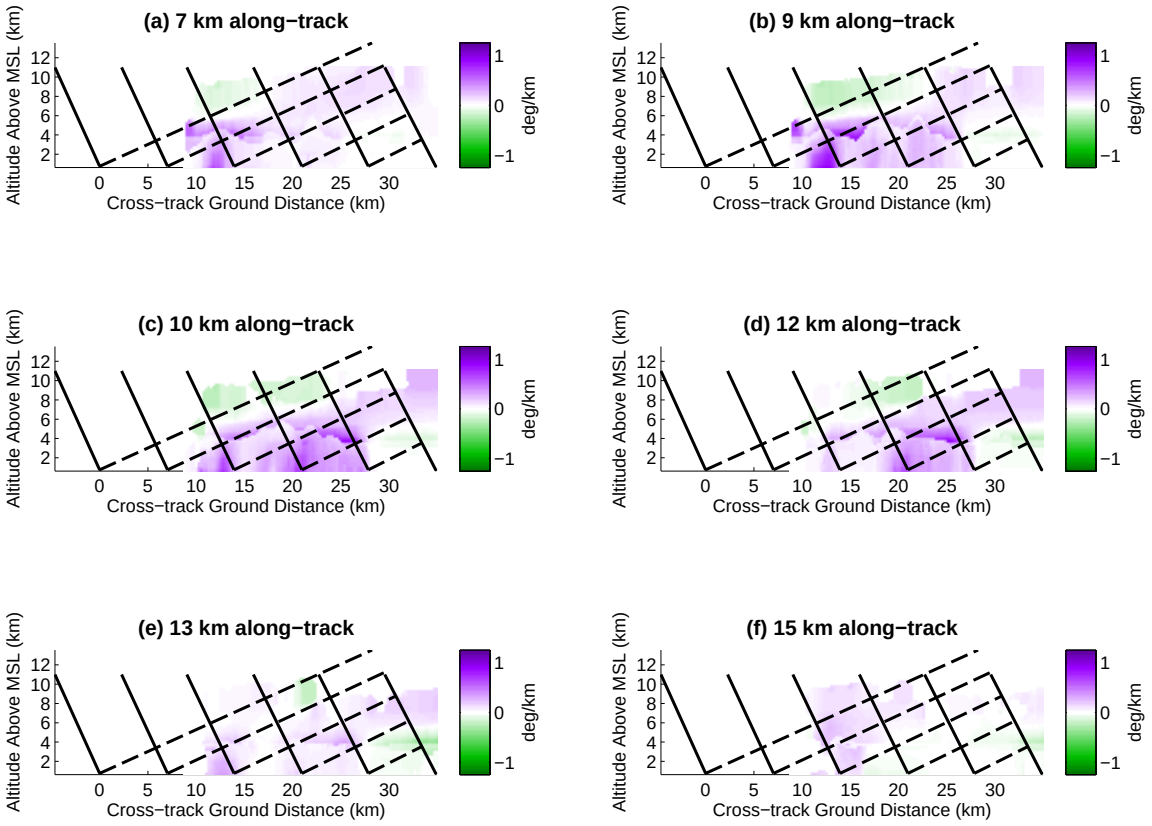

Figure 6.35: Simulated X-band K_{dp} at the 6 slice locations of Fig. 6.32.

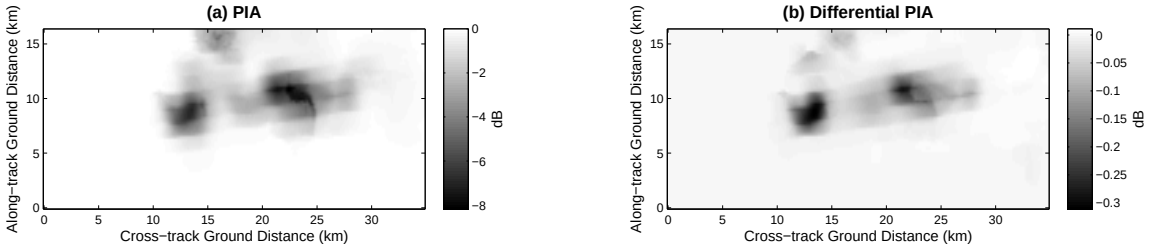

Figure 6.36: Simulated path integrated attenuation and differential attenuation within the SAR swath

Integrating along the SAR beam path, and considering the whole wavefront, the simulated data can be projected to the ground. Path integrated attenuation (PIA) is shown in Fig. 6.36a with a peak attenuation level of close to -8 dB. The two high intensity storm cells are clearly visible in the PIA image as well as in the differential PIA depicted in Fig. 6.36b. Differential PIA, however, is only around -0.25 dB in these regions. The volumetric horizontal RCS eta_h that the SAR would observe due to the storm is given in Fig. 6.37a. Meanwhile Fig. 6.37b considers the effect of the PIA and Fig. 6.37 shows the difference between horizontal and vertical volumetric RCS after attenuation is applied. Using the K_{dp} in Fig. 6.35, Φ_{dp} projected to the surface is shown in Fig. 6.38, although most of it is almost negligible at less than 3°. These results can then be added to a real SAR image to show the propagation effects of this storm.

6.3.3 Comparison of Simulated to Actual Observations

Ideally, a rain free SAR surface backscatter image could be estimated from the multiple acquisitions over the region of the storm. Unfortunately, due to the drastic changes in this particular region, as discussed in Section 6.3.1, such an estimation is not feasible. However, the 100621 acquisition was only 8 days prior to the 100629 storm and the surface changes are minimal relative to the others, so this was selected to incorporate the simulated storm effects. Once the attenuation and volumetric backscatter are added, comparisons to the case without rain can be made. Fig. 6.39 shows the power span ratio between the rain and no-rain cases where the attenuation overcomes the backscatter in most of the region except to the near-range side of the swath. This figure also indicates why the eastern cell appeared more attenuated in the real SAR image (Fig. 6.32) as we see that the level

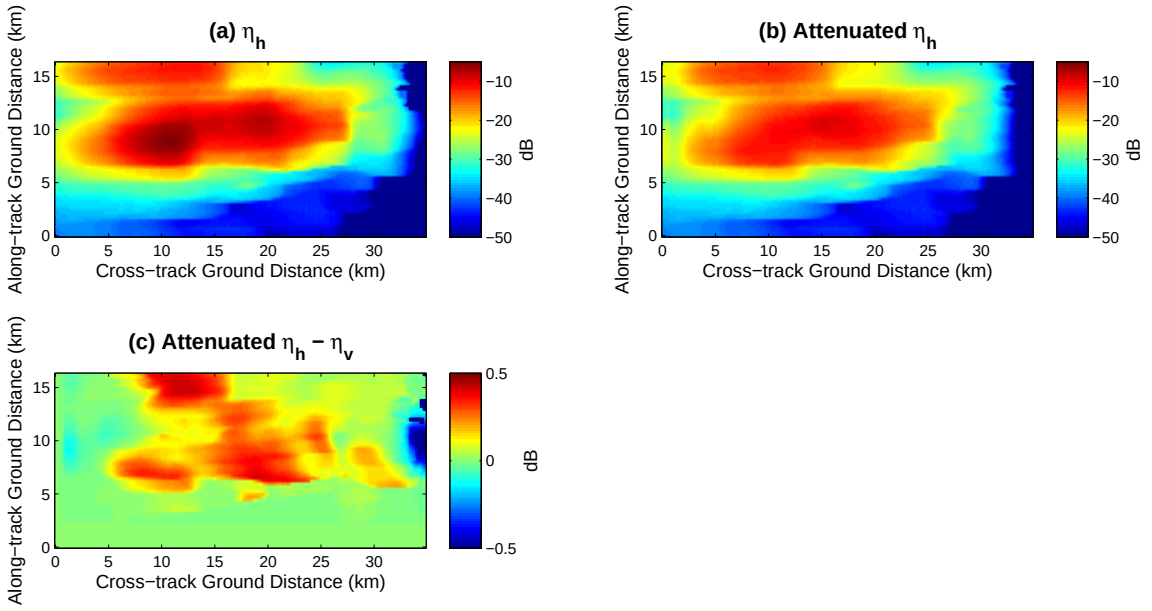

Figure 6.37: (a) The simulated volumetric radar cross section η_h from SAR with swath indicated in Fig. 6.31. (b) The attenuated η_h for the same swath. (c) The attenuated $\eta_h - \eta_v$.

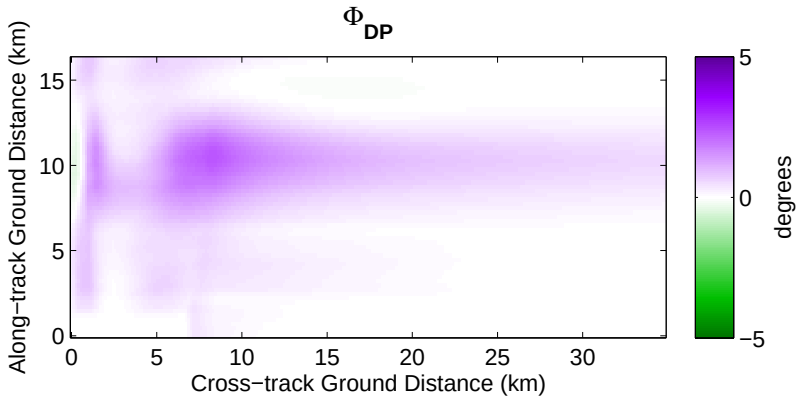

Figure 6.38: Simulated differential phase Φ_{dp} in the SAR swath.

of attenuation is reduced for the western cell between 10 and 15 km cross-track due to backscatter. Differential reflectivity changes from propagation effects are displayed in Fig. 6.40. Here we see that the western cell has a decrease of Z_{dr} of approximately 4−7 dB and in general, a decrease occurred throughout the area affected by precipitation. From Fig. 6.41 a higher HH is indicated by the fact that much of the scene has more red than green. Therefore, the storm decreases this Z_{dr} toward that of the storm itself. The ΔZ_{dr} shown in Fig. 6.40 is not solid like the attenuation because it is more dependent on the surface

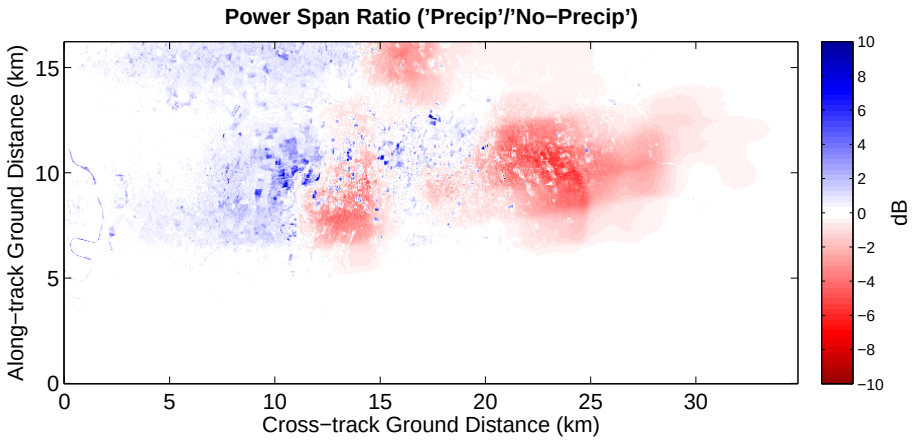

Figure 6.39: The span power ratio of the data with the storm over the original 100621 scene.

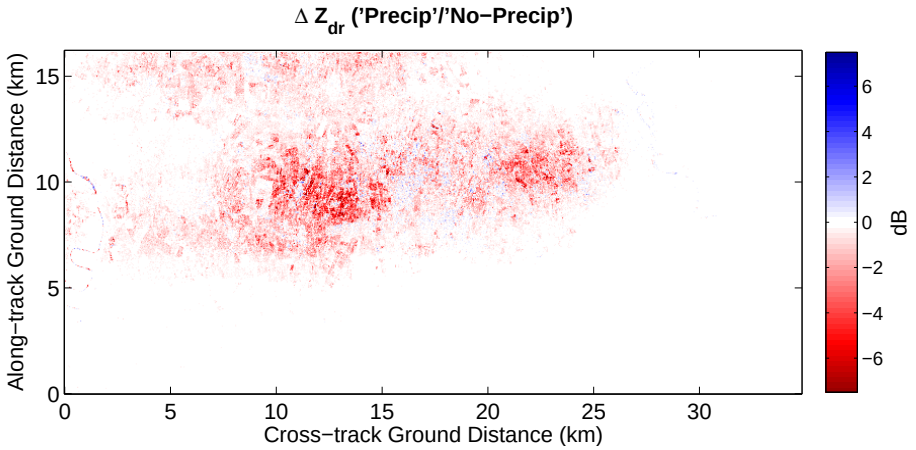

Figure 6.40: Differential reflectivity caused by the storm.

features and decreases more over the agricultural fields that had a higher HH return.

Color composite images of the 100621 acquisition with and without the simulated storm, plus the actual storm image of 100629 are shown in Fig. 6.41. As mentioned previously, the histogram limits for each channel were set to the same level for all acquisitions for comparison, resulting in reduced contrast with the simulated storm once it was added as seen in Fig. 6.41b. However, we can still see that the simulated version is not drastically different than the real one, although the location of the eastern cell is slightly further north than then real one. A power span of the simulated storm SAR and the real version is given in Fig. 6.42 where a better qualitative comparison can be made in a decibel scale. Considering that propagation effects visible in SAR images are always relative to the surface backscatter, the visual illusion can be somewhat deceiving.

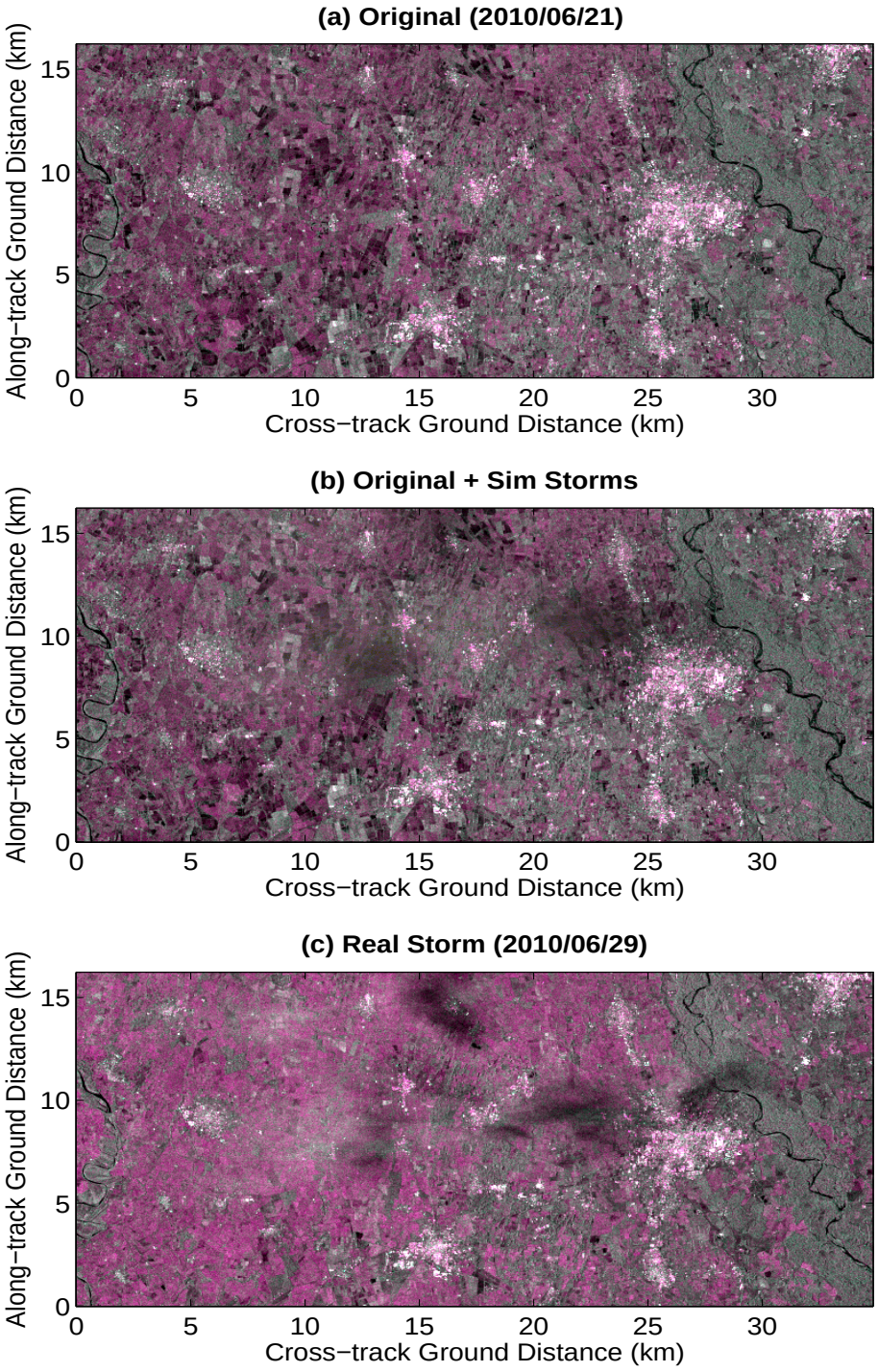

Figure 6.41: The simulated storm was added to the acquisition just prior to the one where the real storm occurred. (a) CSK data on 100621 (b) the storm added to 100621 (c) the real storm on 100629

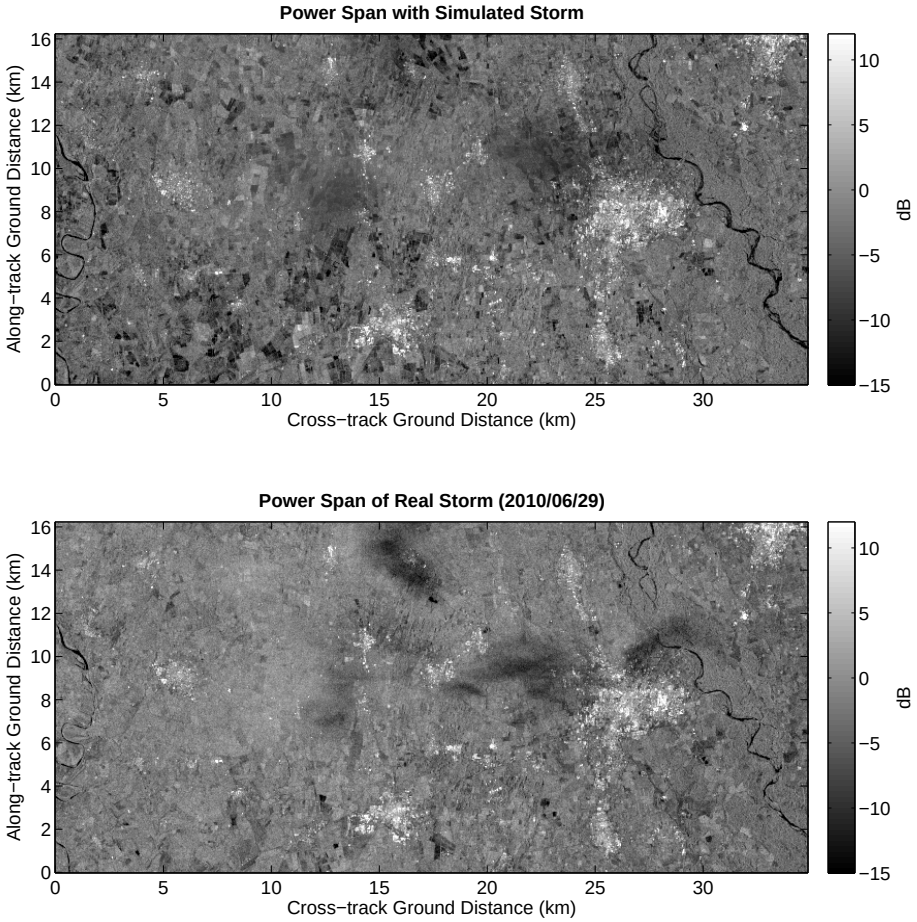

Figure 6.42: The power span of 100621 with the storm added (top) and the span of the 100629 data with the real storm.

Fig. 6.43 provides smoothed 1D slant range NRCS (β^0) values at four of the slices for a more quantitative analysis. At each slice indicated, the HH data is shown above the VV and a simple moving average filter with a window length of 7 was applied after averaging data to a resolution of approximately 150 m^2 grid cells. The blue lines indicate the original 100621 data while the green represents 100629 data with the real storm. In red is the 100621 data plus the simulated storm effects. At 7.2 km along-track, Fig. 6.43a shows the real storm decreasing HH power by roughly 5 dB from 10 to 15 km cross-track if we assume about a 1 dB increase from backscatter. In the simulated version, it only drops by 4 dB, but is obviously close to the real level. In Fig. 6.43b, however, the decrease is much closer at 8.8 km along-track , and 12 to 16 km cross-track, considering that the rain free case drops about 2 dB, as well as 19 to 26 km. At 10.2 km along-track, the simulated

attenuation is larger in the region from 20 to 30 km cross-track in Fig. 6.43c, but this is likely due to the combination of misalignment of the simulated data to the real storm and the low resolution of the simulation that causes a spreading effect. On the other hand, the slice at 14.8 km along-track shown in Fig. 6.43 indicates much stronger backscatter and attenuation, potentially up to 12 dB below the peak, than does the simulated data. This severe attenuation is also seen in Fig. 6.32 between 13 and 16 km along-track however, is not indicated by any of the ground radar measurements, including the raw data. Obviously, a feature not observed by the ground radar cannot be simulated, but this provides strong evidence that spaceborne high frequency SAR can be used to aid the study of meteorology as they might measure effects not seen on the ground.

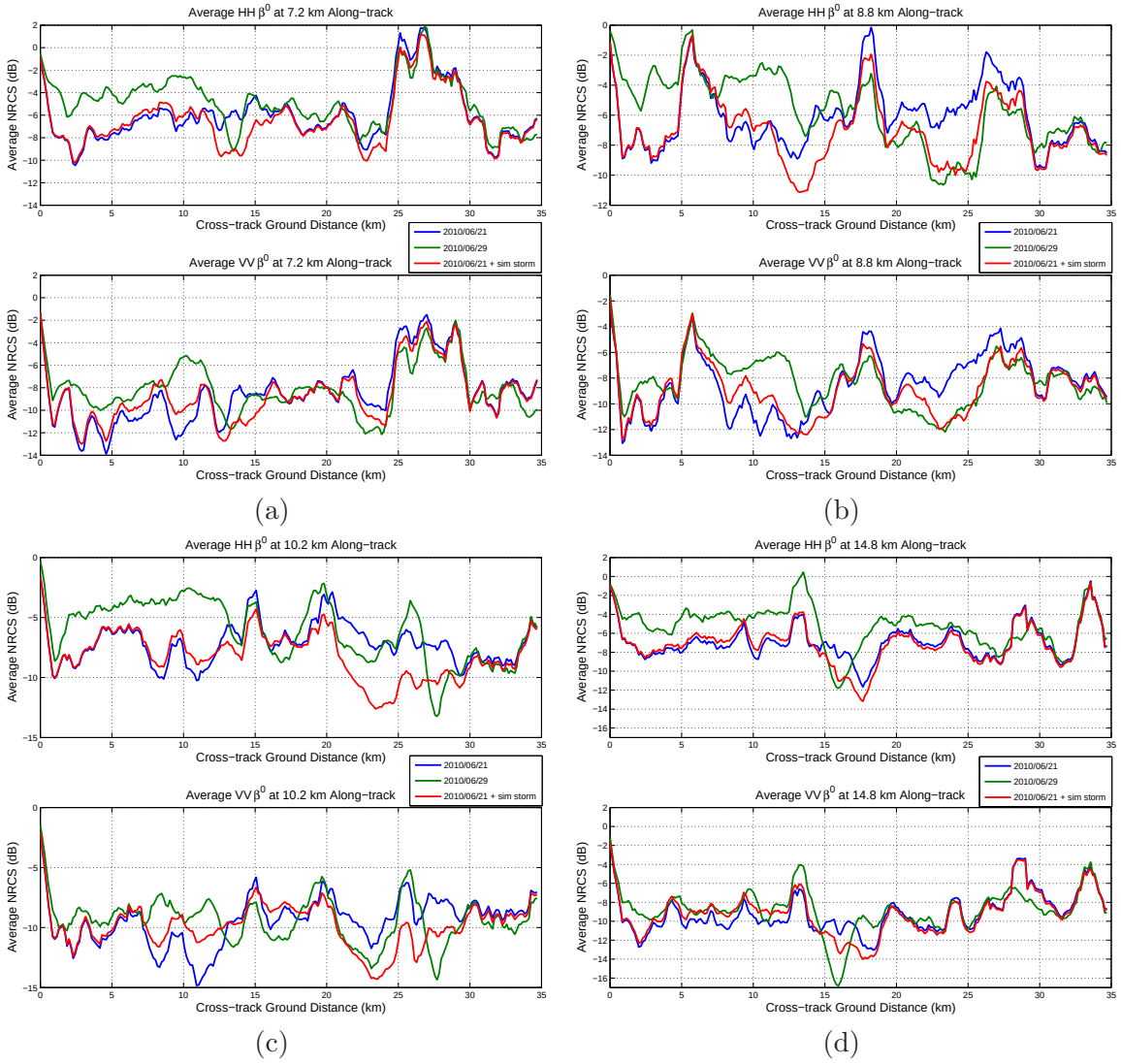

Figure 6.43: The averaged slant range HH and VV normalized radar cross-section at four of the 6 slices for the storm date (100629 in green) and the previous acquisition (100621 in blue). In addtion, the 100621 data with the simulated storm added is shown in red. While the simulated version did not line up exactly with the the real one, parts were very close and attenuation and backscatter similar. (a) 7.2 km (b) 8.8 km (c) 10.2 km (d) 11.8

6.4 Summary

Analyzing real simultaneous observations of convective storms by X-band satellite based SAR and ground-based weather radars provides validation for the theoretical models and simulated results presented in earlier chapters. The TerraSAR-X (TSX) and COSMO-SkyMed (CSK) SAR systems captured data of storms in HH and VV polarizations, while horizontal polarization S-band or fully polarimetric C-band weather radars operated on the ground. The theoretical relationship between S-band horizontally polarized reflectivity at low elevation angles with fully polarized X-band observations was then given for the TerraSAR-X and WSR-88D scenario.

Following the theory was the presentation of two cases, 8 and 19 August 2008, where the TSX observed storms over central Florida, USA using HH and VV polarized signals in the same operating mode. These two acquisitions, and the subsequent one on 30 August 2008, were co-registered for temporal comparisons between rain and no-rain states. The resulting images were shown to exhibit strong attenuation and even some noticeable backscatter, which was occasionally stronger in the HH channel. By comparing the georeferenced TSX data with a gridded 3D volume of ground-based S-band weather radar reflectivity, associations between precipitation levels and SAR observations were made. Attenuation was only apparent at reflectivity values above approximately 40 dBZ. Meanwhile, backscatter was not consistently visible, but it exists along the near-range side close to values reaching 50 dBZ. At other near-range locations, backscatter may go unnoticed without comparison to additional acquisitions in the same region.

A quantitative analysis of the TSX radar brightness and NEXRAD radar reflectivity provided more detailed evidence of the effect of rain on X-SAR images. Several cross-track zones and three larger rectangular zones were identified for analysis. By slicing the 3D reflectivity volume at the same location as the cross-track zones, it becomes more clear what the SAR wave travels through en route to and from the surface. In slant range space, observations from adjacent TSX acquisitions without severe rainfall were subtracted from that of the storm to provide a better indication of backscatter and attenuation, although they also include surface changes. When the near-range side of a convective cell was within

the SAR swath, backscatter most likely due to precipitation was present as predicted by the spatial model. However, in some cases backscatter was observed well into the highly reflective core as opposed to near the ice to water transition zone. In addition, the theoretical PIA based on the reflectivity slice showed reasonable similarity to the actual attenuation in most cases even though the entire reflectivity volume was modeled as rain without frozen particles.

Polarization related parameters were also quantitatively analyzed for further evidence of precipitation effects on the TSX observations. The convective squall line on 8 August 2008 in particular exhibited polarization dependent backscatter and attenuation. Beyond the histogram analysis, direct spatial comparison between rain and no-rain acquisitions reveals effects than cannot be attributed to surface change alone, although there exists some spatial correlation with surface features. The higher HH backscatter seen in Zones F and H near the high ground-based radar reflectivity is also indicative of oblate hydrometeors. All rectangular zones, except for D, also show an increase in co-polar correlation magnitude, and a reduction in extreme (close to 180°) co-polar phase shifts which also reduces observations $|S_{hh} - S_{vv}|$. These trends are both consistent with radar wave propagation through precipitation. Zone D, however, showed a reduction in $|\rho_{co}|$ and a nearly uniform distribution of phase difference between channels in addition to drastic attenuation. These are all signs that the signal is in or near the noise floor which was confirmed by the noise parameters supplied with the TSX data.

The second part of the chapter analyzed the CSK data with polarimetric C-band ground radar measurements. Using the theoretical models developed in Chapter 4 and the procedure outlined in Chapter 5, a simulation of X-band SAR observations was generated from the ground radar at the same incidence angle as the CSK acquisitions. Aligning the grid of weather radar data to the SAR image simplified the process of comparison between the two, although the georeference process will not be exact and is dependent on the accuracy of SAR geolocation parameters and the earth model used. Attenuation correction was also applied due to the wavelength, and near zero K_{dp} estimates were recalculated in the areas of high reflectivity to account for the low resolution. After converting the gridded volume to

X-band, parameters were integrated to obtain PIA and backscatter due to the precipitation and added to the CSK acquisition 8 days prior to the storm by more than 4 dB in some areas. Despite the fact that the surface backscatter was lower on this date, the storm simulated from ground radar data was comparable. Without data to create a "rain free" SAR image it was more challenging to ascertain the accuracy of the simulation. Further analysis at specific slice locations, however, showed that while the simulated storm did not exactly align with the real one, attenuation and backscatter were similar in most cases. By taking the ratio of power span and differential reflectivity from the simulated storm to the original data, a clearer picture emerged supporting the case that the model can be effectively used to recreate the SAR observations from ground radar data.

Certainly, alterations in the surface will exhibit polarimetric and backscatter fluctuations as demonstrated by using more than one "no-rain" reference case for the Florida storms and CSK acquisition prior to the storm date. However, with the aid of simultaneous ground-based weather radar observations, the results presented here show strong evidence of both propagation and backscatter effects from severe storms. This evidence provides further motivation for investigating meteorological phenomena using space-based X-band or Ku-band SAR systems, especially if they are polarimetric. These results also highlight the challenges in extracting precipitation effects and parameters over heterogeneous land with highly variable natural cover and high dynamic range. In cases where the differences between observations and theoretical PIA were more pronounced, there are numerous contributing factors. These factors include data quality from both systems, relatively low resolution of weather radar data and inaccuracies in the reflectivity corresponding to the precise SAR acquisition time that does not account for advection and inaccuracies in georeference locations. In addition, surface changes, incorrect hydrometeor classification and possible displacement of attenuation due to the hydrometeor Doppler velocity in the cross-track direction will all contribute to differences between the simulated values and the real ones. Overall, however, these results indicate that it is reasonable to accomplish and present the case for further research to improve the process.

CHAPTER 7

SUMMARY AND CONCLUSIONS

Today's scientists have substituted mathematics for experiments,
and they wander off through equation after equation, and
eventually build a structure which has no relation to reality.

- Nikola Tesla

7.1 Summary

The primary goal of this research was to characterize the impact of precipitation on synthetic aperture radars operating in the X band and higher in a quantitative fashion that has previously not been done to this extent. This was demonstrated by providing the theoretical foundation using a microphysical model of electromagnetic scattering of hydrometeors and the methodology to simulate SAR observations of a storm from real polarimetric ground-based radar measurements. Model validation was achieved by analyzing real SAR acquisitions of precipitation with coincident weather radars on the ground. Several cases were investigated with various degrees of polarized radars considering that the ideal case of fully polarimetric ground *and* space-based radar does not yet exist.

Chapter 2 presented the background of radar, polarimetry and SAR. The radar range equation was derived and the differences between weather radar and SAR were shown, and the radar cross section was discussed, especially in terms of Rayleigh and Mie scattering effects. Definitions of polarimetric weather radar observations were given as well as the construction of the scattering and covariance matrices. This was followed by the fundamentals of polarimetric SAR and a brief description of the instruments used in this research. Finally, a basic presentation of the minimal resource allocation radial basis function neural network applied to the modeling problem was discussed.

In Chapter 3, results from a study of precipitation induced land backscatter change were presented. Changes in the σ^0 caused by (near) surface water has implications for TRMM and potentially future missions that utilize a surface reference technique to estimate rain rate. The results shown, however, are preliminary, but the data covers one of the more challenging terrain types: coastal and inland lakes regions. SAR exhibits the potential to better characterize the surface change in order to improve rain rate estimates.

Following the σ^0 study, the microphysical model was presented in Chapter 4 allowing transformation of ground-based low elevation angle measurements to high elevation (low incidence) angle observations at shorter wavelengths. This model includes small frozen and melting particles as well as rain and hail with radar cross-sections beyond the Rayleigh scattering limit. Smaller particles can use simple least squares regression analysis to determine coefficients of polynomial and power law models. For rain and hail, a novel approach was developed using an adaptive neural network (ANN) to account for the oscillations that occur when the particle size approaches and exceeds the wavelength. For rain, this model was compared to common curve fit models to show that it performs equally as well for simulated data. The results applied to real data may have appear noisier; however, this occurs because it accounts for the inter-relation of multiple observation variable. The comparable attenuation model, however, had problems when $K_{dp} < 0$ vs. the ANN which assured $A_h \geq 0$ with little variation at lower reflectivity levels. The chapter wrapped up by presenting wavelength conversion results to X and Ku bands for real storms that were analyzed in more detail.

In Chapter 5, the methodology for using ground-based radar measurements of precipitation to simulate spaceborne SAR observations of the same storm was presented. Two real storms observed by the CSU-CHILL radar were used to simulate X-band SAR data: a supercell case from the STEPS experiment and a squall line with hail that melted before hitting the ground. For the supercell, two scenarios were devised by only using the convective region in one case and then by effectively looking at the opposite side of the storm for the other, including the stratiform region. The procedure to calculate the attenuation, backscatter and differential phase was then executed and the results added to rain free TSX

acquisitions over Florida with qualitative comparison to real storm observations in the same region.

Chapter 6 then investigated several real cases of multi-polarization SAR observations of storms and simultaneous ground radar data. Real data from TSX over Florida were analyzed, although only single polarization ground radar observations were available. However, using two ground radars with nearly opposite viewing angles of the storm allowed for an improved estimate of meteorological parameters at the time of SAR acquisition. Observed attenuation showed close resemblance to the theory when all ground measurements were considered to be rain. Following this case was a storm in June, 2010 observed in HH and VV by a COSMO-SkyMed SAR and a C-band polarimetric ground radar. Although the two SAR channels were not coherent, they did provide relative power information. In addition, the surface of the specific region had very low temporal coherence so a good "rain free" surface backscatter response was not possible. Despite the lace of a no-rain case, the use of a polarimetric ground radar allowed for the application of the modeling procedure detailed in Chapter 5 to simulate the SAR observations and then compare them.

7.2 Conclusions

The primary goal of this research was to establish how precipitation effects multi-polarization SAR imagery at frequencies in X-band and higher in a quantitative fashion. To meet the primary goal, three secondary goals of this research were to develop a microphysics based model to simulate storm observations from a short wavelength spaceborne radar using real ground-based polarimetric radar data, analyze and compare model results to real polarimetric X-SAR observations of storms with simultaneous data from ground-based weather radars and characterize surface backscatter changes caused by recent or active precipitation as seen from spaceborne radar. Other researchers have investigated this problem, and some have created basic models of precipitation as viewed by a spaceborne SAR, but this is the first to define the methodology and models to simulate spaceborne SAR precipitation observations using real ground radar data. It is also the first to investigate storm effects on high frequency polarimetric SAR measurements. Chapter 4 achieved the first goal, which demonstrated the simulation of any X or Ku band spaceborne radar observations at lower

incidence angles from either S or C band ground radar data. This can be applied to using SAR satellites for meteorology and it has implications for the off-nadir view angles of TRMM and GPM. Even hail models are included using the ANN approach, which is even more applicable at frequencies above X-band, and the results with real data fall well within the expected theoretical values. In addition, no modifications to the models were necessary to accommodate different input data from very different storms and radars, although a different set of network weights and biases are needed for each pair (e.g., horizontal S-band to 25° incidence angle Ku-band or horizontal C-band to 35° X-band).

While the model presented in Chapter 4 has applications for all high frequency spaceborne radars with beams pointed at off-nadir angles, it is applied to simulate SAR observations at X-band with promising results using the procedure spelled out in Chapter 5. A variation of this model is used when only single polarization data were available from the ground, but the estimated attenuation was within a few dB when the alignment between space and ground data was good. When polarimetric ground radar data was available, the and the simulated results from applying the full model are very similar to the real observations accounting for a much lower resolution and a spatial offset for part of the storm. Overall, however, the model demonstrated robustness as it is able to handle very noisy data without resulting in unrealistic output. There is also a region that was much more intense, i.e., causing higher attenuation and backscatter, in the SAR data than was observed by the ground radar indicating that SAR could improve the overall analysis of convective precipitation over a single ground radar alone.

Chapter 3 presented results of C-band SAR and TRMM observations of surface backscatter. These results provide strong evidence of the correlation of recent rainfall and increased surface backscatter that can be analyzed in detail with regular high resolution SAR acquisitions to characterize the change. However, this can vary dramatically between geographic regions and requires regular, short interval acquisitions to accurately characterize the surface. For regions such as Florida that have significant inland bodies of water or easily saturated soil, though, SAR can provide valuable information to improve the accuracy of the TRMM SRT result when it is known to vary significantly.

As a whole, the research presented here makes significant progress toward the study of precipitation from spaceborne SAR systems. It also establishes a precedent for modeling the propagation characteristics using polarimetric ground-based weather radars.

7.3 Suggestions for Future Work

There are a number of ways to carry this research forward with the ultimate goal of creating algorithms to estimate rain rate from high frequency spaceborne SAR by improving the model of the forward problem. These fall into four general categories: frequency conversion model improvements, SAR data processing, weather radar data processing and new data. More details are provided below.

1. Frequency conversion model

    - Optimize the A-RBF training algorithm to achieve the best result for the quickest training time.
    - Use spatial relationships for the final converted product to avoid discontinuities at the boundaries of hydrometeor classes, and/or
    - Modify the output of the hydrometeor classification to create transitional boundaries between classes.
    - Investigate allowing the ANN to adapt to the real data. This requires a target value which could be determined by the median of adjacent grid cells that have already been calculated, e.g., the graupel and snow particles that do not use a neural network.

2. SAR data processing

    - Apply a/the real antenna pattern to weight the data when resampling into the SAR coordinate system versus the ideal beam used in this work.
    - Process the SAR data through the orthorectification step to determine an accurate georeferenced location of each pixel in the slant range. This requires the SAR processing software to save the affine transform applied to each pixel.

Simply projecting the slant range coordinates to one of the standard elliptical models (e.g., WGS84) is not accurate enough for some data such as those from COSMO-SkyMed.

- Investigate the storm effect on co-polar phase shift. The theoretical estimates did not correspond well with the real ones, potentially due to the image formation processing.
- Process from raw SAR data and consider system parameters (e.g., noise). The results presented here essentially assumed the SAR data came from a real aperture without considering system noise and processing for image formation (i.e., matched filtering). While this is the best starting point, the next step would be to consider that the real beam is very wide, which is a potential cause of the problems matching co-polar phase. Attenuation could reduce signal strength to the noise floor and the scattering affects make the Doppler Centroid estimation much more challenging. Processing from what is commonly referred to as "raw phase history" (the complex voltage for each pulse) and using the backprojection algorithm to form the SAR image could provide a deeper understanding of the precipitation impact on SAR observations. It is also possible that modifications to the SAR image formation processing could yield better "focus" on the storm itself versus the surface. An investigation into SAR processing for moving target identification (MTI) or traffic monitoring applications would be warranted.

3. Weather data processing

- Explore advection correction algorithms to account for the ground radar volume collection time relative to the SAR acquisition time
- Explore the Doppler shift in SAR observations due to hydrometeor motion relative to the SAR platform
- Improve the geo-location of the gridded data, possibly incorporating a Digital Elevation Model (DEM)
- Investigate improvements from a network of ground-based radars

- Improve data filtering. Filtering too much can reduce the peaks of backscatter and attenuation, but not filtering enough can result in unrealistic gaps. The ANN could potentially help in this regard considering it is a model of the relationship between radar observation types for a given hydrometeor class. Using the ANN would fall under the category of model-based processing and could also identify mis-classified data.

4. New data

    - Acquire and analyze more data of X-SAR observations of storms with simultaneous ground radar measurements, ideally with fully polarimetric radars for both space and ground
    - Investigate surface backscatter change relative to precipitation events using a higher frequency SAR, ideally with regular acquisitions that will overlap with a TRMM observation
    - If the data becomes available, investigate additional aspects such as bistatic SAR, along-track interferometry or cross-track interferometric phase change induced by the precipitation

BIBLIOGRAPHY

Alberga, V., 2004: *Comparison of polarimetric methods in image classification and SAR interferometry applications*. Ph.D. thesis, Institut für Hochfrequenztechnik und Radarsysteme Oberpfaffenhofen (DLR).

Andsager, K., K. V. Beard, and N. F. Laird, 1999: Laboratory measurements of axis ratios for large raindrops. *J. Atmos. Sci.*, **56**, 2673–2683.

Atlas, D., 1994: Footprints of storms on the sea: a view from spaceborne synthetic aperture radar. *J. Geophys. Research*, **99**, 7961–7969.

Atlas, D. and R. K. Moore, 1987: The measurement of precipitation with synthetic aperture radar. *J. Atmos. Ocean Tech.*, **4**, 368–376.

Aydin, K., V. N. Bringi, and L. Liu, 1994: Rain-rate estimation in the presence of hail using S-band specfic differential phase and other radar parameters. *J. Appl. Met.*, **34**, 404–410.

Aydin, K., T. Seliga, and B. V., 1986: Remote sensing of hail with a dual linear polarization radar. *J. Appl. Met. Clim.*, **25**, 1475–1484.

Aydin, K. and Y. Zhao, 1990: A computational study of polarimetric radar observables in hail. *IEEE Trans. Geosci. Remote Sensing*, **28**, 412–422.

Balakrishnan, N. and D. Zrnic, 1990: Use of polariztion to characterize precipitation and discriminate large hail. *J. Atmos. Sci.*, **47**, 1525–1540.

Beard, K. V. and C. Chuang, 1987: A new model for the equlibrium shape of raindrops. *J. Atmos. Sci.*, **44**, 1509–1524.

Bohren, C. and L. Battan, 1980: Radar backscattering in inhomogeneous precipitation particles. *J. Atmos. Sci.*, **37**, 1821–1827.

Bolen, S. and V. Chandrasekar, 2003: Quantitative estimation of tropical rainfall mapping mission precipitation radar signals from ground-based polarimetric radar observations. *Radio Sci.*, **38**, doi:10.1029/2002RS002625.

Born, G., J. Dunne, and D. Lame, 1979: Seasat mission overview. *Science*, **204**, 1405–1406.

Bringi, V., V. Chandresaker, J. Hubbert, G. E., W. L. Randeu, and M. Schoenhuber, 2003: Raindrop size distribution in difference climatic regimes from disdrometer and dual-polarized radar analysis. *J. Atmos. Sci.*, **60**, 354–365.

Bringi, V. N. and V. Chandrasekar, 2001: *Polarimetric Doppler Weather Radar: Principles and Applications*. Cambridge University Press.

Bringi, V. N., T. Tang, and V. Chandrasekar, 2004: Evaluation of a new polarimetrically based ZR relation. *J. Atmos. Ocean Tech.*, **21**, 612–623, doi:10.1175/1520-0426(2004)021¡0612:EOANPB¿2.0.CO;2.

Buckreuss, S., W. Balzer, P. Mühlbauer, R. Werninghaus, and W. Pitz, 2003: The TerraSAR-X satellite project. *IEEE Internatl. Geosci. Remote Sensing Symp. IGARSS '03 Proceedings*, IEEE, volume 5, 3096 – 3098.

Bundas, D., 2006: Global Precipitation Measurement mission - architecture and mission concept. *IEEE Aerospace Conference 2006 Proceedings*.

Campa, G., M. Fravolini, and M. Napolitano, 2002: A library of adaptive neural networks for control purposes. *Intnatl. Symp. Comp. Aided Contr. Sys. Design Proc.*, IEEE.

Chandrasekar, V. and D. Khajonrat, 2009: Simulation of space-borne radar observations of precipitation at Ku and Ka band. *34th Conf. on Radar Meteorology*, Am. Meteor. Soc., Williamsburg, VA.

Chandrasekar, V., S. Lim, and E. Gorgucci, 2006: Simulation of X-band rainfall observations from S-band radar data. *J. Atmos. Ocean Tech.*, **23**, 1195–1205.

Cheng, L. and M. English, 1983: A relationship between hailstone concenration and size. *J. Atmos. Sci.*, **40**, 204–213.

Cheng, L., M. English, and R. Wong, 1985: Hailstone size distributions and their relationship to storm thermodynamics. *Journal of Applied Meteorology and Climatology*, **24**, 10591067.

Cloude, S. R. and K. P. Papathanassiou, 1998: Polarimetric SAR interferometry. *IEEE Trans. Geosci. Remote Sensing*, **36**, 1551–1565.

Cloude, S. R. and E. Pottier, 1996: A review of target decomposition theorems in radar polarimetry. *IEEE Trans. Geosci. Remote Sensing*, **34**, 498–518.

Conradsen, K., A. A. Nielsen, J. Schou, and H. Skriver, 2003: A test statistic in the complex Wishart distribution and its application to change detection in polarimetric SAR data. *IEEE Trans. Geosci. Remote Sensing*, **41**, 4–19.

Contreras, R., W. Plant, W. Keller, K. Hayes, and J. Nystuen, 2003: Effects of rain on ku-band backscatter from the ocean. *J. Geophys. Research*, **108**, doi:10.1029/2001JC001255.

CSA, 1995: RADARSAT-1 components and specifications. website.
URL http://www.asc-csa.gc.ca/eng/satellites/radarsat1/components.asp

Cumming, I. and F. Wong, 2005: *Digital Processing of Synthethic Aperture Radar Data: Algorithms and Implementation*. Artech House.

Curlander, J. C. and R. N. McDonough, 1991: *Synthetic Aperture Radar: Systems and Signal Processing*. Wiley Series in Remote Sensing, John Wiley & Sons, Inc.

Danklmayer, A., B. Doring, M. Schwerdt, and M. Chandra, 2008: Analysis of atmospheric propagation effects in TerraSAR-X images. *IEEE Internatl. Geosci. Remote Sensing Symp. IGARSS '08 Proceedings*.

Danklmayer, A., B. Döring, M. Schwerdt, and M. Chandra, 2009: Assessment of atmospheric propagation effects in SAR images. *IEEE Trans. Geosci. Remote Sensing*, **47**, 3507–3518.

Doerry, A. W., 2006: Performance limits for synthetic aperture radar - second edition. Technical Report SAND2006-0821, Sandia National Laboratories, Albuquerque, NM USA.

El-Magd, A., V. Chandrasekar, V. Bringi, and W. Strapp, 2000: Multiparameter radar and in situ aircraft observations of graupel and hail. *IEEE Trans. Geosci. Remote Sensing*, **38**, 570–578.

Freeman, A. and S. Durden, 1998: A three-component scattering model for polarimetric SAR data. *IEEE Trans. Geosci. Remote Sensing*, **36**, 963–973.

Freeman, A., J. van Zyl, J. Klein, H. Zebker, and Y. Shen, 1992: Calibration of stokes and scattering matrix format polarimetric SAR data. *IEEE Trans. Geosci. Remote Sensing*, **30**, 531–539.

Fritz, J. and V. Chandrasekar, 2008: The impact of adaptive speckle filtering on multichannel SAR change detection. *Proc. IGARSS*.

— 2009a: Analyzing radar backscatter of land within the TRMM footprint using high resolution SAR. *Proc. IGARSS*, IEEE, Cape Town, South Africa.

— 2009b: Simultaneous observations of a tropical cyclone from dual-pol TerraSAR-X and ground-based weather radar. *Proc. Radar Conf.*, IEEE, Pasadena, USA.

— 2009c: Simultaneous observations of X-band polarimetric SAR and ground-based weather radar during a tropical storm to characterize the propagation effects. *Proc. EUCAP*, Berlin, Germany.

— 2010a: Simulating spaceborne X-band polarimetric SAR observations of precipitation using ground-based S-band weather radar data. *Proc. SPIE*, K. I. Ranney and A. W. Doerry, eds., volume 7669.

— 2010b: Simultaneous observations and analysis of severe storms using polarimetric X-band SAR and ground-based weather radar. *IEEE Trans. Geosci. Remote Sensing*, **48**.

Hanssen, R. F., 2001: *Radar Interferometry*, volume 2 of *Remote Sensing and Digital Image Processing*. Kluwer Academic Publishers.

Haykin, S., 1999: *Neural Networks: a comprehensive foundation*. Prentice Hall, New Jersey, 2d edition.

Hélière, F., L. C., F. Fois, M. Arcioni, A. Lecuyot, C. Mangenot, K. Klooster, P. Rinous, M. Aloisio, and N. Gallou, 2010: Microwave technology activities for future SAR candidate earth explorer core missions. *8th Euro. Conf. on Synth. Aper. Radar*, Aachen, Germany.

Herrmann, J. and A. G. Bottero, 2007: TerraSAR-X mission: The new generation of high resolution satellites. *Anais XIII Simpósio Brasileiro de Sensoriamento Remoto*, INPE, Florianópolis, Brazil, 7063–7070.

Jameson, A. R., F. K. Li, S. L. Durden, Z. S. Haddad, B. Holt, T. Fogarty, E. Im, and R. K. Moore, 1997: SIR-C/X-SAR observations of rain storms. *Remt. Sens. Environ.*, **59**, 267–279.

Kampes, B. and S. Usai, 1999: Doris: The Delft Object-oriented Radar Interferometric Software. *Proc. ITC 2nd ORS Symp.*.

Khajonrat, D., 2008: *Simulation of space-based radar observations of precipitations*. Ph.D. thesis, Colorado State University.

Kummerow, C., W. B. T. Kozu, J. Shiue, and J. Simpson, 1998: The Tropical Rainfall Measuring Mission (TRMM) sensor package. *J. Atmos. Ocean Tech.*, **15**, 809–817, doi:10.1175/1520-0426(1998)015¡0809:TTRMMT¿2.0.CO;2.

Lakshmanan, V., T. Smith, K. Hondl, G. J. Stumpf, and A. Witt, 2006: A real-time, three dimensional, rapidly updating, heterogeneous radar merger technique for reflectivity, velocity and derived products. *Weather and Forecasting*, **21**, 802–823.

Lakshmanan, V., T. Smith, G. J. Stumpf, and K. Hondl, 2007: The Warning Decision Support System - Integrated Information (wdss-ii). *Weather and Forecasting*, **22**, 592–608.

Lang, T., J. Miller., M. Weisman, S. Rutledge, L. Barker III, V. N. Bringi, V. Chandrasekar, A. Detwiler, N. Doesken, J. Helsdon, C. Knight, P. Krehbiel, W. A. Lyons, D. Macgorman, E. Rasmussen, W. Rison, W. D. Rust, and R. J. Thomas, 2004: The severe thunderstorm electrification and precipitation study. *Bull. Amer. Meteor. Soc.*, **85**, 1107–1125, doi:10.1175/BAMS-85-8-1107.

Lascody, R., 2002: The onset of the wet and dry seasons in east central florida- a subtropical wet-dry climate? Website.
URL http://www.srh.noaa.gov/mlb/wetdry/WetDrySeason.html

Lee, J.-S., M. R. Grunes, T. L. Ainsworth, L.-J. Du, D. L. Schuler, and S. R. Cloude, 1999: Unsupervised classification using polarimetric decomposition and the complex Wishart classifier. *IEEE Trans. Geosci. Remote Sensing*, **37**, 2249–2258.

Li, Y., N. Sundararajan, and P. Saratchandran, 2000: Analysis of minimal radial basis function network algorithm for real-time identification of nonlinear dynamic systems. *IEE Proc. Control Theory Appl.*, **147**, 476–484.

Liao, L. and R. Meneghini, 2005: On modeling air/spaceborn radar returns in the melting layer. *IEEE Internatl. Geosci. Remote Sensing*, **43**, 2799–2809.

Lim, S., V. Chandrasekar, and V. Bringi, 2005: Hydrometeor classification system using dual-polarization radar measurements: model improvements and in situ verification. *IEEE Trans. Geosci. Remote Sensing*, **43**, 792–801.

Lin, I.-I., W. Alpers, V. Khoo, H. Lim, T. K. Lim, and D. Kasilingam, 2001: An ERS-1 synthetic aperture radar image of a tropical squall line compared with weather radar data. *IEEE Trans. Geosci. Remote Sensing*, **39**, 937–945.

Liu, C., E. Zipser, D. Cecil, S. Nesbitt, and S. Sherwood, 2008: A cloud and precipitation feature database from nine years of TRMM observations. *J. Appl. Met. Clim.*, **47**, 2712–2728, doi:10.1175/2008JAMC1890.1.

Liu, H., V. Chandrasekar, and G. Xu, 2001: An adaptive neural network scheme for radar rainfall estimation from WSR-99D observations. *J. Appl. Met.*, **40**, 2038–2050.

Marzano, F. and J. Weinman, 2008: Inversion of spaceborne X-band synthetic aperture radar measurements for precipitation remote sensing over land. *IEEE Trans. Geosci. Remote Sensing*, **46**, 3472–3487.

Marzano, F., J. Weinman, A. Mugnai, and N. Pierdicca, 2006: Rain retrieval over land from X-band spaceborne synthetic aperture radar: a model study. *Proceedings of ERAD 2006*.

Maxwell Garnett, J. C., 1904: Colours in metal glasses and in metallic films. *Philos. Tran. R. Soc. London, Sect. A*, **203**, 385–420.

Melsheimer, C., W. Alpers, and M. Gade, 1998: Investigation of multifrequency/multipolarization radar signatures of rain cells over the ocean using SIR-C/X-SAR data. *J. Geophys. Research*, **103**, 18867–18884.

— 2001: Simultaneous observations of rain cells over the ocean by the synthetic aperture radar aboard the ERS satellites and by surface-based weather radars. *J. Geophys. Research*, **106**, 4665–4677.

Meneghini, R., T. Iguchi, T. Kozu, L. Liao, K. Okamoto, J. A. Jones, and J. Kwiatkowski, 2000: Use of the Surface Reference Technique for path attenuation estimates from the TRMM Precipitation Radar. *J. Appl. Met.*, **39**, 2053–2070.

Meneghini, R. and L. Liao, 1996: Comparisons of cross sections for melting hydrometeors as derived frm dielectric mixing formulas and numerical methods. *J. Appl. Met.*, **35**, 1658–1670.

Mishchenko, M., L. Travis, and D. Mackowski, 1996: T-matrix computations of light scattering by nonspherical particles: A review. *J. Quant. Spectrosc. Radiat. Transfe*, **55**, 535–575, doi:10.1016/0022-4073(96)00002-7.

Moore, R., K. Soofi, and S. Purduski, 1980: A radar clutter model: average scattering coefficients of land, snow, and ice. *IEEE T. Aero. Elec. Sys.*, **AES-16**, 783–799.

Moore, R. K., A. Mogili, Y. Fang, B. Beh, and A. Ahamad, 1997: Rain measurement with SIR-C/X-SAR. *Rem. Sensing Env.*, **59**, 280–293.

NASA, 2010: NASA radar finds ice deposits at moon's north pole. http://www.nasa.gov/. URL mission_pages/Mini-RF/multimedia/feature_ice_like_deposits.html

NASDA, 2001: *TRMM Data Users Handbook*. Earth Observation Center: National Space Development Agency of Japan, Japan.

Oki, T., S. Seto, and K. Musiake, 2000: Land surface monitoring by backscattering coefficient from trmm/pr 2a21. *IEEE Internatl. Geosci. Remote Sensing Symp. IGARSS '00 Proceedings*, 2032–4.

Oliver, C. and S. Quegan, 2004: *Understanding Synthetic Aperture Radar Images*. SciTech Publishing, Raleigh, NC.

Olson, W., P. Bauer, N. Viltard, D. Johnson, W. Tao, R. Meneghini, and L. Liao, 2001: A melting-layer model for passive/active microwave remote sensing applications. part I: Model formulation and comparison with observations. *J. Appl. Met.*, **40**, 1145–63.

Pichugin, A. P. and Y. G. Spiridonov, 1985: Spatial structure of precipitation zones on space radar images. *Issled. Zemli iz Kosmosa*, **5**, 20–28.

Platt, J. C., 1991: A resource allocation network for function interpolation. *Neural Computation*, **3**, 213–225.

Probert-Jones, J., 1962: The radar equation in meteorology. *Quart. J. Roy. Meteor. Soc.*, **88**, 485–495.

Raney, R. K., A. Freeman, R. W. Hawkins, and R. Bamler, 1994: A plea for radar brightness. *IEEE Internatl. Geosci. Remote Sensing Symp. IGARSS '94 Proceedings*.

Ray, P., 1972: Broadband complex refractive indices of ice and water. *Applied Optics*, **11**, 1836–1844.

Seto, S. and T. Iguchi, 2007: Rainfall-induced changes in actual surface backscattering cross secions and effects on rain-rate estimates by spacebourne precipitation radar. *J. Atmos. Ocean Tech.*, **24**, 1693–1709.

Smith, P., 1984: Equivalent radar reflectivity factors for snow and ice particles. *J. Appl. Met. Clim.*, **23**, 1258–1260.

Steiner, M., R. A. Houze, and S. E. Yuter, 1995: Climitalogical characterization of three-dimensional storm structures from operational radar and rain gauge data. *J. Appl. Met.*, **34**, 1978–2007.

Stewart, S. and J. Beven, 2009: Tropical cyclone report: Tropical storm fay. Technical Report AL062008, National Hurricane Center.

Tabb, M., T. Flynn, and R. Carande, 2004: Full Maximum Likelihood Inversion of PolInSAR Scattering Models. *IEEE Internatl. Geosci. Remote Sensing Symp. IGARSS '04 Proceedings*.

Testud, J., E. Le Bouar, E. Obligis, and M. Ali-Mehenni, 2000: The rain profiling algorithm applied to polarimetric weather radar. *J. Atmos. Ocean Tech.*, **17**, 332–356.

Torres, S. and C. Curtis, 2006: Design considerations for improved tornado detecion using super-resolution data on the NEXRAD network. *Proceedings of ERAD*.

Ulaby, F. T. and M. C. Dobson, 1989: *Handbook of Radar Scattering Statistics for Terrain*. Artech House.

Ulaby, F. T. and C. Elachi, eds., 1990: *Radar polarimetry for geoscience applications*. Artech House Remote Sensing Library, Artech House.

Ulaby, F. T., R. K. Moore, and A. K. Fung, 1986: *Microwave Remote Sensing Active and Passive: Volume II. Radar Remote Sensing and Surface Scattering and Emission Theory*. Remote Sensing, Artech House.

Ulbrich, C. W., 1983: Natural variations in the analytical form of the raindrop size distribution. *J. Appl. Met.*, **22**, 1764–1775.

USDC/NOAA, 2006: *Federal Meteorological Handbook No. 11: Doppler Radar Meteorological Observations. Part D: WSR-88D Unit Description and Operational Applications*. Office of the Federal Coordinator for Meteorological Services and Supporting Research. U.S. Department of Commerce/National Oceanic and Atmospheric Administration, Washington, D. C.

van Zyl, J., C. Papas, and C. Elachi, 1987: On the optimum polarizations of incoherently reflected waves. *IEEE Trans. Antennas and Propagation*, **35**, 818–825.

Vulpiani, G., F. Marzano, V. Chandrasekar, A. Berne, and R. Uijlenhoet, 2006: Polarimetric weather radar retrieval of raindrop size distribution by means of a regularized artificial neural network. *IEEE Trans. Geosci. Remote Sensing*, **44**, 3262–3275, doi:10.1109/TGRS.2006.878438.

Vulpiani, G., F. Marzano, V. Chandrasekar, and S. Lim, 2005: Constrained iterative technique with embedded neural network for dual-polarization radar correction of rain path attenuation. *IEEE Trans. Geosci. Remote Sensing*, **43**, 2305–2314, doi:10.1109/TGRS.2005.855623.

Wang, Y. and V. Chandrasekar, 2009: Algorithm for estimation of the specific differential phase. *J. Atmos. Ocean Tech.*, **26**, 2565–2578.

Weinman, J. and F. Marzano, 2008: An exploratory study to derive precipitation over land from X-band synthetic aperture radar measurements. *J. Appl. Met. Clim.*, **47**, 562–575.

Wessel, P. and W. H. F. Smith, 1995: New version of the generic mapping tools released. *EOS Trans. AGU*, **76**, 329.

Willis, P. T., 1984: Functional fits to some observed drop size distributions and parameterization of rain. *J. Atmos. Sci.*, **41**, 1648–1661, doi:10.1175/1520-0469(1984)041¡1648:FFTSOD¿2.0.CO;2.

Xiao, R. and V. Chandrasekar, 1997: Development of a neural network based algorithm for rainfall estimation from radar observations. *IEEE Trans. Geosci. Remote Sensing*, **35**, 160–171, doi:10.1109/36.551944.

Yokoyama, T. and H. Tanaka, 1984: Microphysical processes of melting layer snowflakes detected by two wavelength radar. part 1. principle of measurement based on model calculation. *J. Meteor. Soc. Japan*, **62**.